THE OHIO STATE UNIVERSITY

Modeling of Reinforced Concrete Members with Discontinuities

Authors:

Md Ferdous Wahid, Ph.D. student (Department of Civil, Environmental and Geodetic Engineering)

Ali Nassiri, Ph.D. (Department of Integrated Systems Engineering)

Halil Sezen, Ph.D. (Department of Civil, Environmental and Geodetic Engineering)

October 2024

Introduction

The analysis and design of reinforced concrete members with discontinuities, such as corbels, deep beams, shear walls with openings, and walking columns, present significant challenges due to their complex behavior under various loading conditions. Traditional analytical methods often fall short in capturing the intricacies of these discontinuities, necessitating the use of advanced numerical tools and methods. The Strut-and-Tie Model (STM), as outlined in ACI 318-19, is commonly employed to model the load transfer mechanism in such members, but its effectiveness varies depending on the structure and design parameters. The Compatible Stress Field Method (CSFM) as a novel shell-based numerical method and traditional 3D finite element analysis (FEA) both provide enhanced capabilities to model and analyze the behavior of these members, offering deeper insights into their load-bearing capacities, stress distribution, and failure modes.

This research focuses on evaluating the structural behavior of different types of reinforced concrete members with discontinuities. Four critical structural elements are examined: corbels, deep beams, shear walls with openings, and walking columns. For each element, numerical simulations using both CSFM (using IDEA StatiCa version 24) and traditional FEA methods (using ABAQUS version 2023) are performed to validate the results against experimental data from published studies. The primary goal of this investigation is to assess the effectiveness of CSFM in modeling these discontinuous members and to compare the results from CSFM-based calculations with those obtained from experiments, STM, and ABAQUS.

To achieve this objective, a series of steps were taken in this study:

- **Reinforced Concrete Corbels**: Seven corbel specimens were analyzed using CSFM and ABAQUS, with their strength and deformation capacities compared to experimental results and design capacities from ACI 318-19 and AASHTO LRFD.
- **Reinforced Concrete Deep Beams**: Five deep beam specimens were studied, focusing on their load-deflection relationship and failure modes. The results were obtained from CSFM analysis and ABAQUS and compared to the experimental data and STM-based calculations in ACI 318-19.
- **Shear Walls with Openings**: Four shear wall specimens were evaluated for their lateral load capacity and drift angle. The study also examined the effects of varying opening sizes and locations on the overall behavior, with results validated against experimental data and numerical simulations. In addition, the specimens were analyzed for the behavior of confined concrete, and the capacity was determined considering the confinement effect of concrete.

- **Walking Columns**: The vertical load capacity of four walking column specimens was assessed using CSFM, ABAQUS, and STM focusing on stress distribution and failure patterns.

By integrating these methodologies, this verification studies provides a comprehensive understanding of the behavior of reinforced concrete members with discontinuities. The findings will contribute to the validation of both the STM and the CSFM and offer recommendations for the application of CSFM in structural engineering practice.

Chapter 1. Modeling and Analysis of Reinforced Concrete Corbels

1.1. Introduction

In this study, the behavior of seven reinforced concrete (RC) corbel specimens is investigated. Their strength and deformation capacities were calculated using IDEA StatiCa and compared with design capacities calculated using the ACI 318-19 (2019) and AASHTO LRFD (2016) procedures. The results were compared with experimental data. One of the tested corbel specimens was selected as a baseline model for further investigation through ABAQUS software (version 2023), where midpoint deflection, principal stress distribution, and crack patterns were computed and compared with those measured during experiments (Wilson, 2017). Additionally, the influence of secondary reinforcement on corbel capacities was investigated in detail.

1.2 Experimental Study

To evaluate the structural performance of corbels, four double-corbel specimens, identified as C0 through C3, were designed based on the strut and tie model (STM) provisions of ACI 318-19 (2014) by Wilson (2017). Another three double-corbel specimens, denoted as S1, S2, and S3, were designed according to the STM provisions of AASHTO LRFD (2016) by Khosravikia et al. (2018). The specimens were designed, fabricated, and tested at the Ferguson Structural Engineering Laboratory of the University of Texas at Austin. Consistency was maintained across the primary reinforcement of the four specimens in category C, while the secondary reinforcement varied. Similarly, specimens S1, S2, and S3 shared the same geometry but had variations in both primary and secondary reinforcements. All seven specimens were exclusively designed to withstand vertical loading, with potential horizontal tensile forces disregarded. Therefore, test setups were simplified, focusing solely on vertical loads, with each specimen supported by two bearing plates. Among all seven specimens, C0 was chosen as the baseline model and was analyzed in ABAQUS.

1.2.1 Corbel Properties and Experimental Details of Category C Specimens

All four specimens (C0, C1, C2, and C3) were designed with similar dimensions, including a width of 14 in. (356 mm), a total corbel height of 24 in. (610 mm), a corbel length of 20 in. (508 mm) on each side, and an extended column height of 12 in. (305 mm). The geometry of the specimens and the reinforcement detailing utilized within each specimen are depicted in Figure 1.1. The design parameters of the corbel specimens are presented in Table 1.1. It is noted that the specimens in Figure 1.1 are presented in the orientation in which they were tested.

Table 1.1: Specimen design parameters (Wilson, 2017). Note: 1 kip = 4.45 kN.

Properties	C0	C1	C2	C3
Shear span-to-depth ratio, a_v/d	0.66	0.59		
Design capacity, kips (kN)	523 (2327)	421 (1872)	523 (2327)	418 (1860)

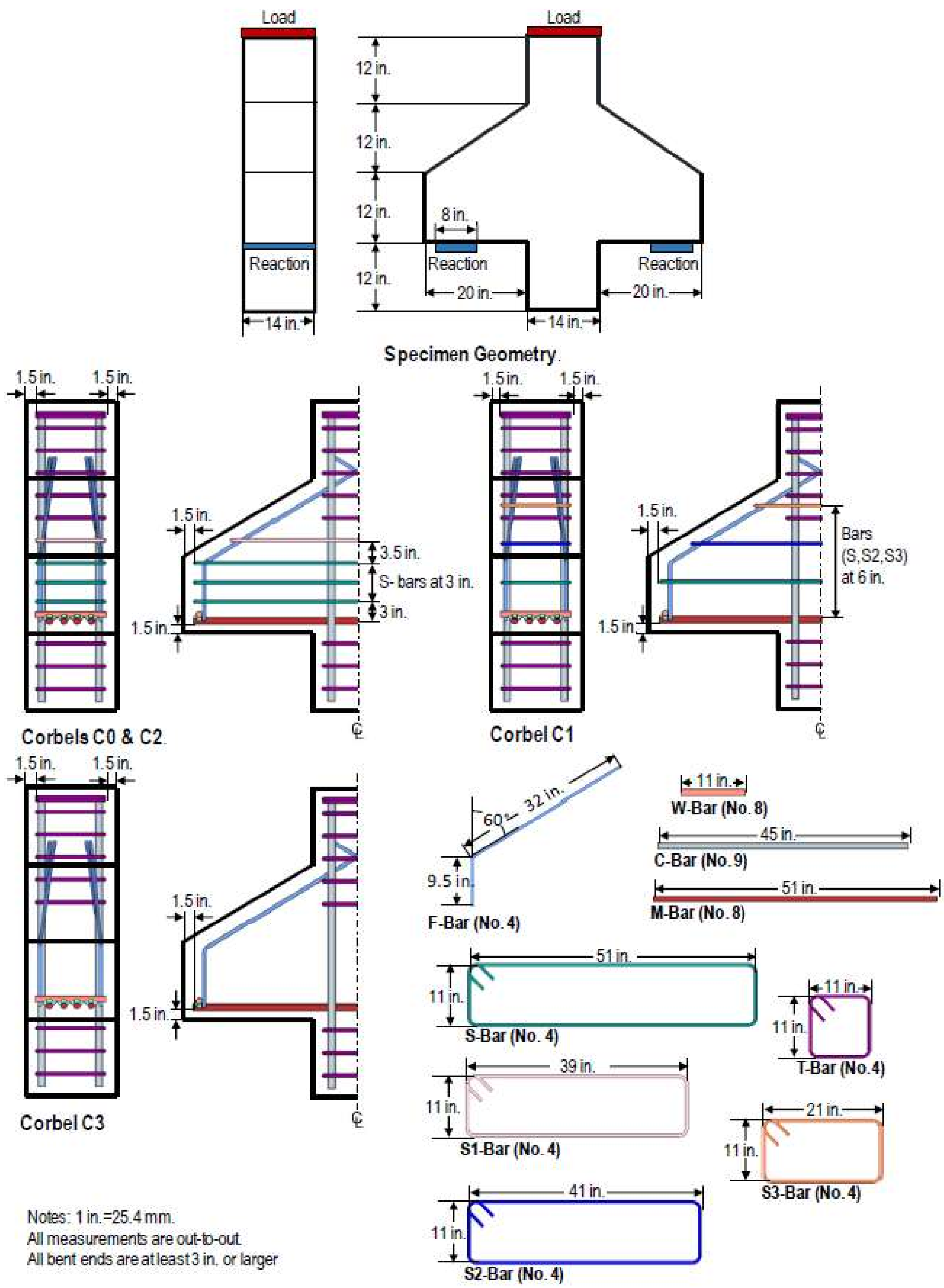

Figure 1.1: Specimen design with reinforcement detailing (Wilson, 2017).

The specimens had identical detailing; however, C0 had a greater shear span-to-depth ratio (a_v/d) compared to all other specimens. The secondary reinforcement utilized in C0 and C2 was detailed according to Sections 16.5.5.2 and 16.5.6.6 of ACI 318-19. With no horizontal forces assumed in design, the total area of secondary reinforcement was assumed as half of the area of the primary reinforcement. Typically, the No. 4 bars constituting the secondary reinforcement in these two specimens were distributed within 2/3 of the effective depth of the corbel at the face of the column (Figure 1.1).

The secondary reinforcement in C1 was designed in accordance with the crack-control requirements outlined in Section 23.5 of ACI 318-19. The No. 4 bars constituting the secondary reinforcement in this specimen were uniformly distributed at 6 in. (15mm) across the inclined strut (Figure 1.1). Consequently, the strut coefficient (β_s) was considered as 0.75 when this specimen was designed using STM.

Specimen C3 was designed without any crack-control, i.e., secondary reinforcement. As a result, a lower β_s value of 0.60 was employed in the strut-and-tie capacity calculations. Designing new corbels without reinforcement to control cracking is not recommended for any application. However, this specimen was specifically designed to investigate the failure mechanisms governing corbel capacity and to evaluate the effects of STM provisions in ACI 318-19 and AASHTO LRFD (2016) to assess whether the strength of existing corbels adheres to recommended design practices.

No. 4 reinforcing bars, spaced at 3.5 in. (89 mm), were included in all specimens within the column region to prevent premature failure in columns. Specimen C0 was constructed before the other specimens to validate fabrication (Figure 1.2) and testing procedures. Specimens C1, C2, and C3 were cast simultaneously to reduce the potential impact of varying concrete mechanical properties on specimen behavior. Wooden formwork was employed for all specimen’s fabrication, as illustrated in Figure 1.2 (a).

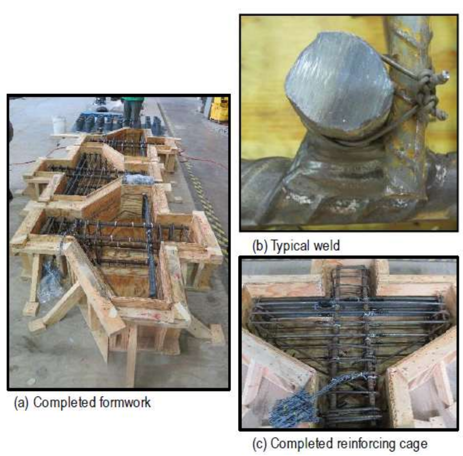

Figure 1.2: Specimen and fabrication details (Wilson, 2017).

Four No. 8 bars of the primary reinforcement (M-bars) were welded together using No. 8 cross bars (W-bars in Figure 1.1) to form a base section for the remaining cage. A typical weld detail is portrayed in Figure 1.2 (b). Following this, No. 9 column longitudinal bars (C-bars in Figure 1.1) were tied onto the No. 8 primary reinforcing bars. Subsequently, the remaining No. 4 bars in the corbel and column areas were tied together. Figure 1.2 (c) illustrates a completed reinforcement cage. Table 1.2 presents the properties of the concrete mixtures utilized for fabricating the specimens.

Table 1.2: Concrete mixture properties (Wilson, 2017). Note: 1 lb/yd^3 = 0.6 kg/m^3, and 1 oz/yd^3 = 38.7 ml/m^3; 1 in. = 25.4 mm.

	Property	C0	C1	C2	C3
Mixture components	Portland cement, lb/yd^3 (kg/m^3)	423 (254)	410 (246)		
	Fly ash, lb/yd^3 (kg/m^3)		150 (90)		
	Coarse aggregate, lb/yd^3 (kg/m^3)		1940 (1164)		
	Coarse aggregate type	Crushed limestone, Maximum size: 1 in. (25.4 mm)			
	Fine aggregate, lb/yd^3 (kg/m^3)	1440 (864)	1467 (880)		
	Water, lb/yd^3 (kg/m^3)	175 (105)	211 (127)		
	Super plasticizer, oz/yd^3 (ml/m^3)	28 (1084)			
	Retarder, oz/yd^3 (ml/m^3)	6 (232)			
	Water-cementitious ratio	0.31	0.38		

A series of 4 in. by 8 in. (100 mm by 200 mm) concrete cylinders were cast simultaneously with all the double-corbel specimens to measure the mechanical properties of the concrete used in each specimen. These cylinders underwent testing following ASTM-compliant procedures. The measured mechanical properties of the concrete and reinforcing bars are compiled and presented in Table 1.3, where f_c' is compressive strength obtained from test of concrete cylinders on the test day, E_c is modulus of elasticity, and f_t is splitting tensile strength of concrete on test day; $f_{c,28}'$ is 28th day compressive strength of concrete, f_y is yield strength of the reinforcement, and f_u is ultimate strength of the reinforcement.

Table 1.3: Summary of measured mechanical material properties (Wilson, 2017). Note: 1 ksi = 6.9 MPa.

Property		Test method	C0	C1	C2	C3
Concrete	$f_{c,28}'$, ksi (MPa)	ASTM C39	4.6 (31.7)	6.5 (44.8)		
	f_c', ksi (MPa)	ASTM C39	5.3 (36.5)	6.5 (44.8)	6.8 (46.9)	5.6 (38.6)
	E_c, ksi (MPa)	ASTM C469	4920 (33,948)	6300 (43,470)	6480 (44,712)	4980 (34,362)
	f_t, ksi (MPa)	ASTM C469	0.55 (3.8)	0.61 (4.2)	0.64 (4.4)	0.66 (4.6)
No. 4 bars	f_y, ksi (MPa)	ASTM A370	69.3 (478)	67.2 (464)		
	f_u, ksi (MPa)		99.0 (683)	95.8 (661)		
No. 8 bars	f_y, ksi (MPa)		73.4 (506)	70.6 (487)		
	f_u, ksi (MPa)		101.6 (701)	99.3 (685)		
No. 9 bars	f_y, ksi (MPa)		74.0 (510)	71.9 (496)		
	f_u, ksi (MPa)		107.5 (741)	105.7 (729)		

The specimens were tested in an inverted configuration, employing the test setup illustrated in Figure 1.3. Load application was facilitated by an 800 kip (3,559 kN) hydraulic ram, pressurized via a pneumatically controlled hydraulic pump. The bearing plates underneath the specimen were supported by a tilt-saddle fixture allowing only rotation and a roller fixture permitting both rotation and translation. The bearing area on these fixtures measured 8 in. by 14 in. (203 mm by 356 mm). Reaction forces during the test were measured by load cells integrated into the support fixtures. Additionally, a series of linear potentiometers distributed around the specimen measured its deformations under load and at the support fixtures, enabling deflection measurements.

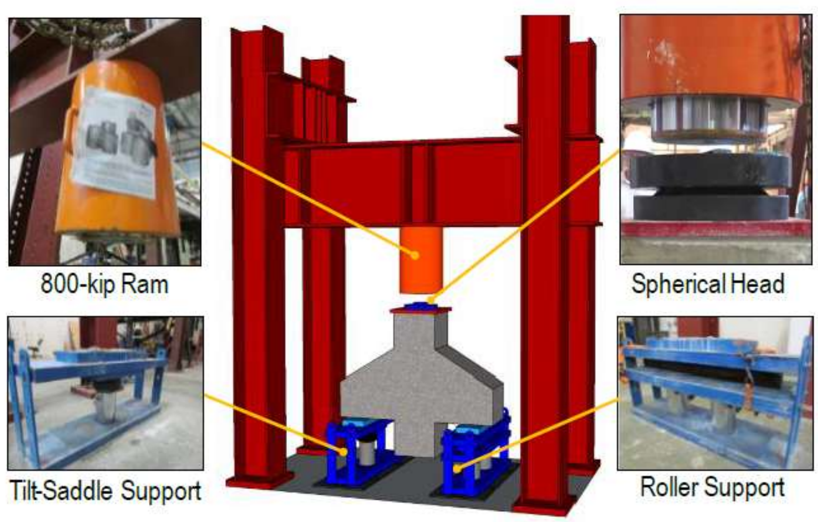

Figure 1.3: Double-corbel test setup (Wilson, 2017).

The effective depth of all the corbel specimens was 22 in. (559 mm) Specimen C0 was tested with a shear span of 14.5 in. (368 mm), yielding a shear-span-to-depth ratio (a_v /d) of 0.66, while the remaining specimens were subjected to a shorter shear span of 13.0 in. (343 mm), resulting in a shear-span-to-depth ratio (a_v /d) of 0.59. Additionally, the specimens were instrumented with four 1 in. (25.4 mm) linear potentiometers (LPs) presented in Figure 1.4, strategically placed on either end of the specimen and under the load application point, to monitor specimen deformation under loading.

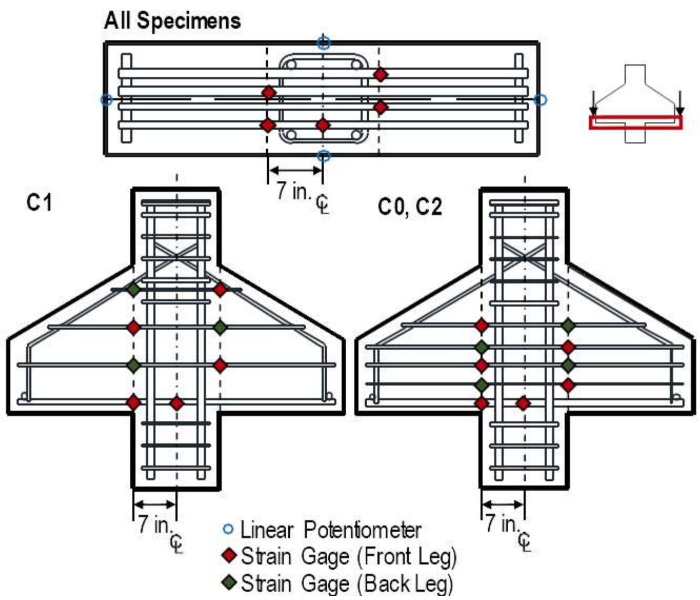

Figure 1.4: Strain gage and linear potentiometer locations. Note: 1 in. = 25.4 mm.

In Figure 1.5, the load versus midpoint displacement plots for all four specimens are illustrated. The figure identifies points corresponding to cracking, first detected yielding, yielding of all primary reinforcing bars, and the ultimate capacity of each specimen. Due to the influence of support deformations on the initial portions of the load-displacement plots, the identification of the first cracking in the specimens is not visually discernible in the plots shown in Figure 1.5. To mitigate the effects of support deformations, the measurements obtained from the linear potentiometers (LPs) at the supports were subtracted from the midpoint deflection, resulting in the adjusted plot shown in Figure 1.6. However, during the structural testing of C3, one of the LPs used to measure the support deformations malfunctioned, and therefore, data from C3 is not included in Figure 1.6.

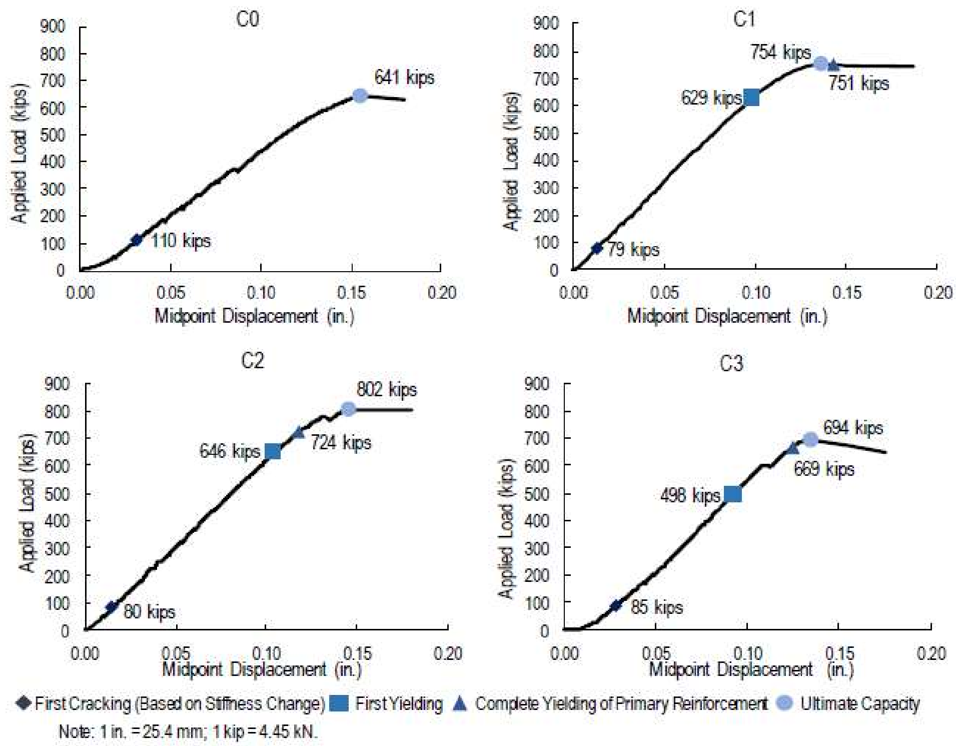

Figure 1.5: Measured load vs. midpoint displacement plots for the specimens C (Wilson, 2017).

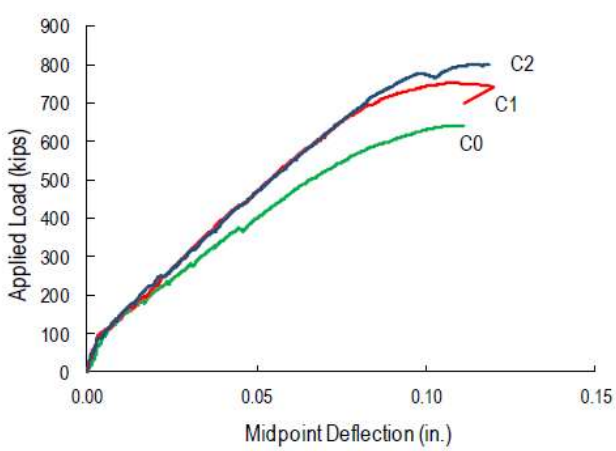

Figure 1.6: Measured load versus deflection comparison of specimens C0, C1, and C2 (Wilson, 2017). Note: 1 in. = 25.4 mm; 1 kip = 4.45 kN.

Table 1.4 presents a summary of observations from the experimental program, where P_{cr} is load at first observed cracking, $P_{cr,st}$ is load corresponding to change in stiffness, and P_{y1} is load at first detected yielding; $P_{y,all}$ is Load corresponding to yielding of all primary reinforcing bars, and P_{max} is peak applied load. The original paper highlights that the reported load values represent the total loads applied to the specimen, signifying twice the shear force applied to each corbel.

Table 1.4: Measured loads corresponding to cracking, yielding, and ultimate strength of the specimens (Wilson, 2017). Note: 1 kip = 4.45 kN

	Location	C0	C1	C2	C3
$P_{cr,}$ kips (kN)	North	144-168 (640-748)	150-180 (667-801)	48-96 (214-427)	90-120 (400-534)
	South	144-168 (640-748)	150-180 (667-801)	96-144 (427-640)	90-120 (400-534)
$P_{cr,st}$, kips (kN)		110 (489)	110 (489)	79 (351)	80 (356)
P_{y1} , kips (kN)		-	-	629 (2798)	646 (2873)
$P_{y,all}$, kips (kN)		-	-	751 (3342)	724 (3221)
P_{max} , kips (kN)		641 (2851)	641 (2851)	754 (3353)	802 (3569)
P_{y1} / P_{max}		-	-	0.834	0.805
$P_{y,all}$ / P_{max}		-	-	0.996	0.902

Prior to each test, a thorough examination was conducted on the specimen to detect any pre-existing cracks, which could have resulted from shrinkage or damage during handling and transportation. No cracks were observed in the test region of any specimen before loading, i.e., the region between each support plate and the column face. The progression of cracking within each specimen until the service-level load and immediately prior to failure is depicted in Figures 1.7 and 1.8, respectively. The service-level load for each specimen was estimated by dividing the design capacity, which was calculated using strut-and-tie method, of the specimen by 1.4. Design capacity (V_n)was obtained without considering ϕ factor in the calculation.

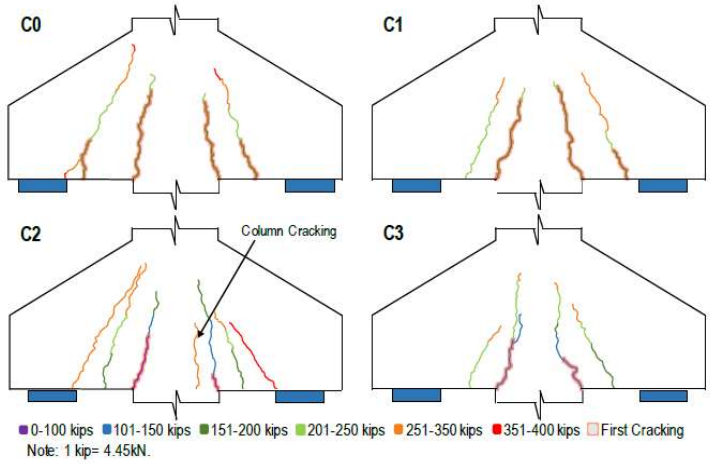

Figure 1.7: Crack patterns at service-level loads (Wilson, 2017).

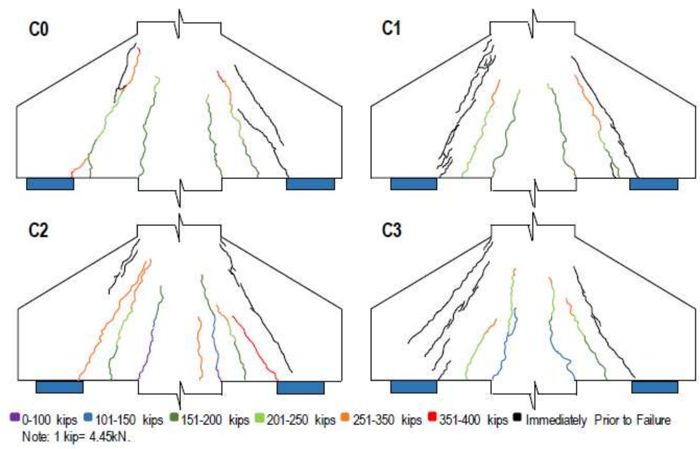

Figure 1.8: Crack patterns immediately prior to failure (Wilson, 2017).

The failure of all specimens was characterized by a sudden loss of load carrying capacity, accompanied by significant damage occurring in a brittle, explosive manner. In specimen C0, compression failure of the inclined strut was observed before the detected yielding of the reinforcement, while in all other specimens, failure occurred through the yielding of the primary reinforcement followed by failure of the inclined strut. The post-failure condition of the specimens is depicted in Figure 1.9.

Failure occurred at the corbel positioned over the tilt-saddle support in all specimens (Figure 1.9). Strut failures in C0, C1, and C2 exhibited similarities, displaying clear signs of compression failure with noticeable spalling of the cover concrete on the inclined strut. In C3, however, the strut exhibited a splitting-type failure due to tensile stresses perpendicular to the inclined crack.

The different design provisions for predicting the load-carrying capacities of the specimens were evaluated using the measured mechanical properties of the materials comprising each specimen. In this report, the ultimate strength of each specimen was calculated, with all load and resistance factors set equal to 1 to capture the actual strength, rather than the design strength.

The different design provisions for predicting the load-carrying capacities of the specimens were evaluated using the measured mechanical properties of the materials comprising each specimen. In this report, the ultimate strength of each specimen was calculated, with all load and resistance factors set equal to 1 to capture the actual strength, rather than the design strength.

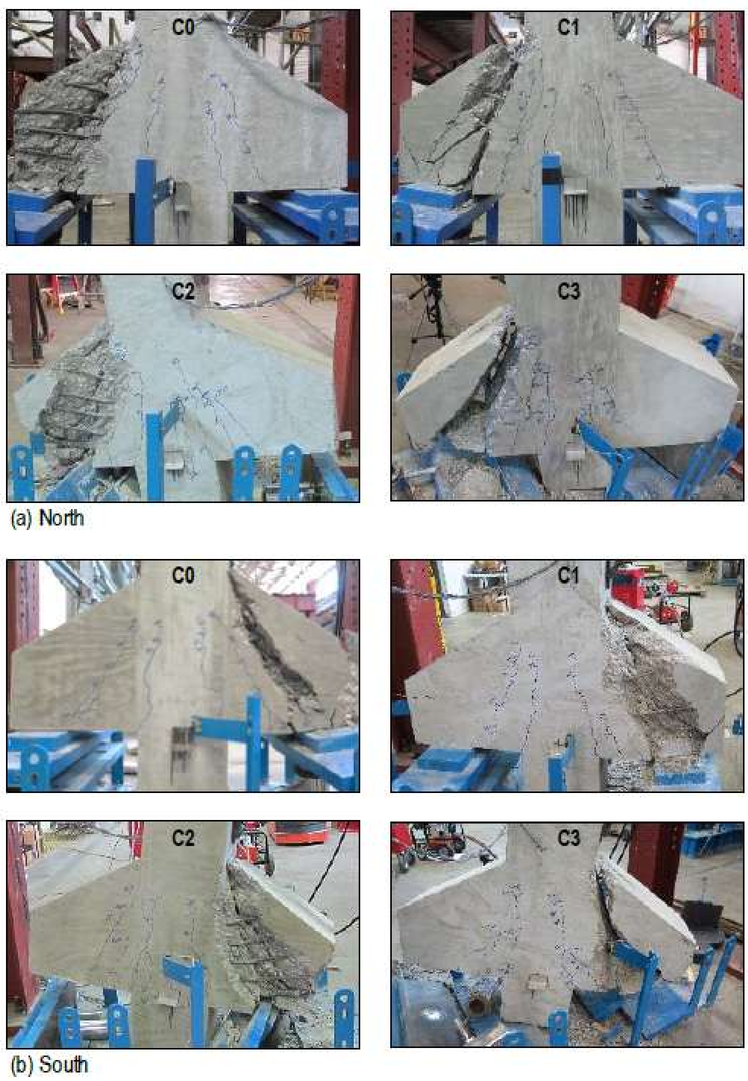

Figure 1.9: Post-failure conditions of the specimens (Wilson, 2017).

1.2.2 Corbel Properties and Experimental Details of Category S Specimens

All three specimens (S1, S2, and S3) possessed nominally identical geometries, as depicted in Figure 1.10, showcasing a symmetrical configuration with a 305 mm (12 in.) thickness and a total corbel height of 610 mm (24 in.) at the column face. Testing was simplified by conducting it in an inverted setup, focusing solely on vertical loads. Each specimen endured vertical loading applied through a 355 mm by 305 mm (14 in. by 12 in.) loading plate, while being supported by two 305 mm by 200 mm (12 in. by 8 in.) bearing plates (Figure 1.10). According to the specifications in Section 5.6.3 of the 2016 interim revisions to the AASHTO LRFD, all specimens were designed and detailed. While secondary or crack-control reinforcement complying with Section 5.6.3.6 was incorporated into specimens S1 and S2. Specimen S3 was constructed without any distributed secondary reinforcement.

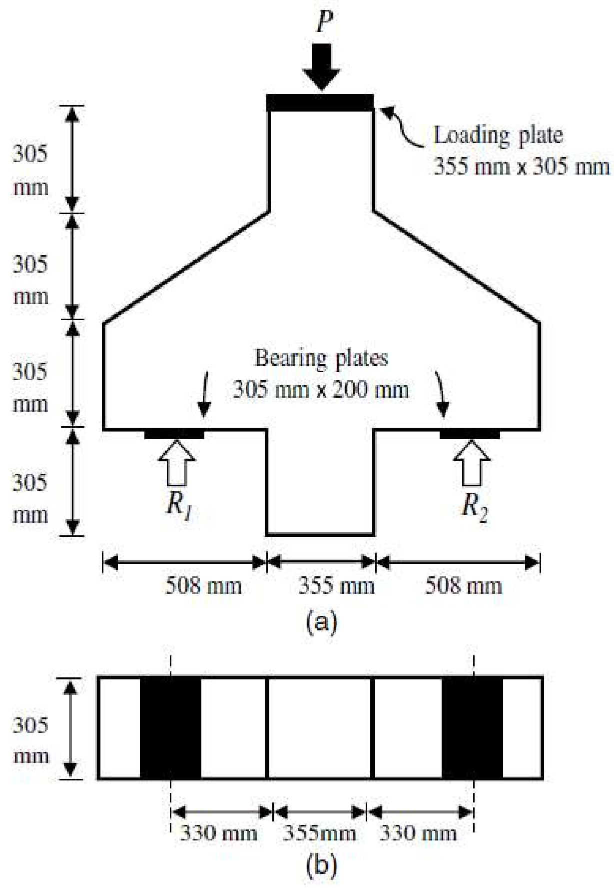

Figure 1.10: Geometry of specimen S (Khosravikia et al., 2018).

Reinforcement details for each specimen are shown in Figure 1.11. Specimens S1 and S2 were designed for a nominal load-carrying capacity of 1,960 kN (440 kips). The primary reinforcement in specimens S1 and S3 was designed with a yield strength of 414 MPa (60 ksi), while specimen S2 used a higher yield strength of 552 MPa (80 ksi). Specimen S3 lacked secondary or crack-control reinforcement and was designed with a lower nominal load-carrying capacity of 1,600 kN (360 kips). Clear covers of 38 mm (1.5 in.) and 19 mm (0.75 in.) were used to the primary and secondary reinforcing bars, respectively.

These assumptions led to the primary reinforcing bars comprising four US No. 8 bars in specimens S1 and S3. Three US No. 8 bars were used as the primary reinforcing bars in specimen S2. The US No. 3 bars constituting the distributed crack-control reinforcement in specimens S1 and S2 had a nominal yield strength of 414 MPa (60 ksi). Additionally, US No. 3 reinforcing ties at 76 mm (3 in.) spacing were added to the column region to prevent premature failure in columns. Finally, the primary reinforcement within the specimens was anchored by a No. 8 cross bar welded at each end (Figure 1.11).

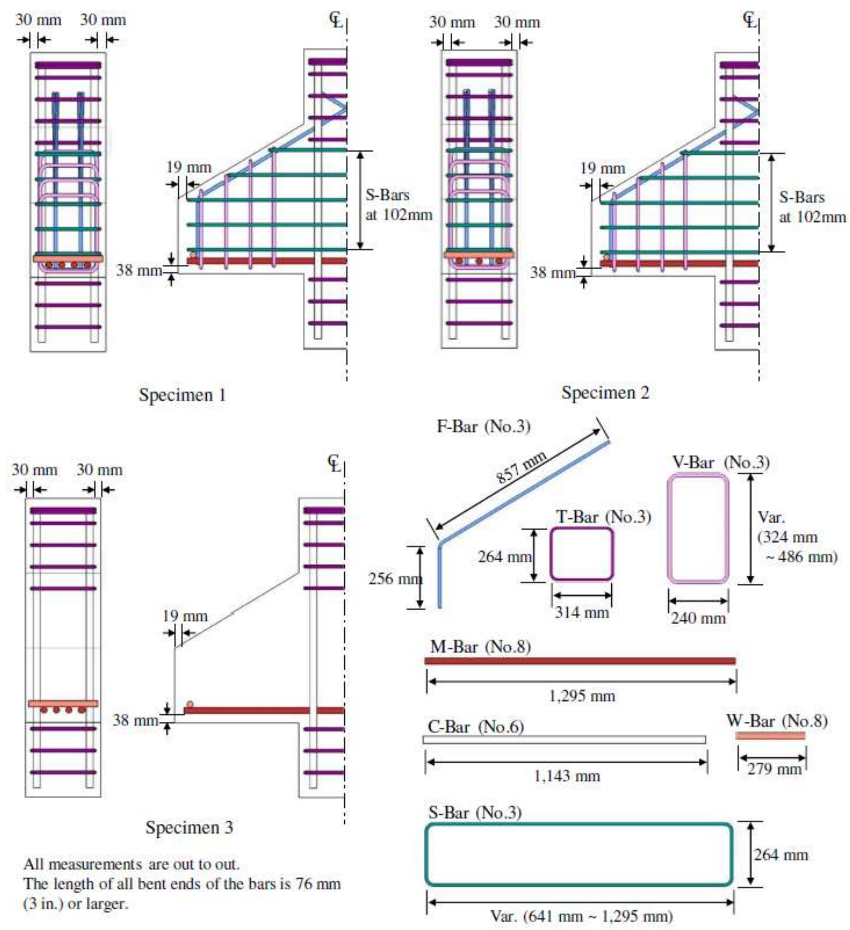

Figure 1.11: Reinforcement details for Specimens S (Khosravikia et al., 2018).

The experimental program utilized the test setup illustrated in Figure 1.12. Each inverted specimen underwent loading from the top by a 3,560 kN (800 kip) ram through a spherical head.

Figure 1.12: Test setup for Specimen S (Khosravikia et al., 2018).

Strain levels exceeding the yield strain of the reinforcing bars were measured by the strain gauges on the crack-control reinforcement in S2. However, the failure load of specimen S2 was slightly greater than that of specimen S1. Minimal differences were observed in the behavior of these two specimens overall. Significant differences were observed in the load-deflection behavior of specimen S3 compared to specimens S1 and S2. No secondary reinforcement was present in S3, leading to a significant reduction (approximately 30%) in its ultimate load [1544 kN (347 kips)] compared to the other two specimens [2100 and 2193 kN (472 and 493 kips)]. Initial crack formation and yielding was not documented for specimen S3 and thus is not depicted in Figure 1.13.

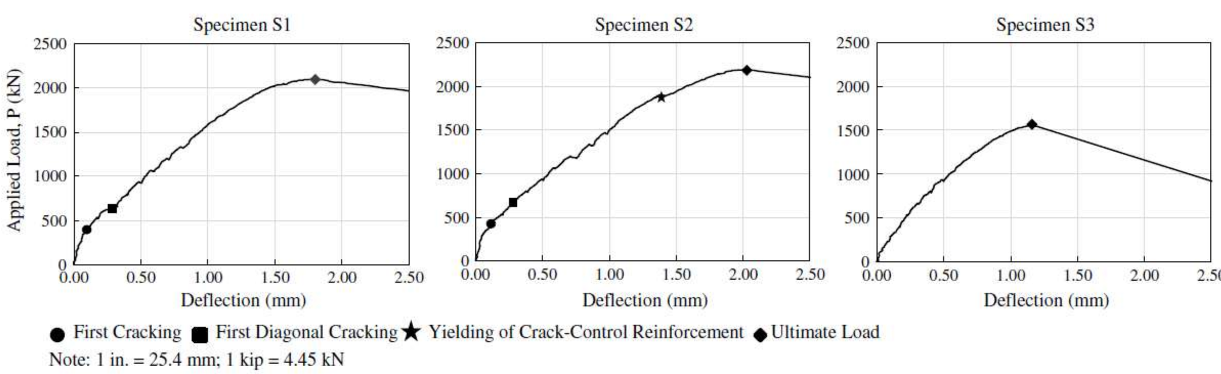

Figure 1.13: Measured load-deformation responses for S Specimens (Khosravikia et al., 2018).

The cracking patterns observed for the corbels are portrayed in Figure 1.14. Cracks are categorized into three groups: first cracks, service-level cracks, and additional cracks that emerged under loads surpassing the estimated service load until failure. The service-level load was determined by dividing the nominal capacity of each specimen by 2.0, calculated from an average load factor of 1.4 divided by a strength reduction factor of 0.70. Table 1.5 displays the measured and nominal capacities. It is evident from this table that the STM provisions of AASHTO LRFD (2016) yielded a reliable estimate for the load-carrying capacities of all three specimens where P_n is nominal capacities of the specimens, and P_{max} is measured capacities of the specimens.

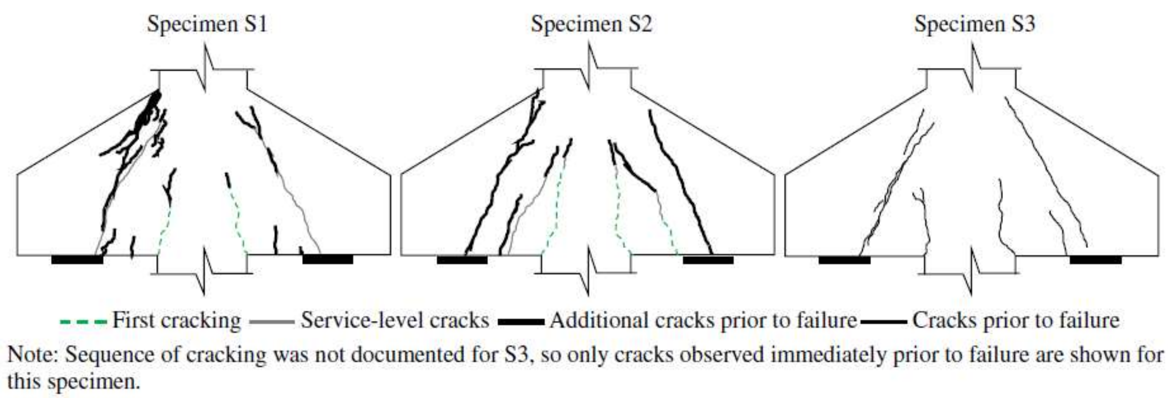

Figure 1.14: Crack patterns observed over the course of testing (Khosravikia et al., 2018).

Table 1.5: Nominal and measured capacities of the specimens

Method	Load	S1	S2	S3
AASHTO LRFD	P_n , kN (kips)	1889 (425)	1859 (418)	1319 (297)
Measured	P_{max} , kN (kips)	2100 (472)	2193 (493)	1544 (347)
Comparison of Load	P_{max} / P_n	1.11	1.18	1.17

1.3 Code Design Calculations per ACI 318-19

The code-based design checks were performed, and the capacities of the corbel specimens were calculated using the strut and tie model (STM), and the crack-control requirements for RC corbels were numerically investigated following the provisions of ACI 318-19. In the strut-and-tie model the concrete members are substituted with a hypothetical truss comprising concrete struts and steel ties, interconnected at nodes. As per the STM provisions of ACI 318-19, adequate reinforcement must be provided to meet the strength demands of each tie. To ensure adequate crack control and prevent excessive strain incompatibility, it is required that the angle between the axis of any strut and any tie entering a node be greater than or equal to 25°. Three types of nodes are categorized:

CCC nodes, indicating nodes with no ties (compression-compression-compression node); CCT nodes, representing nodes with one tie; and CTT nodes, denoting nodes with two or more ties.

The strut-and-tie truss model used for designing these specimens is illustrated in Figure 1.15. The horizontal alignments of Nodes A and A' were aligned with the center of the bearing plates, while Nodes B and B' were positioned at the quarter points within the column width. The vertical positioning of Nodes B and B' was determined as the midpoint of the rectangular compression block at the column face. The design process involved verifying the yield strength of Tie AA', the compressive strength of Struts AB, A'B', BB', BC, and B'C', and the back, bearing, and inclined faces of Nodes A, A', B, and B'. The angle (θ) between the strut and tie at Nodes A and A' was calculated as 48.22°. Table 1.6 presents the design checks identified for corbel specimens from ACI 318-19.

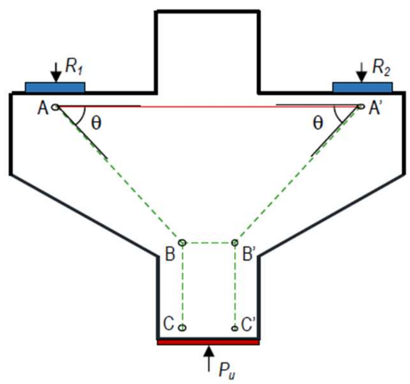

Figure 1.15: Strut-and-tie model (Wilson, 2017).

Table 1.6: Summary of the items checked from ACI 318-19

Checked Item	Reference
Effective concrete compressive strength in a strut or nodal zone	ACI 318-19 (2019), Eqn. 23.9.2
Capacity of the Node	ACI 318-19 (2019), Eqn. 23.9.1
Length of the Node	ACI 318-19 (2019), Section 23.2.2
Length of the inclined face of Node	ACI 318-19 (2019), Figure 23.2.6b
Calculated shear-force capacity of the specimen based on the tensile capacity of Tie	ACI 318-19 (2019), Eqn. 23.7.2
Cross-sectional area of the inclined strut	ACI 318-19 (2019), Section 23.4.1
Calculated capacity of the inclined strut	ACI 318-19 (2019), Eqn. 23.4.1

The structural integrity of concrete elements is rigorously assessed through various checked items, each referencing the American Concrete Institute (ACI) 318-19 building code. The effective concrete compressive strength in a strut or nodal zone is determined according to Equation 23.9.2 of the ACI 318-19 code. Similarly, the capacity of the node is calculated utilizing Equation 23.9.1. The length of the node is determined following the guidelines outlined in Section 23.2.2 of the same code. Moreover, the length of the inclined face of the node is established with reference to Figure 23.2.6b within the ACI 318-19 standard. Additionally, the calculated shear-force capacity of the specimen, based on the tensile capacity of the tie, is derived from Equation 23.7.2. Furthermore, the cross-sectional area of the inclined strut is determined in accordance with Section 23.4.1, and the calculated capacity of the inclined strut is obtained using Equation 23.4.1. These references ensure adherence to standardized procedures and methodologies in evaluating the structural performance of concrete elements.

A summary of the results is provided in Table 1.7, where P_{max} is the measured capacity from the experiments and $P_{ACI, STM}$ is the capacity calculated based on Chapter 23 of ACI 318-19. Details about the strut-and-tie model as per the ACI 318-19 is presented in Section 1.3. Table 1.7 shows that the actual capacity of the test specimens is approximately 40% larger than these calculated using the STM. This may be expected that STM is approximate and can be considered as lower bound capacity.

Table 1.7: Comparison of calculated and measured capacities of the specimens (Wilson, 2017). Note: 1 kip = 4.45kN

	C0	C1	C2	C3
$P_{max,}$ kips (kN)	641 (2851)	754 (3353)	802 (3567)	694 (3087)
$P_{ACI, STM,}$ kips (kN)	448 (1993)	556 (2473)	558 (2482)	468 (2081)
$P_{max} / P_{ACI, STM}$	1.43	1.36	1.44	1.49

Table 1.8 outlines a summary of capacity calculations for S Specimens, detailing the load capacities determined using STM following the guidelines of AASHTO LRFD (2016). The table encompasses three specimens (S1, S2, and S3), with load capacities presented in kN. Additionally, the measured capacity ratio ($P_{max} / P_{AASHTO\ LRFD, STM}$) for each specimen is provided, indicating the maximum measured load capacity relative to the calculated capacity based on AASHTO LRFD.

Table 1.8: Summary of capacity calculations for specimen S

	S1	S2	S3
$P_{AASHTO\ LRFD, STM}$, kN (kips)	1889 (425)	1859 (418)	1319 (297)
$P_{max} / P_{AASHTO\ LRFD, STM}$	1.11	1.18	1.17

1.4 IDEA StatiCa Analysis

Seven reinforced concrete corbels described in the Sections 1.2.1 and 1.2.2 were modeled in IDEA StatiCa to simulate the response of these specimens. The measured compressive strength of concrete, yield strength of reinforcing steel, and ultimate strength of reinforcing steels, as presented by Wilson (2017) for specimens C0, C1, C2, and C3 (Table 1.3), and by Khosravikia et al. (2018) for specimens S1, S2, and S3, were incorporated into the IDEA StatiCa software.

1.4.1 Analysis of Baseline Model (Specimen C0)

The IDEA StatiCa model was developed for the baseline (C0) model using the measured material properties (Table 1.3). The materials factor for concrete (φc) and reinforcing steel (φs) in IDEA StatiCa was set to 1.0 to accurately capture the experimental behavior of the corbel specimens. Two types of loads were considered for the analysis: the self-weight of the corbel and the applied load. The applied load was gradually increased to 580 kips (2578 kN) in 100 increments from zero to obtain the load versus mid-point deflection plot of the corbel specimen. Since the corbel specimens were tested inversely, a bearing plate was assigned under the load on the column. The dimensions of the bearing plate were taken as 14 in. by 14 in. (355.6 mm by 355.6 mm), as specified by Wilson (2017), with a thickness of 2 in (50.8 mm). The right support of the corbel was fixed in the vertical or z direction to act like a roller support, while the left support was fixed in one horizontal (x) and z directions representing a pin support. As the model was developed to capture the experimental behavior of the corbel specimen, the IDEA StatiCa analysis only focused on the ultimate limit state (ULS) load combination by assigning load factors of 1.0 for both load patterns, i.e., self-weight and applied load.

For the capacity calculation, the loads were gradually increased until any of the following was achieved:

1) The concrete reaches 100% of its strength capacity under the applied load.
2) The reinforcing steel reaches 100% of its strength capacity under the applied load.
3) The anchorage steel reaches 100% of its strength capacity under the applied load.

When the applied load reached 580 kips (2578kN), the concrete reached 99.5% of its capacity, while the reinforcing bars reached 98% of their strength capacity, and the anchoring steel reached 99.9% of its capacity (Figure 1.16). Further increments of the applied load would exceed the capacity of the anchoring steel, thus being considered the maximum load by IDEA StatiCa. Under the load of 580 kips (2578 kN), the mid-point deflection of the corbel specimen was recorded as 0.098 in., and the maximum strain in the reinforcement was calculated as 0.0021, which is slightly larger than the yield strain of 0.002. Figure 1.16 shows the detailed results for corbel specimen C0 obtained using IDEA StatiCa under the maximum applied load of 580 kips (2578 kN).

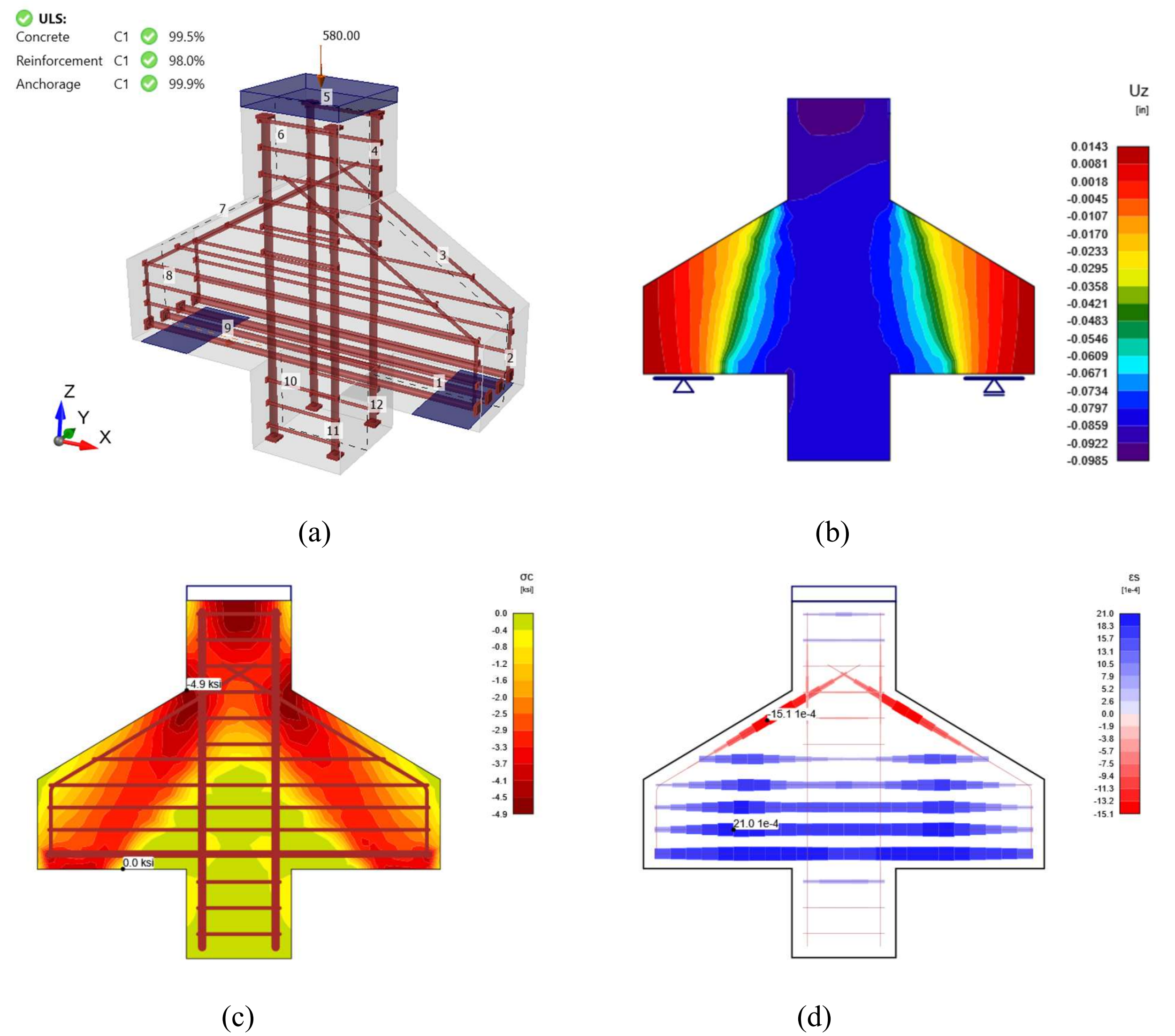

Figure 1.16: (a) Corbel C0 at 580 kips (2578 kN) loading, (b) deflection of C0 under 580 (kips) loading, (c) concrete principal stress σ_c of C0 at 580 (kips) loading, and (d) strain in the reinforcement steel.

1.4.2 Analysis of C Specimens

Following the same procedure described for the baseline model in Section 1.4.1, the IDEA StatiCa model was developed for Specimens C1, C2, and C3 considering the shear span to depth ratio (a_v /d) of 0.59. It was observed for Specimen C1 from the incremental loading that, when the applied load was 642 kips (2856 kN), the concrete reached 99.5% of its capacity, reinforcing bars reached 100% of their strength capacity, and anchoring steel reached 99.9% of its capacity (Figure 1.17). The maximum midpoint deflection was found to be 0.803 in (20.4 mm).

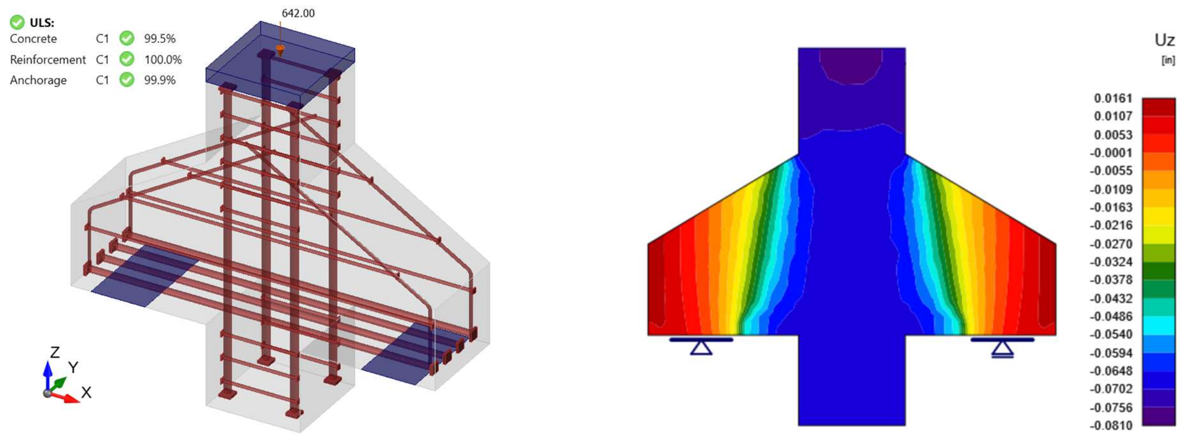

(a) (b)

Figure 1.17: (a) Specimen C1 at 642 kips (2856 kN) loading, and (b) deflection of C1 at 642 (kips) loading.

It was observed for Specimen C2 that, the strength capacity of the reinforcement and anchorage reached 100% of their capacity at the applied load of 720 kips (3203 kN) presented in Figure 1.18. The mid-point deflection was found larger for Specimen C2 than C1. The discrepancy in mid-point deflections between Specimens C1 and C2 in IDEA StatiCa may be attributed to variations in material properties, mesh density, modeling assumptions, and software settings.

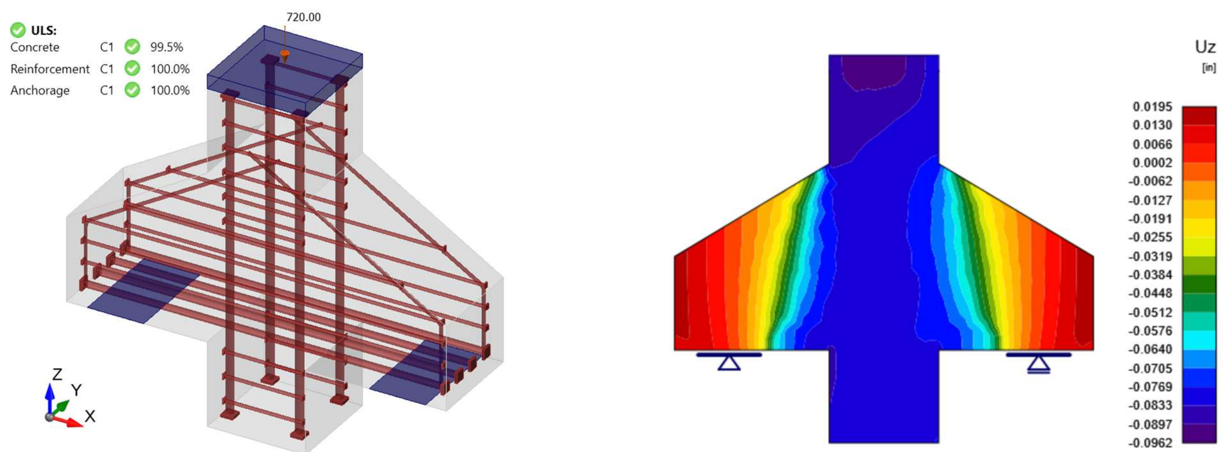

(a) (b)

Figure 1.18: (a) Specimen C2 at 720 kips (3203 kN) loading, and (b) deflection of C2 at 720 (Kips) loading.

In calculating the maximum load-carrying capacity for Specimen C3 using IDEA StatiCa, it was observed that, when the applied load corresponds to the 516 kips (2295.29 kN), the concrete and the anchorage reached 99.5% and 99.99% of their capacity, respectively while the reinforcement reached 89.2% of its capacity. The maximum deflection observed was 0.084 in (2.134 mm) (Figure 1.19).

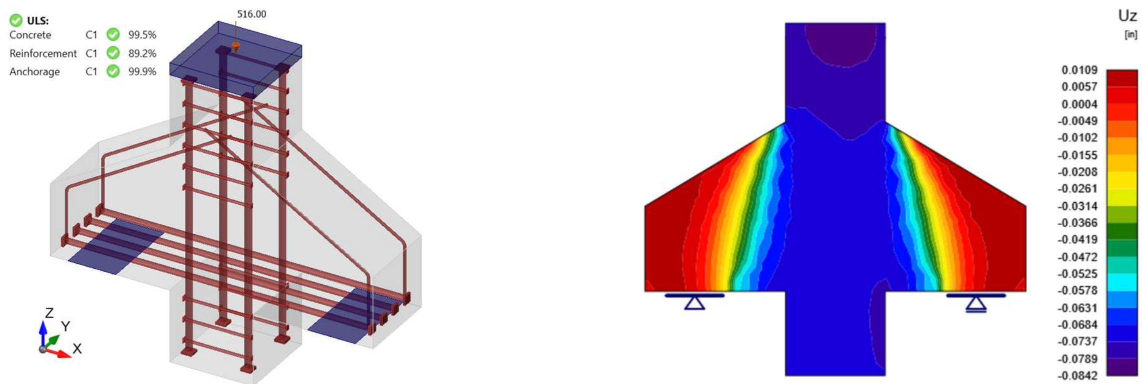

(a) (b)

Figure 1.19: (a) Specimen C3 at 516 Kips (2295 kN) load, and (b) deflection of C3 at 516 (Kips) load.

1.4.3 Analysis of S Specimens

IDEA StatiCa analysis was performed for corbel Specimens S1, S2, and S3 following the same procedure mentioned for baseline model in Section 1.4.1. For Specimen S1 IDEA StatiCa analysis showed that the reinforcement reached 100% of its capacity when the applied load was 2132 kN (479.3 kips). The concrete and anchorage reached 99.5% and 99.9% of their capacity, respectively (Figure 1.20). The deflection obtained from IDEA StatiCa under the load of 2132 kN (479.3 kips) was 2.45 mm (0.096 in.).

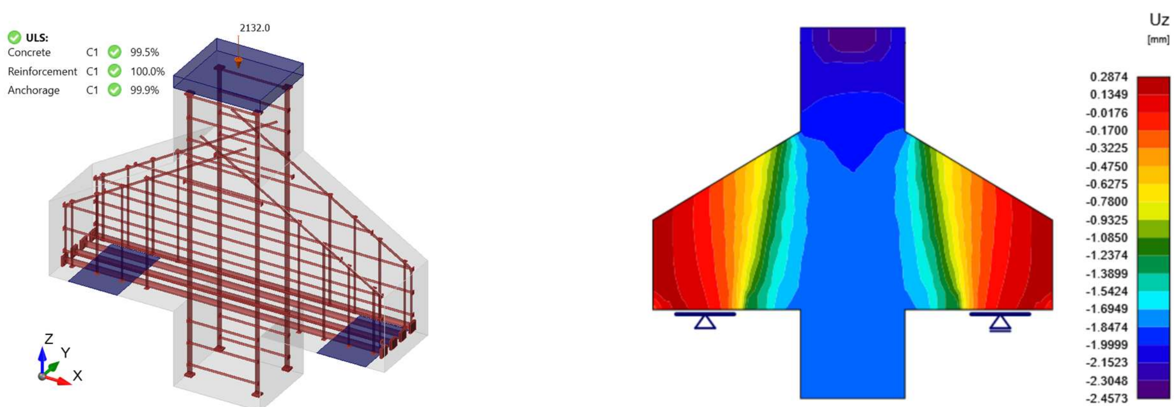

(a) (b)

Figure 1.20: (a) Specimen S1 under 2132 kN (479.4 kips) loading, and (b) deflection of S1 under 2132 kN (479.4 kips) loading.

The IDEA StatiCa model for specimen S2 was developed following the procedure obtain for Specimen S1, altering the primary reinforcement. The number of primary reinforcement in specimen S2 was reduced to 3 # 8 bars. It was observed that the reinforcement reached full capacity before the concrete. The concrete and anchorage steel reached 99.5% and 99.99% of their capacity under the applied load of 2048 kN (460.5 kips) (Figure 1.21). The deflection found under the maximum load was 2.54 mm (0.100 in.).

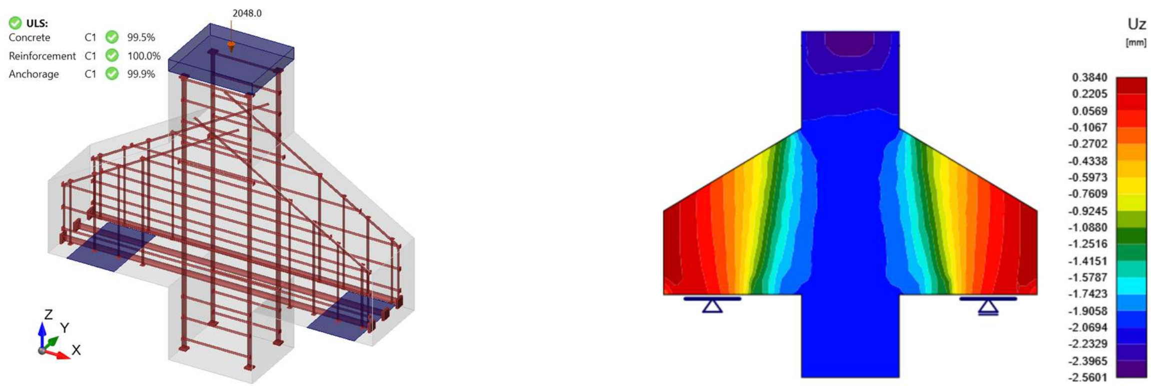

(a) (b)

Figure 1.21: (a) Specimen S2 at 2048 kN (460.5 kips) load, and (b) deflection of S2 at 2048 kN (460.5 kips) load.

Since there was no secondary reinforcement in the corbel specimen S3, the IDEA StatiCa model for specimen S3 was developed from S1 by deleting the secondary or crack-control reinforcement. It was observed that under the maximum applied load of 1592 kN (358.0 kips), the anchorage reached to a 99.99% of its capacity and concrete reached to the 99.5% of its capacity while reinforcement reached to a 66.5% capacity only (Figure 1.22).

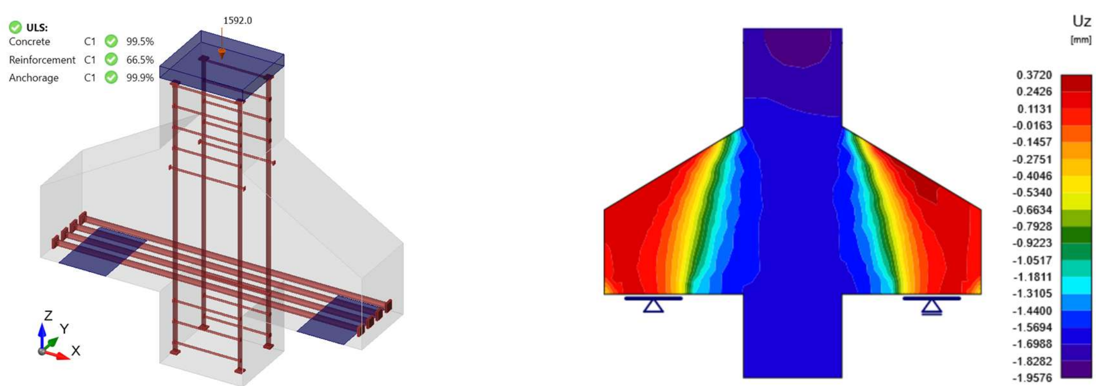

(a) (b)

Figure 1.22: (a) Specimen S3 under 1592 kN (358.0 kips) loading, and (b) Deflection of S3 under 1592 kN (358.0 kips) loading.

1.5 ABAQUS Model Development and Analysis

In this section, the baseline model developed in Section 1.4.1 (i.e., Specimen C0) was reconstructed using ABAQUS software (version 2023) for finite element (FE) analysis, and the results were compared with those obtained from IDEA StatiCa. In the model, in addition to the self-weight, the vertical load of 592 kips (2633 kN) was imposed to the top bearing plate as illustrated in Figure 1.23a. Two boundary conditions similar to the experimental tests and IDEA StatiCa model (i.e., roller type in right and tilt-saddle type in left) were applied to Specimen C0 (see Figure 1.23b). In ABAQUS, the element size was chosen to be 0.5 in. (12.7 mm) after routine mesh sensitivity analysis, resulting in a total of 202,720 elements in the model. The 3D stress, 8-node linear brick reduced integration (i.e., C3D8R) was selected as the element type for the concrete, while the beam element was chosen for the reinforcement bars.

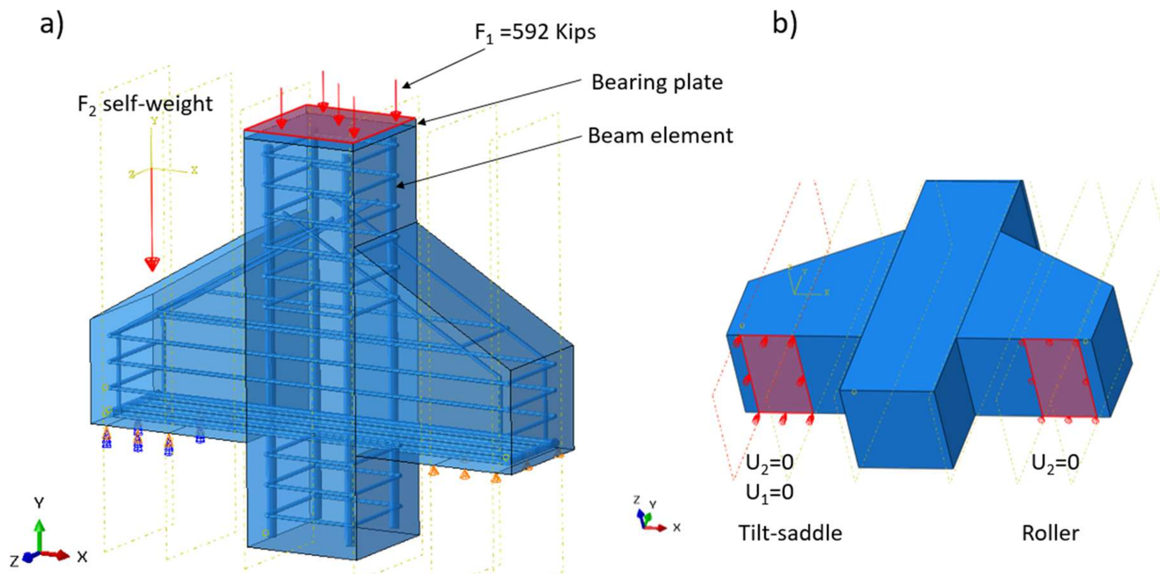

Figure 1.23: a) Model setup in ABAQUS, and b) implementation of two boundary conditions in ABAQUS.

The embedded region constraint was utilized to incorporate the steel reinforcement within the concrete corbel C0 (see Figure 1.24). Also, a general surface-to-surface contact was defined between the bearing plate and the concrete specimen. In ABAQUS, the Concrete Damage Plasticity (CDP) constitutive model was used. The required parameters to describe this model were obtained from the experimental test after calibration as they were not explicitly indicated in Ref. (Wilson, 2017). For the steel bars, the material behavior was modeled using simple bi-linear plasticity. Other parameters, including density, elastic modulus, and Poisson's ratio were taken from the IDEA StatiCa materials library. The numerical simulation was carried out on a virtual machine with 16 processors (Intel Xenon® Gold Processor 6430 @2.10GHz) and took approximately 56 minutes to finish, while the IDEA StatiCa completed the calculation in less than one minute.

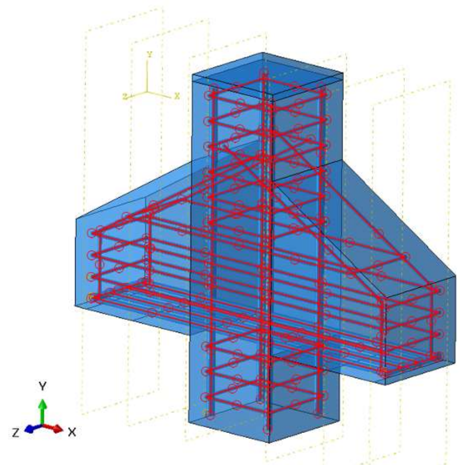

Figure 1.24: Embedded region constraint depicted in red between the reinforcement bars and concrete.

Figures 1.25a and 1.25b show the schematics of crack patterns from experimental tests. The predicted crack patterns from ABAQUS were compared with the experimental results (see Figures 1.25c-1.25f). While the experimental data reported that the four significant cracks appeared when the load reached 96 kips (427 kN), ABAQUS predicted similar crack patterns when the load was 99.5 kips (442.1 kN). This implies a slightly stiffer response from the traditional FEA model compared to the Compatible Stress Field Method (CSFM).

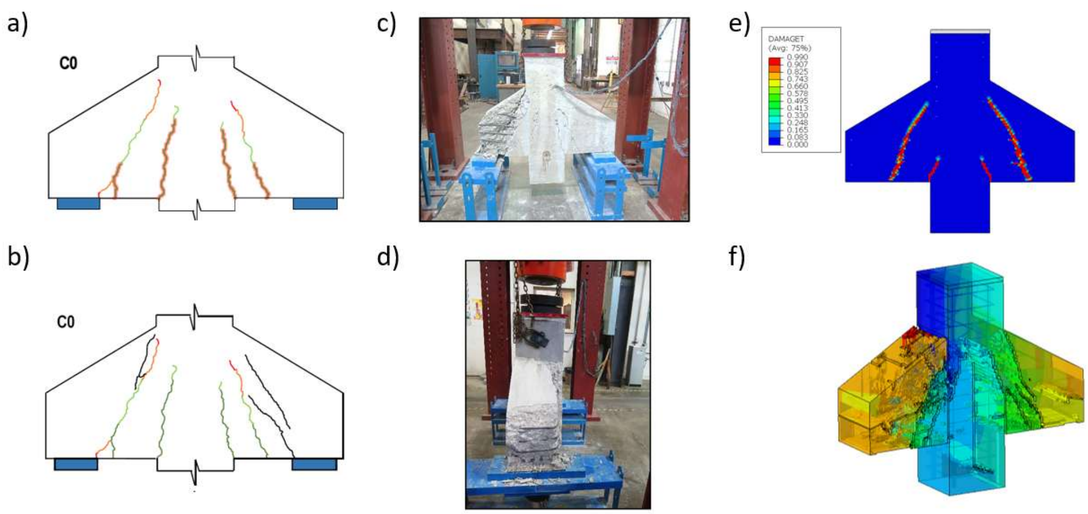

Figure 1.25: a) Schematic of crack patterns from the experimental test for specimen C0 at service-level load, b) immediately prior to failure, c) post-failure condition (front view), d) post-failure

condition (side view), e) predicted crack patterns by ABAQUS, and f) predicted crack propagation prior to failure by ABAQUS.

Comparisons of the vertical displacement and directions of principal stresses between the two software are shown in Figures 1.26 and 1.27, respectively. Both models offer comparable results. However, it appears deformation and stresses are more distributed in ABAQUS while IDEA StatiCa results are more concentrated. Stress distributions also show that the diagonal compressive stress seems more prismatic in IDEA StatiCa while the stress distribution looks more like bottle shapes struts. Similarly, a wider band or strut is observed in ABAQUS model. The minor discrepancy in the results is most likely associated with the way that boundary conditions and load (e.g., point load vs. distributed load) were applied in each software.

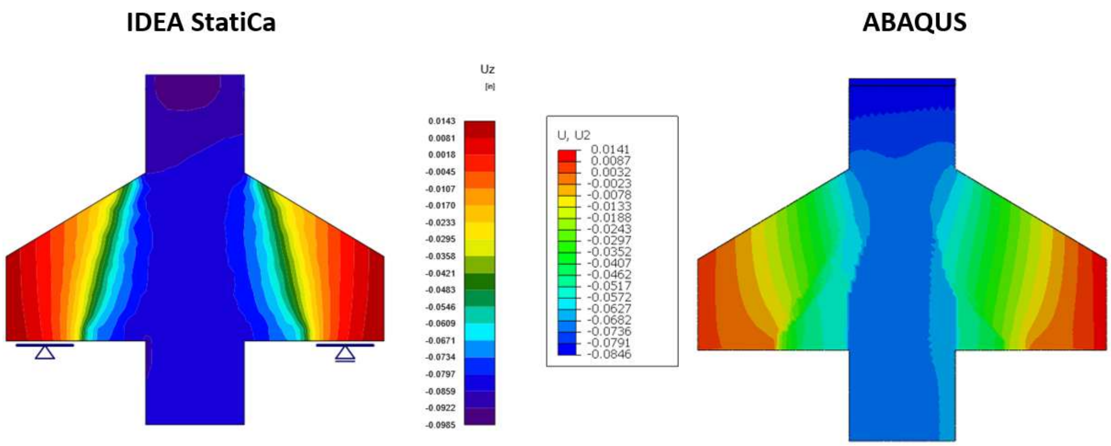

Figure 1.26: Comparison of the vertical displacement between IDEA StatiCa and ABAQUS.

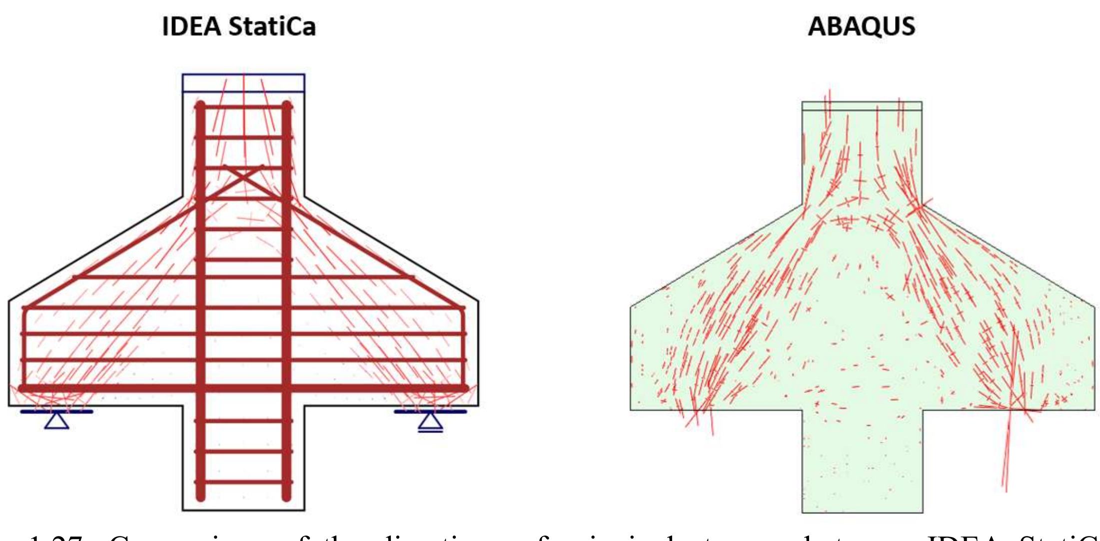

Figure 1.27: Comparison of the directions of principal stresses between IDEA StatiCa and ABAQUS.

Figure 1.28 demonstrates the comparison between the calculated principal stress in concrete by IDEA StatiCa and the predicted one by the ABAQUS model. In IDEA StatiCa, the minimum predicted stress was -4.9 ksi (–33.8 MPa), while the ABAQUS model captured a minimum stress of -4.85 ksi (–33.4 MPa) at the same location. The slight difference in stress distribution is likely due to several factors, including the application of boundary conditions, the utilization of finer mesh in ABAQUS, and differences in the constitutive model for concrete between IDEA StatiCa and ABAQUS (e.g., neglecting failure criterion in terms of strain for concrete in compression in IDEA StatiCa). Additionally, differences in element types (i.e., solid element in ABAQUS versus shell element in IDEA StatiCa) and the employment of the embedded region constraint in ABAQUS may have contributed to the discrepancies. Note that the authors performed a routine mesh sensitivity analysis for the IDEA StatiCa model, which revealed some inconsistencies in the results. Furthermore, the predicted von Mises stress by ABAQUS upon reaching the concrete's ultimate strength is depicted in Figure 1.28.

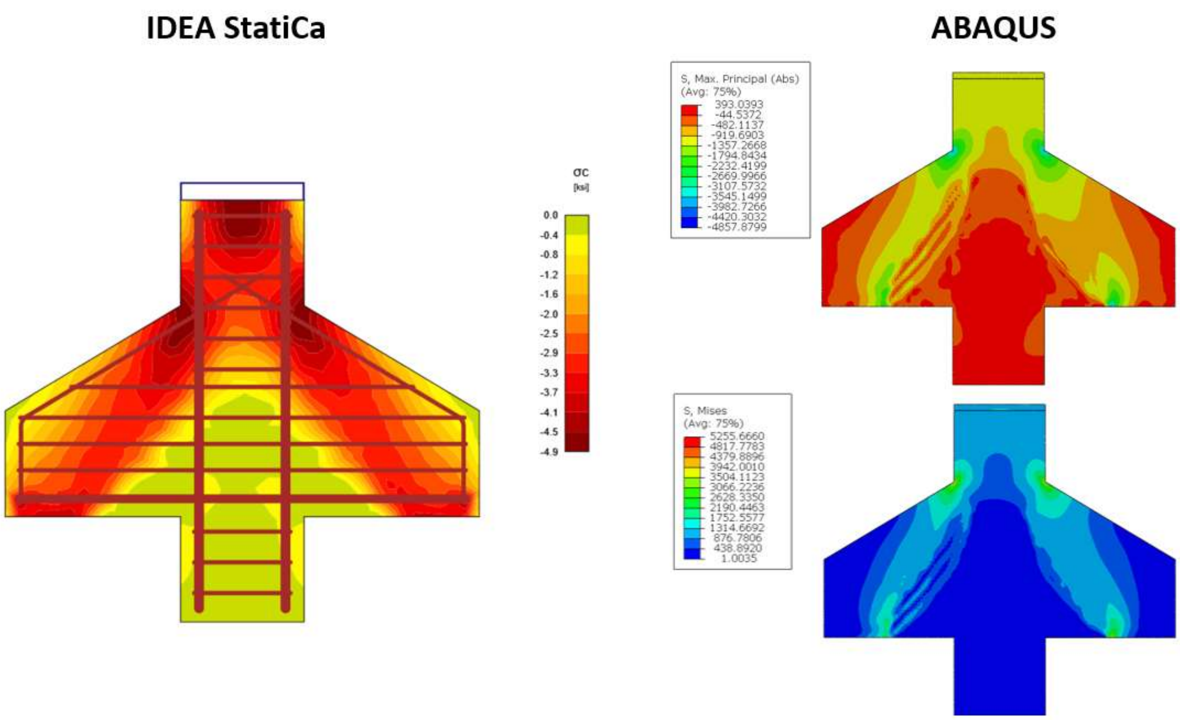

Figure 1.28: Comparison of the calculated principal stresses in concrete between IDEA StatiCa and ABAQUS. Predicted von Mises stresses by ABAQUS upon reaching the concrete ultimate strength is also shown in bottom right.

Figure 1.29 illustrates the comparisons of the reinforcement stress and strain between IDEA StatiCa and ABAQUS. In ABAQUS, the predicted maximum and minimum stress values are 62.1 kips and -52.3 kips (-233 kN), respectively, while in IDEA StatiCa, these values are slightly different at 67.9 kips (302 kN) and -43.7 kips (-194.4 kN), respectively. This discrepancy may be attributed to the neglect of tensile strength and the tension stiffening effect in the CSFM method utilized by IDEA StatiCa.

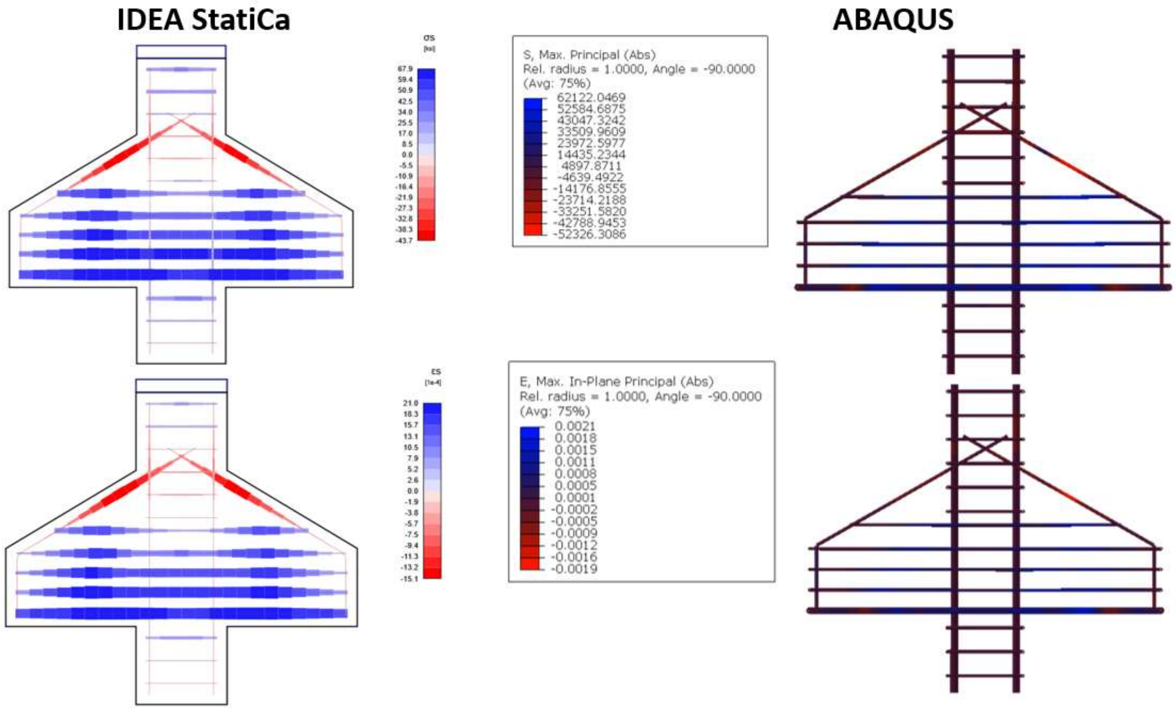

Figure 1.29: Top row) comparison of the reinforcement stress between IDEA StatiCa and ABAQUS, and bottom row) comparison of the reinforcement strain between IDEA StatiCa and ABAQUS.

1.6 Summary and Comparison of Results

Seven reinforced concrete corbels were investigated using IDEA StatiCa and following the provisions of strut-and-tie method per ACI 318-19 for four different corbels (C0, C1, C2, C3) and per AASHTO LRFD (2016) for three different corbel specimens (S1, S2, S3). Also, the results from the IDEA StatiCa baseline model (i.e., Corbel C0) were compared with those from the equivalent ABAQUS model. The specimens were modeled and analyzed using IDEA StatiCa to capture the experimental behavior of the corbels. The maximum load-carrying capacity of the corbels and the load versus mid-point deflection curves were plotted with the results obtained from IDEA StatiCa and compared with the measured data.

In Figure 1.30, comparisons of the loads obtained from experiments, strut and tie method (STM) and IDEA StatiCa for specimens C are presented. The results highlight the effectiveness of $P_{IDEA\ StatiCa}$ in closely aligning with experimental results, surpassing traditional methods such as the STM in providing near-accurate predictions of corbel performance. Across all specimens (C0, C1, C2, and C3), $P_{IDEA\ StatiCa}$ consistently demonstrates close agreement with the experimental maximum load capacities (P_{max}). The properties of the specimens C0 and C2 were the same but the specimen C0 was tested with a greater a_v/d ratio. This exhibits the effect of a_v/d ratio on the load-carrying capacity of corbel. The capacity of the corbels inversely varied with the a_v/d ratio.

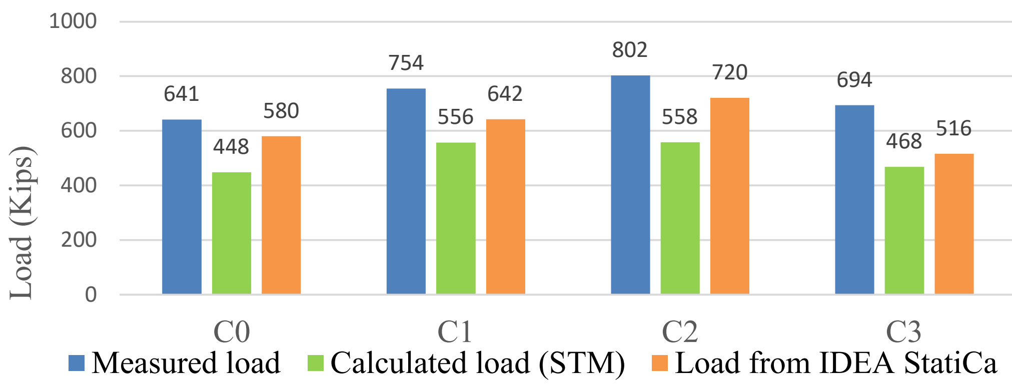

Figure 1.30: Comparison of measured, calculated (STM) and maximum load from IDEA StatiCa for C specimens.

The results presented in Figure 1.31 indicate that IDEA StatiCa closely aligns with the experimental maximum load capacities (P_{max}) for corbel specimens S1, S2, and S3. Across all specimens, the predicted strengths obtained from IDEA StatiCa exhibit minimal deviation from the experimental values compared to the strut and tie method (STM) from AASHTO LRFD (2016). Specifically, for specimens S1 and S3, IDEA StatiCa predicts slightly higher strengths compared to the experimental results, with deviations of 32 and 48 units, respectively. Conversely, for specimen S2, IDEA StatiCa predicts a slightly lower strength compared to the experimental value, with a deviation of 145 kN (33 kips).

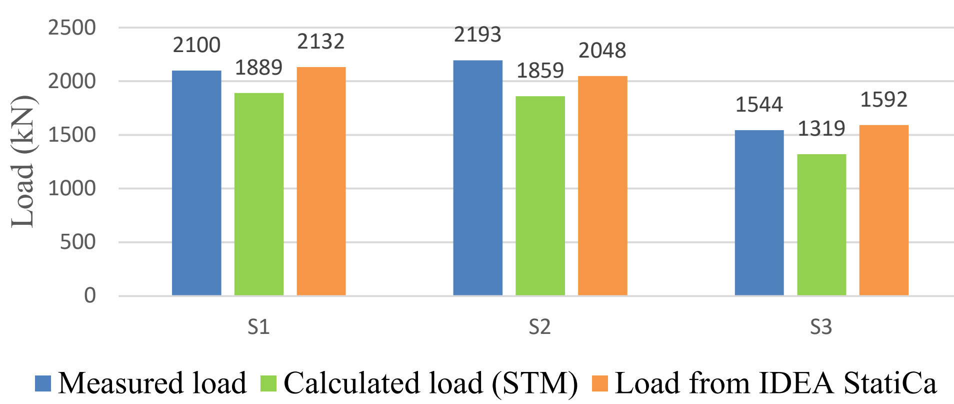

Figure 1.31: Comparison of measured, calculated (STM), and maximum load from IDEA StatiCa for S specimens.

The close agreement between IDEA StatiCa and experimental results suggests that IDEA StatiCa provides reliable estimates of corbel performance. However, the slight discrepancies observed for specimens S1, S2, and S3 may be related to potential issues in the experimental testing process. These discrepancies could arise from factors such as variations in material properties, boundary conditions, or experimental procedures. Additionally, it is possible that the analytical model used in IDEA StatiCa may offer a more comprehensive representation of the corbel behavior, leading to slightly higher predicted strengths compared to the experimental values.

The results shown in Figure 1.32 reveal that the calculated strengths obtained from both IDEA StatiCa and ABAQUS for corbel specimen C0 closely match each other. There is only a small difference of 12 kips (53.4 kN) between their predictions. This similarity suggests that both software tools are good at estimating how well corbel performs.

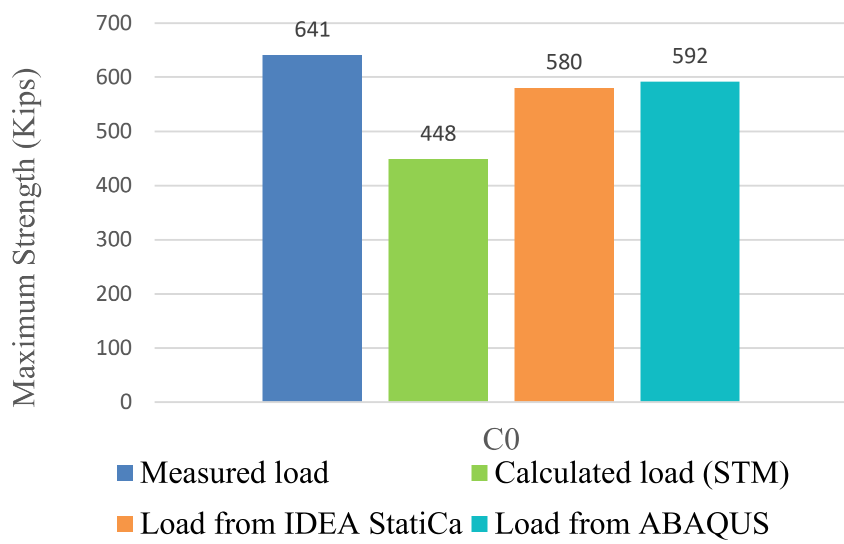

Figure 1.32: Comparison of measured, calculated (STM), and maximum strengths from IDEA StatiCa and maximum strength from ABAQUS for baseline model (C0).

Upon comparison of the results obtained from both IDEA StatiCa and ABAQUS software, it is evident that similarities exist in the calculated stress values, albeit with slight differences (Figure 1.32). In the case of the minimum stress prediction for concrete, it was observed that IDEA StatiCa forecasted approximately -4.9 ksi (–33.8 MPa), whereas a slightly lower value of approximately - -4.85 ksi (–33.4 MPa) was shown by ABAQUS at the same location (Figure 1.28). Similarly, for the maximum stress values, it was found that ABAQUS predicted approximately 62.1 kips (276 kN) and -52.3 kips (233 kN), while IDEA StatiCa depicted slightly different values of around 67.9 kips (302 kN) and -43.7 kips (-194.4 kN), respectively (Figure 1.33). The overall trend suggests that reasonably close predictions of stress distributions within the analyzed structure are provided by both software tools.

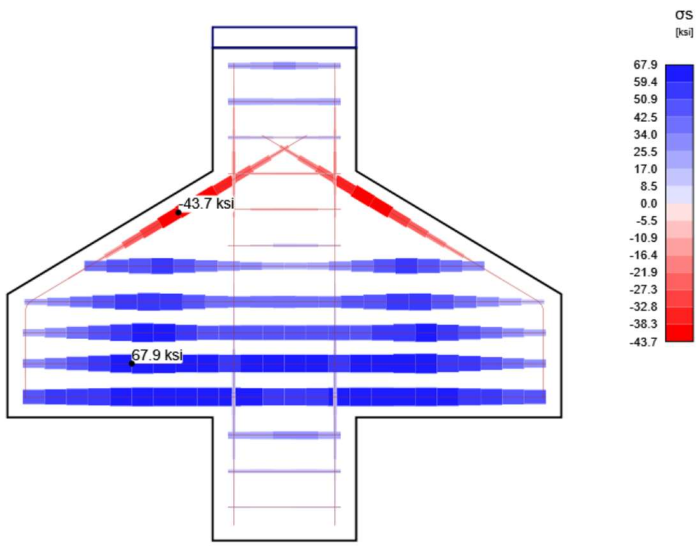

Figure 1.33: Reinforcement stress obtained from IDEA StatiCa for Specimen C0.

The load versus displacement curves for specimens C0 to C3, depicted in Figures 1.34 through 1.37, indicate consistent patterns across all specimens. Notably, it is observed that the calculated midpoint displacements from IDEA StatiCa consistently appear lower than the measured midpoint displacements. This trend suggests a discrepancy between the analytical predictions provided by IDEA StatiCa and the actual experimental behavior observed during the test. Despite the consistent nature of this disparity across multiple specimens, it is essential to recognize potential factors contributing to these differences.

One factor could be the inherent simplifications and assumptions within the analytical model used by IDEA StatiCa. Such simplifications might lead to conservative estimations of displacement, as the model may not fully capture all aspects of the corbel's complex structural behavior. Moreover, variations in material properties, boundary conditions, or environmental factors during experimental testing could also contribute to differences between calculated and measured displacements. For example, the sliding along the diagonal cracks is possibly larger during the experiments, which may not be captured in a finite element program unless sliding and friction between the surfaces of the crack is explicitly modeled in the program. These variations highlight the importance of rigorous experimental protocols and careful calibration of analytical models to ensure accurate predictions of structural behavior.

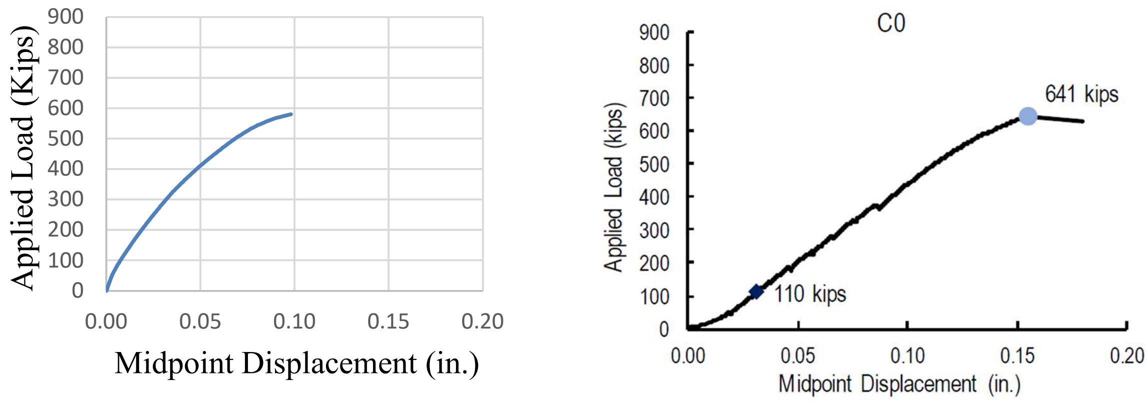

(a) (b)

Figure 1.34: (a) Calculated load versus displacement curve for Specimen C0 at $P_{IDEA\ StatiCa}$, and (b) measured load vs. displacement curve for Specimen C0 (Wilson, 2017).

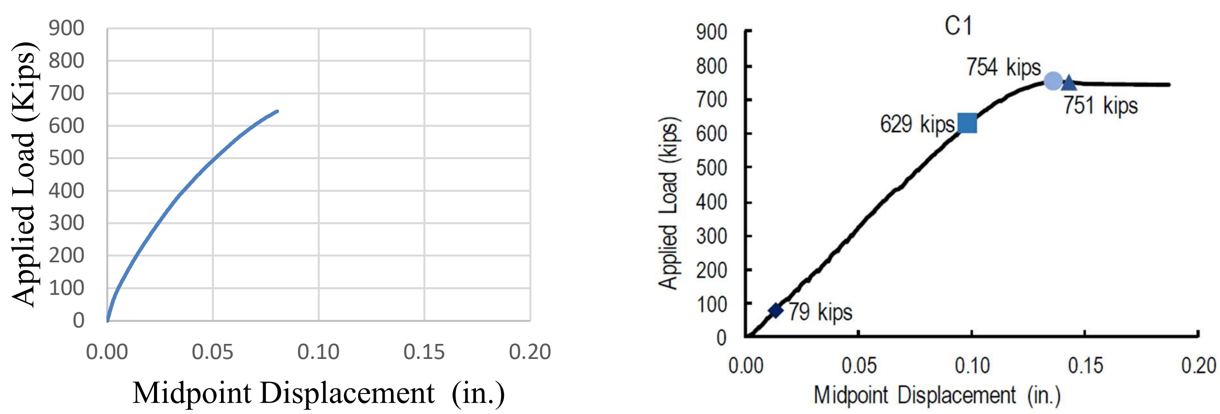

(a) (b)

Figure 1.35: (a) Calculated load versus displacement curve for Specimen C1 at $P_{IDEA\ StatiCa}$, and (b) measured load versus displacement curve for specimen C1 (Wilson, 2017).

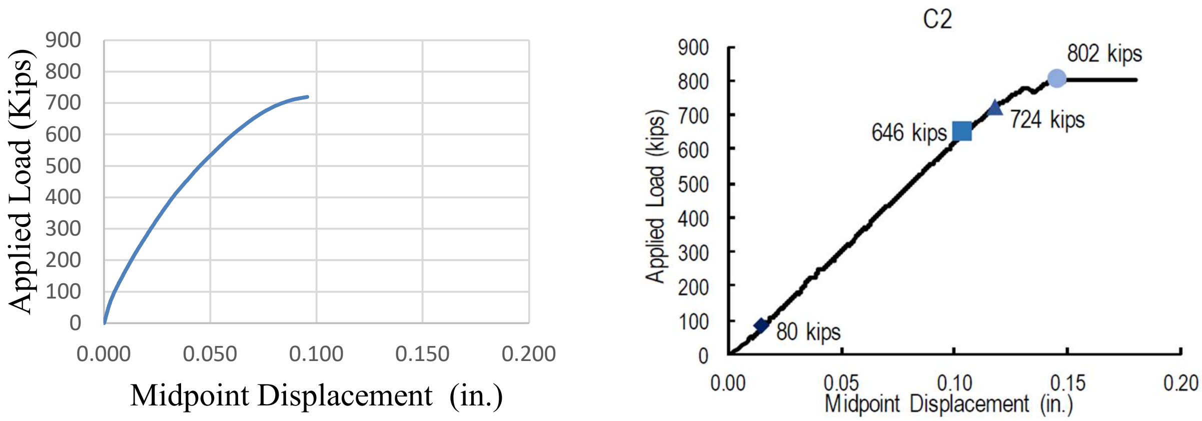

(a) (b)

Figure 1.36: (a) Calculated load verses displacement curve for Specimen C2 at $P_{IDEA\ StatiCa}$, and (b) measured load verses displacement curve for Specimen C2 (Wilson, 2017).

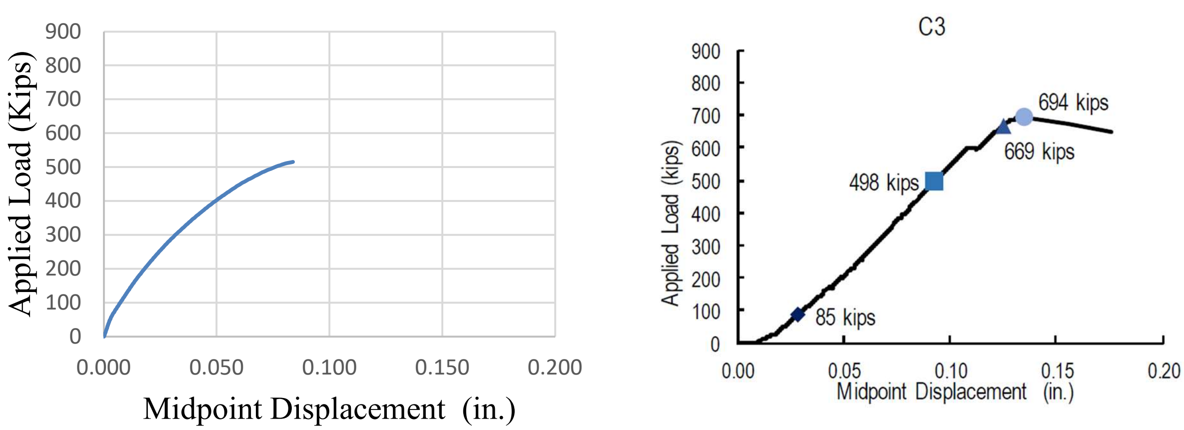

(a) (b).

Figure 1.37: (a) Calculated load versus displacement curve for Specimen C3 at $P_{IDEA\ StatiCa}$, and (b) measured load versus displacement curve for Specimen C3 (Wilson, 2017).

In the load versus deflection curves depicted in Figures 1.38 through 1.40 for corbel specimens S1, S2, and S3, it is observed that the deflection values calculated by IDEA StatiCa closely match the measured deflections for specimens S1 and S2. However, a notable difference is observed for specimen S3, where the deflection value obtained from IDEA StatiCa is lower compared to the measured deflection. This is consistent with the calculated deflections for C specimens (Figure 1.34 through 1.37).

This discrepancy in deflection values, particularly for specimen S3, may be attributed to the absence of secondary or crack reinforcement in the corbel. The absence of such reinforcement could lead to different (more brittle) structural response, impacting the overall deflection behavior observed during testing. While the deflection values for specimens S1 and S2 closely align with the measured deflections, suggesting good agreement between analytical predictions and experimental results.

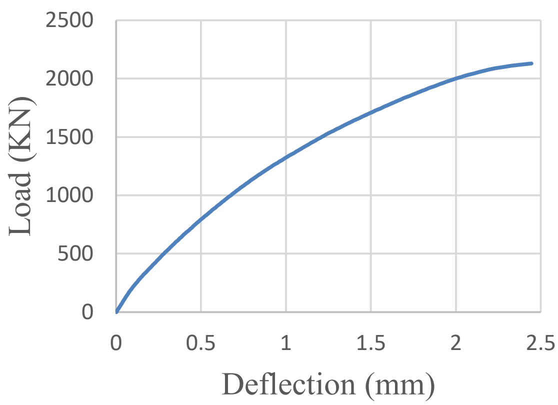

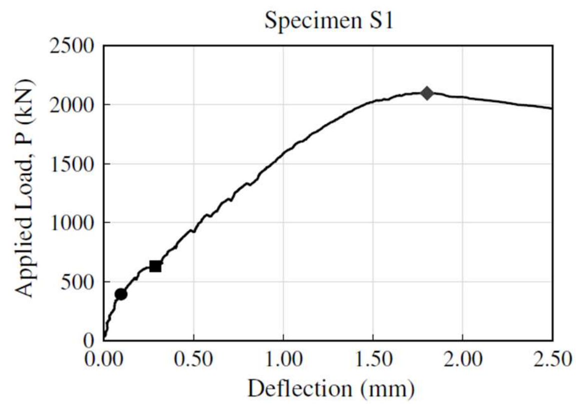

(a) (b)

Figure 1.38: (a) Calculated load versus deflection curve for Specimen S1 at $P_{IDEA\ StatiCa}$, and (b) measured load versus deflection curve for specimen S1 (Khosravikia et al., 2018).

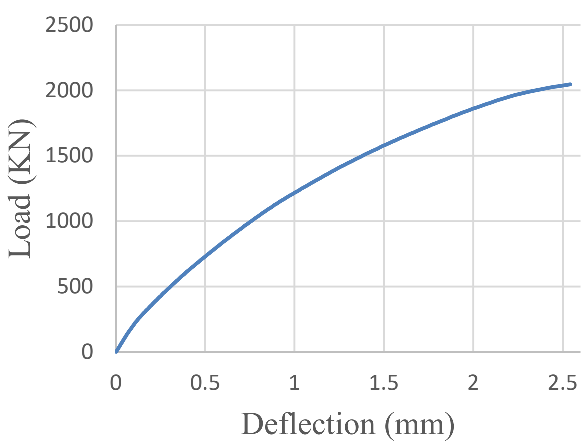

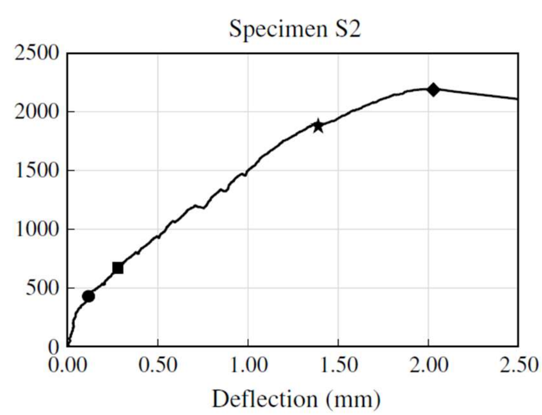

(a) (b)

Figure 1.39: (a) Calculated load versus deflection curve for Specimen S2 at $P_{IDEA\ StatiCa}$, and (b) measured load versus deflection curve for Specimen S2 (Khosravikia et al., 2018).

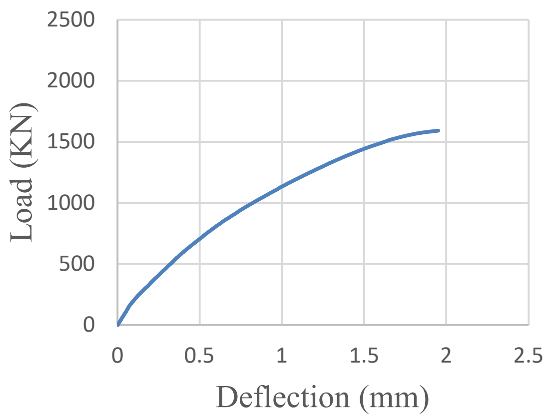

(a)

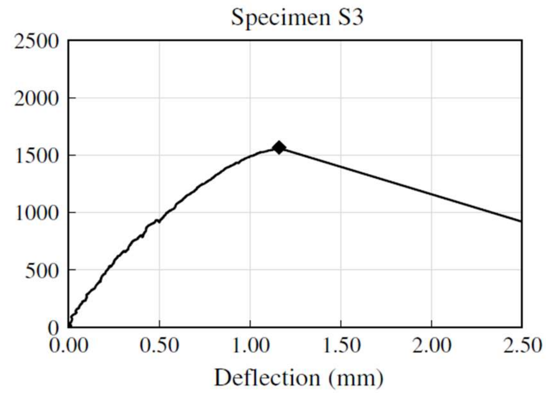

(b)

Figure 1.40: (a) Calculated load versus deflection curve for Specimen S3 at $P_{IDEA\ StatiCa}$, and (b) measured load versus deflection curve for Specimen S3 (Khosravikia et al., 2018).

In summary, across all seven corbel specimens (C0 to C3 and S1 to S3), the maximum loads predicted by IDEA StatiCa consistently surpassed those of the STM and closely aligned with experimental results, apart from specimens S1 and S3. Specifically, for S1 and S3, the maximum loads derived from IDEA StatiCa exceeded the measured values by 1.5% and 3.1%, respectively. Notably, cracks observed in failed specimens consistently fell within the range indicated by IDEA StatiCa across all specimens. Furthermore, deflections calculated by IDEA StatiCa at maximum loads were notably lower for category C specimens and closely mirrored measured deflections for Specimens S. Overall, the results from experimental testing, the strut and tie model (STM), IDEA StatiCa, and ABAQUS compare reasonably.

Regarding the performance of IDEA StatiCa, it is apparent that results are comparable to those of ABAQUS. This indicates that IDEA StatiCa is capable of accurately simulating and analyzing structural behavior. The effectiveness and reliability of the software for engineering analysis and design tasks are underscored by its ability to deliver results in line with established tools like ABAQUS. Nonetheless, it is always advisable to ensure accuracy and reliability for specific applications by validating results from any software with experimental data or alternative numerical methods. Further refinement and validation of analytical models could enhance the accuracy of predictions, ensuring more robust structural analysis and design processes.

References

Wilson, H. R. (2017). *Investigation of corbels designed according to strut-and-tie and empirical methods* (Master's thesis). The University of Texas at Austin. http://dx.doi.org/10.26153/tsw/2767

Khosravikia, F., Kim, H. S., Yi, Y., Wilson, H., Yousefpour, H., Hrynyk, T., & Bayrak, O. (2018). *Experimental and numerical assessment of corbels designed based on strut-and-tie provisions.* Journal of Structural Engineering, ASCE, ISSN 0733-9445. DOI: 10.1061/(ASCE)ST.1943-541X.0002137

ACI Committee 318. (2014). *Building Code Requirements for Structural Concrete (ACI 318R-19).* Farmington Hills, Michigan: American Concrete Institute.

American Association of State Highway and Transportation Officials (AASHTO). (2016). *AASHTO LRFD Bridge Design Specifications, 7th Edition-with 2015 and 2016 Interim Revisions.* Washington, DC.

ASTM. (2004). ASTM C496/C496M: *Standard Test Method for Splitting Tensile Strength of Cylindrical Concrete Specimens.* West Conshohocken, PA: ASTM.

ASTM. (2014). ASTM C469/C469M: *Standard Test Method for Static Modulus of Elasticity and Poisson's Ratio of Concrete in Compression.* West Conshohocken, PA: ASTM.

ASTM. (2017). ASTM A370: *Standard Test Methods and Definitions for Mechanical Testing of Steel Products.* West Conshohocken, PA: ASTM.

ASTM. (2017). ASTM C39/C39M: *Standard Test Method for Compressive Strength of Cylindrical Concrete Specimens.* West Conshohocken, PA: ASTM.

Chapter 2. Modeling and Analysis of Reinforced Concrete Deep Beam

2.1. Introduction

The behavior of five reinforced concrete (RC) deep beam specimens was investigated in this chapter. Their strength and deformation capacities were assessed using IDEA StatiCa and compared with design capacities determined through the strut and tie methods (STM) included in ACI 318-05 (2005) and ACI 318-19 (2019). The results were juxtaposed with experimental data.

One of the deep beam test specimens was chosen as a baseline model for further examination through ABAQUS software (2023). This involved the computation and comparison of load-deflection relationship, principal stress distribution, and crack patterns with those observed during experiments (Huizinga, 2007). Additionally, a detailed investigation into the impact of secondary reinforcement on deep beam capacities was undertaken.

2.2 Strut and Tie Method (STM) per ACI 318-19

When designing reinforced concrete members, engineers typically assume that strains vary linearly over the height of a section. This principle, known as the Bernoulli hypothesis or beam theory, governs the mechanical or flexural behavior of a beam by assuming that plane sections remain plane. The region of a member where the Bernoulli hypothesis holds true is termed a B-region, with B representing beam or Bernoulli. In these B-regions, the internal stress state can be determined by balancing forces at a specific cross-section, commonly known as sectional design.

A deep beam is characterized by having a relatively small shear span-to-depth ratio (*a/d*), potential nonlinear shear strains dominating its behavior. Nonlinear strain distributions arise from sudden changes in geometry or loading conditions, creating regions of discontinuity known as D-regions. D stands for discontinuity or disturbance. According to elastic stress analysis, the localized effects of a concentrated load or geometric discontinuity dissipate roughly one member depth (*d*) away from the discontinuity, a principle known as St. Venant's Principle. Consequently, D-regions are assumed to extend one member depth from the load or discontinuity. Figure 2.1 illustrates both a B-region and a D-region for an asymmetrically loaded simply supported beam. Figure 2.2 depicts B and D regions defined by the ACI 318-19. In Figure 2.2, the shaded regions are the D-regions and the regions outside of the D-regions are termed as B-regions.

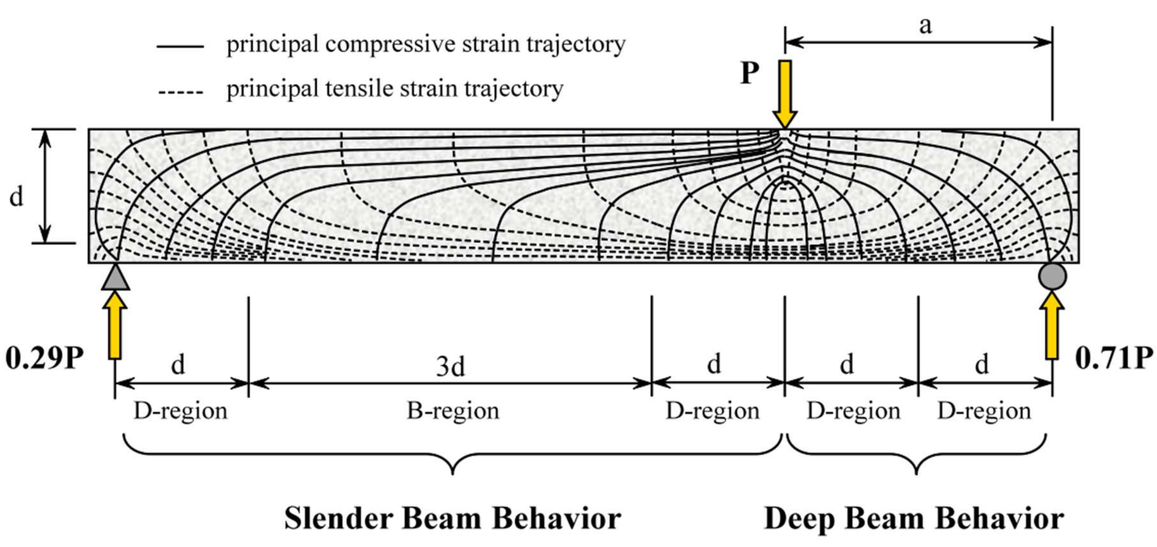

Figure 2.1: Strain Distribution in Deep and Slender Portion of a Beam (Tuchscherer et al., 2009).

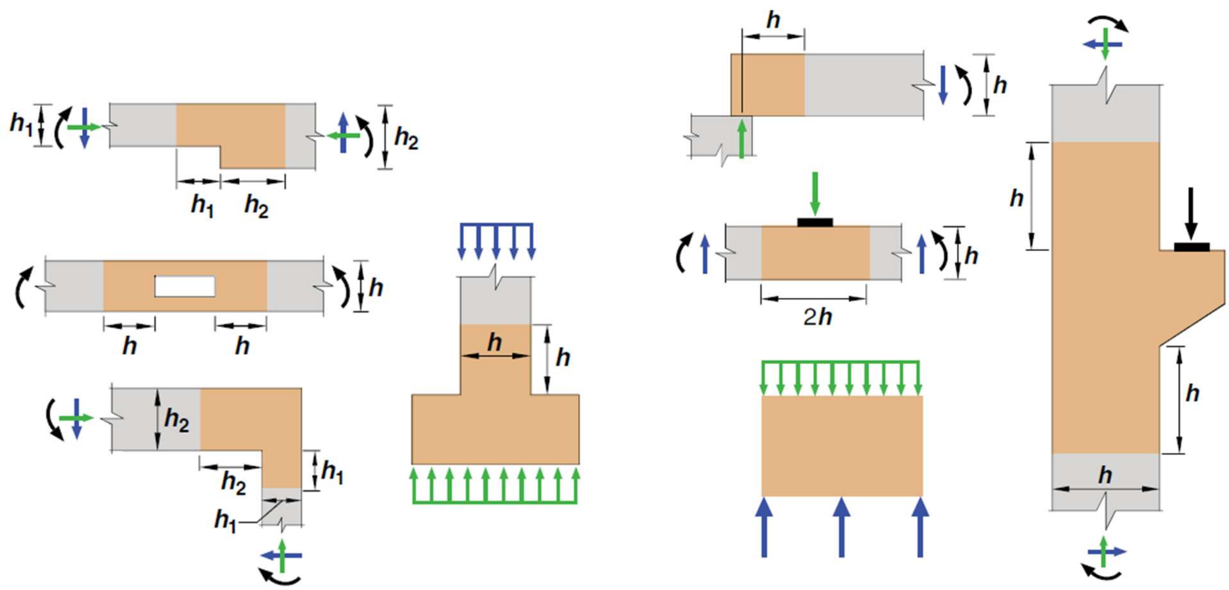

(a) geometric discontinuities (b) loading and geometric discontinuities

Figure 2.2: D-regions and discontinuities (Figure R23.1 in ACI 318-19).

Strut-and-tie model (STM) involves representation of a concrete members with an abstract truss consisting of struts (concrete in compression) and ties (steel bars in tension) interconnected at nodes. To ensure sufficient crack control and mitigate strain incompatibility, it is imperative that the angle between the axis of any strut and any tie entering a node remains at 25° or higher as per the ACI 318-19. Figures 2.3 and 2.4 illustrates the basic elements of a strut and tie model for a deep beam. Nodes are classified into three types as shown in Figure 2.4: CCC nodes, indicating nodes without ties (compression-compression-compression node); CCT nodes, representing nodes with a single tie (compression-compression-tension node); and CTT nodes, denoting nodes with two or more ties.

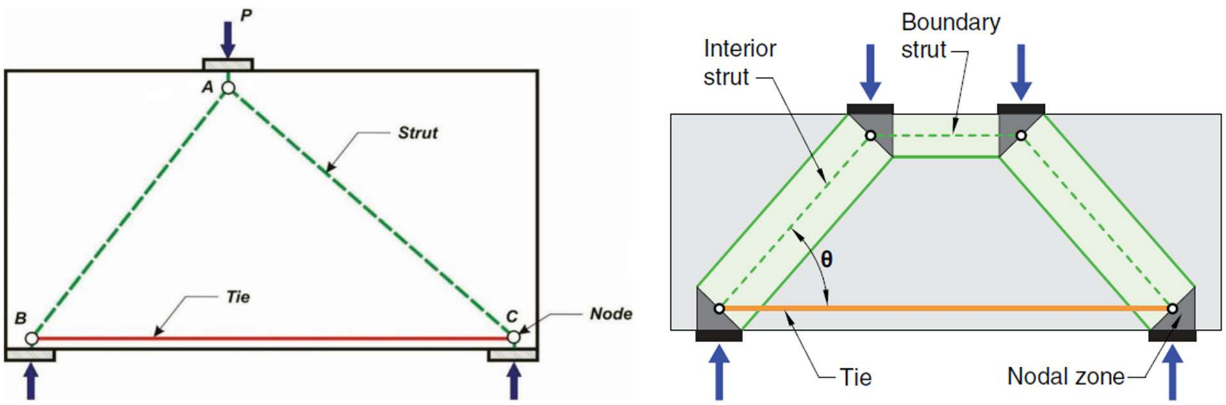

Figure 2.3: Basic elements of a strut-and-tie model for a deep beam (ACI PRC-445.2-21).

For equilibrium, each node in a strut-and-tie model should experience at least three forces, as depicted in Figure 2.5. The lightly shaded area in Figure 2.6 represents an extended nodal zone. This zone encompasses the part of a member delineated by the intersection of the effective strut width (w_s) and the effective tie width (w_t).

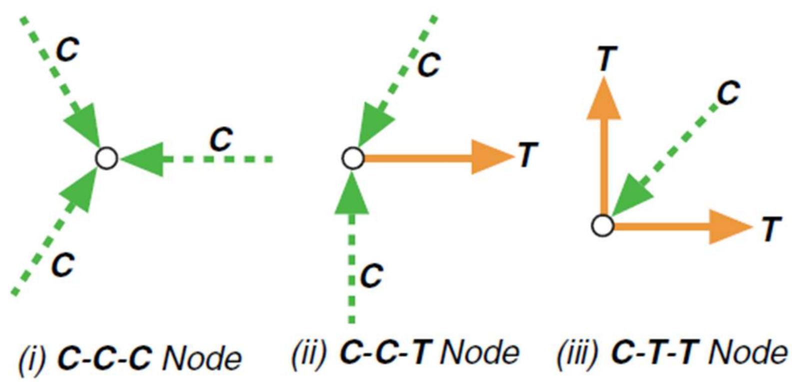

Figure 2.4: Classification of nodes (Figure R23.2.6c in ACI 318-19).

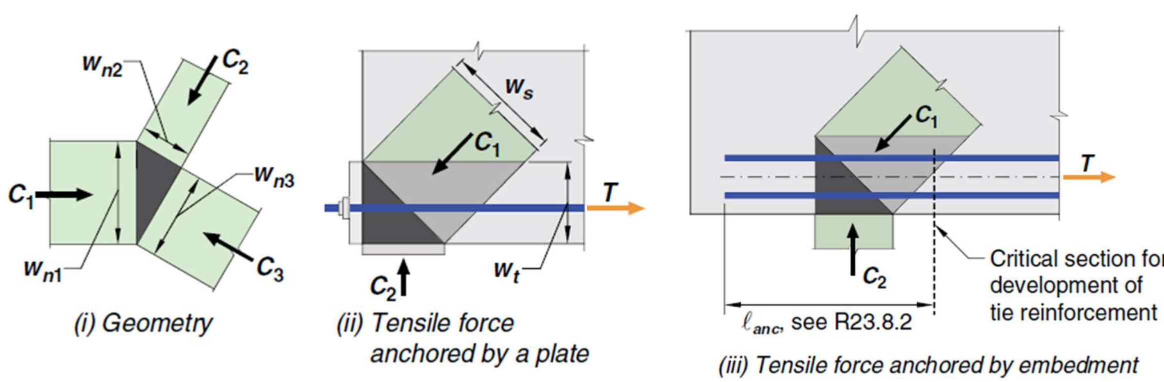

Figure 2.5: Hydrostatic nodes (Figure R23.2.6a in ACI 318-19).

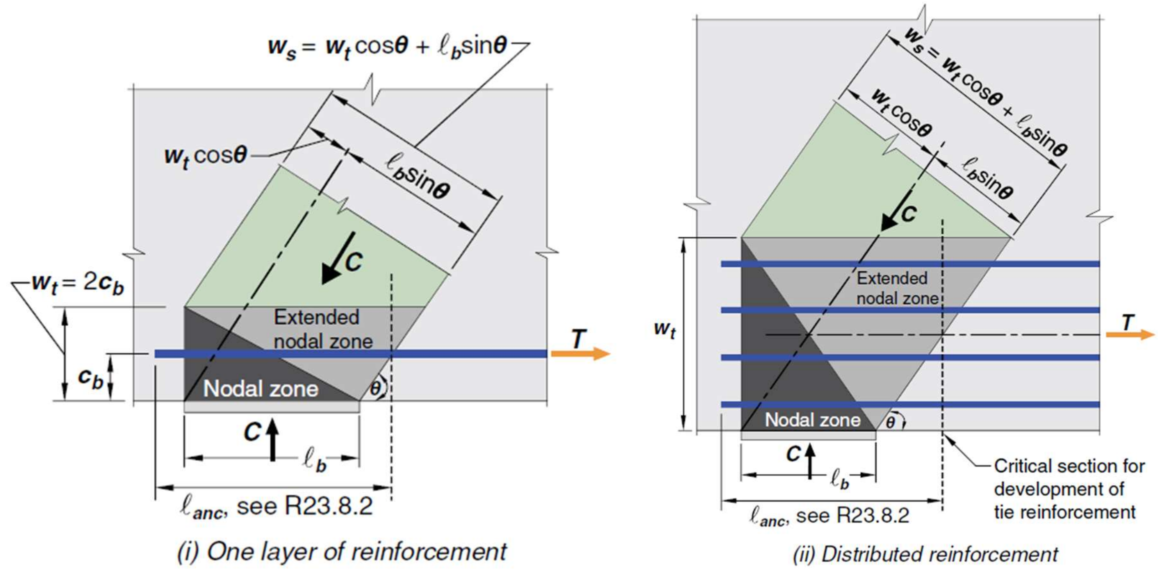

Figure 2.6: Extended nodal zone showing the effect of the distribution of the force (Figure R23.2.6b in ACI 318-19).

For each relevant factored load combination design strength of every strut, tie, and nodal zone within a strut-and-tie model must meet the condition mentioned in the Section 23.3.1 of ACI 318-19, $\phi S_n \geq U$, encompassing requirements (a) through (c):

(a) Struts: $\phi F_{ns} \geq F_{us}$ (2.1)

(b) Ties: $\phi F_{nt} \geq F_{ut}$ (2.2)

(c) Nodal zones: $\phi F_{nn} \geq F_{un}$ (2.3)

The symbol ϕ represents the strength reduction factor, S_n is the nominal capacity, U is the strength of a member or cross section required to resist factored loads, F_{ns} is the nominal compressive strength of a strut, F_{nn} is the nominal compressive strength of a nodal zone, F_{us} is the factored compressive force in a strut, F_{ut} denotes the factored tensile force in a tie, and F_{un} represents the factored force on the face of a node. F_{ns} is evaluated at each end of the strut and taken as the lesser value, A_{cs} is the cross-sectional area at the end of the strut under consideration, A_s' is the area of compression reinforcement along the length of the strut, and f_s' is the stress in the compression reinforcement at the nominal axial strength of the strut. It is permitted for Grade 40 and 60 reinforcement to take f_s' equal to f_y.

The effective compressive strength of concrete f_{ce} in a strut is calculated using Equation 2.4 (Equation 23.4.3 of ACI 318-19).

$$f_{ce} = 0.85\, \beta_c\, \beta_s f_c' \tag{2.4}$$

where the strut coefficient β_s is calculated in accordance with Table 2.1 and strut and node confinement modification factor β_c is in accordance with Table 2.2.

Table 2.1: Strut coefficient β_s (Table 23.4.3 (a) in ACI 318-19)

<table>
<tr><th>Strut location</th><th>Strut type</th><th>Criteria</th><th>β_s</th></tr>
<tr><td>Tension members or tension zones of members</td><td>Any</td><td>All cases</td><td>0.40</td></tr>
<tr><td rowspan="5">All other cases</td><td>Boundary struts</td><td>All cases</td><td>1.00</td></tr>
<tr><td rowspan="4">Interior struts</td><td>Reinforcement satisfying (a) or (b) of Table 23.5.1</td><td>0.75</td></tr>
<tr><td>Located in regions satisfying 23.4.4</td><td>0.75</td></tr>
<tr><td>Beam-column joints</td><td>0.75</td></tr>
<tr><td>All other cases</td><td>0.40</td></tr>
</table>

Table 2.2: Strut and node confinement modification factor β_c (Table 23.4.3 (b) in ACI 318-19)

<table>
<tr><th>Location</th><th colspan="2"></th></tr>
<tr><td rowspan="2">End of a strut connected to a node that includes a bearing surface.
Node that includes a bearing surface</td><td rowspan="2">Lesser of</td><td>$\sqrt{A_1/A_2}$, where A_1 is defined by the bearing surface</td></tr>
<tr><td>2.0</td></tr>
<tr><td>Other cases</td><td colspan="2">1.0</td></tr>
</table>

The nominal compressive strength of a strut, F_{ns} is calculated using Equation 2.5 and 2.6 as defined in Section 23.4.1 of ACI 318-19.

(a) Struts without longitudinal reinforcement:

$$F_{ns} = f_{ce} A_{cs} \tag{2.5}$$

(b) Struts with longitudinal reinforcement:

$$F_{ns} = f_{ce} A_{cs} + A_s' f_s' \tag{2.6}$$

The nominal tensile strength of a tie, F_{nt} can be calculated using Equation 2.7 per Section 23.7.2 of ACI 318-19.

$$F_{nt} = A_{ts} f_y \tag{2.7}$$

Where, A_{ts} is the area of non-prestressed reinforcement in a tie. The nominal compressive strength of a nodal zone F_{nn} can be calculated using Equation 2.8 (Equation 23.9.1 in ACI 318-19).

$$F_{nn} = f_{ce} A_{nz} \tag{2.8}$$

where, A_{nz} represents the area of each face of a nodal zone determined as described in Section 23.9.4 of ACI 318-19. It is taken as the smaller of

(a) area of the face of the nodal zone perpendicular to the line of action of F_{us} and
(b) area of a section through the nodal zone perpendicular to the line of action of the resultant force on the section.

The effective compressive strength of concrete at a face of a nodal zone, f_{ce}, is calculated by Equation 2.6 according to Section 23.9.2 of ACI 318-19.

$$f_{ce} = 0.85\, \beta_c\, \beta_n f_c' \tag{2.9}$$

where, β_c and β_n can be obtained from Tables 2.2 and 2.3 respectively.

Table 2.3: Nodal zone coefficient βn (ACI 318-19)

Configuration of nodal zone	β_n
Nodal zone bounded by struts, bearing areas, or both	1
Nodal zone anchoring one tie	0.8
Nodal zone anchoring two or more ties	0.6

Design verifications for deep beams were conducted based on relevant building codes, utilizing the strut and tie model (STM) to assess their capacities, while numerical investigations evaluated crack-control requirements for reinforced concrete (RC) deep beams in accordance with ACI 318-05 provisions.

2.3 Experimental Study

To assess the structural performance of deep beams, five reinforced concrete (RC) deep beam specimens **i**dentified as 1A, 1B, 2A, 3A, and 3B were examined. These specimens were designed by Huizinga (2007) following the strut and tie model (STM) provisions of ACI 318-05 (2005). Fabrication and testing of the specimens were conducted at the Ferguson Structural Engineering Laboratory of the University of Texas at Austin. Consistency in primary reinforcement was maintained across all specimens, while variations were introduced in web reinforcement. The specimens were exclusively designed to withstand vertical loading, with potential horizontal tensile forces disregarded. Test setups were simplified accordingly, focusing solely on vertical loads, with each specimen supported by two bearing plates (Figures 2.7 and 2.8). Among the specimens, 1A was selected as the baseline model and subjected to further analysis using ABAQUS software.

2.3.1 Experimental Setup

All five specimens (1A, 1B, 2A, 3A, and 3B) featured a cross-section measuring 36 in. by 48 in. (914.4 mm by 1219.2 mm) with a total length of 284 in (7214 mm). Design of these deep beams primarily focused on varying the amount of web reinforcement, the distribution of transverse reinforcement or stirrup across the web, and the size of the load plate as the main variables. In all specimens, the design included a consistent clear concrete cover of 2 in. (50.8 mm) on all sides.

In the initial phase of testing, a particular specimen was subjected to a concentrated load intentionally placed off-center near one end of the beam. This arrangement aimed to achieve a shear span-to-effective depth (*a/d*) ratio of 1.85. The test setup is illustrated in Figures 2.7 through 2.9. Subsequently, after completing the test on one side of the specimen, the hydraulic ram (i.e., the concentrated load) was relocated to the opposite side of the beam for another test, maintaining the same *a/d* ratio. The selection of an *a/d* ratio of 1.85 was deliberate chosen to be able to observe shear failure within the short span (near the left support in Figures 2.7 and 2.9) as the possibility for shear failure increases with decreasing shear span-to-effective depth ratios (Huizinga, 2007).

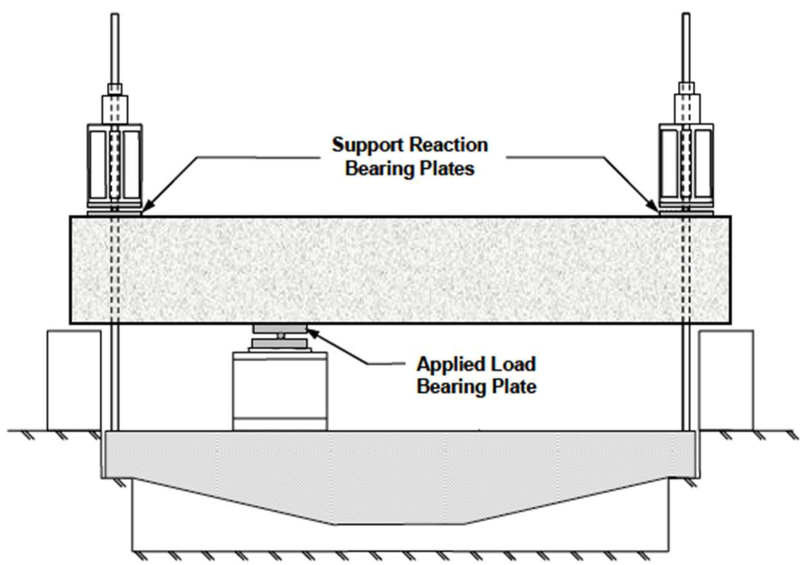

Figure 2.7: Test setup, elevation view for deep beam (Huizinga, 2007).

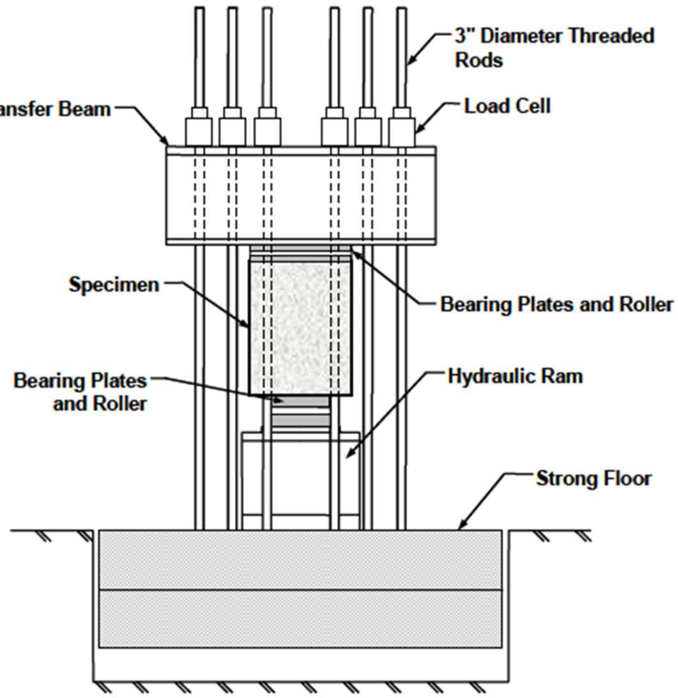

Figure 2.8: Test setup, elevation view for deep beam (Huizinga, 2007).

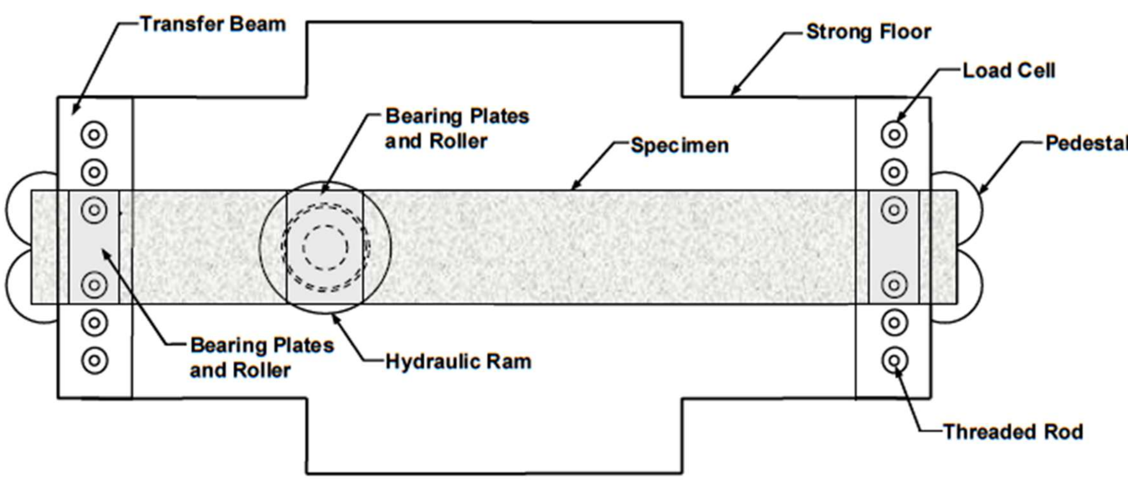

Figure 2.9: Test setup, plan view for deep beam (Huizinga, 2007).

The two loading points and shear spans are labeled as A and B, respectively, as depicted in Figures 2.10 and 2.11. After experiencing shear failure in shear span, A, the span was securely clamped together as shown in Figure 2.11. This clamping allowed for testing of the second shear span of the specimen without jeopardizing the overall stability of the specimen.

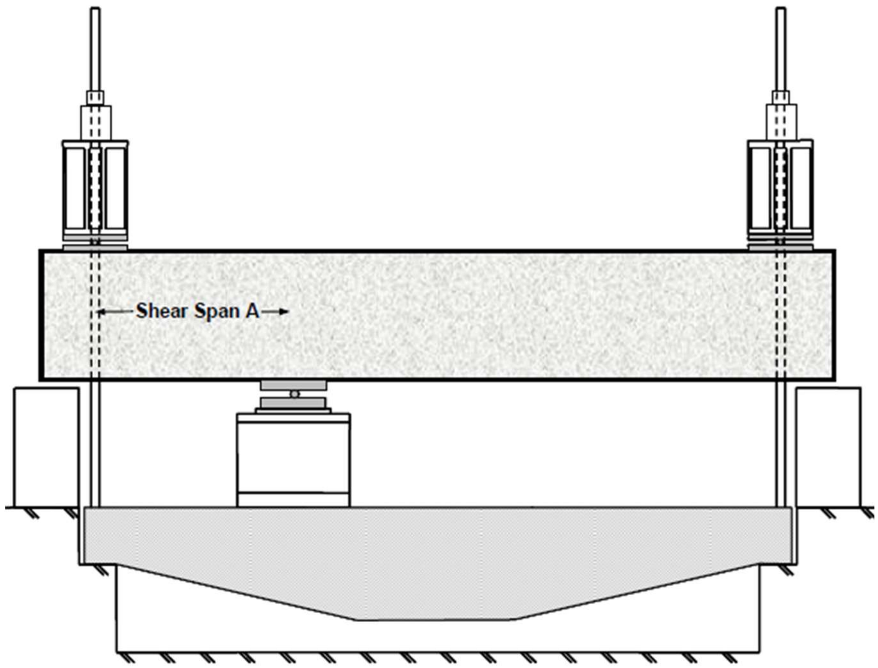

Figure 2.10: Loading configuration for Shear Span A (Huizinga, 2007).

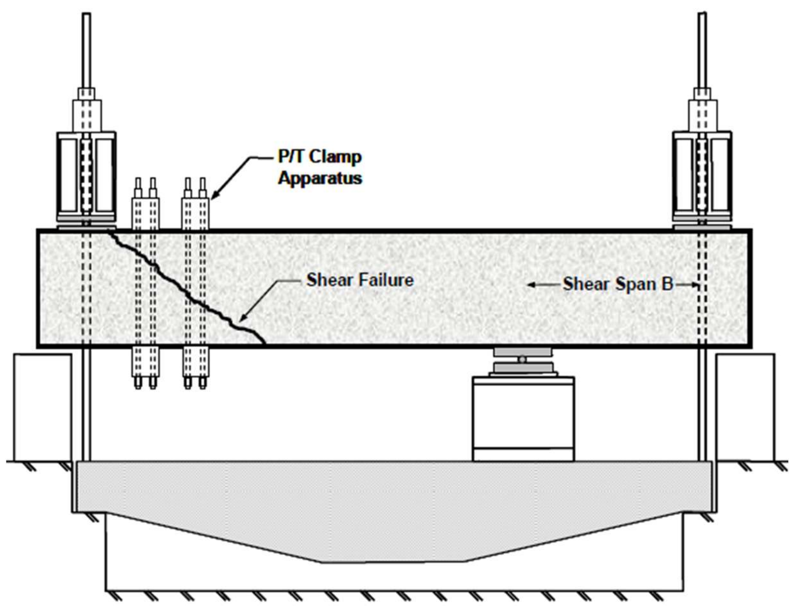

Figure 2.11: Loading configuration for Shear Span B (Huizinga, 2007).

2.3.2 Deep Beam Properties and Reinforcement Detailing

The deep beam details are outlined in Table 2.4. This table provides information on the shear span tested, the compressive strength (f_c'), and the quantity of stirrup legs for each specimen. For instance, specimens M-03-4-CCC2436 and M-09-4-CCC2436 were tested under shear span 1A and 1B respectively, with a compressive strength of 4100 psi (28.27 MPa) and four stirrup legs. Similarly, specimens M-03-2-CCC2436, M-02-4-CCC2436, and M-03-4-CCC0812 were tested under different shear spans with varying compressive strengths and number of stirrup legs, as detailed in Table 2.4. In all cases the load plate size was 24 in. by 36 in. (610 mm by 914.4 mm) except deep beam 3B, where the load plate size was 8 in. by 12 in. (203.2 mm by 304.8 mm). Beam cross sections including stirrups and shear spans are shown in Figures 2.12 through 2.17 for these test specimens.

Table 2.4: Deep beam details (Huizinga, 2007)

ID	Shear span tested	$f_{c,}'$ psi (MPa)	Quantity of stirrup legs	Load plate, in. x in. (mm x mm)
M-03-4-CCC2436	1A	4100 (28.27)	4 legs	24 x 36 (610 x 914.4)
M-09-4-CCC2436	1B	4100 (28.27)	4 legs	24 x 36 (610 x 914.4)
M-03-2-CCC2436	2A	4900 (33.79)	2 legs	24 x 36 (610 x 914.4)
M-02-4-CCC2436	3A	2800 (19.31)	4 legs	24 x 36 (610 x 914.4)
M-03-4-CCC0812	3B	3000 (20.68)	4 legs	8 x 12 (203.2 x 304.8)

In the test setup, the specimen necessitated the insertion of a pair of high strength threaded rods through its end regions. To accommodate this requirement, two 3.75 in. (95.25 mm) diameter aluminum ducts were incorporated into the specimen at the beam's reaction points, enabling the passage of the rods at the support locations. Consequently, adjustments had to be made to the placement of the longitudinal reinforcing bars. As shown in Figure 2.12, as a result, it was not feasible to uniformly space the longitudinal bars.

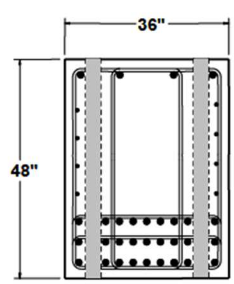

Figure 2.12: Specimen cross section with aluminum ducts (Huizinga, 2007).

In Figure 2.13, the cross-section and reinforcement detailing for deep beam 1A are presented. The primary reinforcement, a 27#11 bars are designated for the beam's main reinforcement, while the compression reinforcement comprises 4#11 bars. Additionally, uniformly distributed #5 bars serve as skin or secondary reinforcement on both sides on the beam cross section. Stirrups, spaced at intervals of 11 in. (279.4 mm) between the left support and applied load, play a crucial role in enhancing shear capacity. In the remaining portion of the beam, a uniform spacing of 4 in. (101.6 mm) is maintained for the stirrups. This reinforcement configuration aims to optimize the beam's ability to withstand heavy loads and resist shear forces effectively.

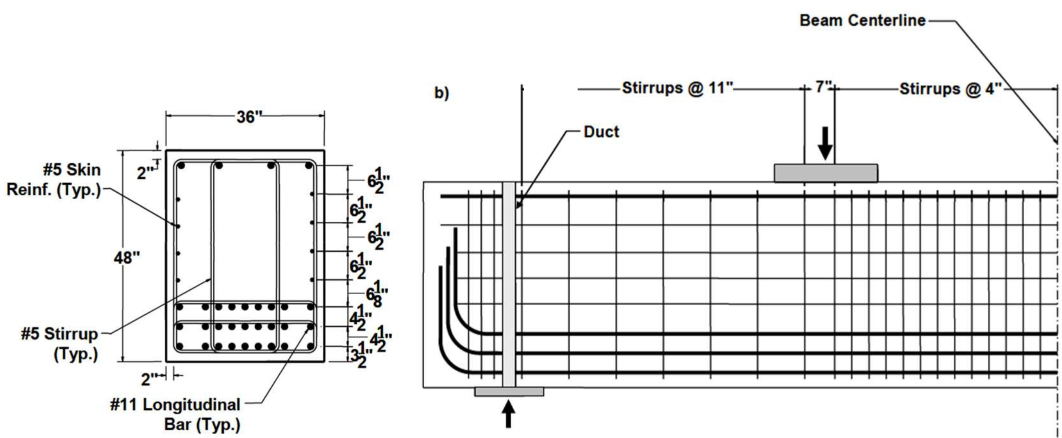

(a) (b)

Figure 2.13: Shear span 1A: a) cross-section, and b) elevation (Huizinga, 2007).

Figure 2.14 illustrates deep beam 1B, which corresponds to the same beam presented in 1A. After completion of testing and experiencing shear failure, the failure zone was securely clamped, as depicted in the figure (Figure 2.11). Subsequently, the hydraulic ram, serving as the concentrated load, was relocated to the opposite side of the beam for test 1B, maintaining the same shear span-to-effective depth (*a/d*) ratio. Notably, the vertical stirrups between the applied load and the right support were spaced at 4 in. center-to-center. All other reinforcement detailing remained consistent with beam 1A.

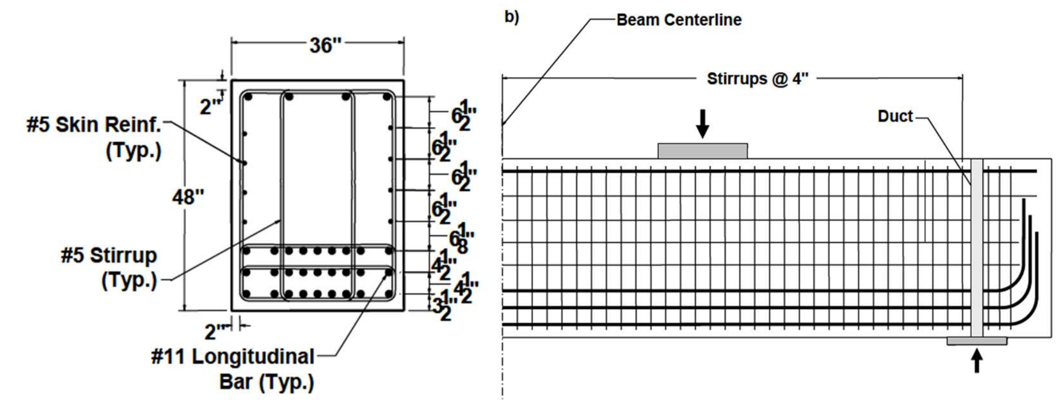

(a) (b)

Figure 2.14: Shear span 1B: a) cross-section, and b) elevation (Huizinga, 2007).

Figure 2.15 shows the cross-section and reinforcement details of deep beam 2A. The main reinforcement of the beam is represented by a 27#11 bars, while the compression reinforcement consists of 4#11 bars. Additionally, #5 bars are employed as secondary horizontal bars, spaced at intervals of 6.5 in. (165.1 mm) center-to-center. Stirrups included two-legged #7 bars. The spacing between the left support and applied load for the stirrups is 11 in. (279.4 mm), while the spacing throughout the rest of the beam is set at 5.5 in. (139.7 mm) center-to-center.

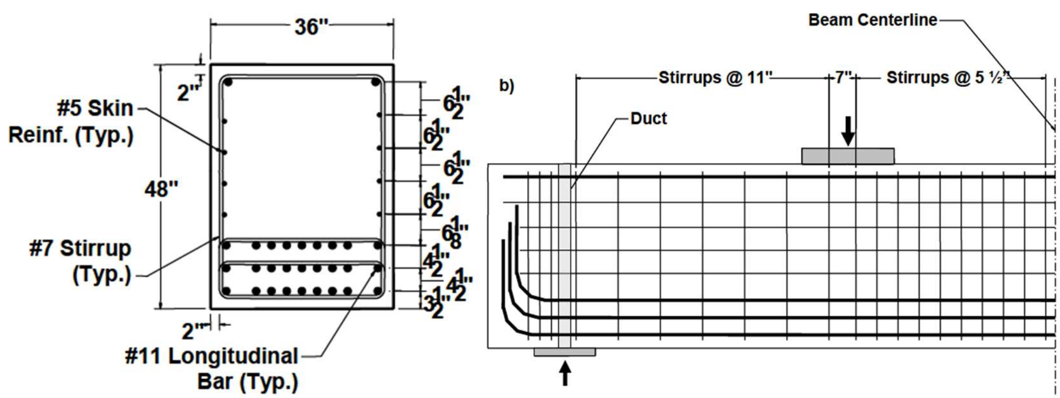

(a) (b)

Figure 2.15: Shear span 2A: a) cross-section, and b) elevation (Huizinga, 2007).

The cross-section and reinforcement detailing for deep beams 3A and 3B are illustrated in Figures 2.16 and 2.17, respectively. In both cases, the stirrups are composed of #4 bars, with a total of four legs. For beam 3A, the horizontal reinforcement between the support and applied load is comprised of three #5 bars spaced at intervals of 8 in. (203.2 mm) center-to-center. The stirrup spacing is maintained at 10 in. (254 mm) between the left support and applied load, and 11 in. (279.4 mm) between the right support and applied load, with a center-to-center spacing of 4 in. (101.6 mm) for the remaining middle portion of the beam. For beam 3B, the horizontal reinforcement between the support and applied load is comprised of four #5 bars spaced at intervals of 6.5 in. (165.1 mm) center-to-center, while the same stirrup configuration as in 3A is maintained.

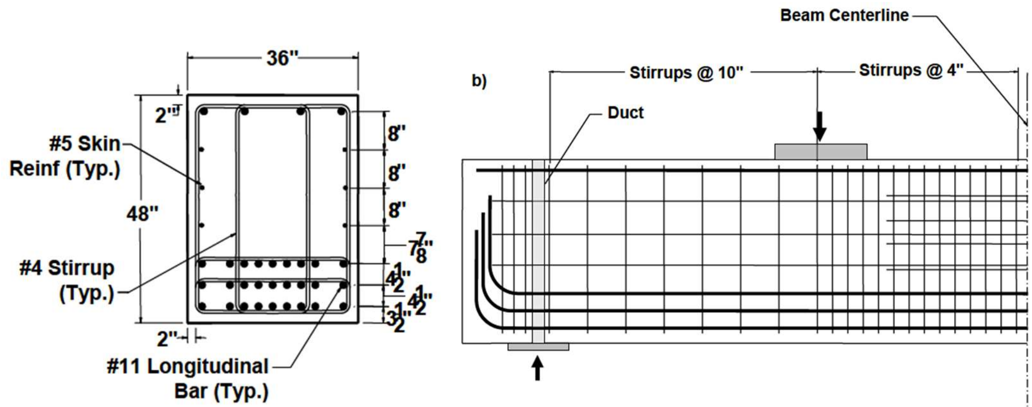

(a) (b)

Figure 2.16: Shear span 3A: a) cross-section, and b) elevation (Huizinga, 2007).

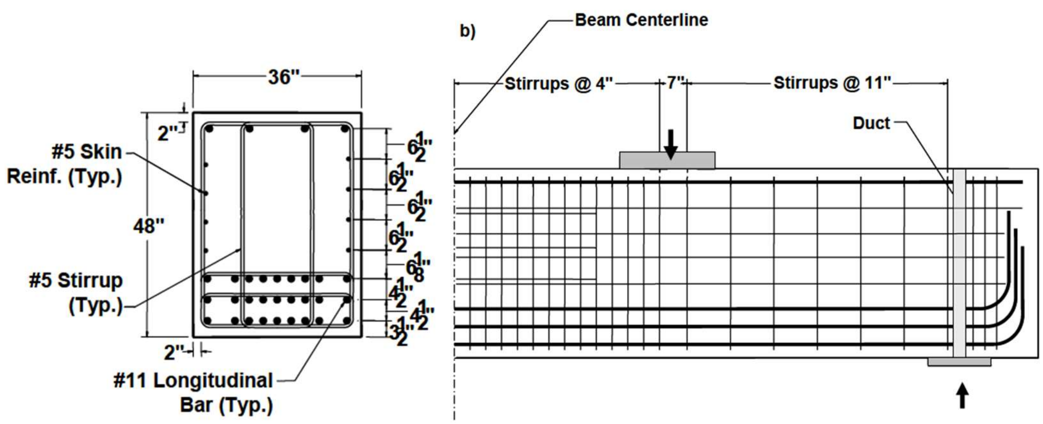

(a) (b)

Figure 2.17: Shear span 3B: a) cross-section, and b) elevation (Huizinga, 2007).

2.3.3 Experimental Results

Coupons from #5 bars are tested in the laboratory. Figure 2.18 shows the measured stress-strain relationship for the #5 bars used in specimens 1A and 1B. Table 2.5 provides the measured properties of reinforcing bars utilized in the specimens, including yield stress and strain.

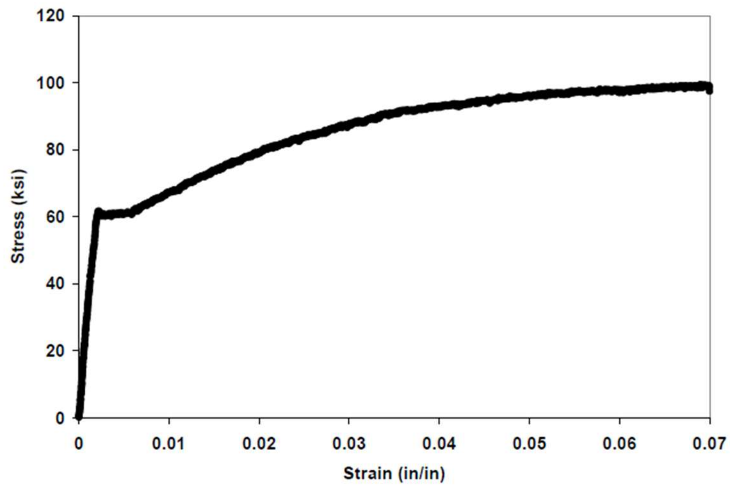

Figure 2.18: Stress versus strain relationship, specimen 1A, and 1B for #5 bars (Huizinga, 2007).

Table 2.5: Reinforcing bar properties (Huizinga, 2007)

Beam Designation	Bar size	Yield stress, ksi (MPa)	Yield strain, in./in. (mm/mm)
1A, 1B	#5	61.0 (420.0)	0.0021 (0.0533)
	#11	67.0 (462.0)	0.0023 (0.0584)
2A	#7	62.0 (427.0)	0.0021 (0.0533)
	#11	68.0 (469.0)	0.0023 (0.0584)
3A, 3B	#4	62.5 (431.0)	0.0022 (0.0559)
	#5	62.5 (431.0)	0.0022 (0.0559)
	#11	65.0 (448.0)	0.0022 (0.0559)

Figure 2.19 shows the 500-kip (2224.5 kN) load cells utilized in the test setup. The support reactions in the test region were measured by these load cells. Additionally, the accuracy of the calculated load was verified through readings obtained from pressure transducers. Displacement data were acquired using a set of four 6 in. (152.4 mm) linear potentiometers. The displacement of the specimens was measured on the bottom face at four points: the load point, mid-span, and at the supports (as depicted in Figure 2.19).

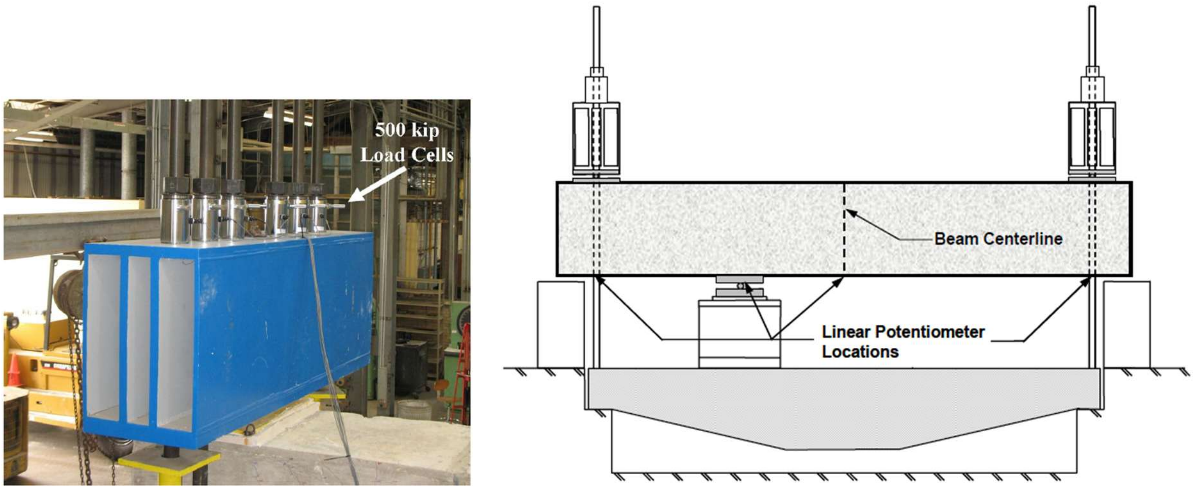

Figure 2.19: 500-kip (2224.5 kN) load cells (left) and linear potentiometer locations (Huizinga, 2007).

Strain gauges were employed to measure both rebar and concrete strains at select locations within the specimens. Strains were measured on several tensile longitudinal bars at each of the two load points. Additionally, in the first specimen, strains were measured along a corner longitudinal bar at various locations adjacent to the reaction bearing plate (Figure 2.20).

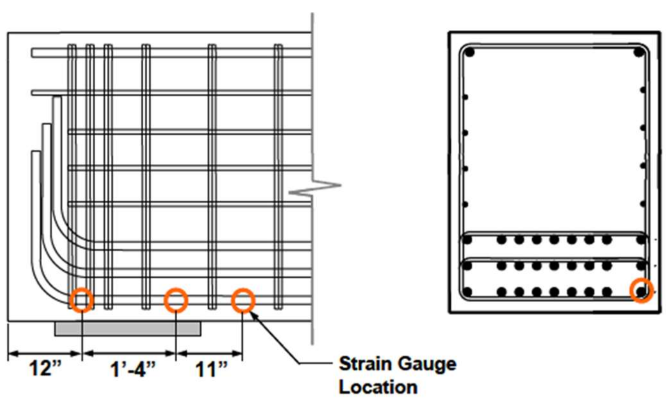

Figure 2.20: Strain gauge locations adjacent to reaction point (Huizinga, 2007).

Figure 2.21 depicts a photograph of the shear failure in the shear span of beam 1A, with bearing plates highlighted for clarity. The shear failure commenced with concrete crushing above the applied load bearing plate. At the failure load, both stirrups and the outermost layer of longitudinal reinforcement had reached or exceeded yielding. Subsequently, load resistance rapidly decreased after shear failure occurred. Deflection at the load point is displayed in Figure 2.22. This behavior was typical of all the shear failures observed in the experimental program.

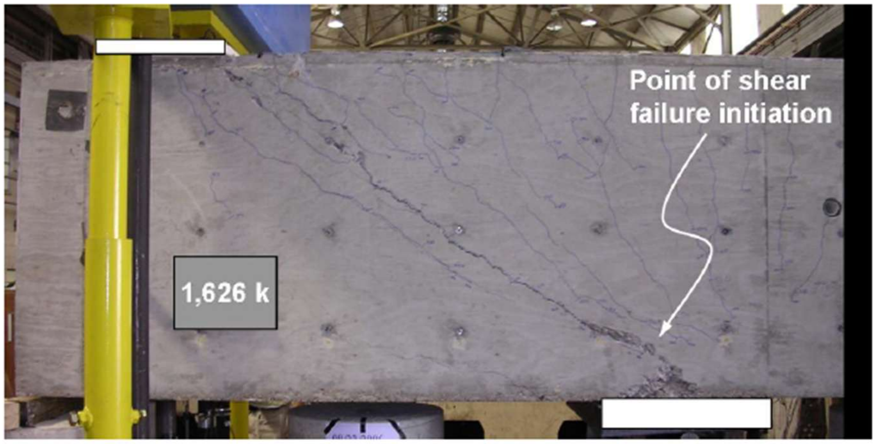

Figure 2.21: Shear failure of deep beam 1A (Huizinga, 2007).

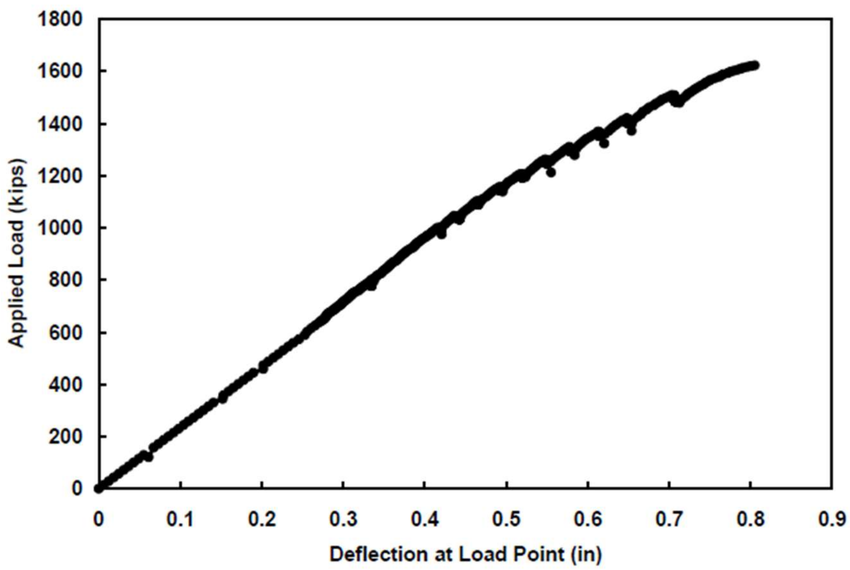

Figure 2.22: Applied load versus deflection relationship for deep beam 1A (Huizinga, 2007).

The testing of the specimens was conducted in an inverted manner (Figure 2.7), leading to the orientation of the applied load and the dead weight of the specimens in opposite directions. Because of the asymmetrical loading of the beams, it was not possible to directly subtract the distributed dead weight of the specimen from the applied load. Therefore, all reported applied loads represent solely the upward load exerted by the hydraulic ram. The distributed dead weight of the specimen may result in slight variations in internal shear at any given point along the specimen. To ensure consistency, all shear values are reported at the midpoint of the shear span.

At approximately 1,650 kips (7339.56 kN) the concrete observed to begin crushing and spalling off the compression side of the test specimen 1B. Interestingly, this load is also approximately the point at which the longitudinal rebar reached nominal yielding in deep beam 1A. At an applied load of approximately 2,050 kips (9118.85 kN), continuous increase in deflection of the specimen was observed without a corresponding increase in load, ultimately leading to failure through the crushing of concrete adjacent to the loading plate (Figure 2.23). The load deformation response depicted in Figure 2.24 shows a flat portion, indicating the yielding of flexural reinforcement prior to failure of the compression region.

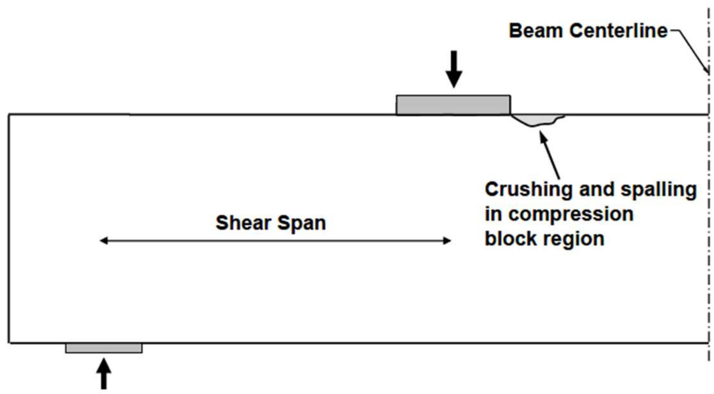

Figure 2.23: Illustration of compression failure (Huizinga, 2007).

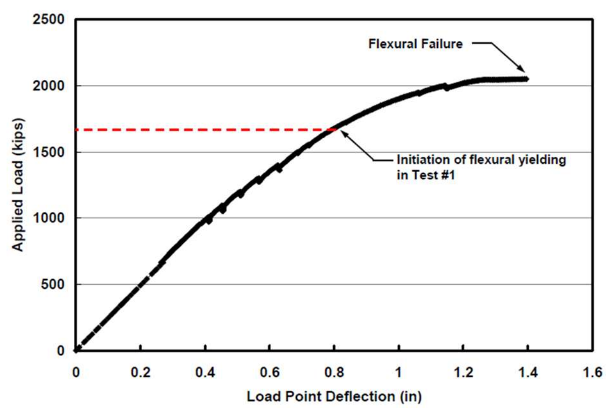

Figure 2.24: Applied load versus deflection curve for deep beam 1B (Huizinga, 2007).

Figures 2.25 and 2.27 present plots of applied load versus longitudinal reinforcement strain for two deep beams (1A and 2A) respectively. The locations of the longitudinal strain gauges, as depicted in Figure 2.26, are representative across all tests. At the failure load, yielding was observed in both stirrups and the outermost layer of longitudinal reinforcement. Notably, while some stirrups yielded at failure, those closer to the bearing plates at load and reaction points experienced lesser strain. At shear failure, yielding began in the outermost layer of tensile longitudinal bars.

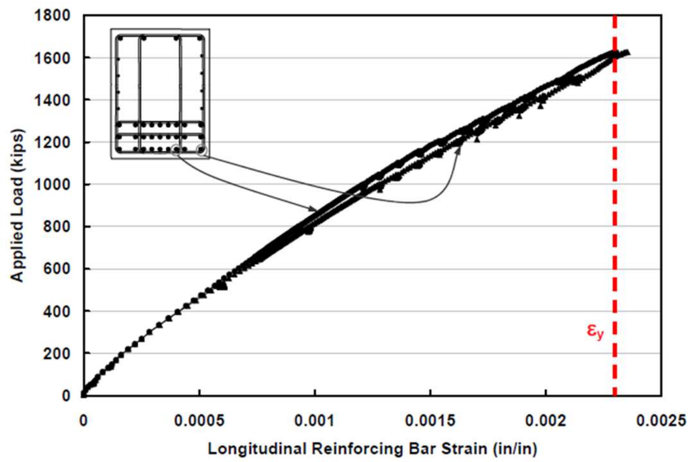

Figure 2.25: Measured load versus longitudinal reinforcement strain in deep beam 1A (Huizinga, 2007).

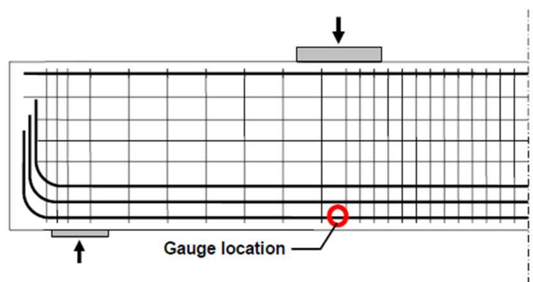

Figure 2.26: Longitudinal strain gauge location in all specimens (Huizinga, 2007).

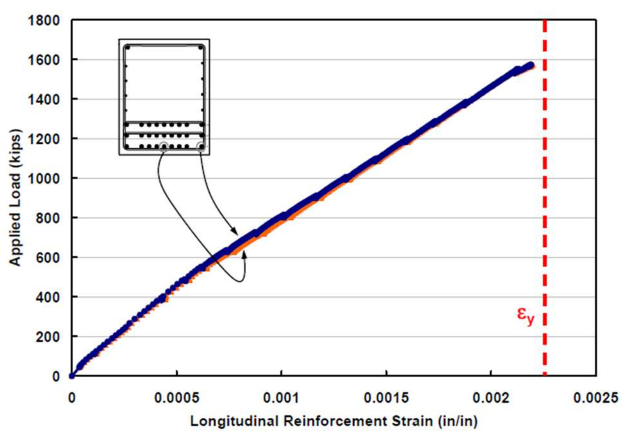

Figure 2.27: Measured load versus longitudinal reinforcement strain in deep beam 2A (Huizinga, 2007).

Regardless of variables such as the applied load bearing area or the amount and detailing of transverse reinforcement, in the initial test the cracking pattern observed remained consistent on each of the five shear spans. Figure 2.28 displays the cracking pattern at the maximum applied load for each of the five tests, The maximum applied load listed in the inset of each photo. The progression of cracking for each of the five tests exhibited remarkable similarity. Figure 2.29 illustrates the progression of surface cracks for deep beam 1A, which was indicative of each of the other five serviceability tests.

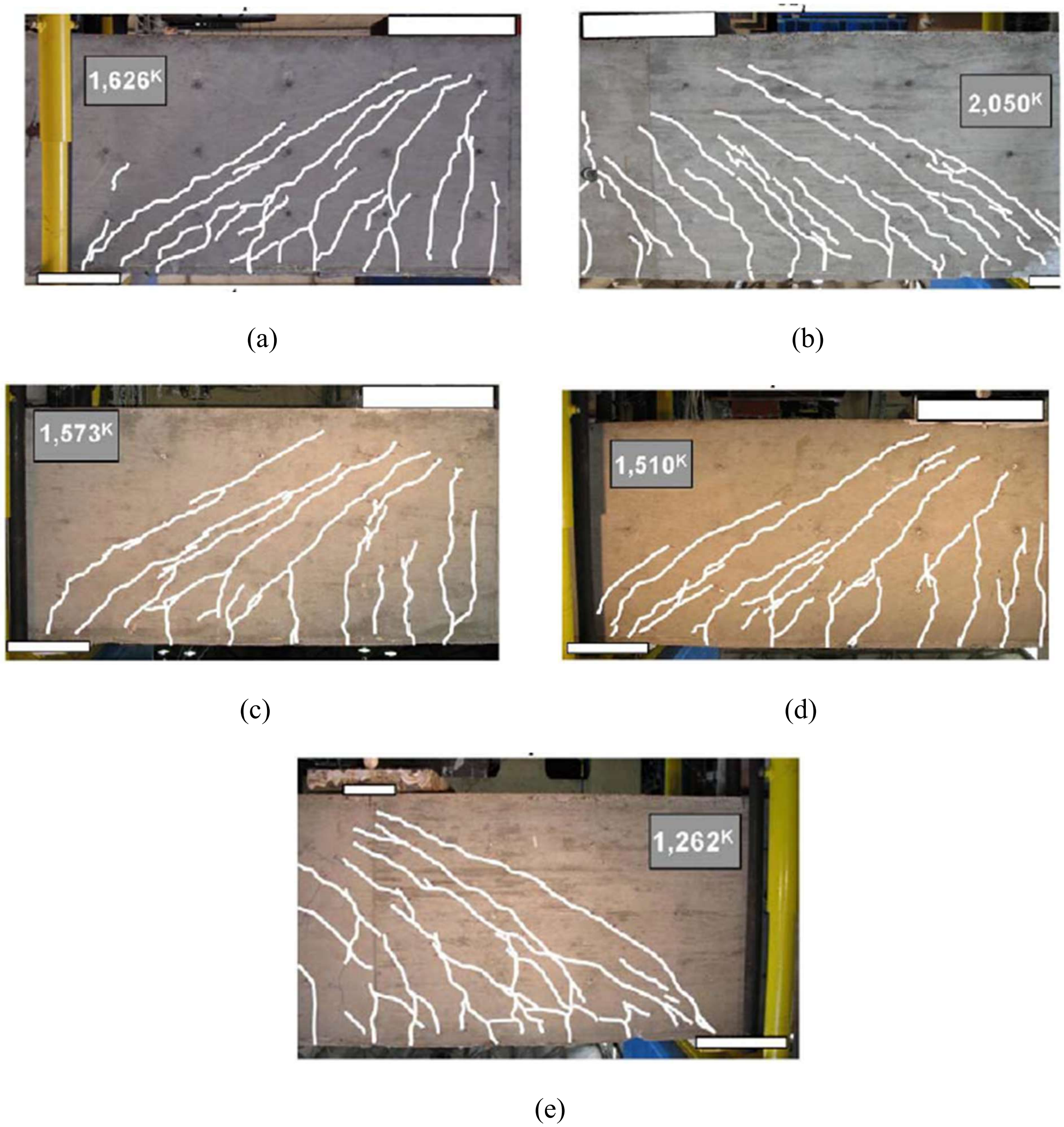

Figure 2.28: Comparison of cracking patterns at maximum applied load for deep beams: a) 1A, b) 1B, c) 2A, d) 3A, and e) 3B (Huizinga, 2007).

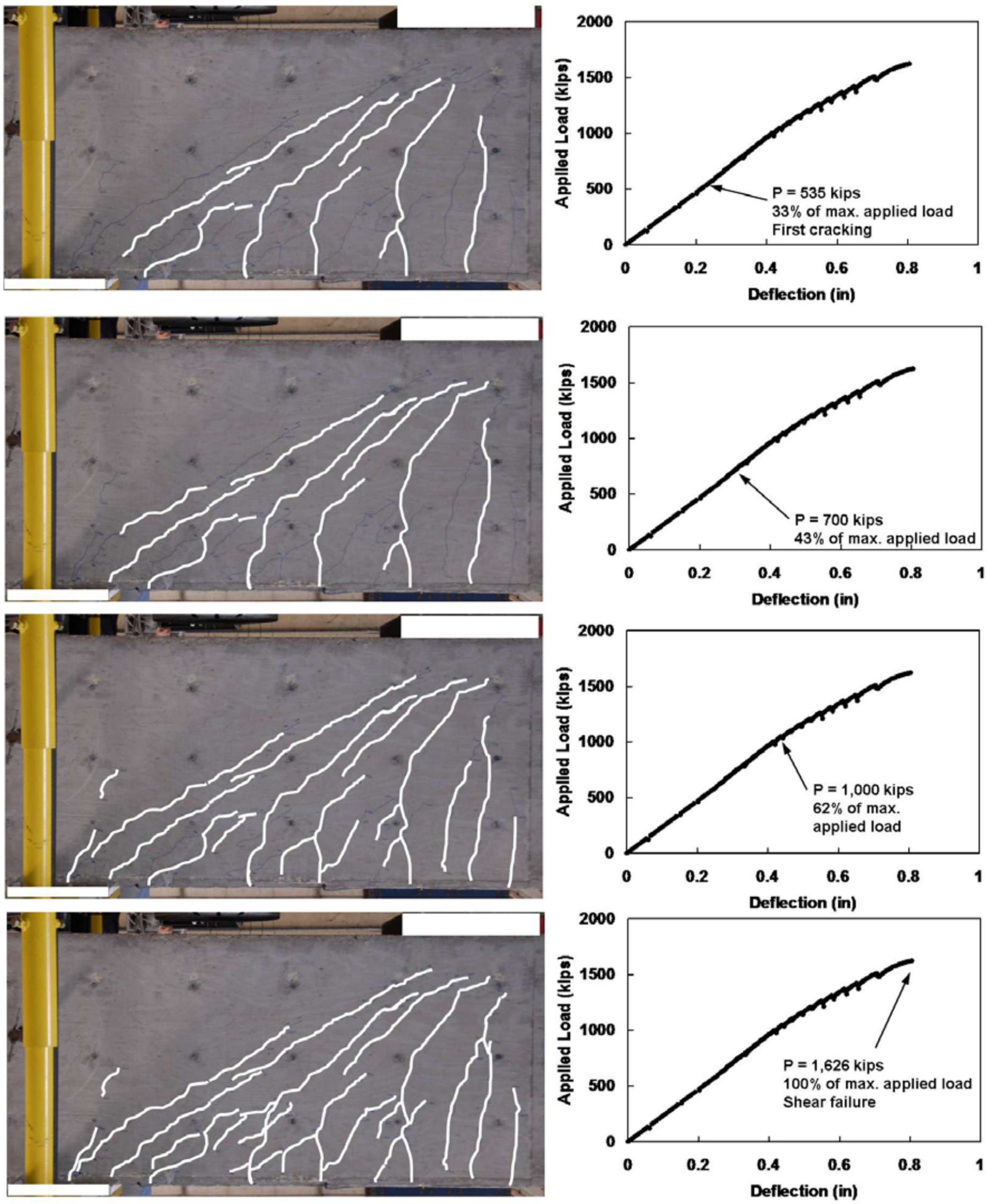

Figure 2.29: Typical progression of cracking in deep beam 1A (Huizinga, 2007).

In a complete STM analysis of each test, consideration would involve constructing a strut-and-tie model of the entire specimen. For convenience, it is common to treat each span individually by dividing the applied load into two loads, each equivalent to the reaction force at each end of the beam, as depicted in Figure 2.30. In this specific study, the strength of the longer span can be determined based on flexural response. Since the short span is susceptible to shear failure, the capacities of test specimens were calculated using STM. It is important to note that load factors and resistance factors were not considered because the goal is to capture the actual response of the deep beams and not necessarily the design, which is based on conservative assumptions for load and resistance factors. Figure 2.31 depicts the STM elements, nodal zones, and the corresponding node naming convention.

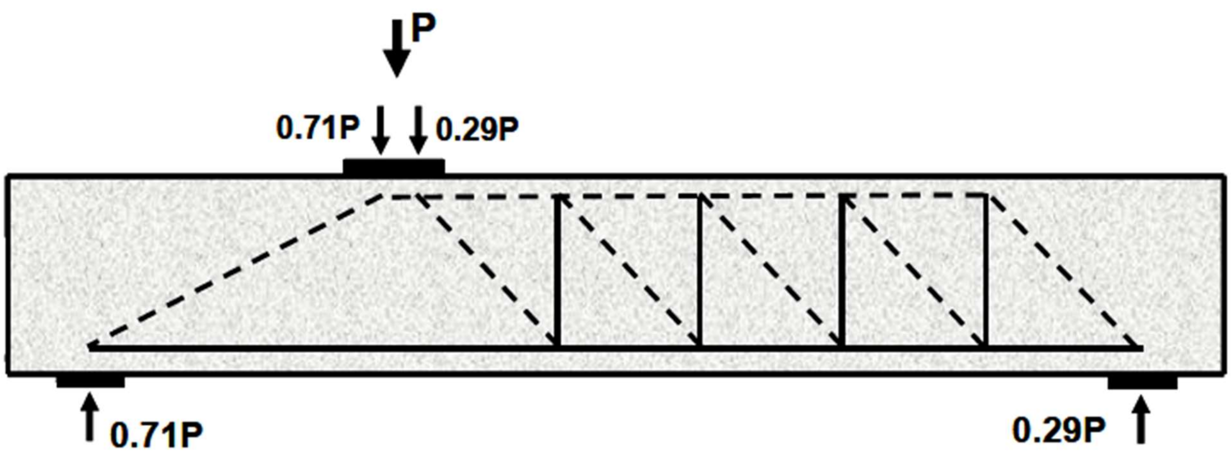

Figure 2.30: Strut-and-tie model of a test specimen (Huizinga, 2007).

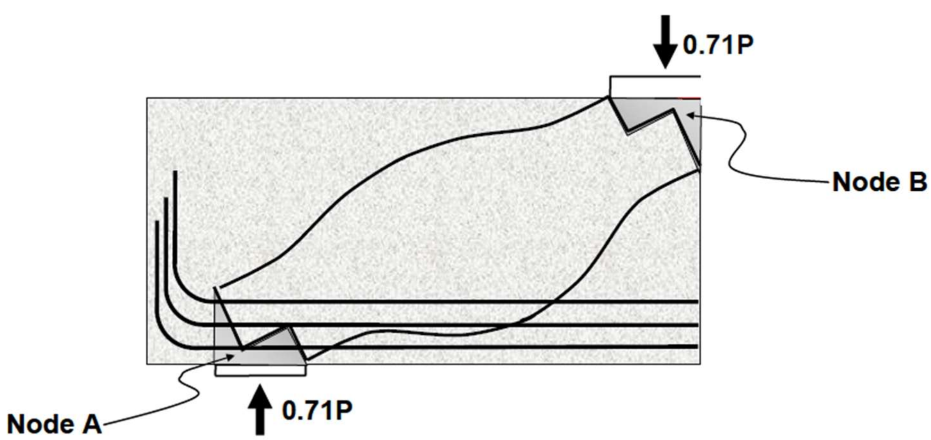

Figure 2.31: STM element naming scheme (Huizinga, 2007).

Figure 2.32 shows the plot of concrete strain and stress (measured by the surface strain gauges) at the ultimate load against distance from the centerline of the bottle-shaped strut. The curve illustrates the flow of force from the load point to the reaction point in a manner consistent with a bottle-shaped strut, thereby justifying the use of a one-panel strut-and-tie model. The strain profile, depicted in Figure 2.32, is overlaid onto the shear span in Figure 2.33, alongside an outline of the bottle-shaped strut corresponding to the strain measurements.

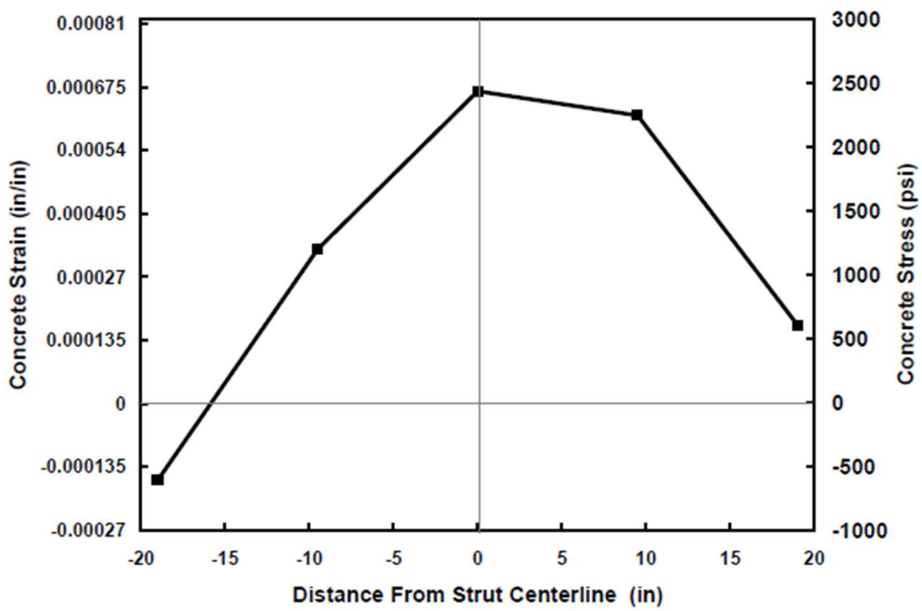

Figure 2.32: Concrete strain and stress versus distance from strut centerline (Huizinga, 2007).

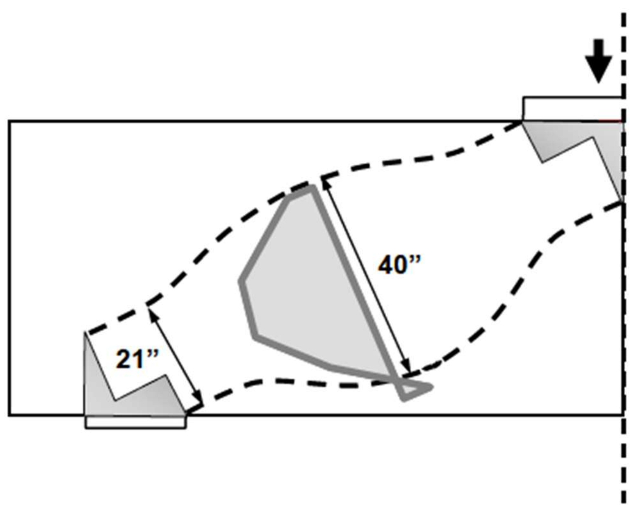

Figure 2.33: Estimation of bottle-shaped strut using concrete strain profile (Huizinga, 2007).

Figure 2.34 illustrates one and two-panel strut-and-tie models overlaid on the cracking pattern of a typical test specimen. It was determined that the efficiency of two-panel models is compromised unless there is a significant presence of vertical transverse reinforcement. Furthermore, the use of a two-panel strut-and-tie model is not justified by the cracking patterns observed in specimens. The crack patterns observed in typical tests suggest that the actual load path consists of a combination of one-panel and two-panel strut-and-tie models.

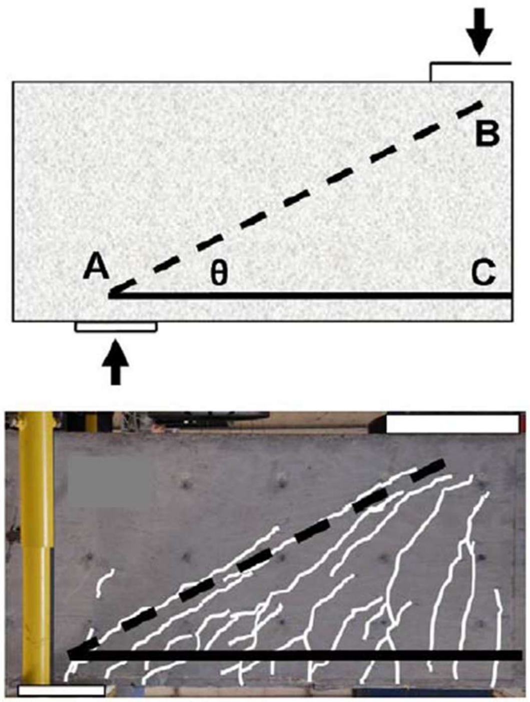

(a)

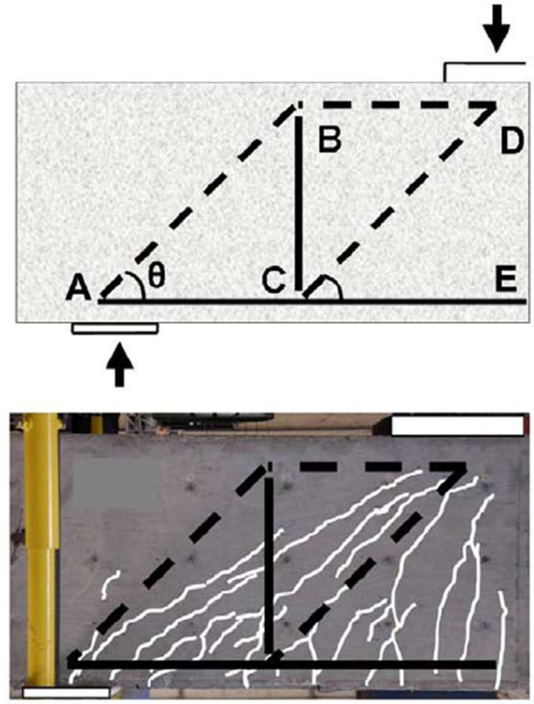

(b)

Figure 2.34: Strut-and-tie model comparison to cracking behavior: a) one-panel strut-and-tie model, and b) two-panel strut-and-tie model (Huizinga, 2007).

Ultimate strengths of all test specimens are calculated using the strut-and-tie modeling (STM) following the provisions of ACI 318-05. The specimens had a shear span-to-effective depth ratio (*a/d*) of 1.85, necessitating a shallow angle of strut inclination when modeled with a one-panel strut-and-tie model. The calculated and measured capacities of the specimens are presented in Table 2.6.

Table 2.6: Measured and calculated capacities of the deep beams (Huizinga, 2007)

Deep Beam	1A	1B	2A	3A	3B
Measured load [P_{max} in kips (kN)]	1626 (7233)	2050 (9119)	1573 (6997)	1510 (6717)	1262 (5614)
Calculated load [P_{STM} in kips (kN)]	1024 (4555)	1024 (4555)	1225 (5449)	697 (3100)	221 (983)

2.4 IDEA StatiCa Analysis

The IDEA StatiCa software was utilized to model and simulate the behavior of the five reinforced concrete deep beams described in Section 2.3.2. The actual or measured compressive strength of concrete, and the yield and ultimate strength of reinforcing steels (as outlined by Huizinga, 2007) were used to model the specimens 1A, 1B, 2A, 3A, and 3B.

2.4.1 Analysis of Baseline Model (Specimen 1A)

Using the measured materials properties presented in Tables 2.4 and 2.5 the IDEA StatiCa model for the baseline specimen was constructed. To validate and improve models and simulations using experimental data, the material factors for concrete (ϕ_c) and reinforcing steel (ϕ_s) in IDEA StatiCa were set to 1.0. The self-weight of the deep beam and the applied load were the two types of loads that considered for the analysis in IDEA StatiCa. The maximum applied load was incorporated in the model gradually with 100 increments from zero to maximum value to obtain the load versus deflection relation of the deep beam specimen.

A 4 in. (101.6 mm) thick bearing plate was introduced to the model under the applied load. The dimensions of the bearing plate were used following the value mentioned in Table 2.4 presented by Huizinga (2007). The left support of the deep beam was fixed in horizontal (x) and vertical (z) directions representing a pin support while the right support was fixed in the vertical (z) direction only to act like a roller support. A point bearing plate support was considered for both the end and the dimensions of the plate were consider as 16 in. by 36 in (406.4 mm by 914.4 mm). The thickness of the support bearing plate was considered as 2 in (50.8 mm). The load factors of 1.0 for both load patterns, i.e., self-weight and applied load were used in the IDEA StatiCa analysis focusing on the ultimate limit state (ULS) load combination.

The capacity calculation process for IDEA StatiCa involved incrementally increasing the applied loads until reaching any of the following conditions:

1. The concrete reached 100% of its strength capacity under the applied load.
2. The reinforcing steel reached 100% of its strength capacity under the applied load.
3. The anchorage steel reached 100% of its strength capacity under the applied load.

At the applied load of 1540 kips (6850 kN), the concrete was operating at 99.6% of its capacity, while the reinforcing bars were at 100% of their strength capacity, and the anchoring steel was at 99.9% of its capacity (Figure 2.35). Further increments of the applied load would surpass the capacity of the reinforcement, thus being deemed the maximum load by IDEA StatiCa. Under the load of 1540 kips (6850 kN), deflection of the deep beam specimen under the load was recorded as 0.679 in. (17.25 mm). Figure 2.35 presents the detailed results for deep beam specimen 1A obtained using IDEA StatiCa under the maximum applied load of 1540 kips (6850 kN).

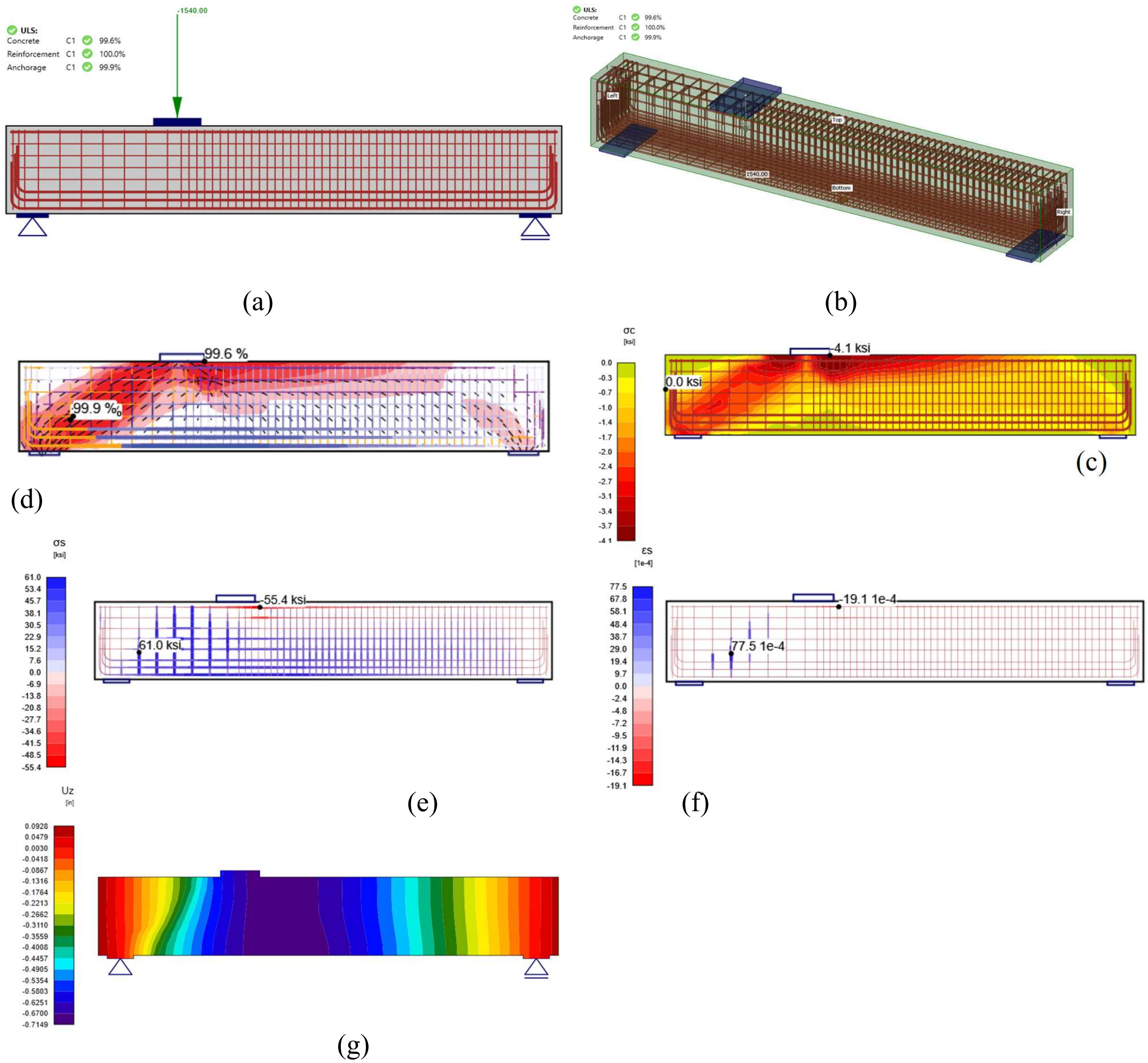

Figure 2.35: Deep beam 1A at 1540 kips (6850 kN) loading: a) IDEA StatiCa results, b) 3D view, c) stress flow, d) concrete principal stress (σ_c), e) stress in the reinforcement, f) strain in the reinforcement, and g) deflection contour.

2.4.2 Analysis of other deep beams

Following the same procedure described for the baseline model in Section 2.4.1, the IDEA StatiCa model was developed for Specimens 1B, 2A, 3A, and 3B considering the shear span to depth ratio (a/d) of 1.85. It was observed for Specimen 1B from the incremental loading that, when the applied load was 1819 kips (8091.32 kN) (, the concrete reached 99.6% of its capacity, reinforcing bars reached 100% of their strength capacity, and anchoring steel reached 99.9% of its capacity (Figure 2.36). The maximum load-point deflection was found to be 0.837 in. (21.26 mm).

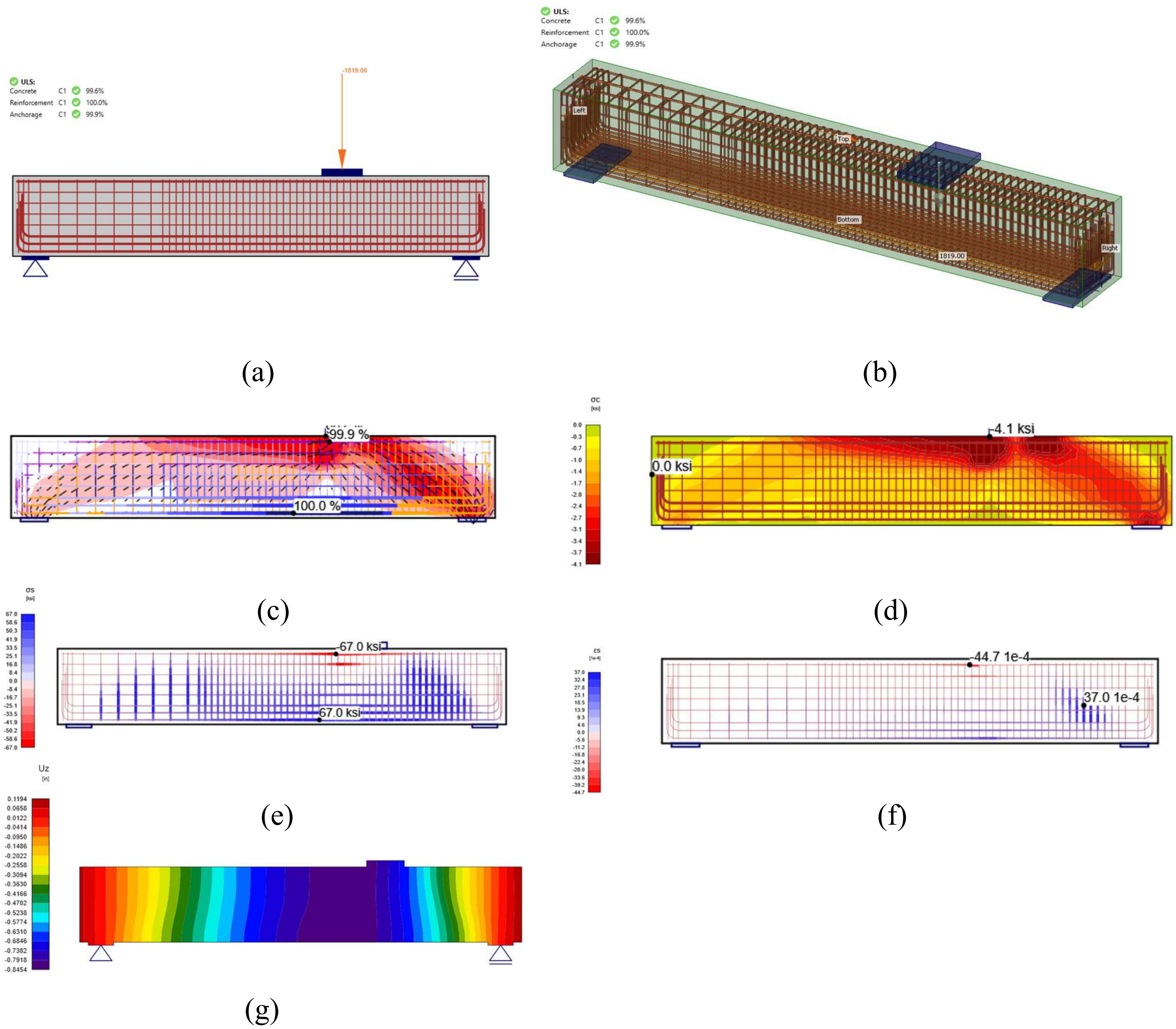

Figure 2.36: Deep beam 1B at 1819 kips (8091.32 kN) loading: a) IDEA StatiCa results, b) 3D view, c) stress flow, d) concrete principal stress (σ_c), e) stress in the reinforcement, f) strain in the reinforcement, and g) deflection contour.

In calculating the maximum capacity for Specimen 2A using IDEA StatiCa, it was observed that, when the applied load corresponds to the 1720 kips (7650.94 kN), the concrete and the anchorage reached 99.6% and 99.9% of their capacity, respectively while the reinforcement reached 100% of its capacity. The maximum deflection observed was 0.808 in. (20.53 mm) (Figure 2.37).

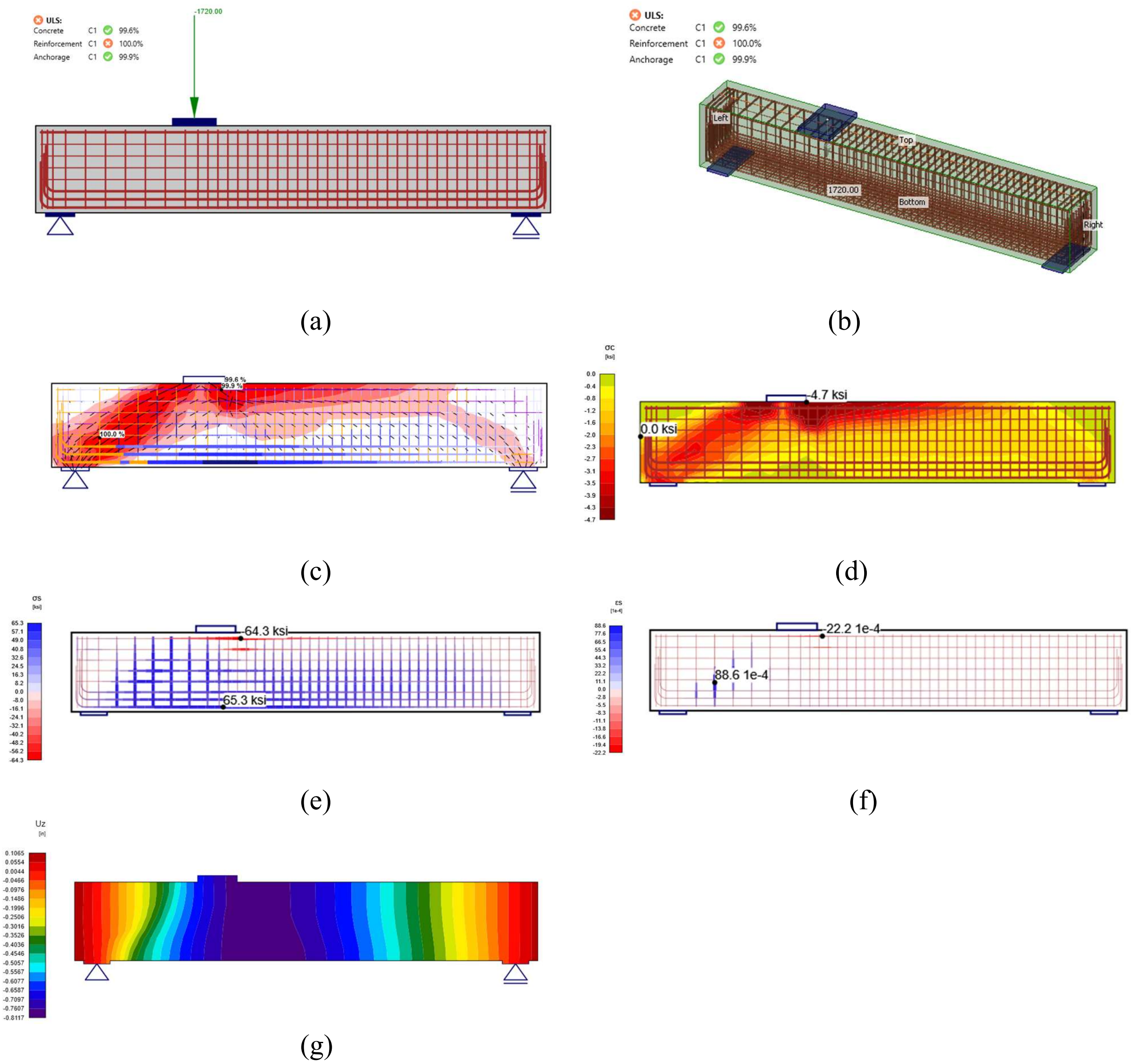

Figure 2.37: Deep beam 2A at 1720 kips (7650.94 kN) loading: a) IDEA StatiCa results, b) 3D view, c) stress flow, d) concrete principal stress (σ_c), e) stress in the reinforcement, f) strain in the reinforcement, and g) deflection contour.

For Specimen 3A IDEA StatiCa analysis showed that the reinforcement reached 100% of its capacity when the applied load was 1117 kips (4968.67 kN). The concrete and anchorage reached 99.6% and 99.9% of their capacity, respectively (Figure 2.38). The deflection obtained from IDEA StatiCa under the load of 1117 kips (4968.67 kN) was 0.578 in. (14.69 mm).

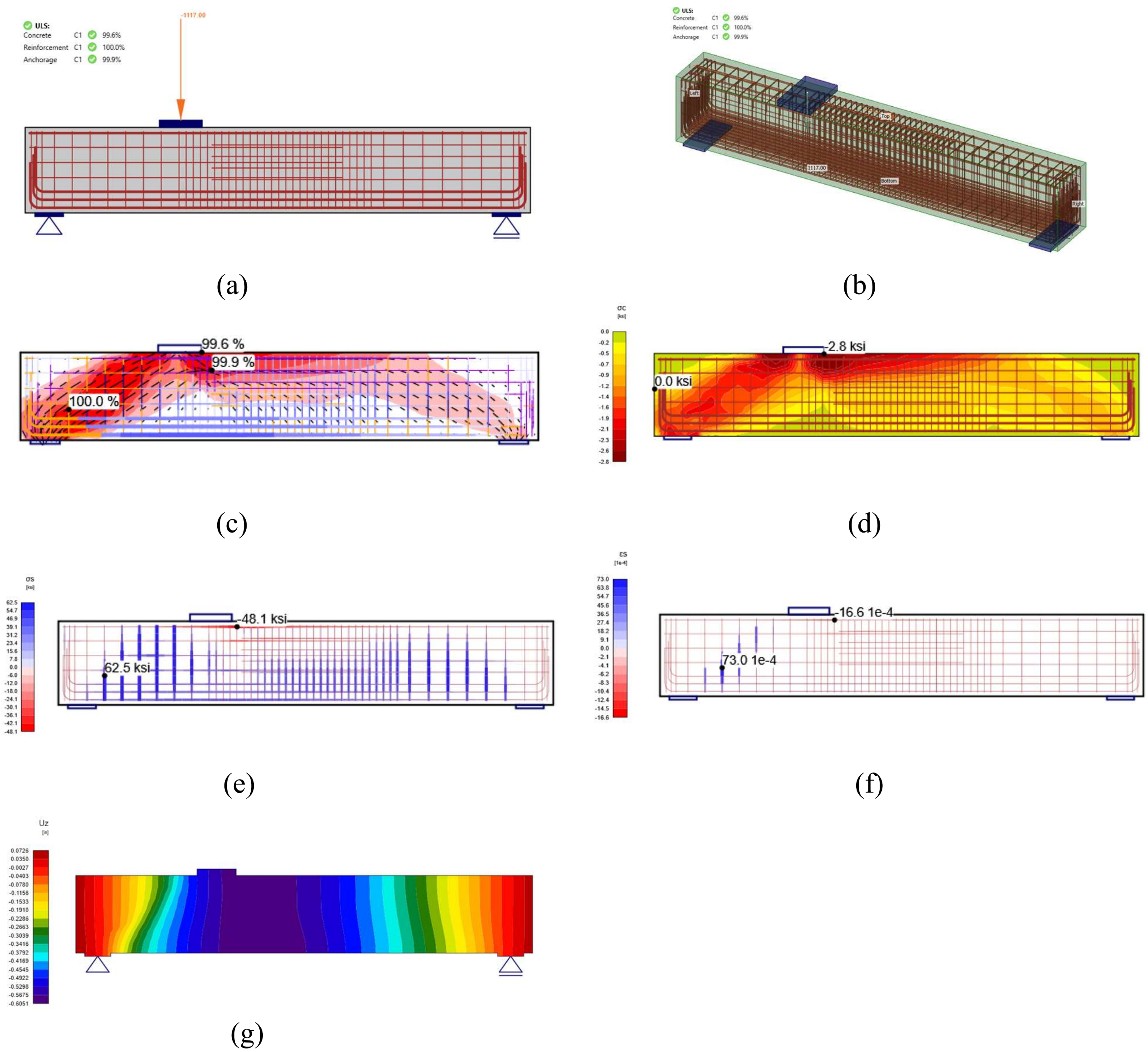

Figure 2.38: Deep beam 3A at 1117 kips (4968.67 kN) loading: a) IDEA StaiCa results, b) 3D view, c) stress flow, d) concrete principal stress (σ_c), e) stress in the reinforcement, f) strain in the reinforcement, and g) deflection contour.

The IDEA StatiCa model for specimen 3B was developed following the procedure obtain for Specimen 3A. It was observed that the reinforcement reached full capacity before the concrete. The concrete and anchorage steel reached 99.5% and 99.9% of their capacity under the applied load of 1088 kips (4839.67 kN) (Figure 2.39). The deflection found under the maximum load was 0.578 in. (14.69 mm).

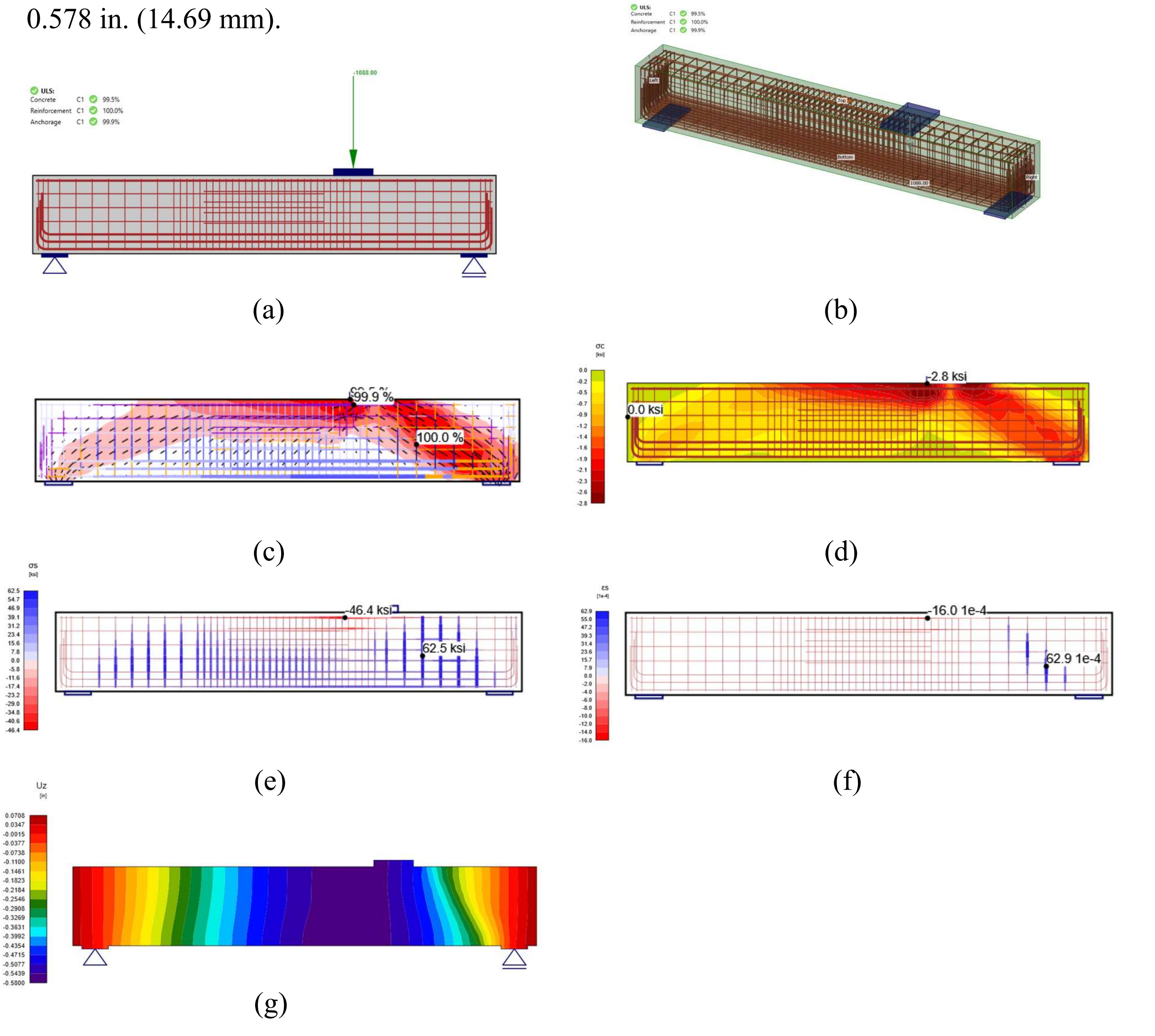

Figure 2.39: Deep beam 3B at 1088 kips (4839.67 kN) loading: a) IDEA StaiCa results, b) 3D view, c) stress flow, d) concrete principal stress (σ_c), e) stress in the reinforcement, f) strain in the reinforcement, and g) deflection contour.

2.5 ABAQUS Model Development and Analysis

In this section, the baseline model developed in Section 2.4.1 (i.e., Specimen 1A) was reconstructed using ABAQUS software (2023) for finite element (FE) analysis, and the results were compared with those obtained from IDEA StatiCa. In the model, in addition to the self-weight, the vertical load of 1,572.5 kips (6995.3 kN) (in 50 kips increments) was imposed to the top load bearing plate with a thickness of 4 in. (101.6 mm) as illustrated in Figure 2.40. Two boundary conditions similar to the experimental tests and IDEA StatiCa model (i.e., simply supported beam) were applied to Specimen 1A (see Figure 2.40 again). In ABAQUS, the element size was chosen to be 0.5 in. (12.7 mm) after routine mesh sensitivity analysis, resulting in a total of 89,510 elements in the model. The 3D stress, 8-node linear brick reduced integration (i.e., C3D8R) was selected as the element type for the concrete, while the beam element was chosen for the reinforcement bars.

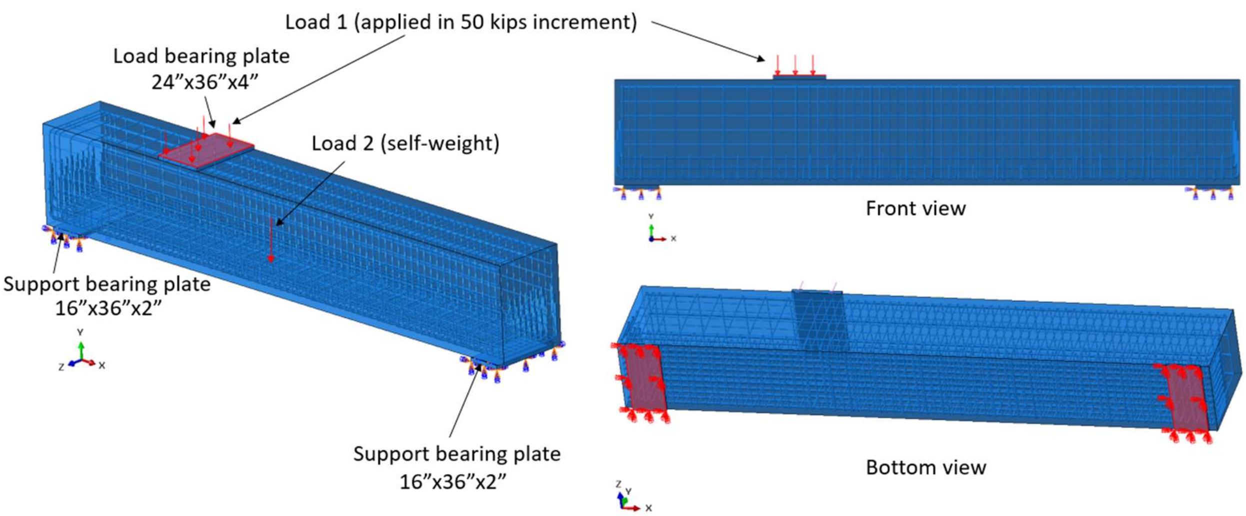

Figure 2.40: Model setup in ABAQUS showing the locations and details of the applied load and boundary conditions.

The embedded region constraint was utilized to incorporate the steel reinforcement within the deep beam A1 (see Figure 2.41). Also, a general surface-to-surface contact was defined between the load and support bearing plates and the concrete specimen. In ABAQUS, the Concrete Damage Plasticity (CDP) constitutive model was used. The required parameters to describe this model were obtained from the experimental data after calibration as they were not explicitly indicated in Ref. (Huizinga, 2007). For the steel bars, the material behavior was modeled using simple bi-linear plasticity. Other parameters, including density, elastic modulus, and Poisson's ratio were taken exactly from the IDEA StatiCa materials library. The numerical simulation was carried out on a virtual machine with 16 processors (Intel Xenon® Gold Processor 6430 @2.10GHz) and took approximately 51 minutes to finish, while the IDEA StatiCa completed the calculation in less than two minutes.

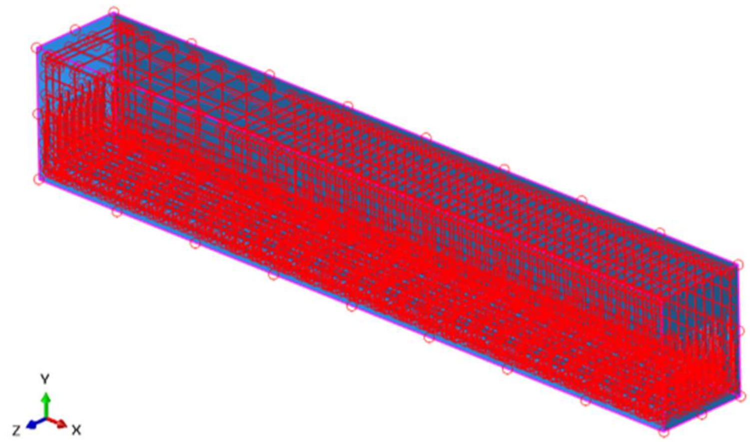

Figure 2.41: Embedded region constraint depicted in red between the reinforcement bars and concrete.

The comparison between crack patterns in experimental tests and ABAQUS is shown in Figures 2.42a and 2.42b. While the experimental data reported that the initial cracks appeared when the load reached 535 kips (2379.8 kN), ABAQUS predicted similar crack patterns when the load was approximately 500 kips (2224.11 kN). The ABAQUS model was also predicted the main diagonal crack and other crack branches at the same spatial locations as the experimental test. To visualize the failure of the structure, the applied load was increased in ABAQUS model, and the result is shown in Figure 2.42c.

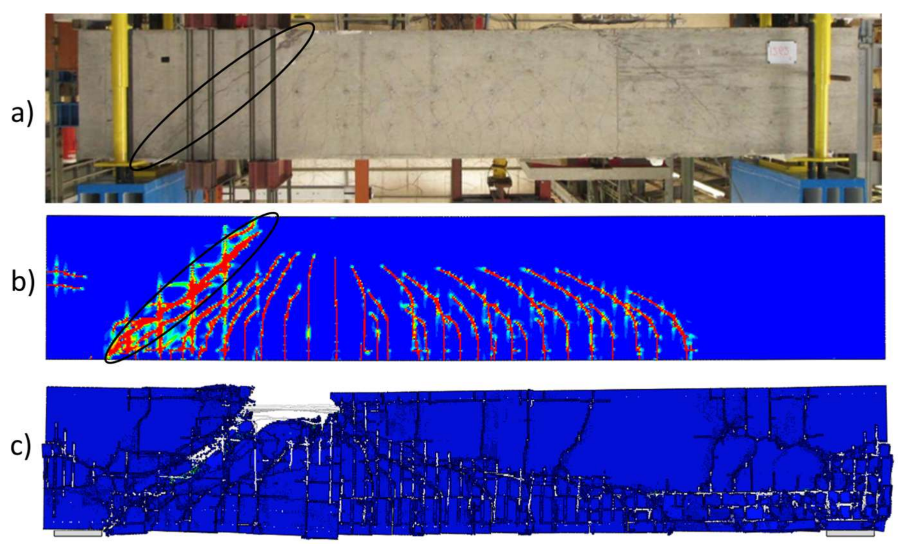

Figure 2.42: a) Crack patterns from the experimental test at service-level load, b) predicted crack patterns by ABAQUS, and c) predicted crack evolution prior complete failure by ABAQUS.

Comparisons of the vertical displacement and directions of principal stresses between the two software are shown in Figures 2.43 and 2.44, respectively. The predicted displacement by IDEA StatiCa is approximately 40% lower than ABAQUS model. Also, it appears deformation and stresses are more distributed in ABAQUS while IDEA StatiCa results are more concentrated. Stress distributions also show that the diagonal compressive stress seems more prismatic in IDEA StatiCa while the stress distribution looks more like bottle shapes struts. Similarly, a wider band or strut is observed in ABAQUS model. These discrepancies in the results are most likely associated with the way that boundary conditions and loads (e.g., point load versus distributed load) were applied in each software as well as the neglect of tensile strength and the tension stiffening effect embedded in the Compatible Stress Field Method (CSFM) developed by IDEA StatiCa.

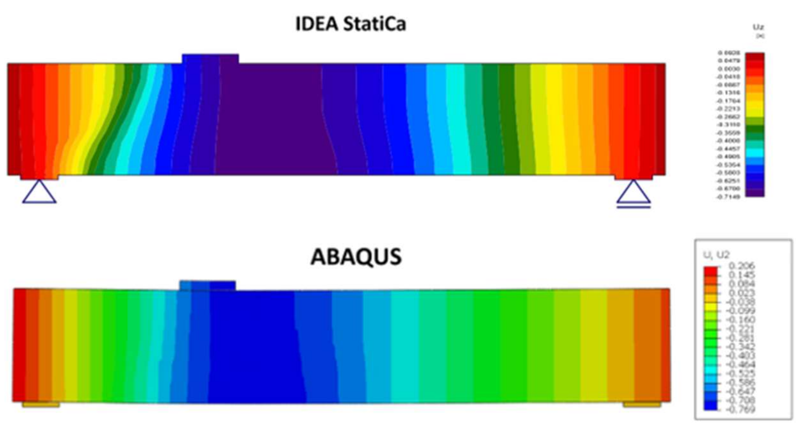

Figure 2.43: Comparison of the vertical displacement between IDEA StatiCa and ABAQUS.

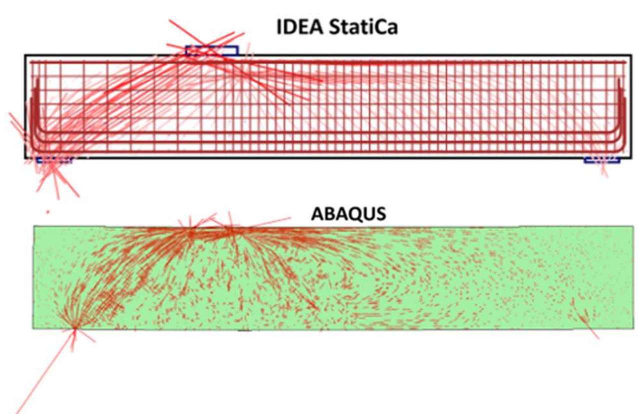

Figure 2.44: Comparison of the direction of principal stresses between IDEA StatiCa and ABAQUS.

Figure 2.45 demonstrates the comparison between the calculated principal stress in concrete by IDEA StatiCa and the predicted one by the ABAQUS model. In IDEA StatiCa, the minimum predicted stress was -4.1 ksi (-28.27 MPa), while the ABAQUS model captured a minimum stress of -4.6 ksi (-31.72 MPa) at the same location. The slight difference in stress distribution is likely due to several factors, including the application of boundary conditions, the utilization of finer mesh in ABAQUS, and differences in the constitutive model for concrete between IDEA StatiCa and ABAQUS (e.g., neglecting failure criterion in terms of strain for concrete in compression in IDEA StatiCa). Additionally, differences in element types (i.e., solid element in ABAQUS versus shell element in IDEA StatiCa) and the employment of the embedded region constraint in ABAQUS in comparison with the bond-slip method in IDEA StatiCa may have contributed to the discrepancies. Note that the authors performed a routine mesh sensitivity analysis for the IDEA StatiCa model (by reducing the default 1 in. mesh size to the smaller values in the setting section), however, inconsistency in the results was observed.

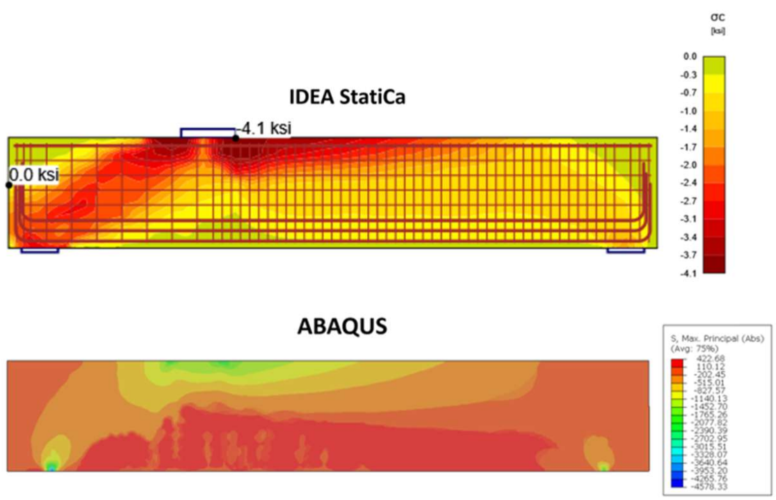

Figure 2.45: Comparison of the calculated principal stresses in concrete between IDEA StatiCa and ABAQUS.

Figures 2.46 and 2.47 depict the comparisons of the reinforcement stress and strain between IDEA StatiCa and ABAQUS. The results from both software are in good agreement. In ABAQUS, the predicted maximum and minimum stress values are 61 ksi (420.59 MPa) and -30.3 ksi (-208.92 MPa) respectively, while in IDEA StatiCa, these values are calculated at 61 ksi (420.59 MPa) and -55.4 ksi (-381.97 MPa) respectively.

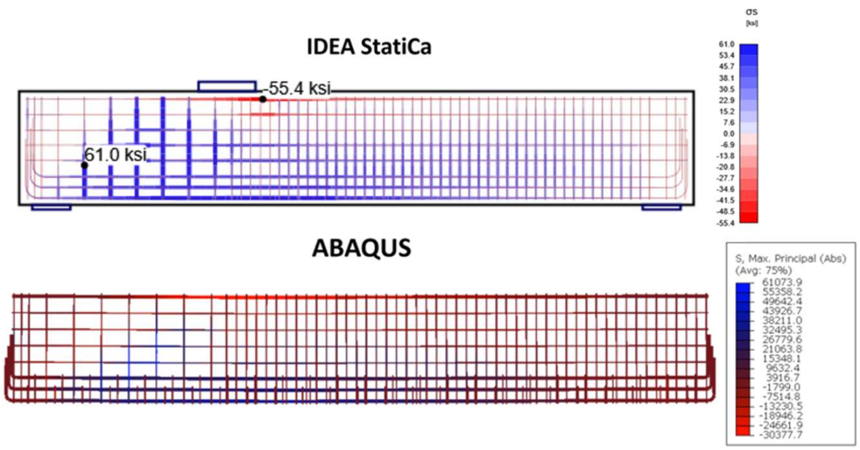

Figure 2.46: Comparison of the reinforcement stress between IDEA StatiCa and ABAQUS.

The maximum and minimum strain values in the reinforcements predicted by ABAQUS are 2.3e-3 and -1e-3, respectively, while the calculated values by IDEA StatiCa are 7.7e-3 and -1.9e-3, respectively.

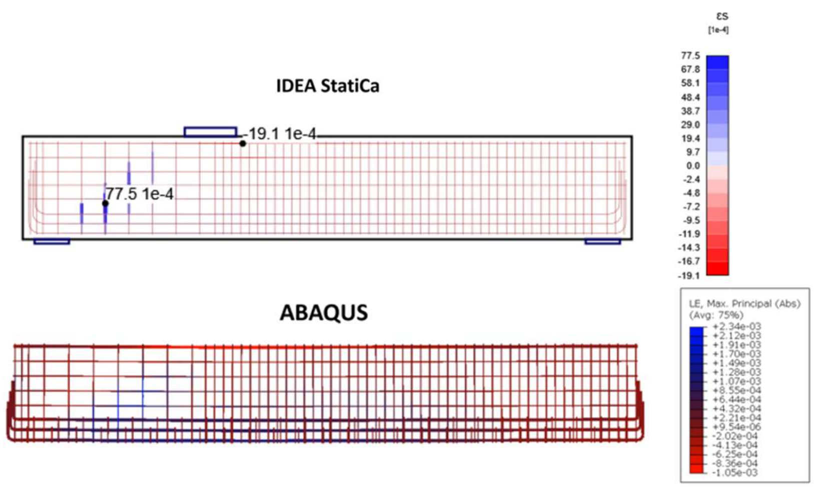

Figure 2.47: Comparison of the reinforcement strain between IDEA StatiCa and ABAQUS.

2.6 Summary and Comparison of Results

The behavior of five reinforced concrete (RC) deep beams was investigated utilizing IDEA StatiCa, and their capacities were also determined using the strut-and-tie method (STM) as specified by ACI 318-05. Furthermore, a comparative analysis was conducted between the results obtained from the IDEA StatiCa model for deep beam 1A and those derived from an equivalent ABAQUS model. The specimens were modeled and analyzed using IDEA StatiCa to simulate their experimental behavior accurately. Subsequently, the maximum load-carrying capacity and load versus deflection relationships determined using the IDEA StatiCa were compared with the measured data.

Figure 2.48 compares the loads acquired from experiments, STM, and IDEA StatiCa for deep beam specimens. The IDEA StatiCa results closely match the experimental results, outperforming conventional methods like the STM in offering nearly precise predictions of deep beam performance. Across all specimens (1A, 1B, 2A, 3A, and 3B), IDEA StatiCa consistently exhibits closer alignment with the measured load capacities (P_{max}). It should be noted that STM is developed for design purposes and is expected to yield conservative results. On the other hand, IDEA StatiCa is expected to capture the maximum measured response of the deep beams.

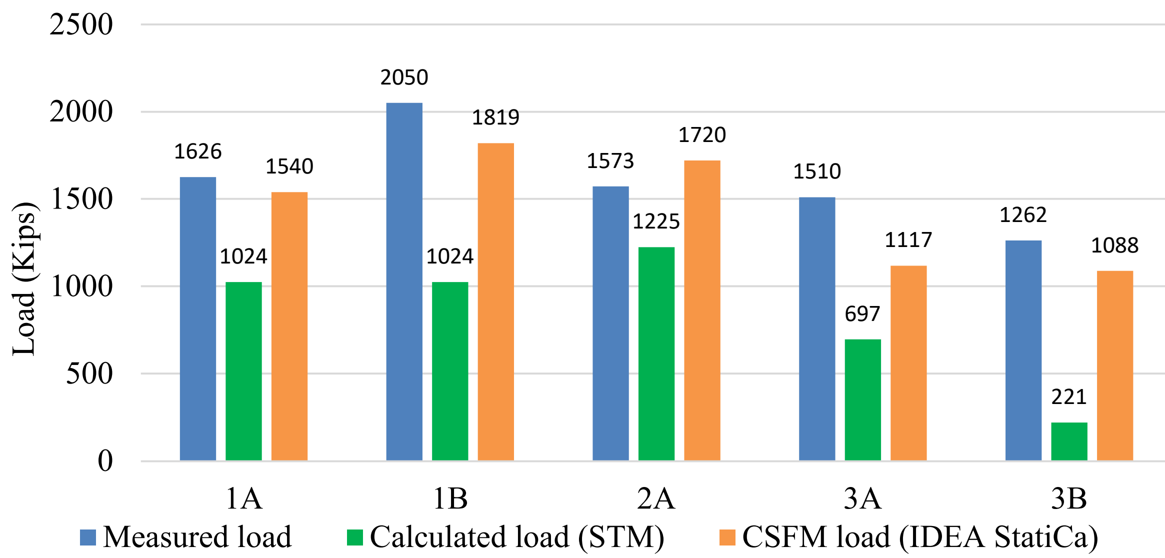

Figure 2.48: Comparison of measured, calculated (STM) and maximum load from IDEA StatiCa for deep beam specimens.

The data presented in Figure 2.48 reveals variations between the measured loads and those calculated using the Compatible Stress Field Method (CSFM) in IDEA StatiCa for the five deep beams. For instance, deep beam 1A exhibits a discrepancy of approximately 5% between the measured load and the CSFM-calculated load. Similarly, deep beam 1B displays a deviation of about 11%. In deep beam 2A, the difference between the measured load and the CSFM-calculated load is approximately 9%. However, the primary objective of the test program was to investigate the shear strength and serviceability behavior of deep beams, with a focus on inducing shear failure in each shear span. The data obtained after flexural yielding began in Test 1B was considered irrelevant for evaluating shear performance. Therefore, all subsequent tests were halted at the onset of flexural yielding. The bearing plate size was then reduced, and the tests were repeated with the aim of causing shear failure instead of flexural failure (Huizinga, 2007). As a result, there may be an error in the experiment and the reported measured capacity for deep beam 2A, as it experienced the initiation of flexural yielding, and the test was stopped. This may have resulted in the experimental value being less than the load-carrying capacity produced by IDEA StatiCa.

Notably, deep beam 3A shows a significant difference, with the CSFM-calculated load being approximately 26% lower than the measured load. Deep beam 3B showcases a deviation of around 13%. Interestingly, the CSFM method estimates the results very closely compared to the STM method, showcasing its robustness in predicting the maximum strength of deep beams. Moreover, the utilization of IDEA StatiCa offers powerful insights into their structural performance (e.g., stress distribution, load path, and failure mode) and load-carrying capacities with improved accuracy and efficiency.

The findings depicted in Figure 2.49 indicate a close correlation between the maximum strengths calculated by both IDEA StatiCa and ABAQUS for deep beam specimen 1A. The measured load for deep beam 1A is 1626 kips (7232.81 kN). A load of 1024 kips (4554.98 kN) kips is calculated by the STM method, which is significantly lower and shows a discrepancy of about 37%. A load of 1540 kips (6850.26 kN) is predicted by IDEA StatiCa, which is closer to the measured value, with a difference of approximately 5.3%. A load of 1573 kips (6997.06 kN) is estimated by ABAQUS, resulting in a difference of about 3.3% from the measured load. Predictions that are relatively close to the measured values are provided by both IDEA StatiCa and ABAQUS, with ABAQUS being slightly more accurate. The robustness and accuracy of these advanced methods in predicting the load-carrying capacities of deep beams are highlighted by this comparison, demonstrating their utility in structural analysis.

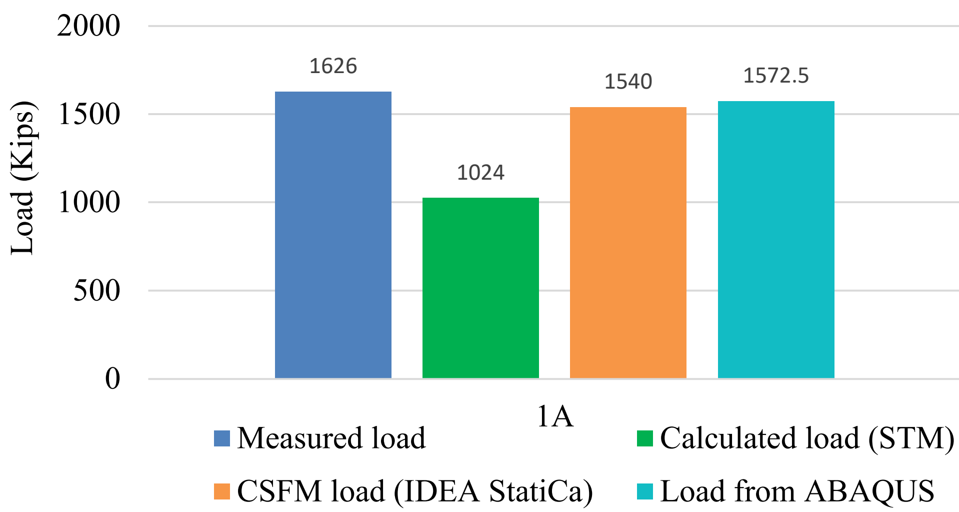

Figure 2.49: Comparison of measured, calculated (STM), maximum strength from IDEA StatiCa, and maximum strength from ABAQUS for baseline model (1A).

Upon comparison of the outcomes from both IDEA StatiCa and ABAQUS software, it is evident that similarities are observed in the calculated stress values, albeit with minor differences (Figure 2.45). For instance, regarding the minimum stress prediction for concrete, around -4.1 ksi (-28.27 MPa) was forecasted by IDEA StatiCa, while a slightly lower value of approximately -4.6 ksi (-31.72 MPa) was shown by ABAQUS at the same location (Figure 2.45). Similarly, for the maximum stress values, approximately 61 ksi (420.59 MPa) and -30.3 ksi (-208.92 MPa) were predicted by ABAQUS, while slightly different values of about 61 ksi (420.59 MPa) and -55.4 ksi (-381.97 MPa) were depicted by IDEA StatiCa, respectively (Figure 2.46). Overall, reasonably close stress distributions are calculated by both software tools.

Figures 2.50 and 2.51 show the load versus displacement curves for specimens 1A, and 1B. It is consistently observed that at the load application point the measured displacements appear higher than the estimated load-point displacements using IDEA StatiCa. This pattern suggests a mismatch between the specimen's actual experimental behavior and the analytical predictions made by IDEA StatiCa.

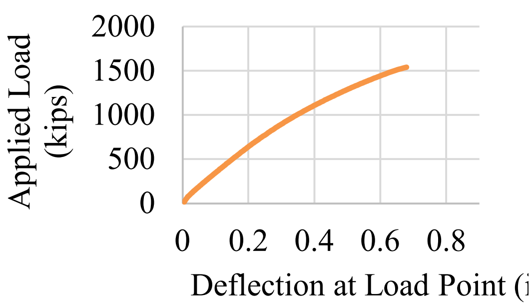

(a)

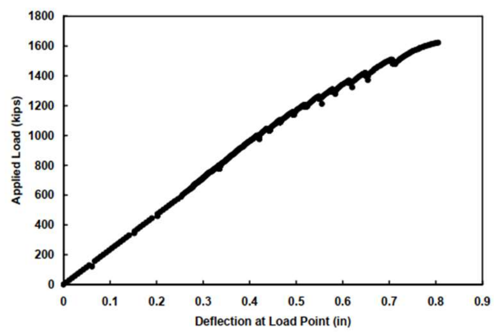

(b)

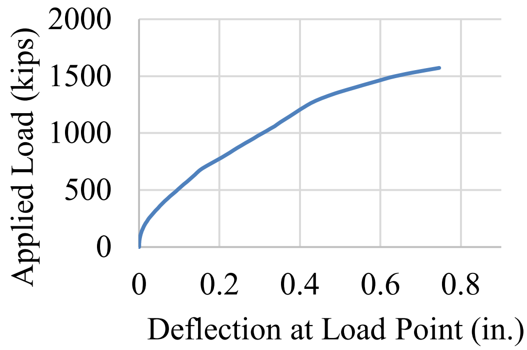

(c)

Figure 2.50: a) Calculated load versus displacement curve for Specimen 1A at $P_{IDEA\ StatiCa}$, b) measured load versus displacement curve for Specimen 1A (Huizinga, 2007), and c) estimated load versus deflection curve for specimen 1A using ABAQUS at 1573 kips (6997.06 kN).

Despite these persistent discrepancies in calculated displacements for specimens 1A and 1B, it is crucial to identify plausible causes for these variations. One contributing aspect could be the analytical model utilized by IDEA StatiCa, which incorporates assumptions and simplifications to improve computational efficiency. These simplified versions might lead to conservative displacement estimates, as the model may not fully encompass every aspect of the intricate structural behavior of the deep beam. Differences between calculated and observed displacements may also arise from alterations in boundary conditions, surrounding factors, or material characteristics during experimental testing.

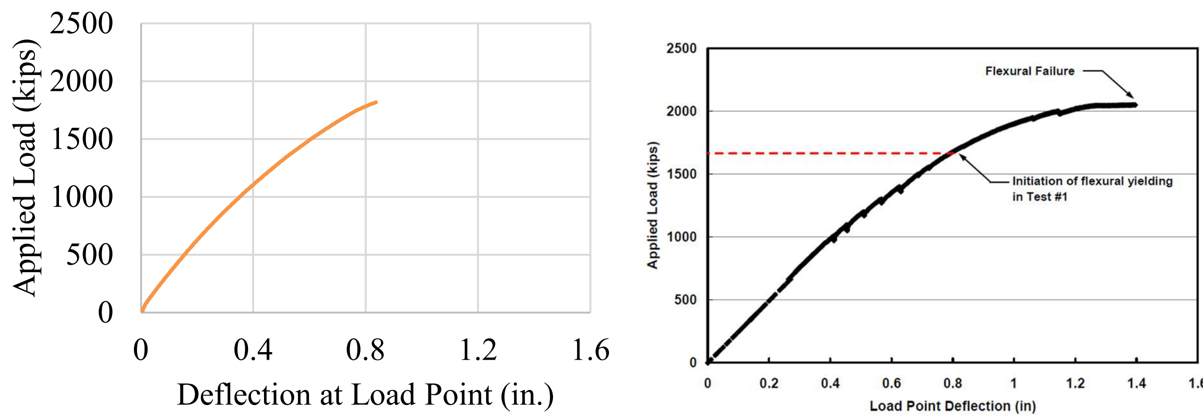

(a) (b)

Figure 2.51: a) Calculated load versus displacement curve for Specimen 1B at $P_{IDEA\ StatiCa}$, and b) measured load versus displacement curve for Specimen 1B (Huizinga, 2007).

Figures 2.52 and 2.53 illustrate the load versus longitudinal reinforcing bar strain in deep beams 1A and 2A, respectively. In both figures, the calculated response from IDEA StatiCa is presented alongside the measured response. In Figure 2.52, deep beam 1A exhibits a calculated maximum strain of 0.0019 from IDEA StatiCa, while the measured maximum strain is 0.00235. The results from IDEA StatiCa are observed to be very close to the measured strain, indicating a strong correlation between the predicted and actual values. Similarly, in Figure 2.53, deep beam 2A shows a calculated strain of 0.0022 from IDEA StatiCa, with the measured strain being approximately 0.00230. Again, the proximity of the calculated strain to the measured strain highlights the accuracy of IDEA StatiCa in predicting the strain in the reinforcement.

Overall, the data in both figures suggest that the predictions made by IDEA StatiCa are highly consistent with the measured responses, underscoring the effectiveness of this analytical tool in modeling and capturing the behavior of longitudinal reinforcing bars in deep beams.

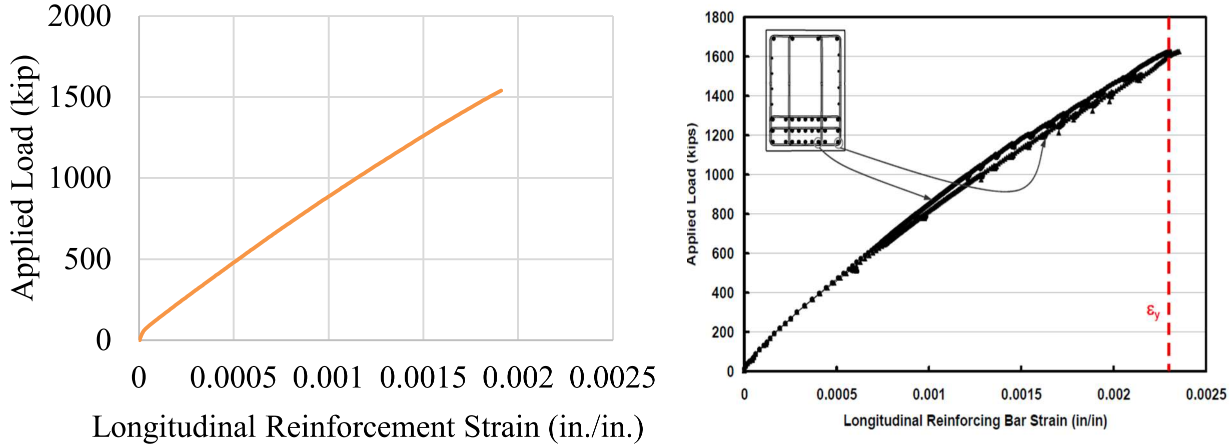

(a) (b)

Figure 2.52 Load versus longitudinal reinforcing bar strain in deep beam 1A: a) calculated response from IDEA StatiCa, and b) measured response.

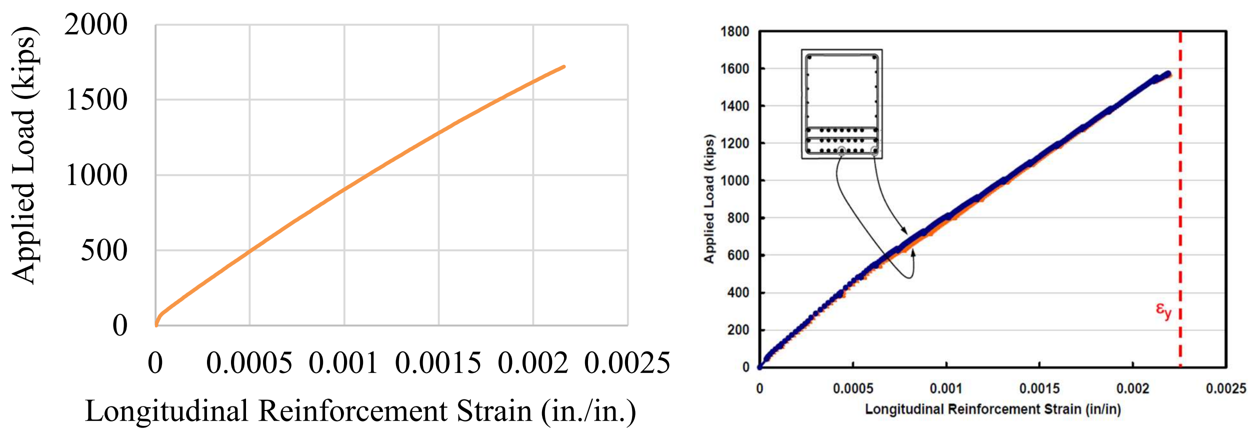

(a) (b)

Figure 2.53 Load versus longitudinal reinforcing bar strain in deep beam 2A: a) calculated response from IDEA StatiCa, and b) measured response.

A parametric study was conducted to investigate the impact of support conditions and plate thickness on the calculated capacity using IDEA StatiCa. In this parametric study, all support conditions were modeled as pin connections, meaning the beam was fixed in both the x and z axes. The primary variables examined were the different thicknesses of the plates, and their influence on the structural capacity under the given support constraints. This approach enabled a comprehensive understanding of how varying these parameters affects the overall performance and capacity of the structure. Figures 2.54 through 2.56 illustrate the influence of support and plate thickness on the IDEA StatiCa analysis for the baseline model (1A). The capacities for different configurations are compared to understand the impact of these variables.

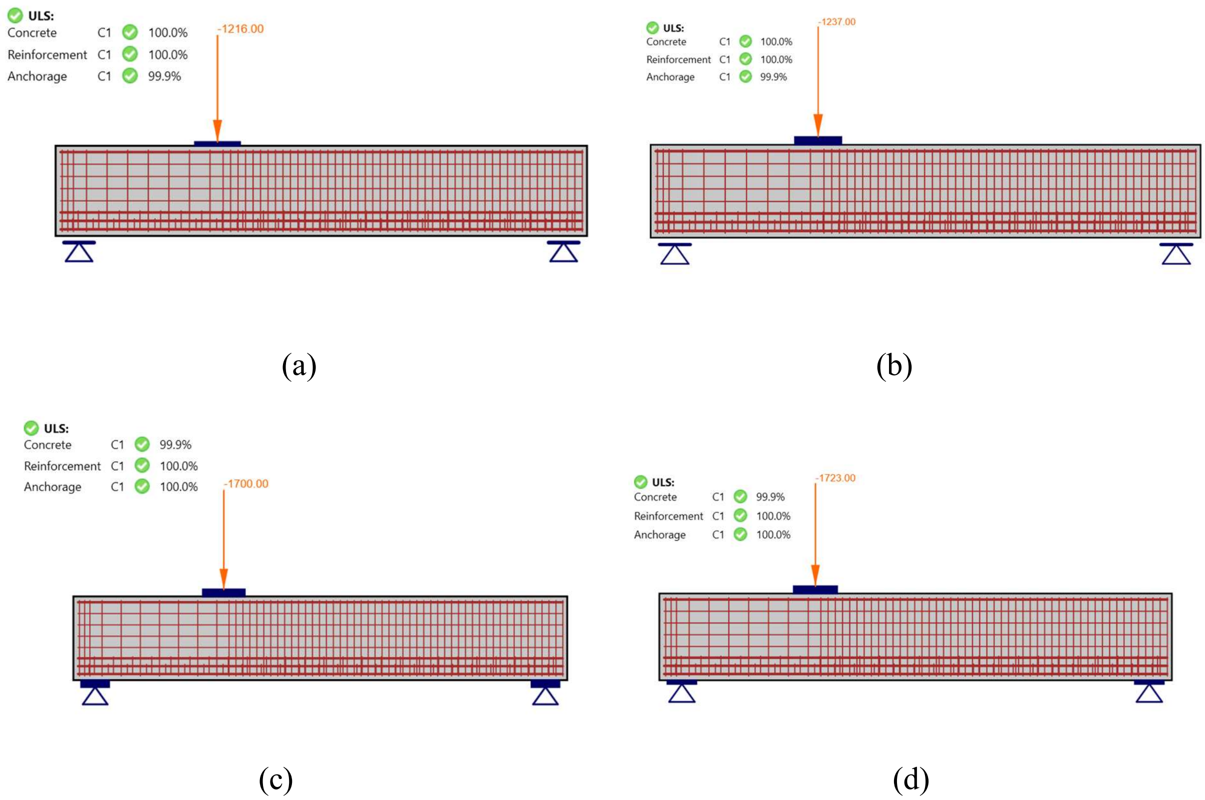

Figure 2.54: Influence of support and plate thickness on IDEA StatiCa analysis for baseline model (1A): a) point distributed (PD) support with 2 in. (50.8 mm) thick load bearing plate, b) PD support with 4 in. (101.6 mm) thick load bearing plate, c) point bearing plate (PB) support with 4 in. (101.6 mm) thick load bearing plate and 4 in. (101.6 mm) thick support bearing plate, and d) PB support with 4 in. (101.6 mm) thick load bearing plate and 2 in. (50.8 mm) thick support bearing plate.

In Figure 2.54(a), the model with point distributed (PD) support and a 2 in. thick load-bearing plate (PD-Top-2”) has a capacity of 1216 kips (5409.04 kN). When the load-bearing plate thickness is increased to 4 in. (PD-Top-4”) as shown in Figure 2.54(b), the capacity slightly increases to 1237 kips (5502.45 kN), which is an increase of approximately 1.73%. A more significant increase is observed in Figure 2.54(c), where using a point bearing (PB) plate support with a 4 in. thick support bearing plate (PB-B4”-Top-4”) raises the capacity to 1700 kips (7561.98 kN), representing a substantial 39.80% increase compared to the initial configuration. Finally, Figure 2.54(d) shows that using a 2 in. thick support bearing plate instead of 4 in. to the previous configuration (PB-B2”-Top-4”) results in a capacity of 1723 kips (7664.29 kN), a marginal additional increase of about 1.35%. These findings highlight that while increasing the load-bearing plate thickness yields minor gains, changing the support type to a point bearing plate with adequate thickness significantly enhances the structural capacity. The analysis using IDEA StatiCa reveals that the boundary conditions, specifically the type of support and the thickness of the load-bearing plates, significantly influence the capacity of deep beams (Figure 2.55).

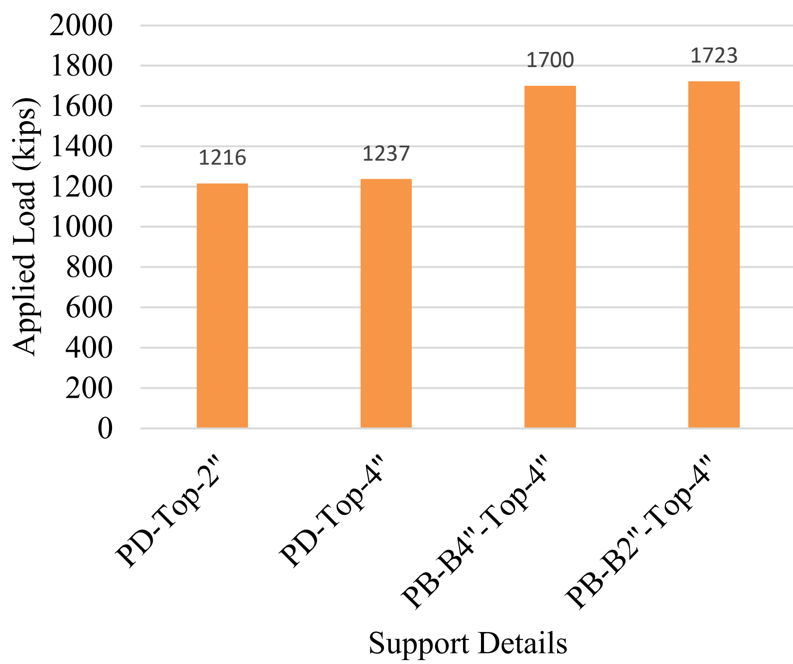

Figure 2.55: Influence of support and plate thickness on the capacity

The effect of plate thickness on the capacity of deep beam 1A with a 4 in. (101.6 mm) top plate using IDEA StatiCa is illustrated in Figure 2.56. The data presented provide insights into how varying plate thickness of point bearing plate supports impacts the maximum calculated load capacity (P_{max}) of the deep beam. The measured capacity of the beam is recorded as 1626 kips (7232.81 kN), while the STM model predicts a significantly lower capacity of 1024 kips (4554.98 kN). As the plate thickness increases from 1.25 in. (31.75 mm) to 2 in. (50.8 mm), there is a noticeable rise in capacity, starting at 1435 kips (6383.2 kN) and peaking at 1720 kips (7650.94 kN). This represents a 19.9% increase in capacity from the experiment to the highest recorded capacity with a 2 in. (50.8 mm) thick plate. However, beyond this point, further increases in plate thickness do not consistently result in higher capacities. For instance, the capacity slightly decreases to 1710 kips (7606.46 kN) with a 3 in. (76.2 mm) thick plate and further declines as the thickness continues to increase, reaching 1655 kips (7361.81 kN) at a thickness of 10 in. (254 mm).

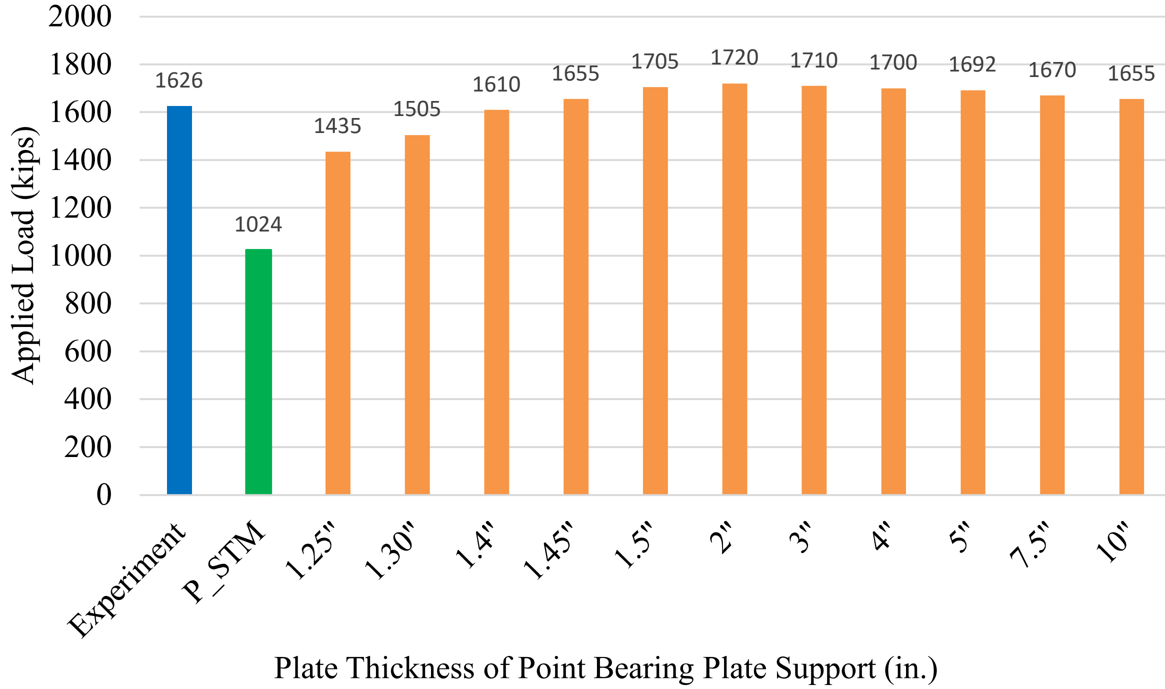

Figure 2.56: Influence of plate thickness on the capacity of deep beam 1A.

These observations suggest that there is an optimal plate thickness around 2 in. (50.8 mm), beyond which additional thickness does not increase the capacity. The detailed capacities for each thickness are summarized in the Figure 2.56 emphasizing the sensitive relationship between plate thickness and structural capacity in IDEA StatiCa calculations. Therefore, careful consideration of boundary conditions is crucial in IDEA StatiCa calculations.

References

ACI Committee 318. (2005). *Building Code Requirements for Structural Concrete (ACI 318R-05).* Farmington Hills, Michigan: American Concrete Institute.

ACI Committee 318. (2019). *Building Code Requirements for Structural Concrete (ACI 318R-19).* Farmington Hills, Michigan: American Concrete Institute.

Dassault Systèmes. (2023). ABAQUS – 2023: Standard User's Guide. Simulia Corp.

Huizinga, M. R. (2007). *Strength and Serviceability Performance of Large-Scale Deep Beams: Effect of Transverse Reinforcement* (master's thesis). The University of Texas at Austin.

Tuchscherer, R. G., Birrcher, D. B., and Bayrak, O. (2011). *Strut-and-tie model design provisions.* PCI Journal, 56(1), 155-170.

American Concrete Institute. (2021). ACI PRC-445.2-21: *Strut-and-tie method guidelines for ACI 318-19*—Guide (First Printing: August 2021). Reported by Joint ACI-ASCE Committee 445.

Chapter 3. Modeling and Analysis of Shear Walls with Openings

3.1 Introduction

In this chapter, the behavior of four reinforced concrete (RC) shear wall specimens with openings is examined. Their lateral load capacity and drift angle (displacement / length) were evaluated using IDEA StatiCa software and compared with experimental data reported by Taleb et al. (2012). The results were also compared with design capacities calculated using the strut and tie model (STM) included in ACI 318-19 (2019). One of the tested shear wall specimens was selected as a baseline model for further analysis using ABAQUS software (2023), where drift angle, principal stress distribution, and crack patterns were computed and compared with those measured during experiments. Additionally, the Mander et al. (1988) confinement model was applied to examine the effect of confined concrete on the shear wall capacities in detail.

3.2 Experimental Study

To evaluate the structural performance of shear walls with openings, four RC single-span structural wall specimens, identified as N1, S1, M1, and L1, were studied. These specimens were constructed and tested by Taleb et al. (2012) at the structural laboratory of Kyoto University under lateral reversed cyclic loading. The walls were scaled to 40%, representing the lower three stories of a six-story RC building. The main goals of these experiments were to analyze the lateral behavior and understand the effects of different opening sizes and locations on crack distribution and shear strength of RC structural walls. Consistency in primary reinforcement was maintained across all specimens, with variations in the opening ratios. Among these specimens, L1 was selected as the baseline model for further analysis using ABAQUS software.

3.2.1 Experimental Setup

The experimental setup and loading system details are shown in Figures 3.1 and 3.2, respectively. The lateral load *Q*, was applied to the loading beam using two 2 MN (449.6 kips) hydraulic jacks, delivering cyclic reversed horizontal loads to the specimens. These loads were applied in both directions, simulating real-world earthquake conditions. In addition to the horizontal loads, vertical axial loads were applied to the columns using two 1 MN (224.8 kips) hydraulic jacks, replicating the loads on the lower three stories of a six-story RC building. The vertical load levels were chosen to reflect the long-term axial loads expected in such a structure, with each jack initially applying a 400 kN (89.9 kips) load to represent the upper stories weight.

The two vertical hydraulic jacks were adjusted to apply axial forces, N_w and N_e, which varied with the lateral load Q, to maintain a shear span ratio (M/Ql) of 1.0. Here, M represents the moment at the base of the wall, Q is the horizontal load, and l is the distance between the centers of the side columns. This setup ensured that shear failure would occur before any flexural yielding of the wall.

The axial load's impact on shear capacity was minimal since the side columns remained intact until the tests concluded.

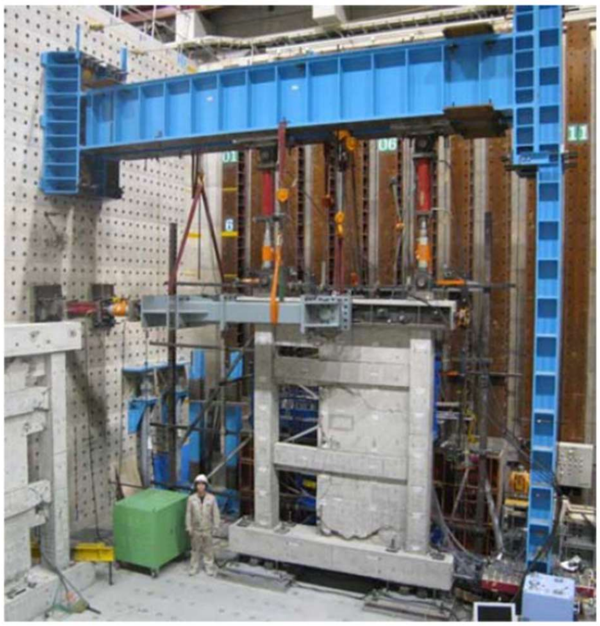

Figure 3.1:Test setup.

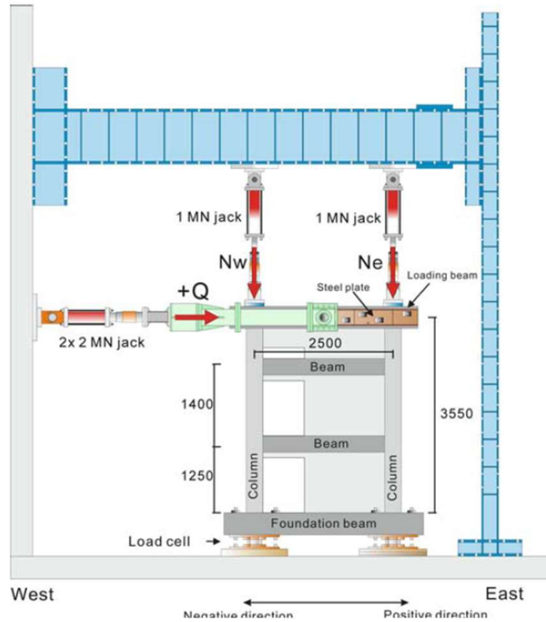

Figure 3.2: Loading system.

3.3 Details of Test Specimens and Material Properties

3.3.1 Test Specimens

Four reinforced concrete wall specimens were constructed and tested at Kyoto University. As illustrated in Figure 3.3, three specimens (S1, M1, L1) featured eccentric openings, while one specimen (N1) had no openings. The primary variables for the three-story specimens with openings were the opening ratio and the location of the openings. One of the main objectives of the experimental tests were to assess the impact of different opening ratios on shear strength of the structural walls. The opening ratios for specimens S1, M1, and L1 were 0.30, 0.34, and 0.46, respectively.

Each specimen had a height of 4150 mm (163.39 in.) and a width of 2800 mm (110.24 in.). The beams measured 200 mm (7.87 in.) in width and 300 mm (11.81 in.) in depth, while the side columns were 300 mm by 300 mm (11.81 in. by 11.81 in.). The wall panels had a thickness of 80 mm (3.15 in.). To ensure a fixed base at the bottom, an RC foundation beam, measuring 600 mm (23.62 in.) in width, 400 mm (15.75 in.) in thickness, and 3600 mm (141.73 in.) in length, was cast integrally with the structural walls and post-tensioned to the reaction floor before testing. The clear span between columns was 2200 mm (86.61 in.), and the column heights for the first, second, and third stories were 1100 mm (43.31 in.), 1100 mm (43.31 in.), and 550 mm (21.65 in.), respectively.

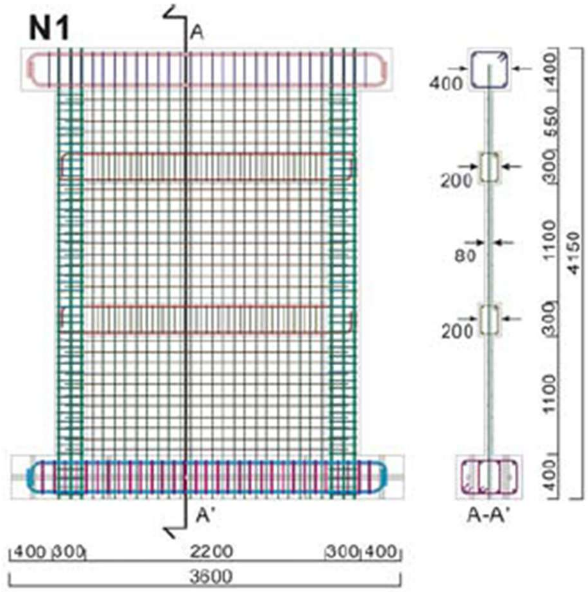

(a)

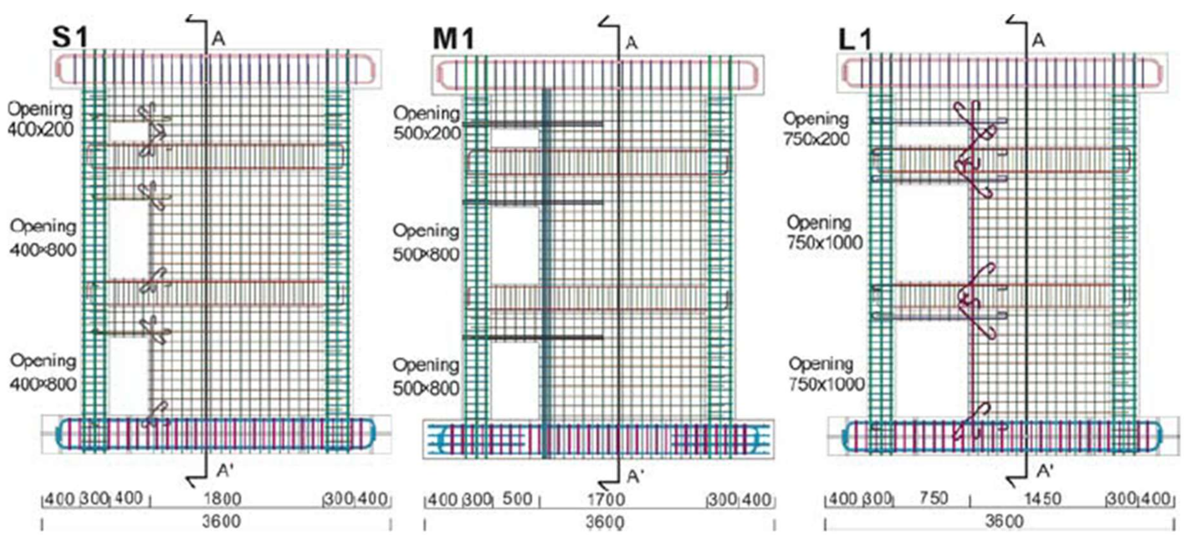

(b)

Figure 3.3: Specimen configurations and reinforcing bar arrangement: a) details and dimension for specimen N1 without opening, and b) dimension and opening details for specimens S1, M1, and L1.

A loading beam, 400 mm wide by 400 mm (15.75 in. by 15.75 in.) deep, was cast at the top of the wall panel. A hydraulic actuator was attached at the mid-span of this loading beam to apply horizontal reversed cyclic loading. The structural walls were subjected to lateral reverse cyclic loading until failure. Since one goal of this study was to examine the influence of opening ratios on shear behavior, all specimens were designed to fail in shear rather than flexure.

3.3.2 Material Properties

The cross-sectional dimensions and reinforcement arrangements for the test specimens are shown in Table 3.1. The typical beam section included two 13-mm diameter (D13) bars for both the top and bottom reinforcement, with D6 closed stirrups uniformly spaced at 100 mm (3.94 in.). The columns were reinforced with eight D19 bars and Φ10 closed stirrups, which were made of high-strength steel with a yield strength of 1033 MPa (149.83 ksi), uniformly spaced at 75 mm (2.95 in.). In contrast, D10 bars, used in other sections such as foundation and loading beams, have a lower yield strength of 352 MPa (51.06 ksi) (Table 3.4). The foundation beam sections incorporated four D25 bars for both top and bottom reinforcement, accompanied by D10 double closed stirrups spaced at 100 mm (3.94 in.). The loading beam sections were reinforced with two D25 bars for both top and bottom reinforcement, with D10 closed stirrups also spaced at 100 mm (3.94 in.). Table 3.2 outlines the reinforcing bars around the openings and the corresponding opening ratios.

Table 3.1: Cross section dimension and reinforcement arrangement

Element	Beam	Column	Wall	Loading beam	Foundation
Section (mm)	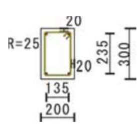	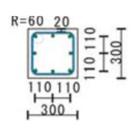	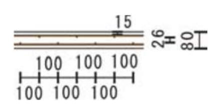	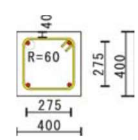	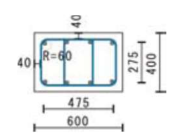
Dimension, mm (in.)	200 × 300 (7.87 × 11.81)	300 × 300 (11.81 × 11.81)	Thickness 80 (3.15)	400 × 400 (15.75 × 15.75)	400 × 600 (15.75 × 23.62)
Main bar	2-D13	8-D19	Vertical: D6@100	4-D25	8-D25
Stirrup	2-D6@100	2- Φ 10@75	Horizontal: D6@100	2-D10@100	4-D10@100

Table 3.2: Reinforcing bars around openings

Specimen	Opening ratio	Vertical reinforcing	Horizontal reinforcing	Diagonal reinforcing
S1	0.30	1-D13	2-D10	1-D13
M1	0.34	3-D13	3-D10	-
L1	0.46	1-D16	2-D13	1-D16

The measured material properties of the concrete and the reinforcement used in the specimens are listed in Tables 3.3 and 3.4, respectively. These tables provide comprehensive details on the properties essential for evaluating the structural performance under the testing conditions.

Table 3.3: Concrete material properties

Specimen	Compressive strength, MPa (ksi)	Tensile strength, MPa (ksi)	Young's modulus, GPa (ksi)
N1	25.9 (3.76)	2.3 (0.34)	21.0 (3045.8)
S1	25.1 (3.65)	2.2 (0.32)	21.7 (3147.3)
M1	21.7 (3.15)	2.1 (0.31)	15.8 (2291.6)
L1	28.9 (4.20)	2.5 (0.37)	26.0 (3771.0)

Table 3.4: Reinforcement properties

Nominal	Yield strength, MPa (ksi)	Maximum strength, MPa (ksi)	Young's modulus, MPa (ksi)
D6	425 (61.65)	538 (78.04)	204 (29588)
D10	352 (51.06)	496 (71.94)	186 (26977.02)
D13	362 (52.51)	529 (76.73)	188 (27267.1)
D19	411 (59.62)	605 (87.75)	189 (27412.14)
D25	387 (56.13)	541 (78.47)	194 (28137.33)
Φ10	1033 (149.83)	1221 (177.10)	204 (295878)

3.4 Experimental Results

Table 3.5 summarizes the maximum measured lateral load and corresponding drift angles for each specimen. In the positive loading direction, specimen N1 resisted a maximum load of 1179 kN (265.05 kips) at a drift angle of 0.48%. Comparatively, specimens S1, M1, and L1 exhibited maximum loads of 967 kN (217.4 kips) (18.0% lower than N1), 889 kN (199.86 kips) (24% lower), and 686 kN (154.22 kips) (41% lower), respectively. In the negative loading direction, specimen N1 withstood a maximum load of 1038 kN (233.36 kips) at a drift angle of 0.42%. In contrast, specimens S1, M1, and L1 showed maximum loads of 838 kN (188.39 kips) (19% less than N1), 723 kN (162.54 kips) (30% less), and 649 kN (145.91 kips) (37% less), respectively.

The selected baseline specimen (L1) exhibited the lowest maximum shear strength in both positive and negative loading directions, attributed to its larger opening ratio. Notably, the maximum strength achieved during positive loading was higher than during negative loading due to the eccentric location of the openings and the resultant shear transfer mechanism. This underscores the significant influence of loading direction on the structural response. Observed damage in the specimens at the end of the tests is depicted in Figure 3.4.

Table 3.5: Maximum lateral loads and corresponding drift angles.

Specimen id.	Positive direction		Negative direction	
	Maximum load kN (kip)	Drift angle (%)	Maximum load kN (kip)	Drift angle (%)
N1	1179 (265.05)	0.48	1039 (233.58)	0.42
S1	967 (217.4)	0.46	838 (188.39)	0.44
M1	889 (199.86)	0.74	723 (162.54)	0.48
L1	686 (154.22)	0.68	649 (145.91)	0.74

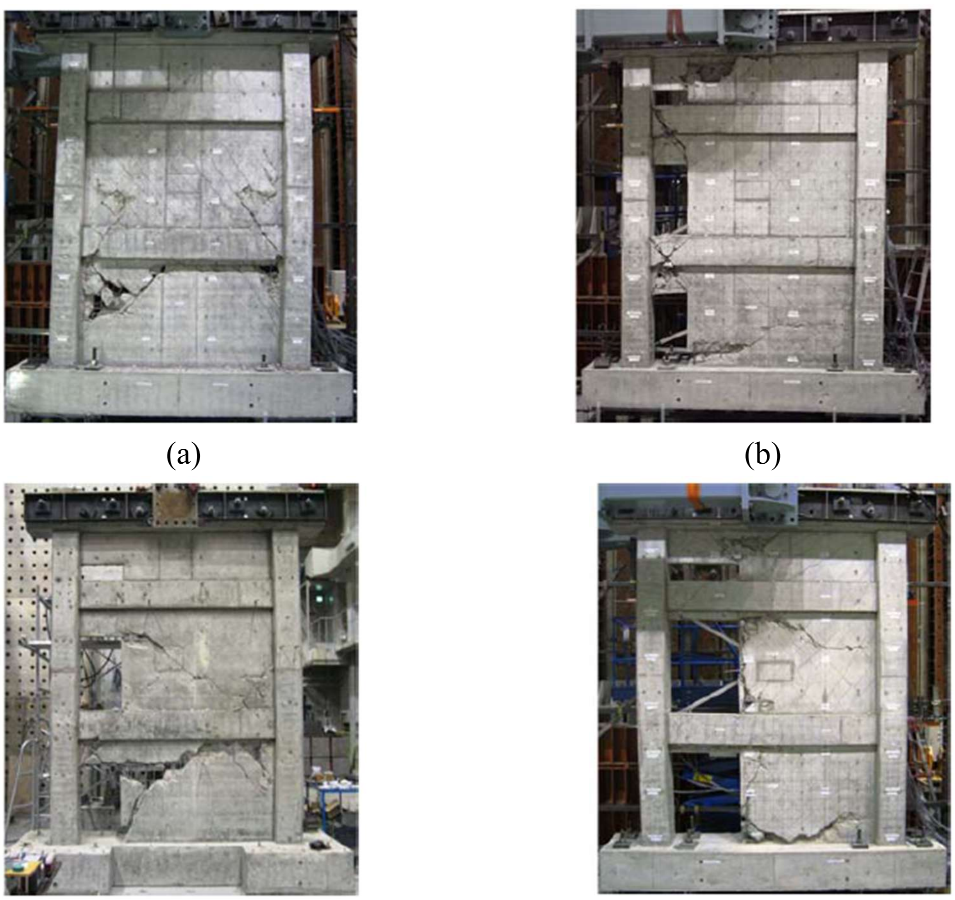

(a) (b) (c) (d)

Figure 3.4: Observed damage at the end of test for: a) specimen N1, b) specimen S1, c) specimen M1, and d) specimen L1.

3.5 IDEA StatiCa Analysis

The behavior of reinforced concrete shear wall specimens with openings, as explored in Section 3.3.1, was analyzed using the IDEA StatiCa software. This study extends previous research by Taleb et al. (2012) and centers on specimens N1, S1, M1, and L1. These specimens were specifically chosen to investigate the influence of varying opening ratios and locations on their structural performance. The modeling methodology in IDEA StatiCa integrated the actual compressive strength of concrete and the yield and ultimate strengths of reinforcing steel bars, following the parameters outlined by Taleb et al. (2012).

3.5.1 Analysis of Baseline Model (Specimen L1)

Based on the measured material properties detailed in Tables 3.3 and 3.4, the IDEA StatiCa model was developed for the baseline specimen in this report. The analysis primarily focused on the vertical and horizontal actuator loads applied to the shear wall with openings. The self-weight of the shear wall was considered a secondary load due to its relatively smaller magnitude. The vertical load consisted of two 400 kN (89.93 kips) downward point loads applied to the columns at both ends of the shear wall. Additionally, a gradually increasing lateral line load was applied along the height of the top beam, executed in 100 increments from zero to its peak value in IDEA StatiCa.

A 101.6 mm (4 in.) thick bearing plate was incorporated into the specimen to support the applied vertical load. This plate's dimensions, 300 mm by 300 mm, matched the dimensions the entire cross-section of the column. Both supports of the shear wall with openings were fixed in the horizontal (x) and vertical (z) directions, simulating a pin support condition at the base. At each end, a point bearing plate support was used, with dimensions of 897 mm by 600 mm (35.31 in. by 23.62 in.) and a thickness of 50.8 mm (2 in.).

In the IDEA StatiCa analysis, load factors of 1.0 were utilized for both load patterns - the self-weight and the applied lateral load - focused on the ultimate limit state (ULS) load combination. To ensure the accuracy of the simulations and their alignment with experimental findings, material factors for concrete (ϕ_c) and reinforcing steel (ϕ_s) within IDEA StatiCa were set to 1.0.

The capacity calculation process for IDEA StatiCa involved incrementally increasing the applied lateral load at the middle of the top beam until reaching any of the following conditions:

1. The concrete at any point in the model reached 100% of its strength capacity under the applied load.
2. The reinforcing steel reached 100% of its strength capacity under the applied load.
3. The anchorage steel reached 100% of its strength capacity under the applied load.

At an applied line load of 1.82 kN/mm (10.4 kip/in.), equivalent to a lateral load of 728 kN (164 kips) for the entire beam height (400 mm), the concrete was at 99.8% of its capacity near the top right corner of the top opening, the reinforcing bars were at their full capacity, and the anchoring steel slightly exceeded its capacity at 100.4% as shown in Figure 3.5a. Any additional increment to the applied lateral load would exceed the capacity of the anchoring steel, marking this as the maximum load capacity according to IDEA StatiCa following the Compatible Stress Field Method (CSFM). Under this lateral load, the deflection in the x-direction for the shear wall specimen L1 was recorded as 31.1 mm (1.23 in.) at the top of the right support. The maximum principal stress in the concrete was recorded as 28.82 MPa (4.18 ksi) at the top right corner of the opening in second story (Figure 3.5b), while the maximum stress in the reinforcement reached 425 MPa (61.65 ksi) at the reinforcements located at the bottom right corner of the opening at first story. Figure 3.5 provides detailed results for shear wall specimen L1 under the maximum applied lateral load of 728 kN (164 kips) obtained from the IDEA StatiCa analysis.

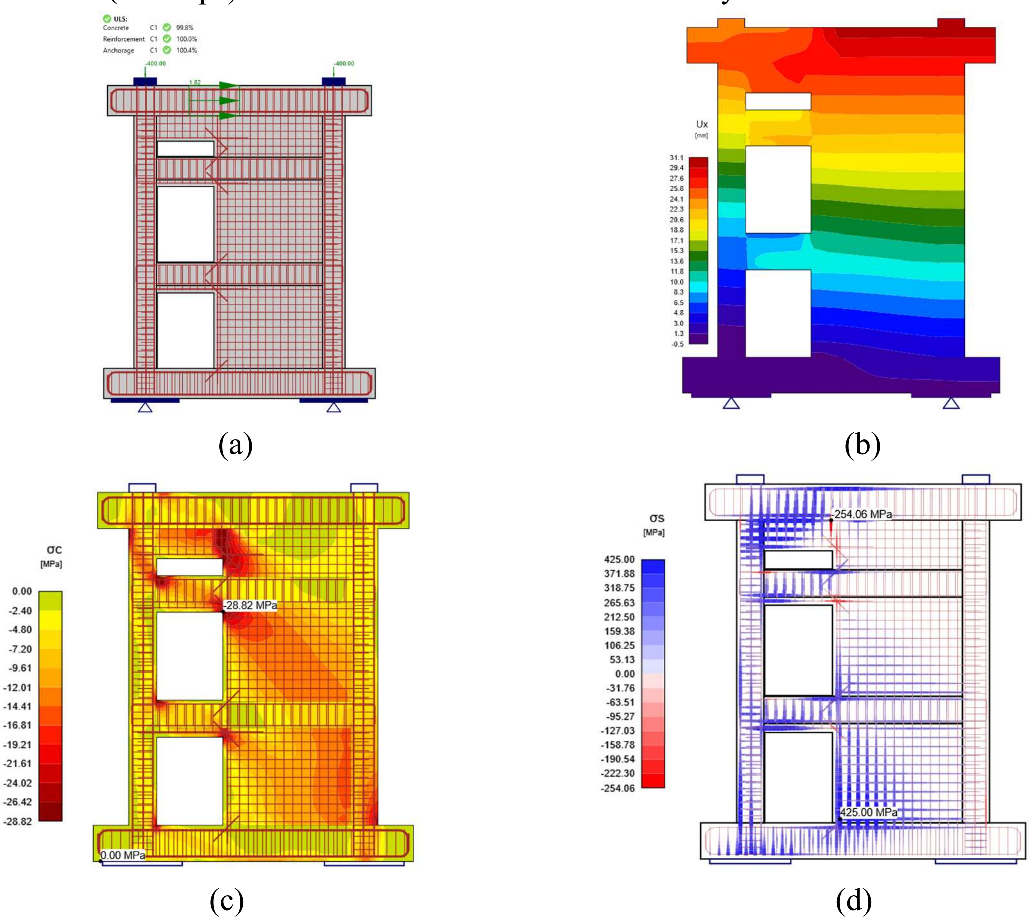

Figure 3.5: Shear wall with openings L1 at 1.82 kN/mm (10.4 kip/in.) lateral load: a) IDEA StatiCa Detail model with results, b) deflection contour, c) concrete principal stresses (σ_c), and d) stresses in the reinforcement (σ_s).

3.5.2 Analysis of other Specimens (N1, S1, and M1) for Positive Loading Direction

Using the same methodology outlined for the baseline model in Section 3.5.1, the IDEA StatiCa model was created for Specimens N1, S1, and M1, incorporating the material properties listed in Tables 3.3 and 3.4. The results from the CSFM analysis for positive lateral loading are shown in Table 3.6 and further presented in Figures 3.6 through 3.8 for shear wall specimens N1, S1, and M1 respectively.

Table 3.6: CSFM results for shear wall with openings under positive lateral loading

Shear wall specimen	Lateral load		Concrete			Steel		Displacement
	Measured, kN (kip)	CSFM, kN (kip)	Specified *fc'*, MPa (ksi)	Maximum principal stress, MPa (ksi)	Location	Maximum stresses in the rebars, MPa (ksi)	Location	Maximum displacement in x direction, mm (in.)
N1	1179 (265)	952 (214)	25.90 (3.76)	21.06 (3.06)	Near the bottom of the right support	418 (60.63)	At the top of wall on the third story	26.40 (1.04)
S1	967 (217)	880 (198)	25.10 (3.65)	24.98 (3.63)	At the lower left corner of the opening on the third story	425 (61.65)	At the bottom right corner of the opening on the first story	22.40 (0.89)
M1	889 (200)	792 (178)	21.70 (3.15)	21.60 (3.14)	At the bottom left corner of the opening on the third story	425 (61.65)	In the bottom right corner of the opening on the first story	19.40 (0.77)
L1	686 (154)	728 (164)	28.90 (4.20)	28.82 (4.18)	At the top right corner of the opening on the second story	425 (61.65)	In the rebars located at the bottom right corner of the opening on the first story	31.10 (1.23)

For Specimen N1, all results are shown in Figure 3.6. Figure 3.6a indicates a high concentration of compressive stress near the bottom of the right support. However, Figure 3.4a shows significant shear cracks in the top corners of the first-story wall and some cracks in the second-story wall from the experiment. The stress plots (Figures 3.6c and 3.6d) and damage observations (Figure 3.4a) suggest that IDEA StatiCa identified most critical areas where cracks might develop and concrete could fail, although it missed some areas in the top left corner of the first story wall. The overall compressive stress flow (shown as a red bend or region in Figure 3.6c) extending from the top left corner to the bottom right corner of the specimen is an indication that a compressive strut can be used in a potential strut and tie model. The CSFM analysis shows that the specimen N1 would fail due to concrete crushing at 21.05 MPa (3.05 ksi) at the bottom right corner of the right support.

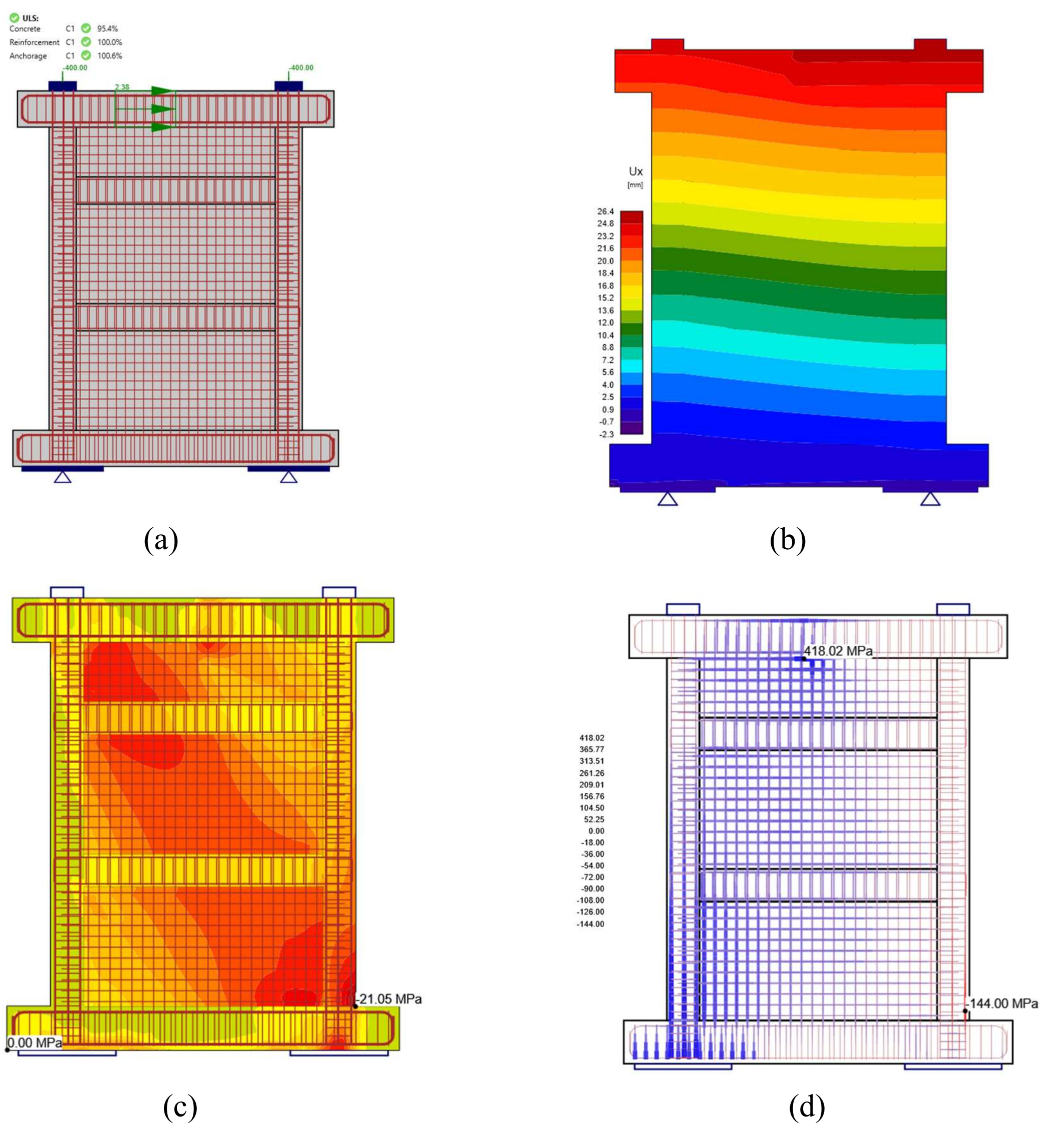

Figure 3.6: Shear wall with openings N1 at 2.38 kN/mm (13.6 kip/in.) lateral load: a) IDEA StatiCa model with results, b) deflection contour, c) concrete principal stresses (σ_c), and d) stresses in the reinforcement (σ_s).

For Specimen S1, all results are presented in Figure 3.7. Figure 3.7c shows the largest concentration of compressive stress at the top right corners of the openings across all three stories, reflecting the experimental behavior accurately. Figure 3.4b reveals shear cracks in the wall and beams, which correspond to areas of high principal stress indicated by IDEA StatiCa. Additionally, a large flexural shear crack was observed at the bottom right corner of the opening on the first story during the experiment (Figure 3.4b), and IDEA StatiCa also showed significant stress accumulation in the reinforcing bars at this location. Overall, IDEA StatiCa effectively captured the behavior of Specimen S1. Based on the CSFM analysis, it can be observed that specimen S1 is likely to fail due to concrete crushing at the bottom left corner of the third-story opening, with the stress reaching 24.98 MPa (3.62 ksi).

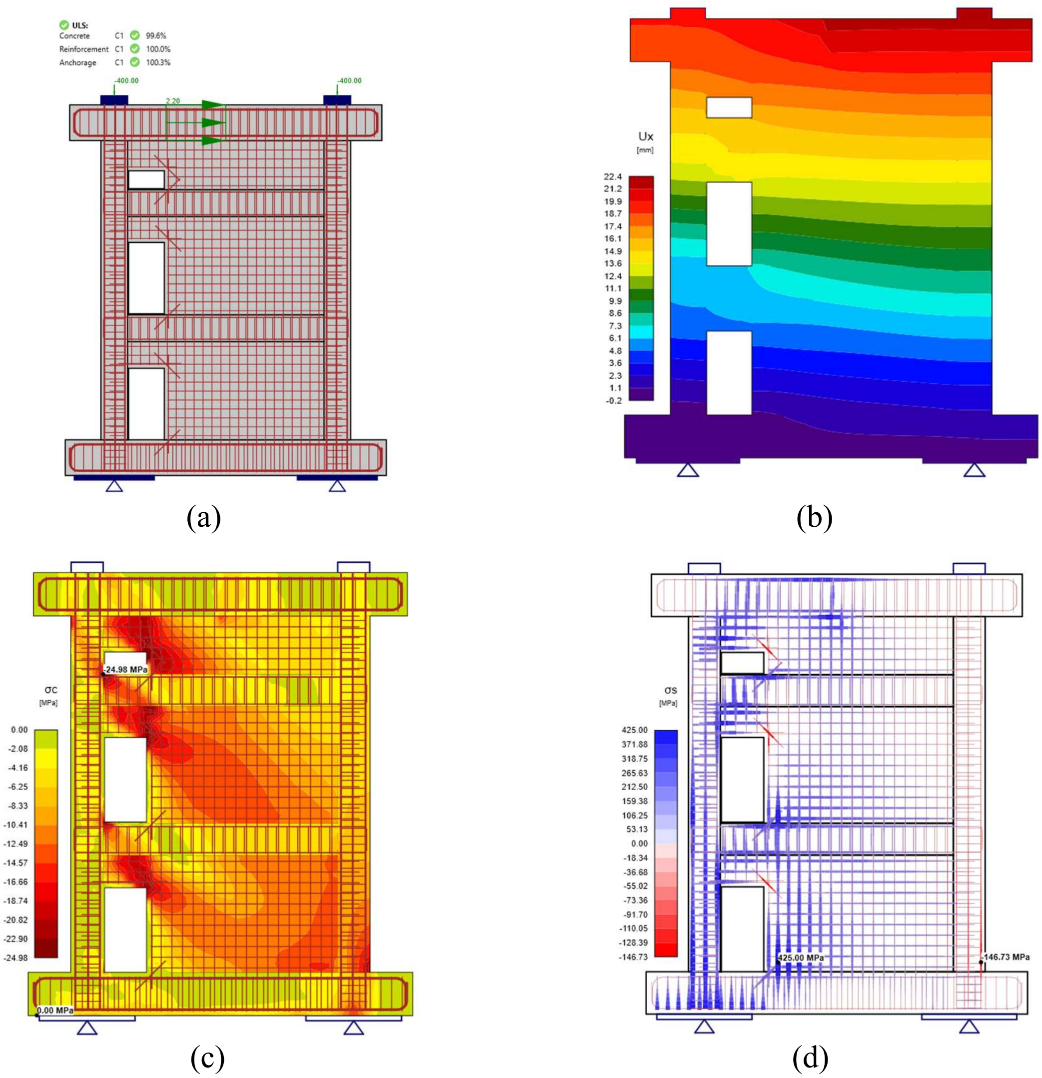

Figure 3.7: Shear wall with openings S1 at 2.2 kN/mm (12.57 kip/in.) lateral load: a) IDEA StatiCa model with results, b) deflection contour, c) concrete principal stresses (σ_c), and d) stresses in the reinforcement (σ_s).

For specimen M1, Figures 3.8 and 3.4 show that both IDEA StatiCa and the experimental observations highlight critical stress areas around the openings. IDEA StatiCa identifies a high concentration of principal stress in concrete near the top right corner of the openings and the bottom left corner of the third story wall. In the experiment, large shear cracks were observed starting from both the bottom and top right corners of the first story opening (Figure 3.4c), which IDEA StatiCa captured accurately. Additionally, flexural shear cracks were seen near the top right corner of the second story opening (Figure 3.4c), although IDEA StatiCa indicated the maximum flexural stress in the vertical bars near the bottom right corner of the first story opening. The CSFM analysis showed large compressive stress in the third story wall near the top right corner of the opening, but no cracks were observed there during the experiment. According to the CSFM analysis, specimen M1 is expected to fail at the bottom left corner of the third-story opening due to concrete crushing, with the stress reaching 21.60 MPa (ksi).

.

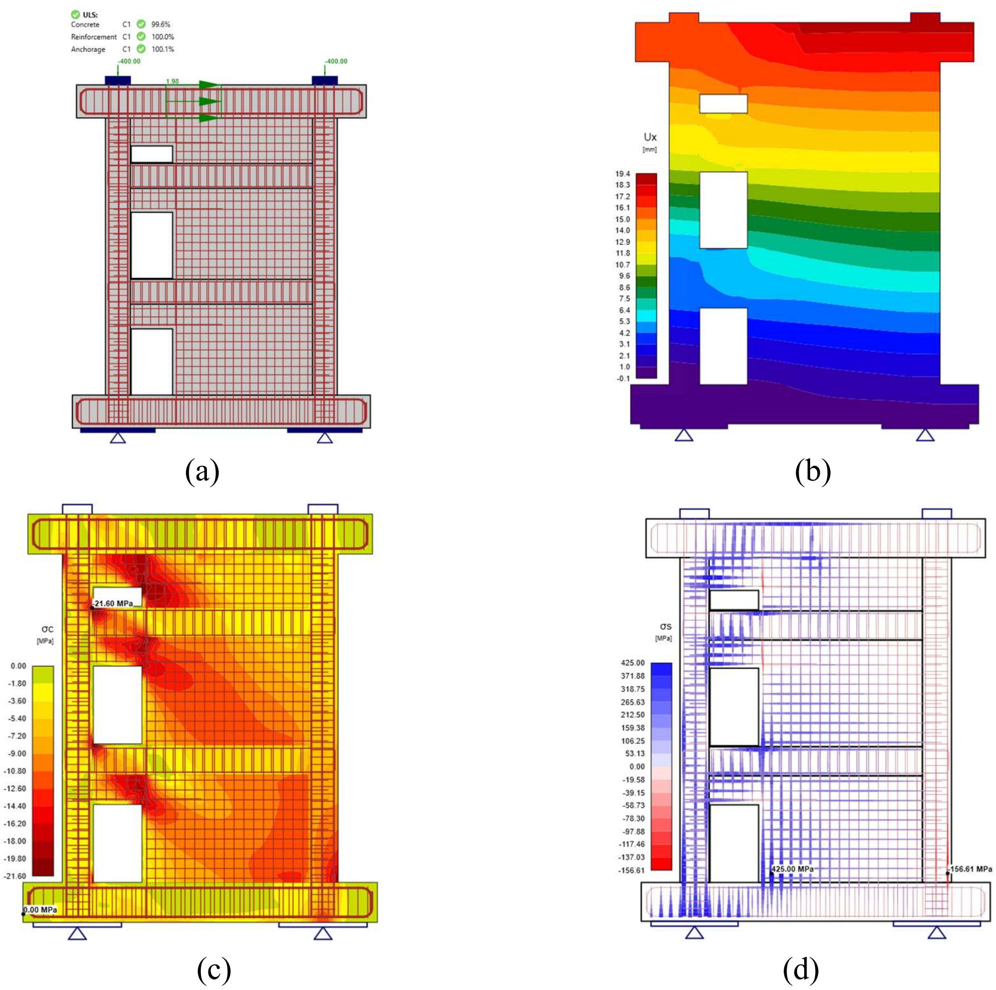

Figure 3.8: Shear wall with openings M1 at 1.98 kN/mm (11.31 kip/in.) lateral load: a) IDEA StatiCa model with results, b) deflection contour, c) concrete principal stresses (σ_c), and d) stresses in the reinforcement (σ_s).

3.5.3 Analysis of Shear Wall with Openings for Negative Loading Direction

Using the same methodology outlined for the baseline model in Sections 3.5.1 and 3.5.2, the IDEA StatiCa model was developed for Specimens L1, N1, S1, and M1. The material properties specified in Tables 3.3 and 3.4 were used consistently across all models. The only variation was the loading direction. In this case, the lateral load was applied in the negative x-direction. The results from the CSFM analysis for negative lateral loading are shown in Table 3.7 and further presented in Figures 3.9 through 3.12 for shear wall specimens N1, S1, M1, and L1 respectively.

Table 3.7: CSFM results for shear wall with openings under negative lateral loading

Shear wall specimen	Lateral load		Concrete			Steel		Displacement
	Measured, kN (kip)	CSFM, kN (kip)	Specified *fc'*, MPa (ksi)	Maximum principal stress, MPa (ksi)	Location	Maximum stress in the rebars, MPa (ksi)	Location	Maximum displacement in x direction, mm (in.)
N1	1039 (234)	956 (215)	25.90 (3.76)	21.13 (3.07)	At the bottom left corner of the left support near the foundation beam	425 (61.65)	In the horizontal bars at the top of the wall on the third story	26.70 (1.06)
S1	838 (188)	928 (209)	25.10 (3.65)	25.07 (3.64)	At the bottom right corner of the opening on the second story	425 (61.65)	In the horizontal bars of the wall at the top of the third story	28.90 (1.14)
M1	723 (163)	784 (176)	21.70 (3.15)	21.63 (3.14)	At the upper left corner of the opening on the first story	406.96 (59.03)	In the vertical bars at the bottom right corner of the foundation beam	16.30 (0.65)
L1	649 (146)	816 (183)	28.90 (4.20)	28.83 (4.19)	At the bottom right corner of the opening on the second story	425 (61.65)	In the vertical bars at the bottom right corner of the opening on the first story	24.30 (0.96)

From the CSFM analysis of specimen L1 shown in Figure 3.9c, large principal stress is observed in the bottom left corner of the first story opening. Maximum stress in the vertical rebars is also indicated in this region (Figure 3.9d). Large flexural cracks were observed where the CSFM analysis showed significant compressive and tensile stress (Figure 3.4d), suggesting that IDEA StatiCa accurately captured the specimen's real behavior. However, the CSFM analysis missed the top right corner of the second story opening, where a large flexural shear crack was observed during the experiment (Figure 3.4d). Based on the CSFM analysis for negative lateral loading, specimen L1 is predicted to fail due to concrete crushing at the bottom right corner of the first and second-story openings, with the stress reaching 28.83 MPa (4.18 ksi).

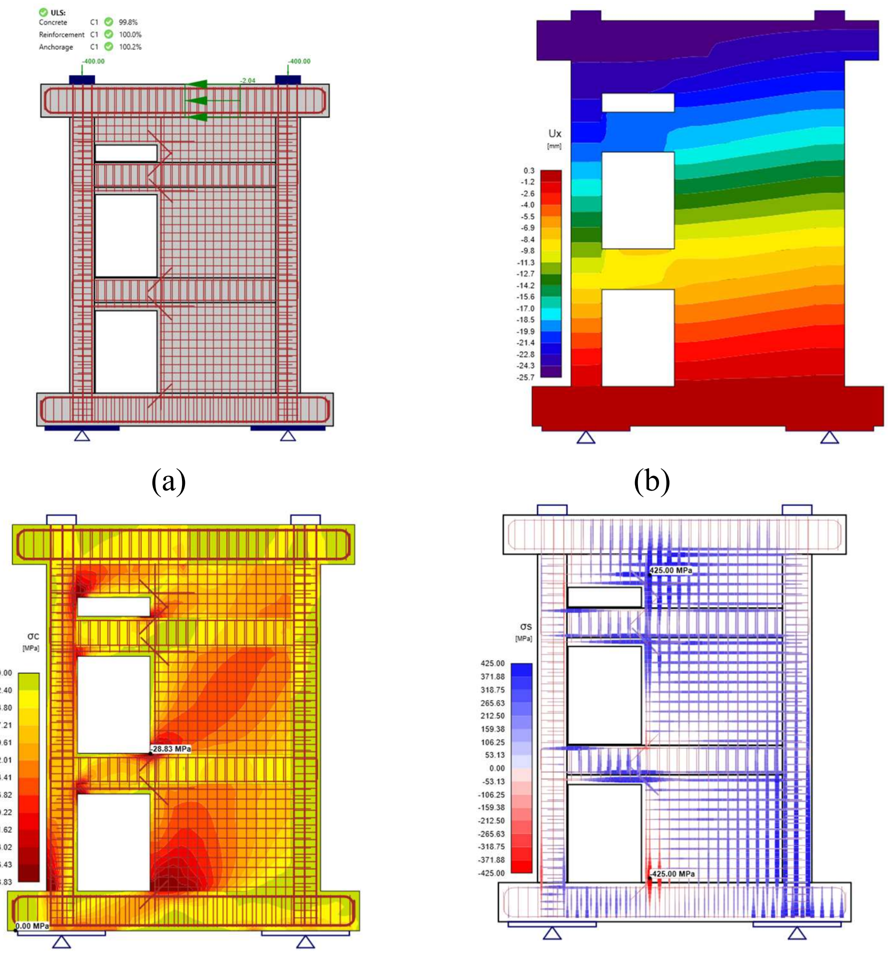

Figure 3.9: Shear wall with openings L1 at 2.04 kN/mm (11.65 kip/in.) lateral load: a) IDEA StatiCa model with results, b) deflection contour, c) concrete principal stresses (σ_c), and d) stresses in the reinforcement (σ_s).

For the negative loading direction for specimen N1 all the results are presented in Figure 3.10. The maximum principal stress in concrete from the CSFM analysis was observed at the bottom of the left column and in the left corner of the first story wall (Figure 3.10c). Figure 3.4a shows large shear cracks in the top corners of the first story wall and some cracks on the second floor from the experiment. While IDEA StatiCa effectively captured the behavior of the first story wall, it missed some critical spots at the bottom corners of the second story wall where shear cracks were observed during the experiment (Figure 3.4a). The CSFM analysis indicates that specimen N1 is expected to fail at the lower left corner of the wall at the first story due to concrete crushing, with the stress reaching 21.13 MPa (3.06 ksi).

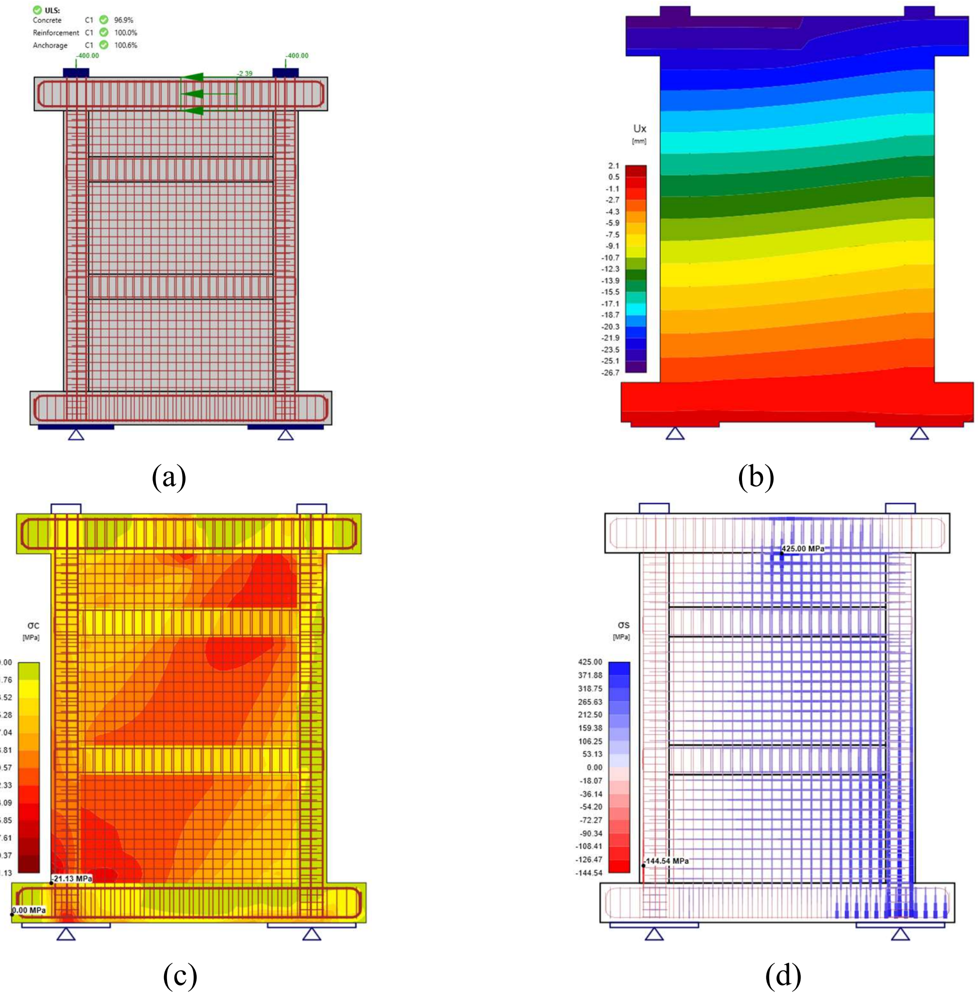

Figure 3.10: Shear wall with openings N1 at 2.39 kN/mm (13.65 kip/in.) lateral load: a) IDEA StatiCa model with results, b) deflection contour, c) concrete principal stresses (σ_c), and d) stresses in the reinforcement (σ_s).

For Specimen S1, all results are presented in Figure 3.11. Figure 3.11c shows a high concentration of compressive stress at the bottom right corners of the openings across all three stories, accurately reflecting the experimental behavior observed in the first story wall. Figure 3.4b reveals flexural shear cracks in the first story wall and in the beams on the first and second stories, corresponding to areas of high principal and flexural stress as indicated by IDEA StatiCa. Overall, IDEA StatiCa effectively captured the behavior of Specimen S1. The analysis using the CSFM method suggests that specimen S1 is likely to experience failure due to concrete crushing at the bottom right corner of the opening on the first or second story, with a predicted failure stress of 25.07 MPa (3.63 ksi).

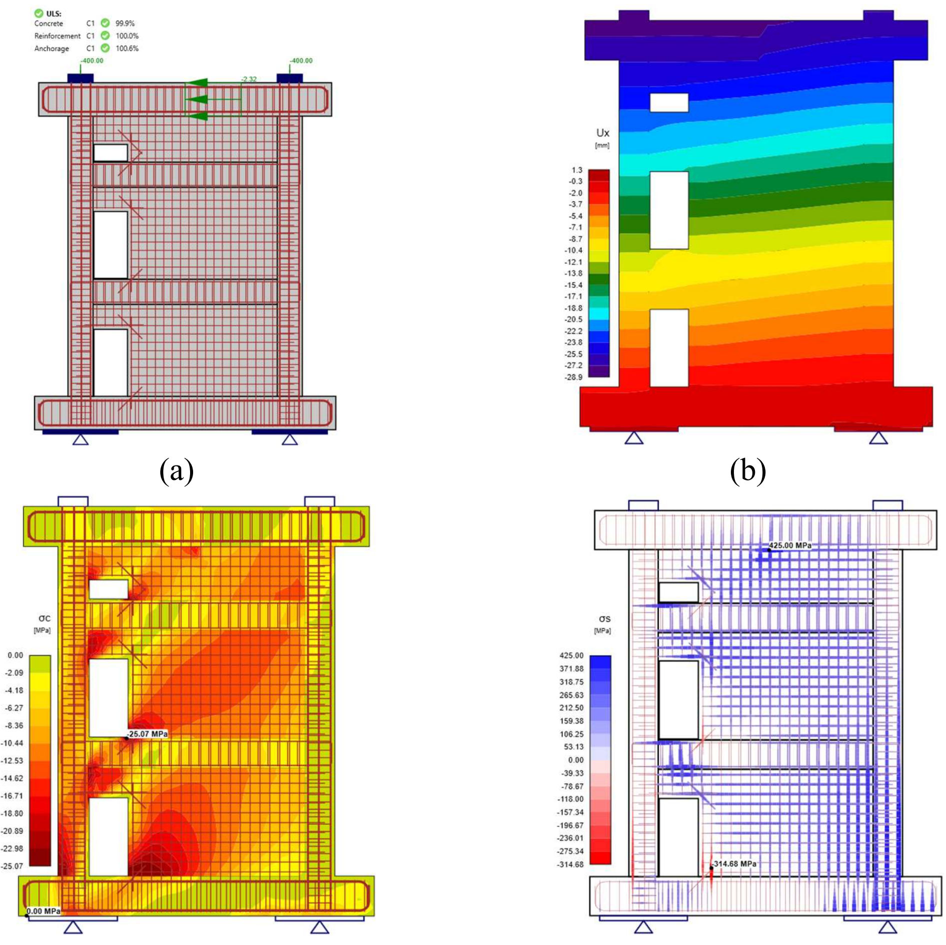

(c) (d)

Figure 3.11: Shear wall with openings S1 at 2.32 kN/mm (13.25 kip/in.) lateral load: a) IDEA StatiCa model with results, b) deflection contour, c) concrete principal stresses (σ_c), and d) stresses in the reinforcement (σ_s).

For specimen M1, all results are presented in Figure 3.12. The IDEA StatiCa analysis shows a high concentration of principal stress in concrete at the bottom right corners of the first- and second story openings, as well as maximum principal stress at the top left corner of the first story opening. During the experiment, large shear cracks were observed starting from both the bottom and top right corners of the first story opening, and flexural shear cracks were observed near the top right corner of the second story opening (Figure 3.4c). IDEA StatiCa accurately captured the behavior of the first story wall but missed the critical areas on the second story. Although IDEA StatiCa indicated maximum flexural stress in the vertical bars at the bottom right corner of the right column, no cracks were observed in these regions during the experiment. According to the CSFM analysis, the predicted failure mechanism for specimen M1 involves concrete crushing at the top right corner of the first story opening at 21.63 MPa (3.14 ksi). Alternatively, concrete crushing may also occur at the bottom right corner of the openings in the first and second stories.

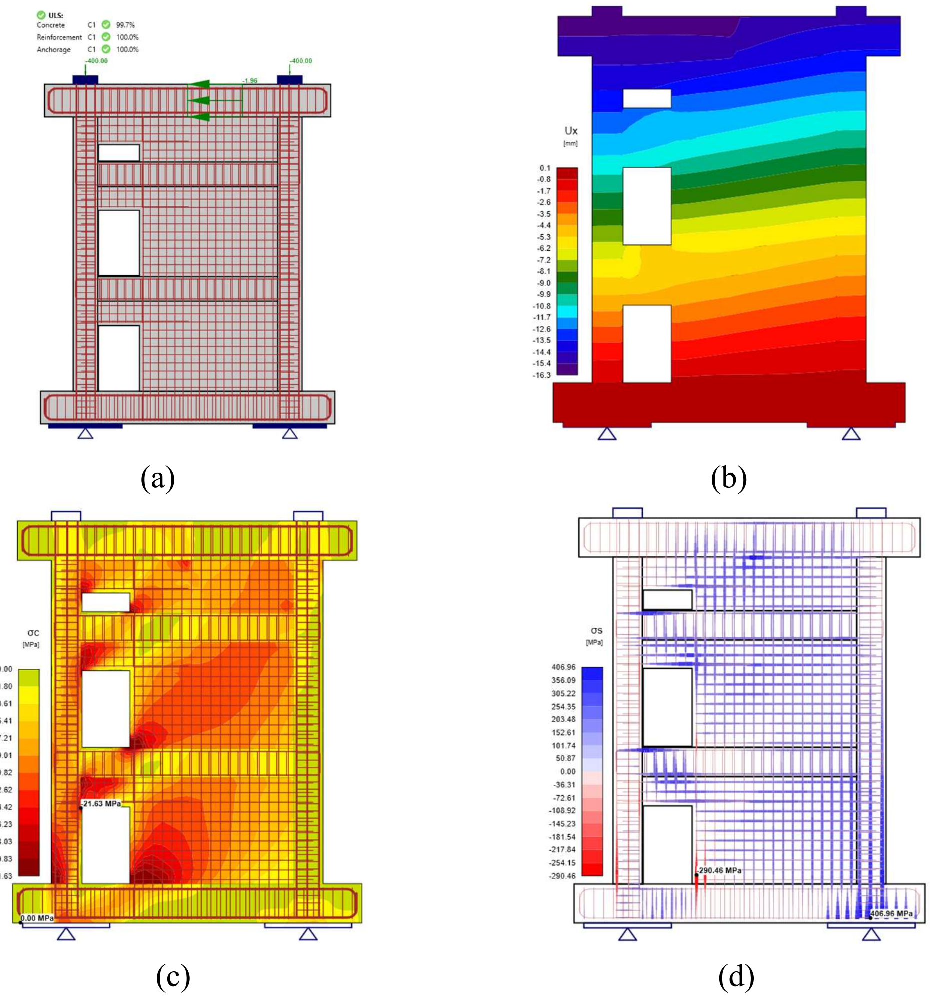

Figure 3.12: Shear wall with openings M1 at 1.96 kN/mm (11.2 kip/in.) lateral load: a) IDEA StatiCa model with results, b) deflection contour, c) concrete principal stresses (σ_c), and d) stresses in the reinforcement (σ_s).

3.5.4 Capacity Calculation from Lateral Load

To calculate the maximum applied lateral load of total lateral capacity of shear walls, the applied line load over the height of 400 mm (15.75 in.) deep top beam is multiplied by the height of the beam (Table 3.6). For the baseline model (L1), the line load was calculated as 1.82 kN/mm (10.4 kip/in.) from IDEA StatiCa (Figure 3.5). Thus, the total capacity was calculated by multiplying this line load by the beam height (400 mm or 15.75 in.), resulting in a total capacity of 1.82 kN/mm × 400 mm = 728 kN (163.7 kips). Similarly, capacities of other shear wall specimens (N1, S1, and M1) are calculated and shown in Table 3.6.

Table 3.8: Applied lateral load or capacity calculation from line load

Shear wall	Lateral load acting toward positive x direction		Lateral load acting toward negative x direction	
	Line load (kN/mm)	$P_{\text{IDEA StatiCa}}$, kN (kips)	Line load (kN/mm)	$P_{\text{IDEA StatiCa}}$, kN (kips)
N1	2.38	952 (214.0)	2.39	956 (214.9)
S1	2.2	880 (197.8)	2.32	928 (208.6)
M1	1.98	792 (178.1)	1.96	784 (176.3)
L1	1.82	728 (163.7)	2.04	816 (183.5)

3.6 Effect of Concrete Confinement on the Capacities of the Shear Walls with Openings

3.6.1 Mander et al. (1988) Model for Confined Concrete

When concrete is confined in the lateral direction its axial capacity increases. Lateral deformation capacity or ductility of reinforced concrete columns or beams can also be improved by providing large amounts of closely spaced transverse steel in the form of ties or hoops. These ties or hoops help maintain the integrity of the confined concrete at large lateral displacements, especially during seismic events. Figure 3.13 illustrates the arching action and effectiveness of confinement over the height of a column. Drawing on the left shows widely spaced column ties and their limited effectiveness in confining concrete under large axial loads. In comparison, the axial strength and deformation capacity of the column on the right are much larger due to better confinement provided by larger amount of transverse steel with closer spacing. As an example, Figure 3.14 shows that axial strength of concrete can be much larger when it is confined (f_{cc}') compared to unconfined concrete with maximum strength f_c'. Similarly, the deformation capacity or maximum axial strain (ε_{cu}) is much larger compared to maximum deformation capacity or maximum strain (ε_{sp}) of unconfined concrete.

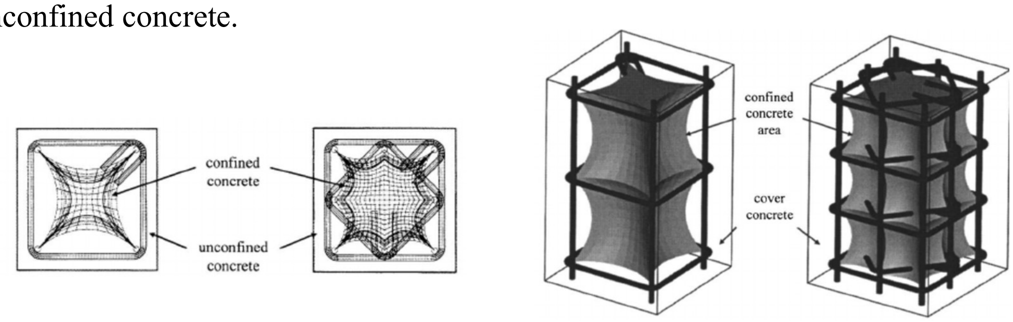

Figure 3.13: Arching action and effectiveness of concrete confinement (Konstantinidis et al., 2007).

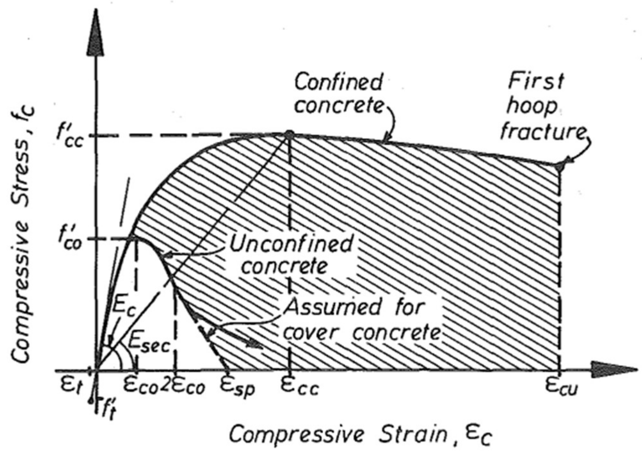

Figure 3.13: Stress-strain model proposed for monotonic loading of confined and unconfined concrete (Mander et al., 1988).

The model proposed by Mander et al. (1988) is used in this research to account for the increase in concrete strength and deformation capacity due to confinement of concrete using transverse steel bars. Mander et al. model is developed to simulate the behavior of confined concrete under uniaxial compressive loading. This model accommodates various configurations of confining steel, including spirals and rectangular hoops. The key concept in the model is the effective lateral confining stress, which is influenced by the geometry and arrangement of both the transverse and longitudinal reinforcing bars. Figure 3.15 depicts the effectively confined core for rectangular hoop reinforcement. The value of confined concrete compressive strength is determined using Equation 3.1, as proposed by Mander et al. (1988).

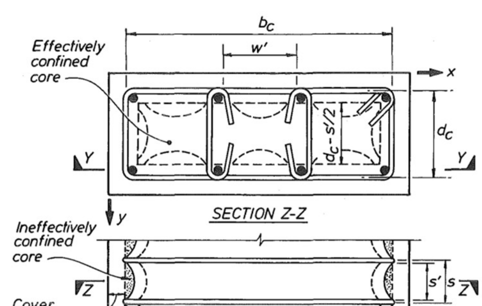

Figure 3.145: Effectively confined core for rectangular hoop reinforcement (Mander et al., 1988).

$$f'_{cc} = f'_{co}(-1.254 + 2.254\sqrt{1 + \frac{7.94 f'_l}{f'_{co}}} - 2\frac{f'_l}{f'_{co}}) \quad (3.1)$$

where, b_c and d_c are the core dimensions to centerlines of perimeter hoop in x and y directions, respectively, where, $b_c > d_c$. w' is the clear distance between adjacent longitudinal bars, s' is the clear vertical spacing between spiral or hoop bars, f'_{cc} is the confined concrete compressive strength, f'_{co} (or f'_c) is the unconfined concrete compressive strength, and f'_l is the effective lateral confining stresses which can be calculated using Equations 3.2 and 3.3.

$$f'_{lx} = k_e \rho_x f_{yh} \quad (3.2)$$

$$f'_{ly} = k_e \rho_y f_{yh} \quad (3.3)$$

where, k_e is the confinement effectiveness coefficient (Equation 3.4), the ratio of transverse reinforcement in the x and y directions can be calculated from Equations 3.5 and 3.6, and f_{yh} is the yield strength of transverse reinforcement.

$$k_e = \frac{(1 - \sum_{i=1}^{n} \frac{(w'_i)^2}{6 b_c d_c})(1 - \frac{s'}{2 b_c})(1 - \frac{s'}{2 d_c})}{(1 - \rho_{cc})} \quad (3.4)$$

$$\rho_x = A_{sx} / s d_c \quad (3.5)$$

$$\rho_y = A_{sy} / s b_c \quad (3.6)$$

where, ρ_{cc} is the ratio of area of longitudinal reinforcement to area of core of section, A_{sx} and A_{sy} is the total area of transverse bars running in the x and y directions, respectively (Figure 3.15).

3.6.2 Confinement Effect on the Strength Properties of Concrete

The confined concrete model proposed by Mander et al. (1988) was applied to the shear wall specimens to calculate the strengths of concrete, considering the confinement effects in various structural elements. This analysis included the foundation beam, right and left columns, floor beams, and the top beam. By incorporating the confinement effects, the model provided a more accurate assessment of the concrete strength in these components. The results of this analysis are presented in Figures 3.16 and 3.17. The Table 3.9 presents the compressive strength results obtained from the Mander et al. confinement model for various structural elements in different specimens.

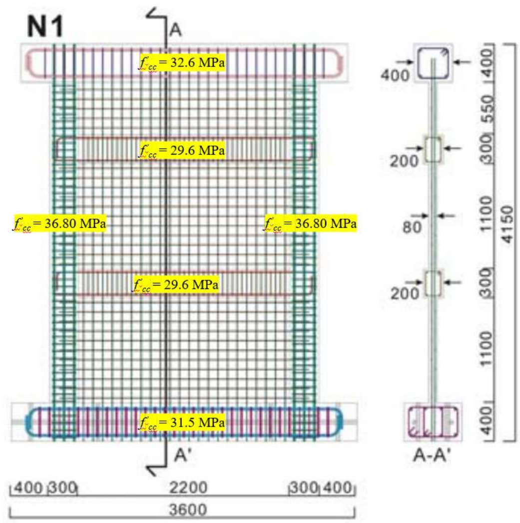

(a) f'_c = 25.90 MPa (3.76 ksi)

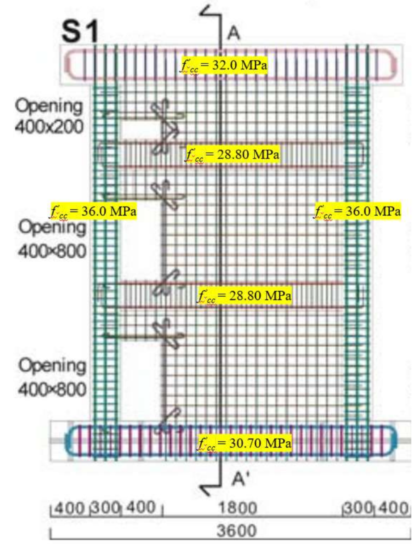

(b) f'_c = 25.10 MPa (3.65 ksi)

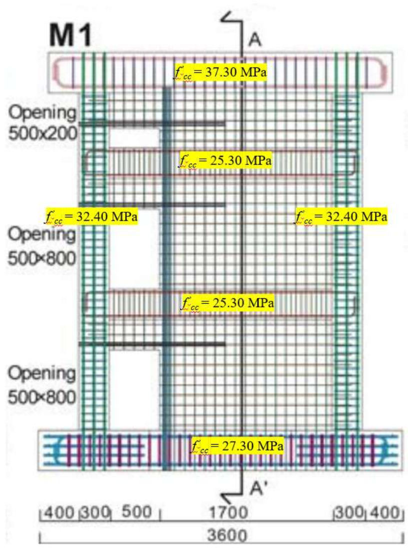

(c) f'_c = 21.70 MPa (3.15 ksi)

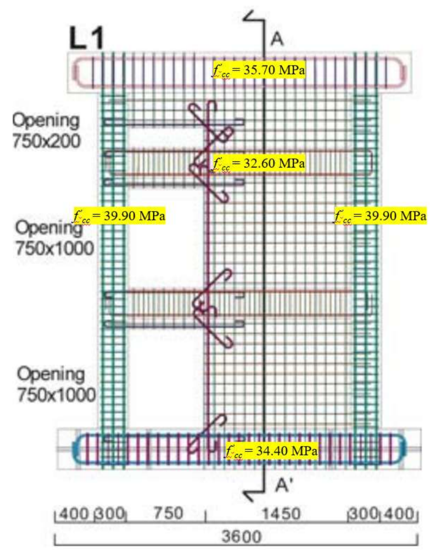

(d) f'_c = 28.90 MPa (4.20ksi)

Figure 3.156: Strength of concrete in different structural elements of shear wall due to confinement effect: a) shear wall specimen N1, b) shear wall specimen S1, c) shear wall specimen M1, and d) shear wall specimen L1.

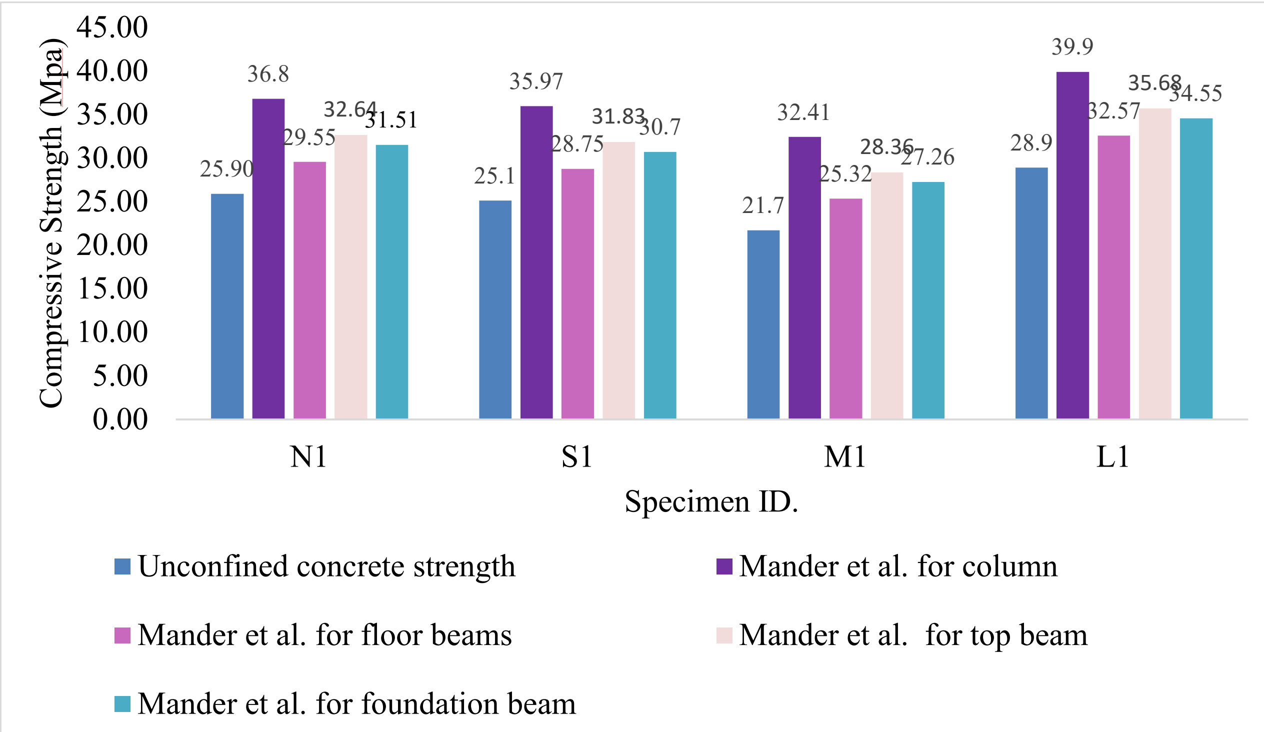

Figure 3.167: Comparison of strength of actual and confined concrete from Mander et al. confined concrete model.

Table 3.9: Results from Mander et al.'s confinement model

Specimen ID	Unconfined compressive stregth of concrete MPa (ksi)	Confined concrete strength for columns, MPa (ksi)	Confined concrete strength for floor beams, MPa (ksi)	Confined concrete strength for top beam, MPa (ksi)	Confined concrete strength for foundation beam, MPa (ksi)
N1	25.90 (3.76)	36.80 (5.34)	29.55 (4.29)	32.64 (4.74)	31.51 (4.58)
S1	25.10 (3.65)	35.97 (5.22)	28.75 (4.17)	31.83 (4.62)	30.70 (4.46)
M1	21.70 (3.15)	32.41 (4.71)	25.32 (3.68)	28.36 (4.12)	27.26 (3.96)
L1	28.90 (4.20)	39.90 (5.79)	32.57 (4.73)	35.68 (5.18)	34.55 (5.02)

For specimen N1, a compressive strength of 36.8 MPa (5.34 ksi) was obtained for the column using the Mander et al. model, which is 42% higher than the unconfined concrete strength of 25.9 MPa (3.76 ksi). An increase of 14% was observed in the floor beam strength, reaching 29.55 MPa (4.29 ksi). The top beam compressive strength was increased by 26% to 32.64 MPa (4.74 ksi), while the foundation beam strength showed a 22% increase, reaching 31.51 MPa (4.58 ksi).

For specimen S1, similar trends were observed. The column compressive strength reached 35.97 MPa (5.22 ksi), representing a 43% increase over the unconfined concrete value of 25.1 MPa (3.65 ksi). The floor beam strength was recorded at 28.75 MPa (4.17 ksi), 14% higher than the unconfined strength. The top beam compressive strength showed a 27% increase to 31.83 MPa (4.62 ksi), while the foundation beam strength increased by 22% to 30.7 MPa (4.46 ksi).

For specimen M1, the Mander et al. model indicated a 49% increase in column strength, reaching 32.41 MPa (4.71 ksi). The floor beam strength increased by 17%, reaching 25.32 MPa (3.68 ksi). A 31% increase in top beam compressive strength was noted, reaching 28.36 MPa (4.12 ksi), and the foundation beam strength was increased by 26% to 27.26 MPa (3.96 ksi).

Specimen L1 exhibited the largest increases, with column compressive strength reaching 39.9 MPa (5.79 ksi), 38% higher than the unconfined concrete value of 28.9 MPa (4.2 ksi). The floor beam strength increased by 13% to 32.57 MPa (4.73 ksi), while the top beam compressive strength increased by 23% to 35.68 MPa (5.18 ksi). The foundation beam strength rose by 19% to 34.55 MPa (5.02 ksi). These results highlight the Mander et al. model's effectiveness in enhancing compressive strength across various structural elements in the specimens.

3.6.3 IDEA StatiCa Analysis Considering Mander et al.'s Confined Concrete Model

The shear wall specimens with openings were analyzed in IDEA StatiCa, taking into account the confinement effects of the foundation beam, columns, floor beams, and top loading beam. For this analysis, the shear wall was modeled as unconfined concrete. The concrete strengths for different structural components are shown in Table 3.9. Due to the complexity of defining confined and unconfined zones within columns or beams in IDEA StatiCa, the confinement effect was applied uniformly across the entire cross-section and length of the member. This approach ensured a comprehensive assessment of the structural performance when concrete is confined.

To prepare the IDEA StatiCa models, the same procedure was followed as described in Section 3.5.1 for the baseline model L1, and Sections 3.5.2 and 3.5.3 for other shear wall specimens N1, S1, and L1, respectively. The only difference is that the concrete strengths for these structural elements are defined separately, as shown in Figure 3.16. The material properties and strengths are defined for different structural elements in specimen L1 in IDEA StatiCa as shown in Figure 3.18. Note that these are the confined concrete properties listed in the bottom row of Table 3.9.

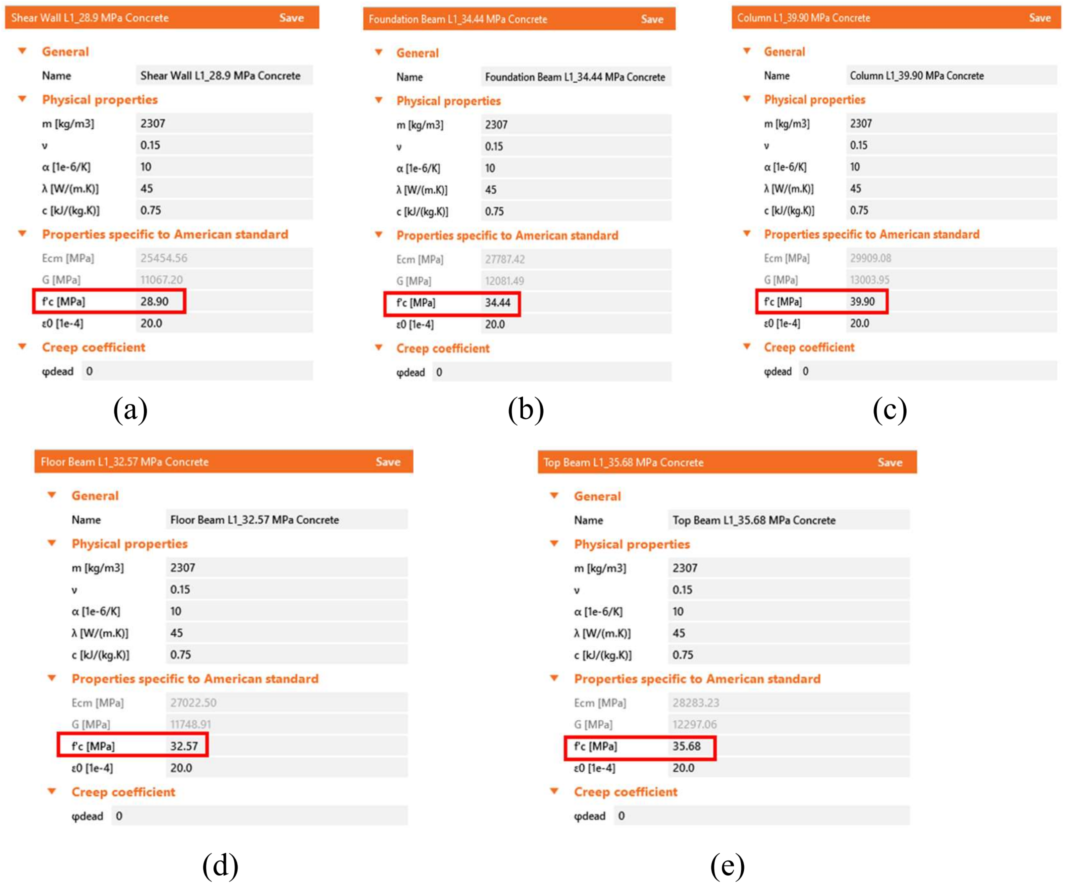

Figure 3.178: Strength properties of confined concrete in IDEA StatiCa for specimen L1.

3.6.4 Analysis of Shear Wall with Openings for Positive Loading Direction Considering Confined Concrete

CSFM results for all shear wall with openings under positive lateral loading are presented in the Table 3.10. The same procedure mentioned in Section 3.5.1 for the baseline model was used to analyze the shear wall with openings considering confined concrete. Materials properties are taken from the Tables 3.3 and 3.4 except the compressive strength of concrete. The strength properties discussed in Section 3.6.3 for compressive strength of concrete were utilized for the preparation of the models in CSFM analysis. Detailed results for specimen N1, S1, M1, and L1 from CSFM analysis are presented in Figures 3.19 through 3.22 respectively.

Table 3.10: CSFM results under positive lateral loading considering confinement effect of concrete

Shear wall specimen	Lateral load		Concrete			Steel		Displacement
	Measured, kN (kips)	CSFM, kN (kips)	Specified unconfined strength (*fc'*), MPa (ksi)	Maximum principal stress, MPa (ksi)	Location	Maximum stress in the rebars, MPa (ksi)	Location	Displacement in x direction, mm (in.)
N1	1179 (265)	964 (217)	25.90 (3.76)	23.88 (3.47)	At the bottom of the right support near the foundation beam	411 (59.62)	In the reinforcing bars within the left column inside the foundation beam.	25.00 (0.99)
S1	967 (217)	908 (204)	25.10 (3.65)	21.61 (3.14)	At the bottom left corner of the third story opening	425 (61.65)	In the vertical bars at the bottom right corner of the first story opening.	24.00 (0.95)
M1	889 (200)	820 (184)	21.70 (3.15)	21.61 (3.14)	At the bottom left corner of the third story opening	425 (61.65)	In the vertical rebars near the bottom right corner of the first story opening.	23.10 (0.91)
L1	686 (154)	756 (170)	28.90 (4.20)	36.13 (5.25)	At the bottom left corner of the third story opening	425 (61.65)	In the rebars located at the bottom right corner of the first story opening.	34.00 (1.34)

For specimen L1, compared to unconfined concrete, less stress was observed in the concrete walls of all stories due to lateral loading (Figures 3.5c and 3.19c). Similar to unconfined concrete, the CSFM analysis indicated high stresses in concrete near the top right corners of the openings in all stories, where cracks were generated during the experiment (Figures 3.4 and 3.19c). A large flexural shear crack was observed near the bottom right corner of the first story opening during the experiment, and high tensile stress of 425 MPa was also shown in this region by the CSFM analysis in the vertical rebars of the first-story wall (Figures 3.4 and 3.19d), indicating that the CSFM analysis accurately captured the experimental behavior of specimen L1. Based on the CSFM analysis using Mander et al.'s (1988) confined concrete model, specimen L1 is predicted to fail due to concrete crushing at the bottom left corner of the third story opening, with a stress of 36.13 MPa (5.24 ksi). Additionally, a flexural crack is likely to cause failure at the bottom right corner of the first story opening, with the reinforcing bars experiencing stress of 425 MPa (61.6 ksi).

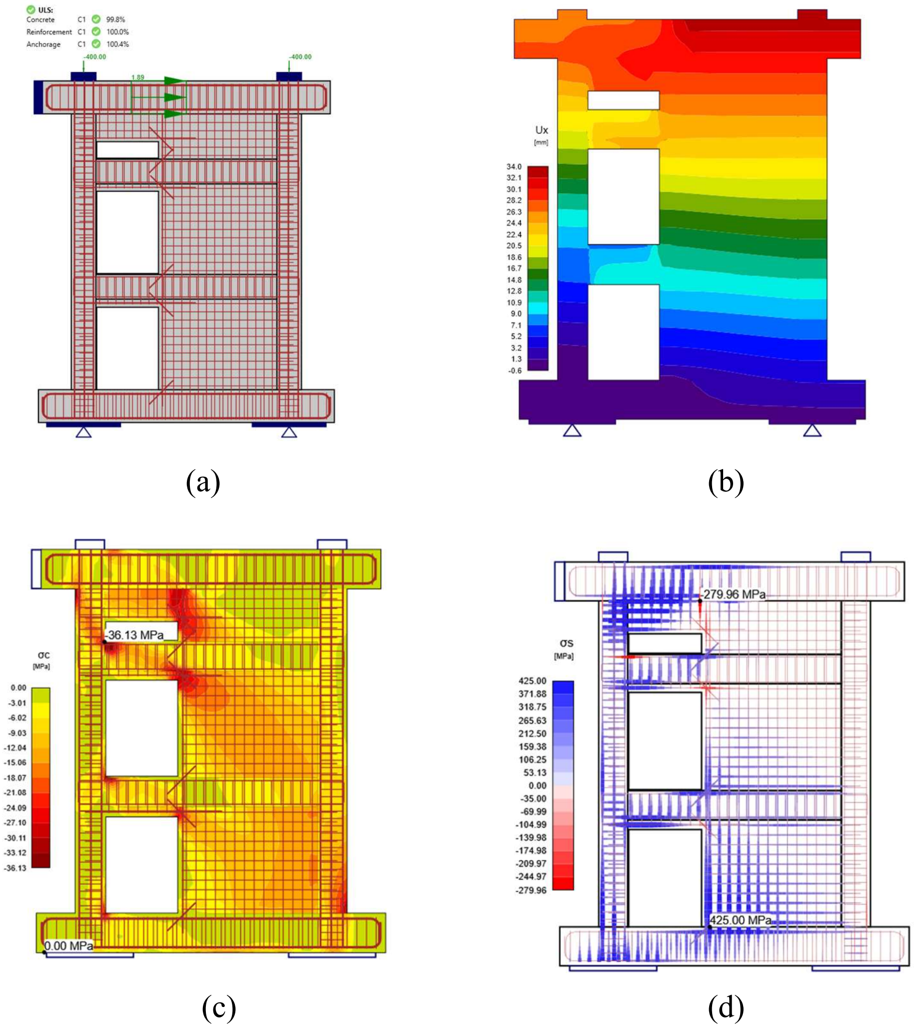

Figure 3.189: Shear wall with openings L1 at 1.89 kN/mm (10.8 kip/in.) lateral load: a) IDEA StatiCa model with results, b) deflection contour, c) concrete principal stresses (σ_c), and d) stresses in the reinforcing bars (σ_s).

For Specimen N1, high concentrations of principal stress were identified by the CSFM analysis in the concrete near the top left corner of the third-story wall, the bottom left corner of the first-story wall, and the bottom of the right column (Figure 3.20c). However, no cracks were observed in these regions during the experiment (Figure 3.4a). In contrast to unconfined concrete, low stresses were detected in the second-story wall by the CSFM analysis. Although the CSFM analysis partially captured the experimental behavior, some critical locations were missed where large cracks were observed, such as the top left corner of the first-story wall and the bottom left corner of the second-story wall (Figure 3.4a). For specimen N1, the CSFM analysis indicates that failure would occur due to concrete crushing at the bottom right corner of the right support at a stress of 23.88 MPa (ksi).

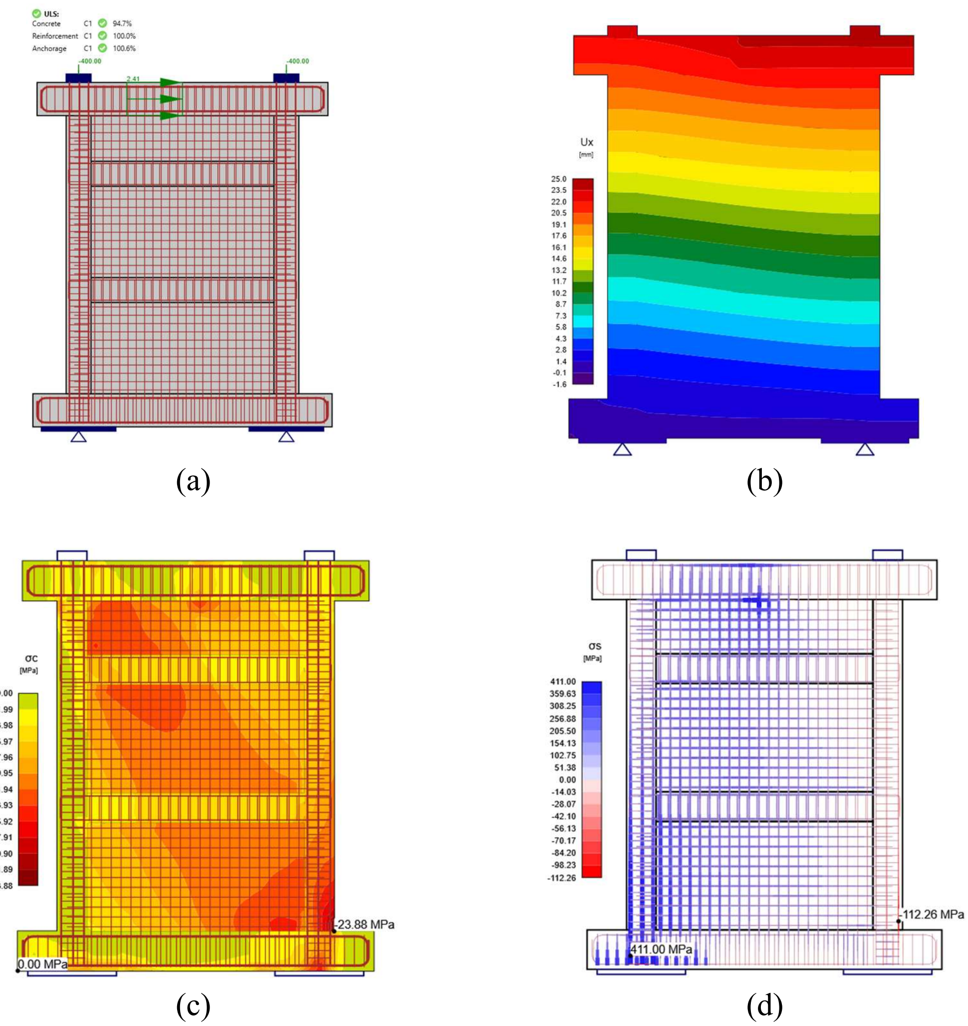

Figure 3.1920: Shear wall with openings N1 at 2.41 kN/mm (13.77 kip/in.) lateral load: a) IDEA StatiCa model with results, b) deflection contour, c) concrete principal stresses (σ_c), and d) stresses in the reinforcing bars (σ_s).

The maximum capacity for Specimen S1 was determined using IDEA StatiCa, considering confined concrete. The analysis showed that at an applied lateral load of 908 kN (204.13 kips), significant concentrations of principal stress appeared near the top right corner of all story openings and in the beam above the second story opening (Figure 3.21c), where shear cracks were observed during the experiment (Figure 3.4b). In the vertical bars near the first story opening, the maximum tensile stress of 425 MPa (61.65 ksi) was recorded (Figure 3.21d), and large flexural cracks were noted in this area during the experiment (Figure 3.4b), suggesting that IDEA StatiCa was able to reasonably capture the experimental behavior of Specimen S1. From the CSFM analysis, specimen S1 would fail due to flexural cracks at the bottom right corner of the first story opening, with the stress in the reinforcing bars reaching 425 MPa (61.6 ksi), or due to concrete crushing at the bottom left corner of the third story opening at 28.61 MPa (4.15 ksi).

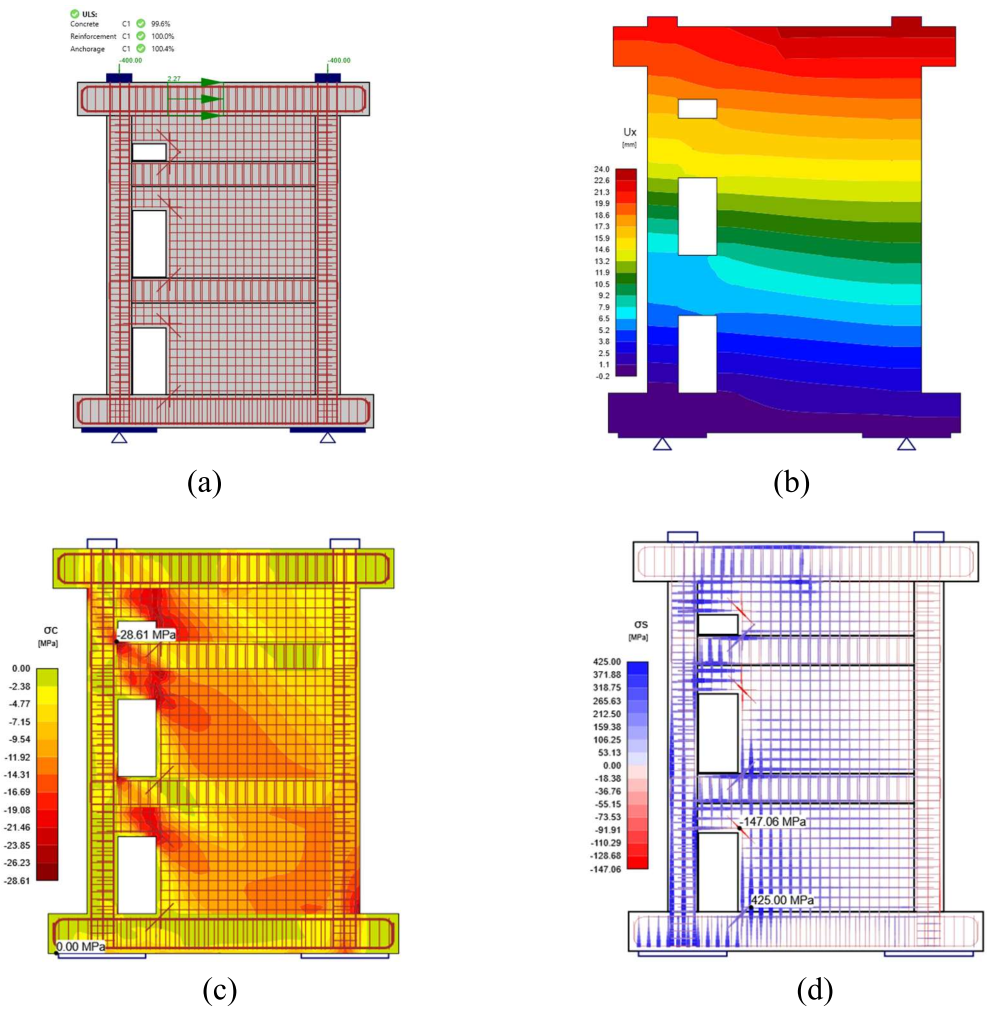

Figure 3.201: Shear wall with openings S1 at 2.27 kN/mm (12.97 kip/in.) lateral load: a) IDEA StatiCa model with results, b) deflection contour, c) concrete principal stresses (σ_c), and d) stresses in the reinforcing bars (σ_s).

For Specimen M1, the analysis using IDEA StatiCa for confined concrete revealed that at an applied lateral load of 820 kN (184.35 kips), significant compressive stresses were observed in the concrete near the top right corner of all story openings (Figure 3.22), similar to the unconfined concrete (Figure 3.8). Large flexural shear cracks were noted near the top right corner of the first and second story openings during the experiment (Figure 3.4c), where the CSFM analysis also showed high principal stresses in the concrete. Although the analysis indicated a principal stress of 21.61 MPa (3.14 ksi) in the concrete on the third-story wall and the left column near the opening, suggesting a probable failure mode according to the CSFM analysis, no cracks or damage were observed in these areas during the experiment (Figure 3.4c).

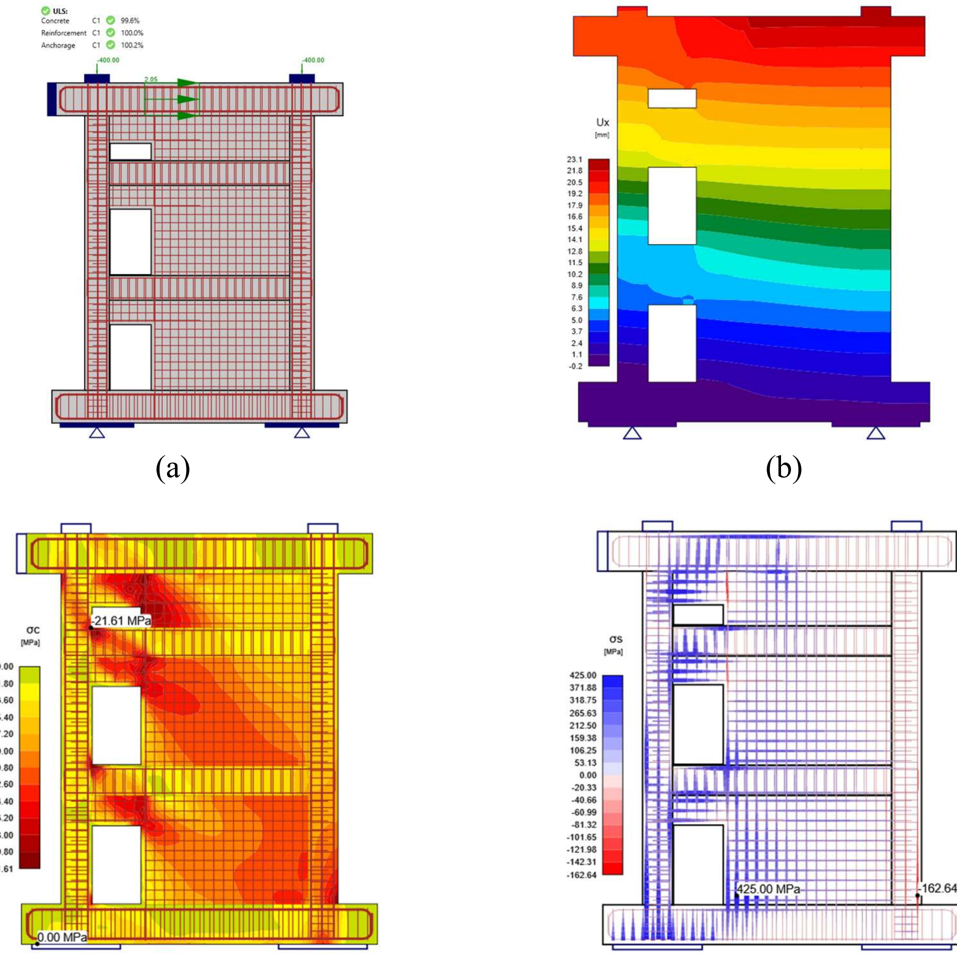

(a) (b)

(c) (d)

Figure 3.212: Shear wall with openings M1 at 2.05 kN/mm (11.71 kip/in.) lateral load: a) IDEA StatiCa model with results, b) deflection contour, c) concrete principal stresses (σ_c), and d) stresses in the reinforcing bars (σ_s).

3.6.5 Analysis of Shear Wall with Openings for Negative Loading Direction Considering Confined Concrete

CSFM results for shear walls with openings subjected to negative lateral loading are summarized in Table 3.11. The same methodology outlined in Section 3.5.1 for the baseline model was applied to analyze these shear walls with openings under confined concrete conditions. Material properties were taken from Tables 3.3 and 3.4, with the exception of the concrete compressive strength. The compressive strength values discussed in Section 3.6.3 were used to develop the models for the analysis. Detailed results for specimens N1, S1, M1, and L1 from the CSFM analysis are illustrated in Figures 3.23 through 3.26.

Table 3.11: Results under negative lateral loading considering confinement effect of concrete

Shear wall specimen	Lateral load		Concrete			Steel		Displacement
	Measured, kN (kips)	CSFM, kN (kips)	Specified unconfined strength (*fc'*), MPa (ksi)	Maximum principal stress, MPa (ksi)	Location	Maximum stress in the rebars, MPa (ksi)	Location	Displacement in x direction, mm (in.)
N1	1039 (234)	968 (218)	25.90 (3.76)	23.99 (3.48)	At the bottom left corner of the left column near the foundation beam	419 (60.74)	In the vertical bars used in the third story wall near the top loading beam.	25.30 (1.00)
S1	838 (188)	952 (214)	25.10 (3.65)	33.69 (4.89)	At the bottom left corner of the left column near the foundation beam	425 (61.65)	In the vertical bars in the wall at the top of the third story near the loading beam.	29.10 (1.15)
M1	723 (163)	932 (210)	21.70 (3.15)	31.43 (4.56)	At the bottom left joint of the left column and foundation beam	425 (61.65)	In the horizontal bars above the second story opening.	30.70 (1.21)
L1	649 (146)	832 (187)	28.90 (4.20)	36.10 (5.24)	At the bottom left corner of the left column near the foundation beam	425 (61.65)	In the vertical bars at the bottom right corner of the first story opening.	25.20 (1.00)

For specimen L1, under a lateral load of 832 kN (187 kips), high concentrations of compressive stress were observed in the concrete near the bottom right corner of the openings on all stories (Figure 3.23c), similar to the observations for unconfined concrete (Figure 3.9c). Spalling of concrete was also noted in these locations during the experiment (Figure 3.4d). High tensile stresses were observed near the top right corners of the first and second-story openings (Figure 3.23d), and flexural shear cracks were seen in these locations after the experiment (Figure 3.4d), demonstrating that IDEA StatiCa accurately captures the real behavior. Although the CSFM analysis indicated a significant principal stress of 36.1 MPa (5.24 ksi) in the concrete at the bottom of the left column (Figure 3.4d), highlighting a probable failure mode due to concrete crushing, no signs of failure were observed at this location for specimen L1. This suggests that while the CSFM analysis provides valuable insights, further refinement may enhance its accuracy in estimating principal stress in this region.

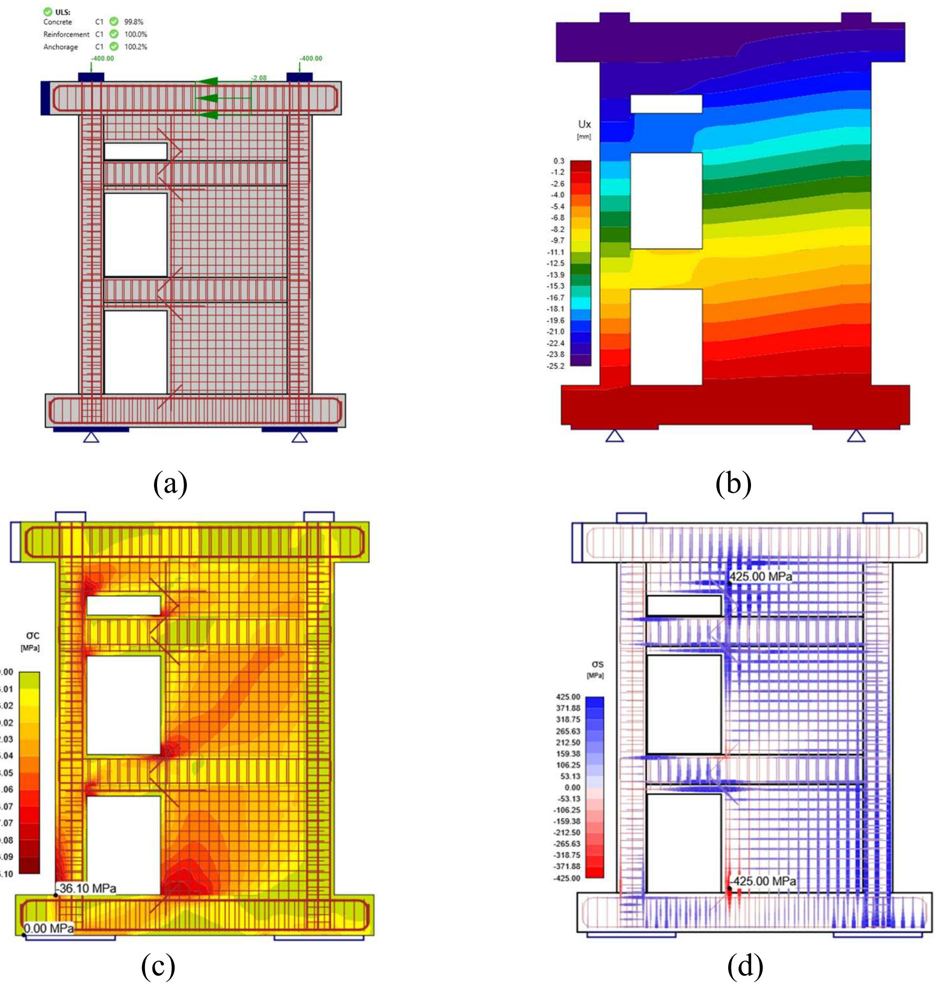

Figure 3.223: Shear wall with openings L1 at 2.08 kN/mm (11.88 kip/in.) lateral load: a) IDEA StatiCa model with results, b) deflection contour, c) concrete principal stresses (σ_c), and d) stresses in the reinforcing bars (σ_s).

For specimen N1, under a negative lateral load of 968 kN (217.62 kips), the maximum principal stress of 23.99 MPa (3.48 ksi) in the concrete was observed at the same location as in the unconfined concrete (Figure 3.24c and Figure 3.10), indicating a probable failure pattern due to concrete crushing at the bottom left corner of the left support, as suggested by the CSFM analysis. The CSFM analysis indicated heavy concentrations of principal stresses near the bottom left corner of the first-story wall and the top right corner of the third-story wall. However, no damage or significant cracks were observed in these locations during the experiment (Figure 3.4a). Failure in the experiment may have initiated from the bottom corners of the second-story wall, where the CSFM analysis showed lower stresses in the concrete and steel, suggesting that it may have missed accurately capturing the behavior of specimen N1 in these areas.

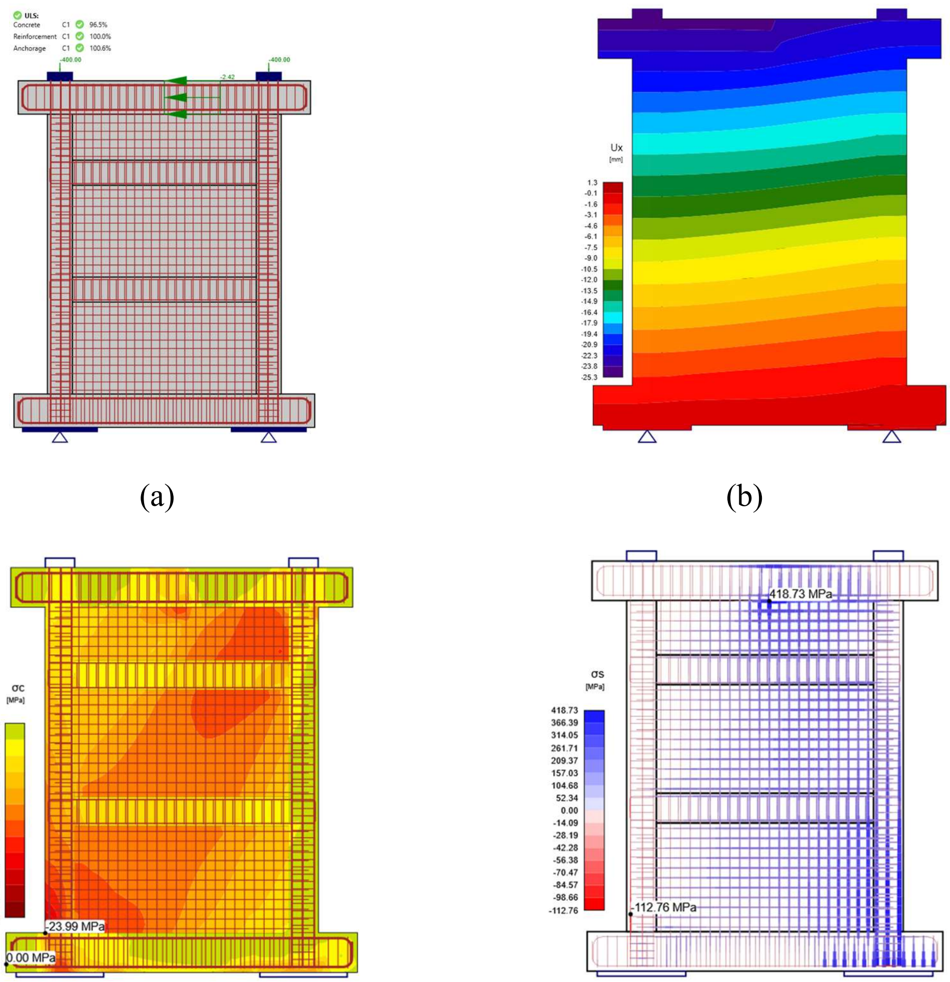

(a) (b)

(c) (d)

Figure 3.234: Shear wall with openings N1 at 2.42 kN/mm (13.82 kip/in.) lateral load: a) IDEA StatiCa model with results, b) deflection contour, c) concrete principal stresses (σ_c), and d) stresses in the reinforcing bars (σ_s).

For specimen S1, under an applied lateral load of 952 kN (214 kips), high compressive stresses were observed in the concrete near the bottom right corner of the openings on all stories, similar to unconfined concrete (Figures 3.11c and 3.25d). During the experiment, cracks were observed in the walls above the first and second-story openings, where the CSFM analysis also indicated higher principal stresses in the concrete (Figures 3.11c and 3.25d). A high tensile stress of 425 MPa (61.65 ksi) was recorded in the vertical rebars at the top of the third-story walls (Figure 3.25d), where flexural cracks were observed during the experiment, indicating that the analysis accurately captured the behavior in this region. Although shear cracks were observed in the beams of the first and second stories (Figure 3.4b), the CSFM analysis showed lower stresses in the beam (Figure 3.25c).

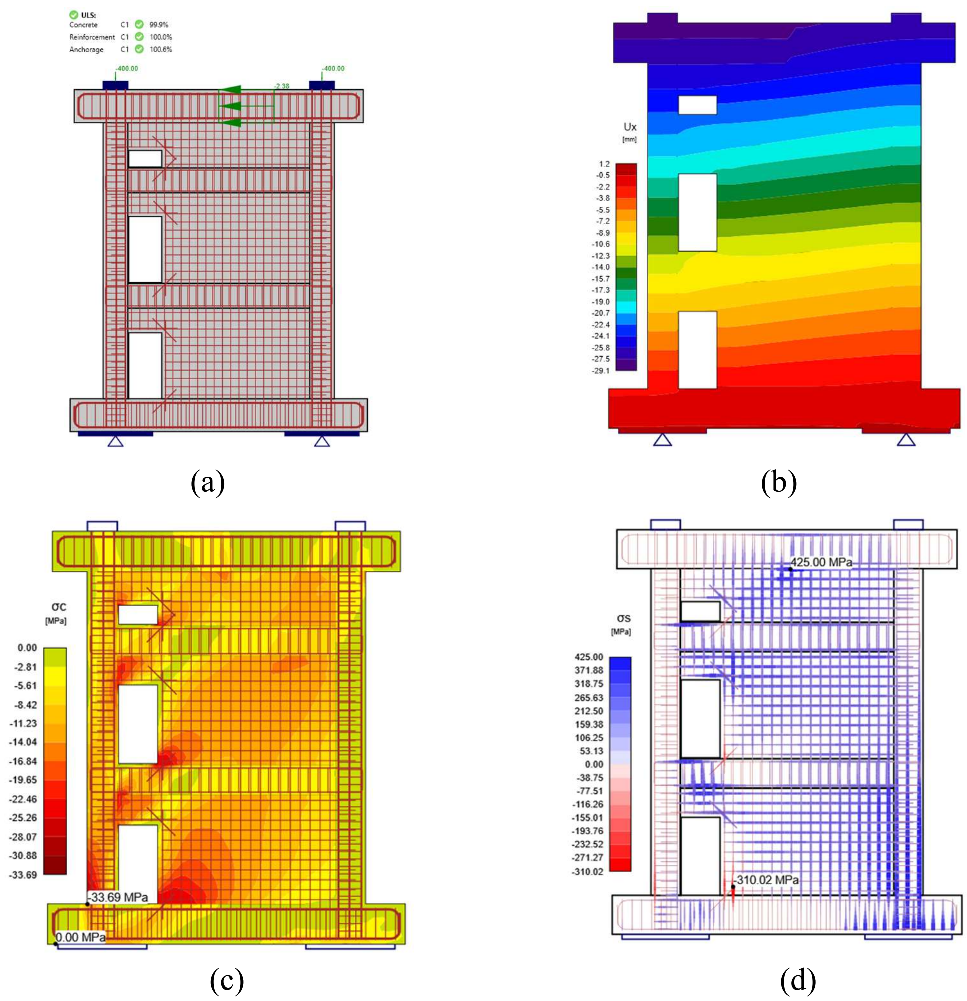

Figure 3.245: Shear wall with openings S1 at 2.38 kN/mm (13.6 kip/in.) lateral load: a) IDEA StatiCa model with results, b) deflection contour, c) concrete principal stresses (σ_c), and d) stresses in the reinforcing bars (σ_s).

For specimen M1, high concentrations of principal stress, reaching 31.43 MPa (4.56 ksi), were indicated by the CSFM analysis at the bottom left joint between the left column and the foundation beam (Figure 3.26c), suggesting a potential failure scenario due to concrete crushing, as predicted by the CSFM analysis. The highest stress in the reinforcing bars was also recorded at 425 MPa (61.65 ksi) in the horizontal bars above the second story opening (Figure 3.26d). Flexural shear cracks were observed during the experiment near the top right corner of the first and second-story openings, as well as the top right corner of the first-story wall (Figure 3.4c). While the CSFM analysis accurately captured much of the experimental behavior of specimen M1, it did not show the stress concentrations in the concrete and steel at the top right corner of the first story opening for confined concrete, where a large crack was visible in the damage plot (Figures 3.26 and 3.4).

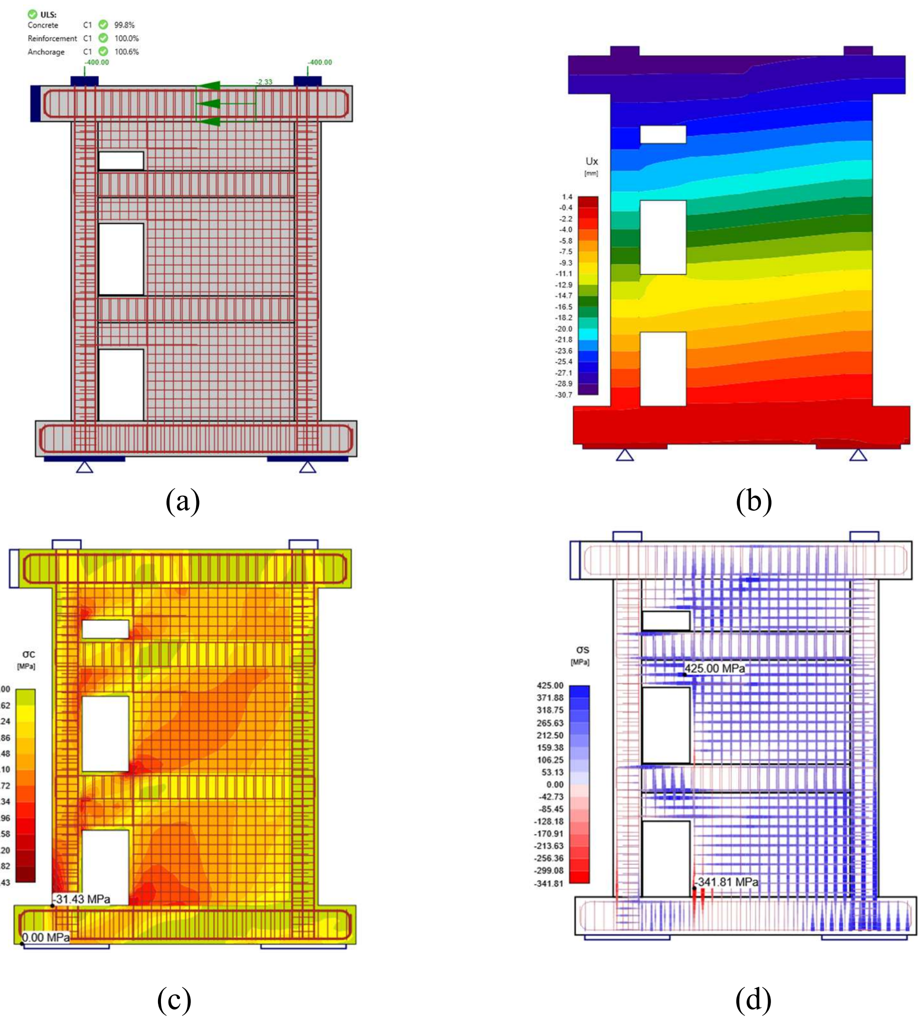

Figure 3.256: Shear wall with openings M1 at 2.33 kN/mm (13.31 kip/in.) lateral load: a) IDEA StatiCa model with results, b) deflection contour, c) concrete principal stresses (σ_c), and d) stresses in the reinforcing bars (σ_s).

3.7 Capacity Calculation Using Strut and Tie Model

The capacities for all shear walls with openings were determined following the provisions for the Strut and Tie Model (STM) as outlined in the American Concrete Institute (ACI 318-19) code, specifically described in Section 2.2. Depending on the location of nodal zones and struts in the, strut and node confinement modification factor (β_c), strut coefficient (β_s), and nodal zone coefficient (β_n) were taken from Tables 2.1 through 2.3 in Chapter 2, respectively. The effective compressive strength of concrete (f_{ce}) in a strut and nodal zone were calculated using Equations 2.4 and 2.9, respectively.

Multiple strut and tie models were developed to identify the best model that would yield the maximum lateral load capacity and location of failure as accurately as possible. To construct the truss models (or STM with struts as compressive truss members and ties as tensile truss members), stress flow diagrams and topology optimization plots from IDEA StatiCa analysis were utilized for all shear wall specimens. The effective volume was 20% in the topology optimization plots generated by IDEA StatiCa.

Developing a truss model or STM involves creating a simplified representation of complex structural behavior using principles of force equilibrium and stress distribution. The specific approach to designing the truss model can vary significantly, depending on the judgement, preferences and expertise of the structural engineers involved. Engineers select from a variety of methods to construct the truss model, with the goal of accurately depicting how stresses and forces are transmitted and distributed within the structure. This process aims to ensure that the truss model effectively represents the overall physical behavior and structural integrity, and it is consistent with the load-bearing requirements of the design.

Navigating the requirements outlined in codes and standards, such as those in the ACI 318-19 (particularly in Chapter 23), presents several challenges in developing a truss model or STM. These standards specify critical factors including member sizing, connectivity, and load paths to ensure structural integrity and safety under varying load conditions. Specific requirements include ensuring all nodes are in equilibrium, balancing vertical and horizontal forces on inclined struts at nodal zones, and preventing struts and ties from intersecting. Additionally, struts must maintain a minimum inclination angle of 25 degrees, and both struts and nodal zones must be adequately sized to withstand applied loads. The dimensions of struts and nodal zones are determined based on effective concrete strengths defined in Sections 2.3 and 2.4 of the Chapter 2.

Based on the topology optimization plot and stress flow diagrams determined from the IDEA StatiCa analysis for shear wall specimen N1, several truss models were developed. Then, these trusses were analyzed using SAP2000 software (2024). This process focused on two main objectives: (a) identifying critical struts, ties, and nodal zones (using stress flow plots from IDEA StatiCa analysis), and (b) assessing the load-bearing capacity of each model (using truss member and reaction forces from SAP2000 analysis). After multiple iterations, the results from the final STM were reported and compared with the measured test data.

This final model for specimen N1 highlights that the capacity of the shear wall can be significantly influenced by the design of the truss model. There are numerous ways to develop the STM, and the capacity can vary greatly depending on the placement of struts and ties, the configuration of nodal zones, and the angle of the struts. Each of these factors plays a crucial role in determining the overall performance and lateral capacity of the shear wall structure. Figure 3.29 presents the results for the STM of specimen N1, including the stress flow diagram (Figure 3.29a), the STM showing force distributions from SAP2000 (Figure 3.29b), and axial forces in members of STM calculated using SAP2000 (Figure 3.29c). The capacity for specimen N1 was found to be 252 kN (56.7 kips) from the STM analysis, which corresponds to an axial force of 362.32 kN (81.47 kips) in the diagonal strut located in the second-story wall. As indicated by the red cross in Figure 3.29b, this was the first element to experience failure. A high concentration of stress in the concrete was revealed by the CSFM analysis in this region, suggesting that the STM and CSFM analyses produced similar behavior.

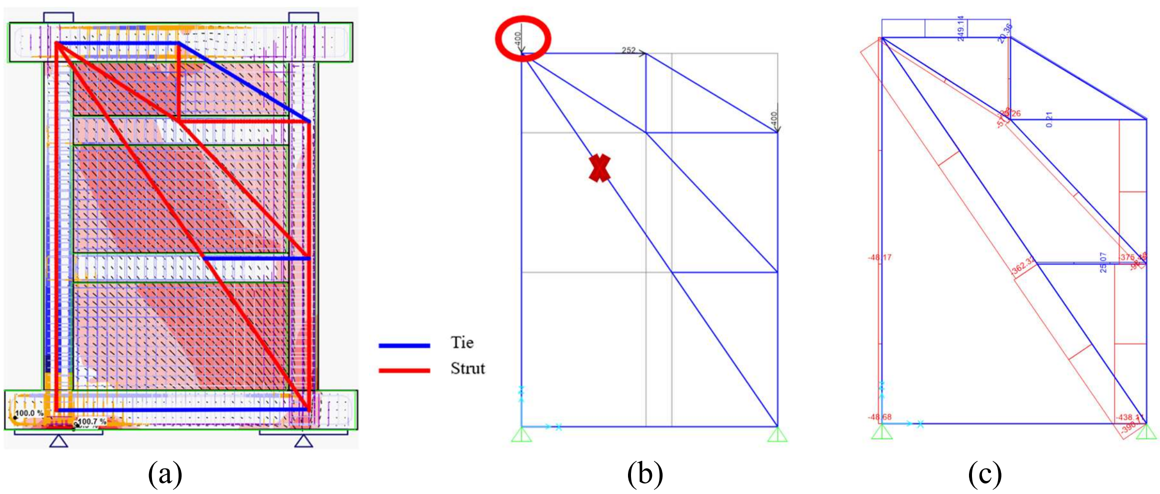

Figure 3.269: Strut and tie model for specimen N1: a) STM with stress flow, b) STM in SAP2000, and c) axial forces in STM members calculated in SAP2000.

Based on the stress flow diagram obtained from the CSFM analysis for specimen N1 (Figure 3.29a), an alternative simplified strut-and-tie model was developed to calculate its capacity, applying the lateral load at the joint between the left column and the top loading beam (Figure 3.30). The STM analysis determined the lateral load capacity of specimen N1 to be 492 kN (110.6 kips) from the new strut-and-tie model, representing a 95% increase from the previous capacity of 252 kN (56.7 kips) presented in Figure 3.29b. At the maximum lateral load, the diagonal strut BC failed under an axial load of 881 kN (198.1 kips), as indicated by the red cross in Figure 3.30. It is important to note that, during the experiment, the lateral load was applied at the center of the top loading beam. To align with the experimental setup, the final capacity for specimen N1 was taken as 252 kN (56.7 kips) from the STM analysis, as shown in Figure 3.29. The same procedure was followed in developing the STM for all other shear wall specimens, with the lateral load applied at the center of the top loading beam, consistent with the experimental conditions.

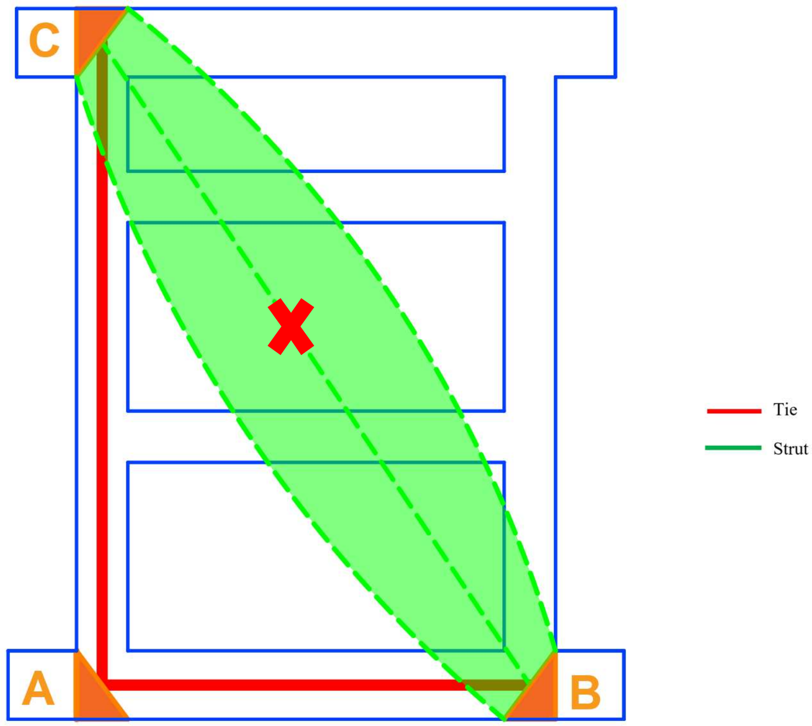

Figure 3.30: Simplified strut and tie model for specimen N1.

For specimen S1, the capacity was calculated as 174 kN (39.12 kips) from SAP2000 analysis of the STM shown in Figure 3.31(c). This corresponds to an axial force of 106.98 kN (24.03 kips) in the diagonal strut above the second story opening, which failed first and has a red cross on it in Figure 3.31(c). Figure 3.30 displays the results for the STM of specimen S1. It includes the topology optimization plot (Figure 3.31a), the Strut and Tie Model (STM) with a stress flow diagram (Figure 3.31b), the STM model showing force distributions from SAP2000 (Figure 3.31c), and the STM model illustrating axial forces from SAP2000 (Figure 3.31d). During the analysis, it was observed that two inclined struts in the second story, as shown in Figure 3.31(c), were particularly vulnerable and led to the final failure. The damage plot of specimen S1 (Figure 3.4b) reveals large shear cracks at the location where the inclined strut failed. The inclined strut showed signs of failure under the maximum load, indicating that it was unable to effectively transfer the applied forces within the structure. This failure mode suggests that the strut's angle or material properties might need to be adjusted or improved to better transfer the load.

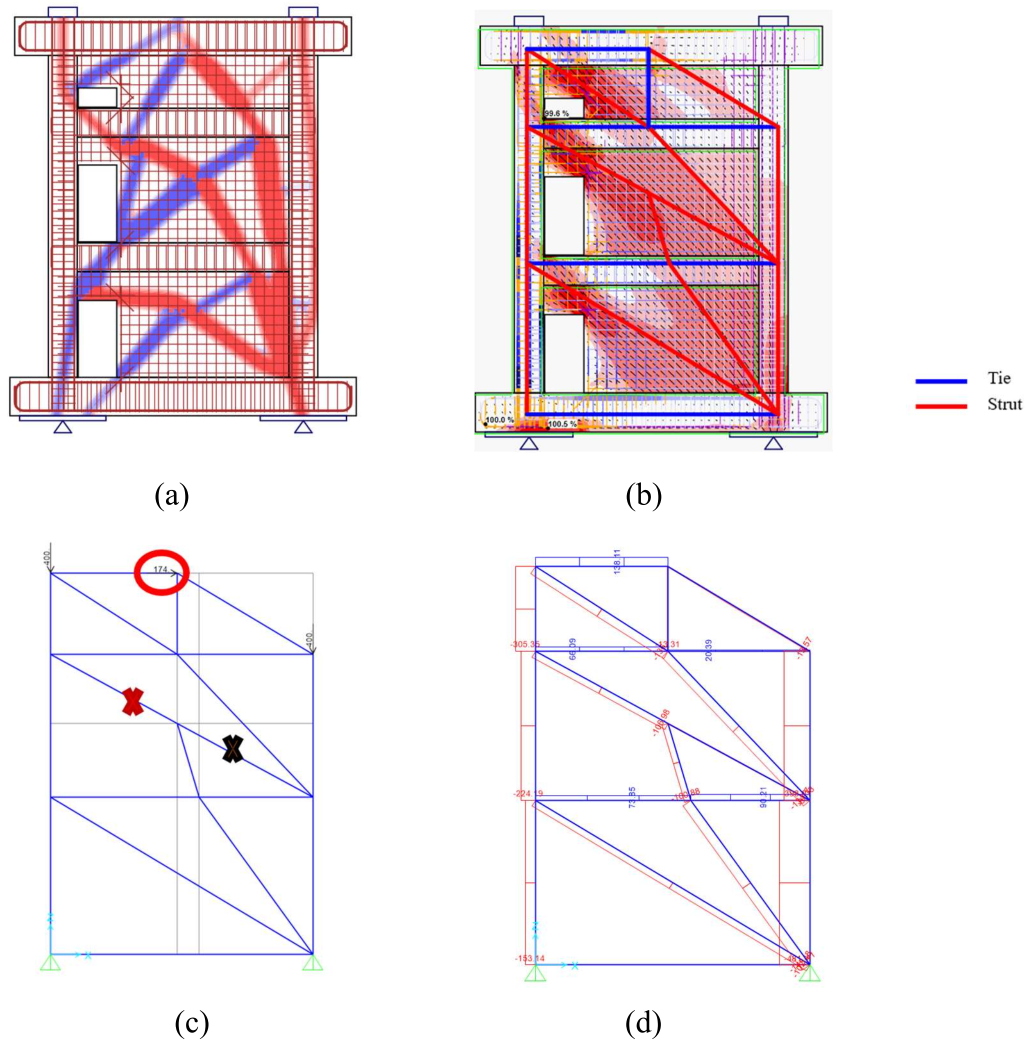

Figure 3.31: Strut and tie model for specimen S1: a) topology optimization from IDEA StatiCa, b) strut and tie model with stress flow, c) STM in SAP2000, and d) STM with calculated axial forces in SAP2000.

For specimen M1, the capacity was calculated to be 129 kN (29.01 kips), which is a reduction from the capacities observed in the previous two shear wall specimens. This decrease in capacity is primarily due to the increased size of openings in the shear wall.

During the analysis, it was observed that one of the critical nodes (a CCC or compression-compression-compression node) failed under the maximum load, as shown in Figure 3.32(c). Figure 3.32 shows the results for the STM model of specimen M1. It features the topology optimization plot (Figure 3.32a), the STM with a stress flow diagram (Figure 3.32b), the STM model illustrating force distributions from SAP2000 (Figure 3.32c), and the STM model depicting axial forces from SAP2000 (Figure 3.32d). Large shear cracks were also observed at this location in specimen M1 during the experiment (Figure 3.4c), consistent with the location of this node that failed in the STM analysis. This scenario underscores the challenge of designing efficient STM or truss models when openings are present, as the placement and angle of struts must be carefully considered to maintain load transfer and overall load-bearing capacity of the shear wall.

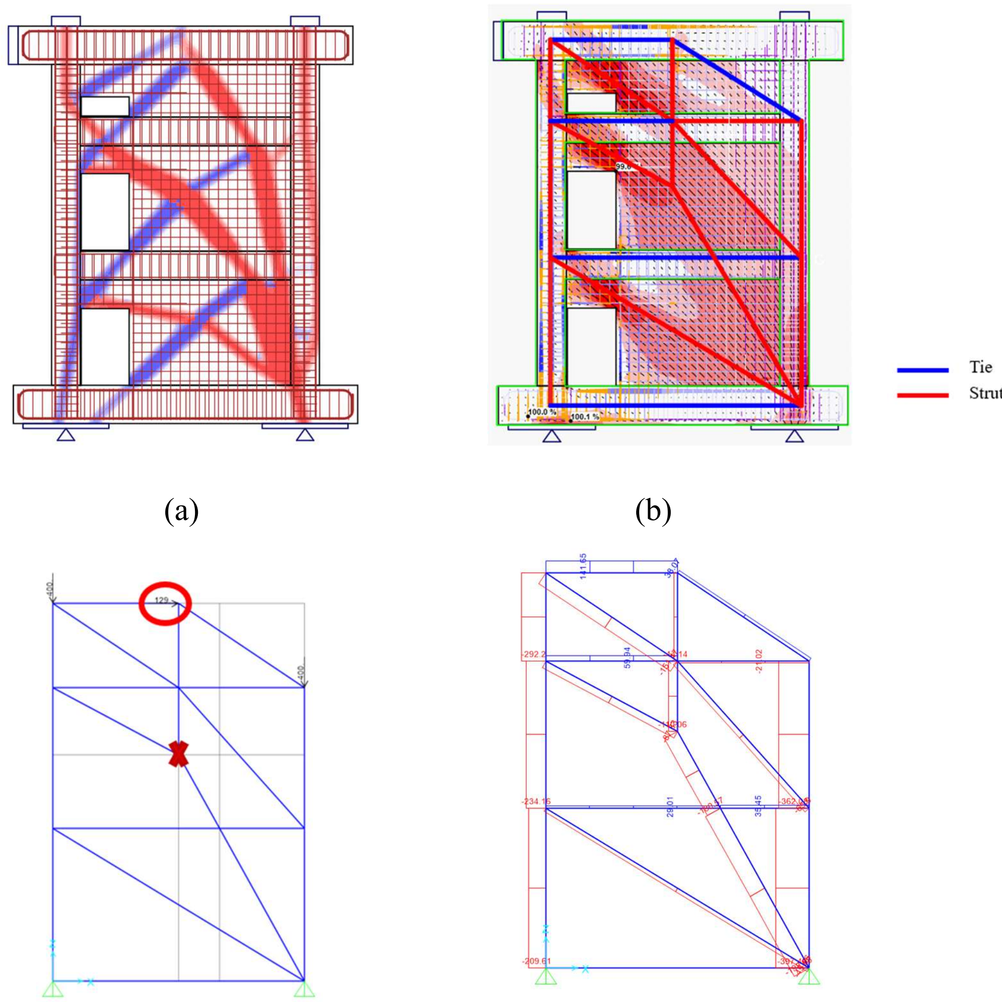

Figure 3.272: Strut and tie model for specimen M1: a) topology optimization from IDEA StatiCa, b) strut and tie model with stress flow, c) STM in SAP2000, and d) STM with calculated axial forces in SAP2000.

Figure 3.33 presents the results for the STM model of specimen L1, which has the largest opening size among all the shear wall specimens, including N1, M1, S1, and L1. For specimen L1, the capacity was calculated to be 101 kN (22.71 kips). At this lateral load, an inclined strut in the wall above the second story opening failed first, experiencing an axial force of 115 kN (25.83 kips), as indicated by the red cross in Figure 3.33c. A large flexural crack also observed in this region during the experiments (Figure 3.4d). The increased size of the opening posed significant challenges for the placement of struts and nodes. Due to the large openings, some struts had to be positioned at the minimum allowable inclined angles (minimum 25 degrees per ACI 318-19), which constrained their optimal placement of struts in the STM and negatively impacted the overall structural performance. Despite the careful arrangement of the STM, the capacity was slightly lower compared to that of specimen M1 (129 kN or 29.01 kips), resulting in the lowest capacity (101 kN or 22.71 kips) among all shear walls with openings.

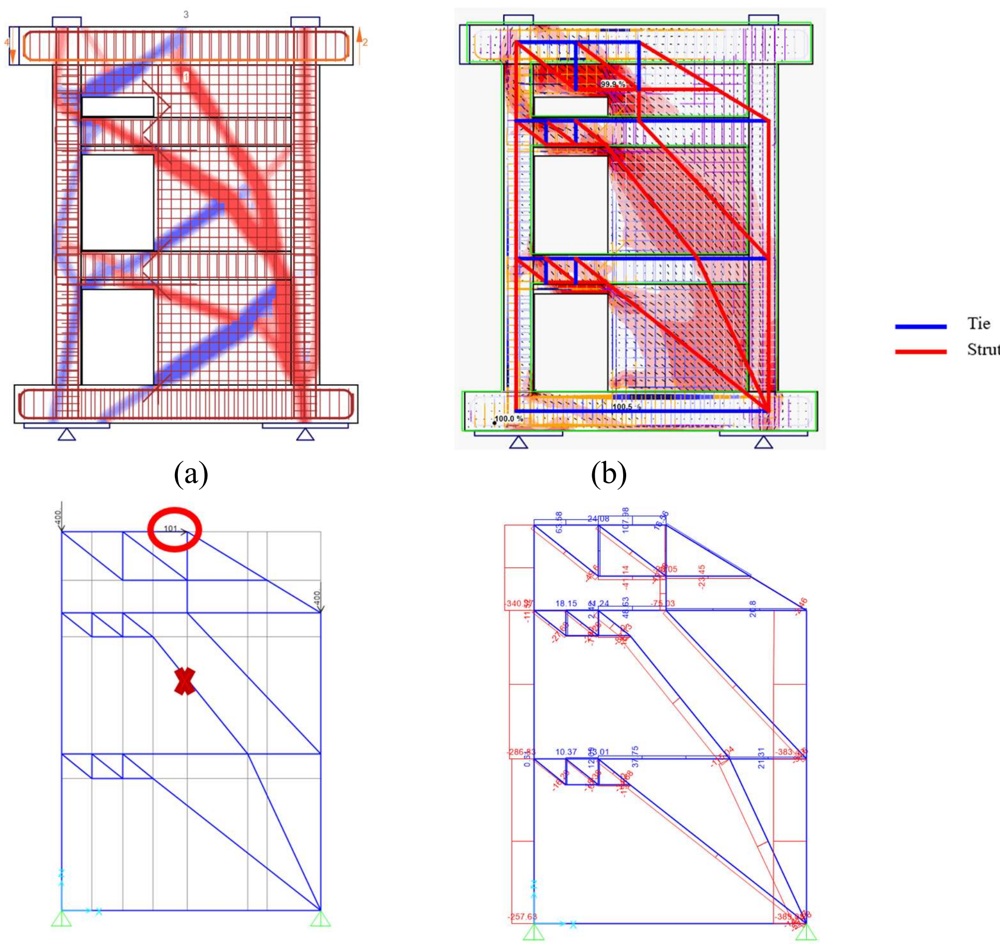

(a) (b)

(c) (d)

Figure 3.283: Strut and tie model 4 for specimen L1: a) topology optimization from IDEA StatiCa, b) strut and tie model with stress flow, c) STM in SAP2000, and d) STM with calculated axial forces in SAP2000.

The failure mode of specimen L1 shows that, in shear walls with large openings, the structural integrity is greatly affected by the size and position of the openings.

3.8 ABAQUS Model Development and Analysis

In this section, the specimen L1, which was modeled and analyzed in Section 3.5.1, was remodeled using ABAQUS software (2023) for finite element (FE) analysis. The results were then compared with those obtained from IDEA StatiCa. Due to the complexity of the structure, the CAD model, including concrete and reinforcement bars, was drawn in Rhino software (McNeel, 2020) and then exported to ABAQUS as a STEP file. The version of Rhino used will be included in the References. Similar to the IDEA StatiCa model, in ABAQUS, in addition to the self-weight (i.e., Load 1), two vertical loads (i.e., Loads 2 and 3), each 400 kN, were applied to two load-bearing plates with a thickness of 4 in., as shown in Figure 3.34. Since the line load can only be used for beam elements in ABAQUS, to mimic the lateral load imposed on the structure in the experimental test and IDEA StatiCa, a horizontal force (i.e., Load 4) was applied to a defined reference point (i.e., RF2) that was coupled to the edges of the top beam to resemble the line load.

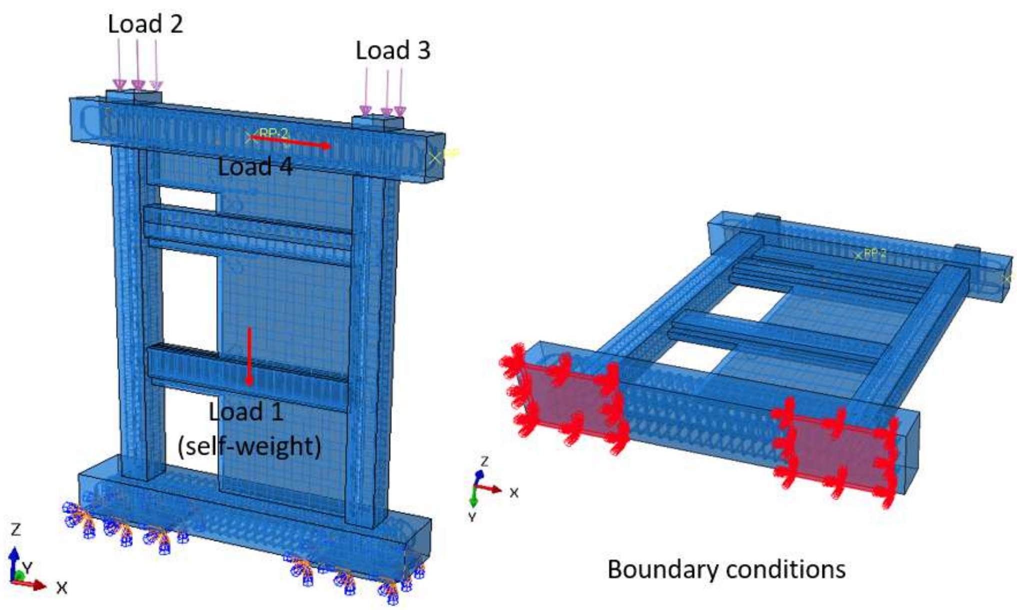

Figure 3.294: Model setup in ABAQUS showing the locations and details of the applied load and boundary conditions.

Two support plates under the structure were fixed to restrain vertical and lateral displacement (see Figure 3.34). To accurately capture the crack initiation and evolution, the element size was chosen to be 20 mm, resulting in a total of 396,505 elements in the model (see Figure 3.35). The 3D stress, 8-node linear brick reduced integration (i.e., C3D8R) element type was selected for the concrete, while the truss element was chosen for the reinforcing bars.

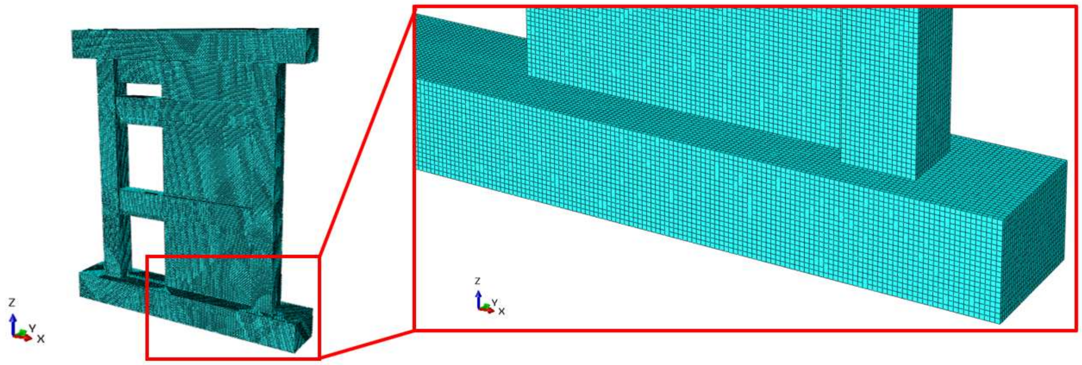

Figure 3.305: Mesh density with element size of 20 mm.

The embedded region constraint was imposed to incorporate the steel reinforcement within the specimen L1 (see Figure 3.36). Additionally, a general surface-to-surface contact was defined between the load and support bearing plates and the concrete part. In ABAQUS, the Concrete Damage Plasticity (CDP) constitutive model was used. The required parameters to describe this model were obtained after calibration from various sources (Federal Highway Administration, 2006, and Watanabe et al., 2004) as they were not explicitly indicated in Taleb et al. (2012). For the steel bars, the material behavior was modeled using bi-linear plasticity. Other parameters, including density, elastic modulus, and Poisson's ratio, were taken exactly from the IDEA StatiCa materials library. The numerical simulation was carried out on a virtual machine with 16 processors (Intel Xeon® Gold Processor 6430 @2.10GHz) and took approximately 185 minutes to finish, while IDEA StatiCa completed the calculation in less than two minutes.

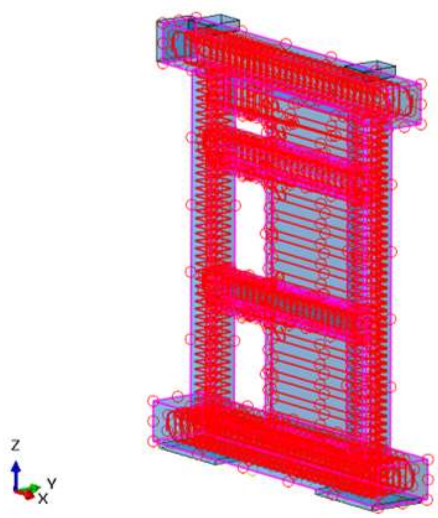

Figure 3.316: Embedded region constraint between the reinforcement bars (depicted in red) and concrete (shown in pink).

The comparison between the crack patterns observed in the experimental test and those calculated using the ABAQUS model is shown in Figure 3.37. In the experimental test, the main crack appeared at the bottom portion of the structure when the lateral load reached 686 kN (154.22 kips) (see Figure 3.37a). Similarly, the ABAQUS model captured the crack initiation at the same location when the lateral force (i.e., Load 4 in Figure 3.34) was approximately 550 kN (123.65 kips) (see Figure 3.37b). The numerical results indicate that the structure initially experienced flexural cracking, which then transitioned to shear cracking.

It is worth noting that the calculated capacity from IDEA StatiCa for specimen L1 was 728 kN (163.67 kips), which is 32% and 6% higher than the capacities predicted by the ABAQUS model and observed in the experimental test, respectively. Figure 3.37c illustrates the schematic of the crack patterns at the end of the experimental test. The predicted crack patterns at the end of the ABAQUS simulation are shown in Figure 3.37d and exhibit good agreement with the experimental results. The minor discrepancies are primarily attributed to the method of load application in the ABAQUS model. To further visualize the failure of the structure, the applied load in the ABAQUS model was increased, and the resulting failure pattern is shown in Figure 3.37e.

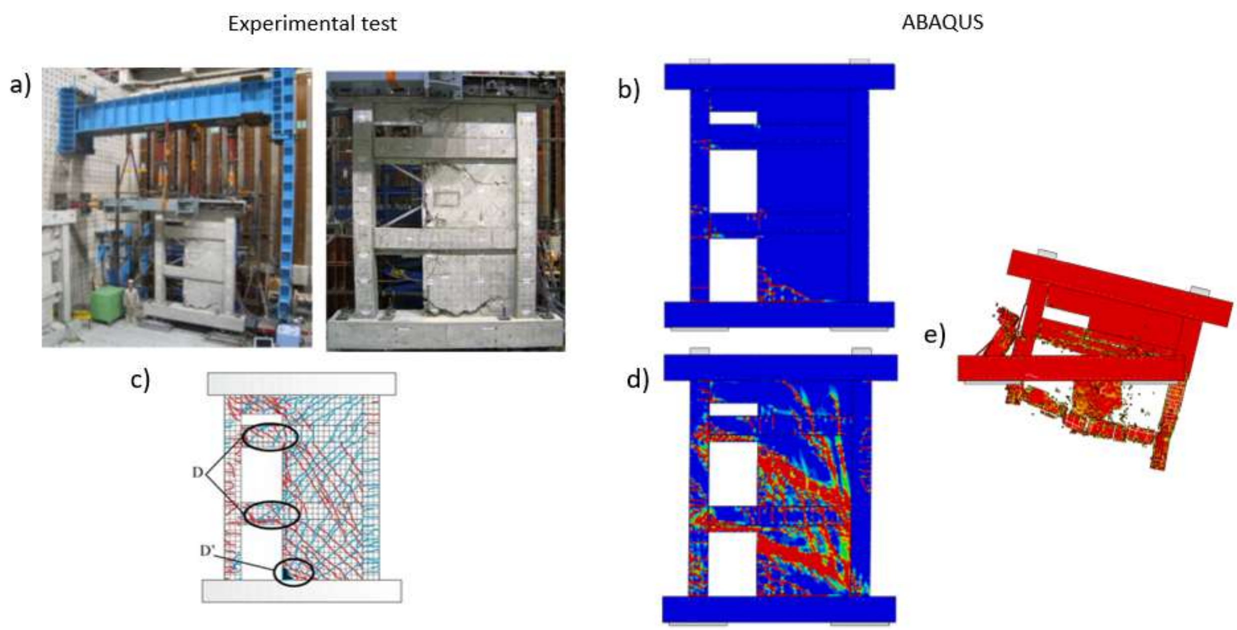

Figure 3.327: a) Crack initiation from the experimental test at maximum load, b) predicted initial cracks by ABAQUS, c) schematic of the crack patterns after the experimental test was completed, d) predicted crack patterns at the end of the simulation, and e) predicted failure pattern by ABAQUS.

Figure 3.38 illustrates the comparison of horizontal displacements predicted by IDEA StatiCa and ABAQUS. The difference between the predicted results is only 3.5%, which is likely attributed to the imposed boundary conditions in the 2D (i.e., IDEA StatiCa) and 3D (i.e., ABAQUS) models.

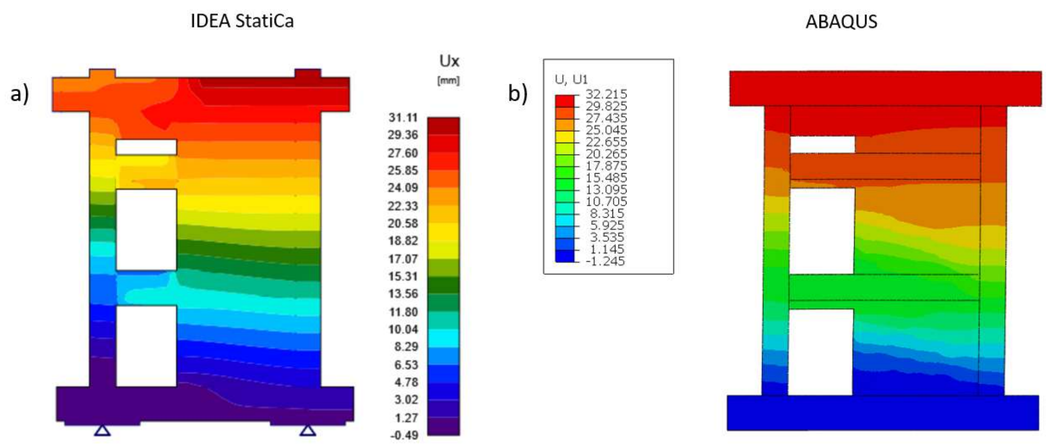

Figure 3.338: Comparison of the horizontal displacement between a) IDEA StatiCa model, and b) ABAQUS model.

The calculated and predicted directions of principal stresses from IDEA StatiCa and ABAQUS, respectively, are shown in Figure 3.39. While the IDEA StatiCa results suggest that more stress could accumulate at the openings, the ABAQUS model predicts that stress concentration will occur at the intersection of the column and the bottom beam. Note that, due to the discontinuities at the crack regions, the directions of the principal stresses are slightly different in ABAQUS compared to the IDEA StatiCa model in which the actual crack cannot be tracked. Additionally, it appears that deformation and stresses are more distributed in ABAQUS, whereas IDEA StatiCa results show more concentrated stresses. The discrepancies in the results are most likely associated with the way boundary conditions and loads were applied in each software, as well as the neglect of tensile strength and the tension stiffening effect embedded in the Compatible Stress Field Method (CSFM) used in IDEA StatiCa. Comparison of calculated principle stresses and their directions shown in Figure 3.39 indicates that the overall response of the specimen is similar and the calculated response can be used to establish a more realistic strut and tie model including some inclined struts and compression nodal zones near the bottom right corner and top left corner of specimen L1 (Figure 3.33).

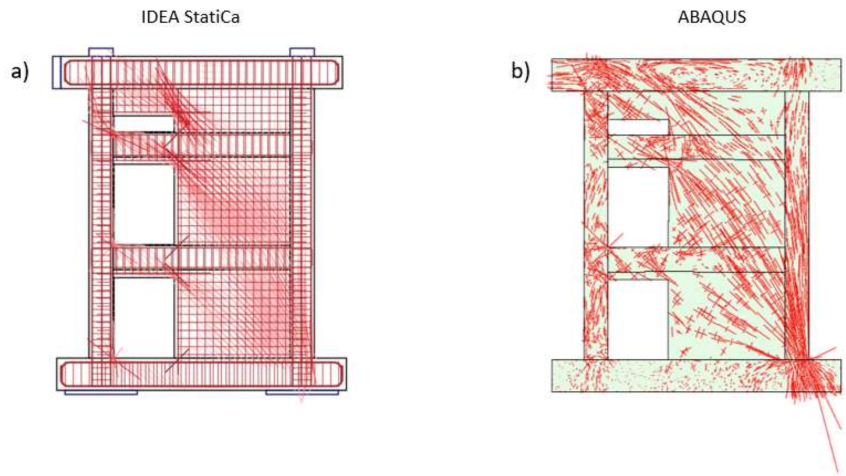

Figure 3.349: Comparison of the direction of principal stresses between IDEA StatiCa and ABAQUS.

Figure 3.40 illustrates the comparison between the calculated principal stresses in concrete using IDEA StatiCa and those predicted by the ABAQUS model. In IDEA StatiCa, the minimum predicted stress was -28.8 MPa (-4.18 ksi), whereas the ABAQUS model predicted a minimum stress of -31.42 MPa (-4.56 ksi) at the same location. The slight discrepancy in stress distribution can be attributed to several factors, including variations in boundary conditions, the finer mesh of the 3D model employed in ABAQUS, and differences in the constitutive models for concrete between IDEA StatiCa and ABAQUS (such as the neglect of strain-based failure criteria for concrete in compression in IDEA StatiCa). Moreover, discrepancies in element types (solid 3D elements in ABAQUS versus 2D shell elements in IDEA StatiCa) and the use of embedded region constraints in ABAQUS versus the bond-slip method in IDEA StatiCa likely contributed to these differences. Additionally, as a 2D solver, IDEA StatiCa cannot capture through-the-thickness properties.

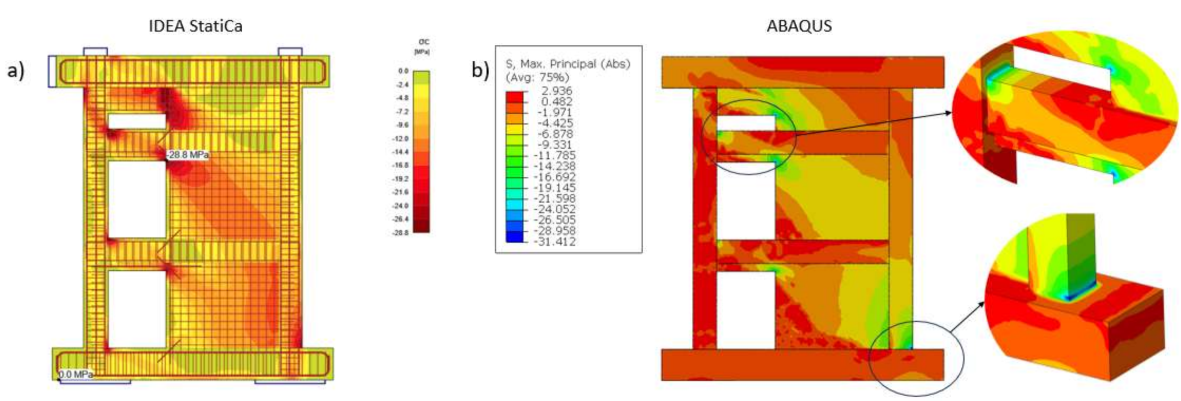

Figure 3.40: Comparison of the calculated principal stresses in concrete a) IDEA StatiCa, and b) ABAQUS.

The calculated and predicted stresses in the steel reinforcement from IDEA StatiCa and ABAQUS are shown in Figure 3.41. In ABAQUS, the predicted maximum and minimum stress values are 426.3 MPa (61.83 ksi) and -276.4 MPa (-40.09 ksi) respectively, while IDEA StatiCa calculates these values as 425 MPa (61.65 ksi) and -254 MPa (-36.84 ksi), respectively. The results show good agreement between the two software.

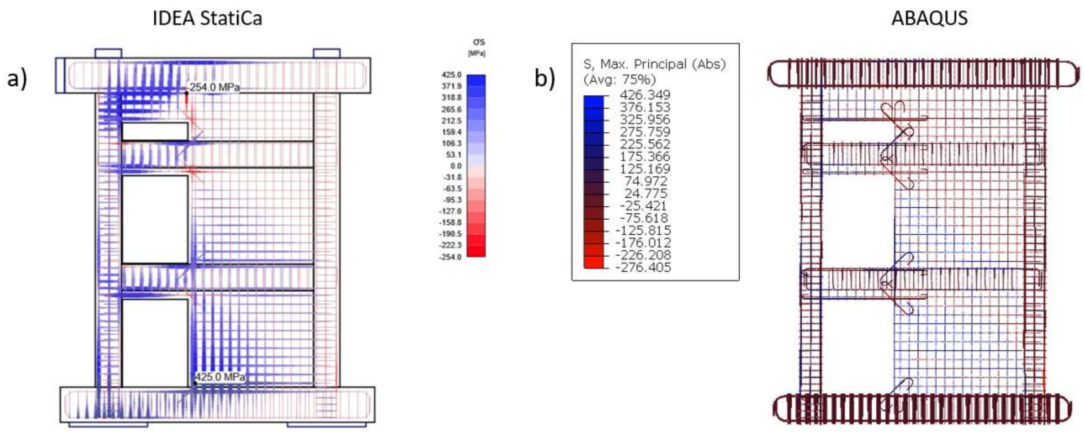

Figure 3.41: Comparison of the stresses in the steel bars between a) IDEA StatiCa, and b) ABAQUS.

Figure 3.42 shows the calculated strains in the steel reinforcement using IDEA StatiCa and ABAQUS. The maximum and minimum strain values predicted by ABAQUS are 5.9e-3 and -0.4e-3, respectively, while the calculated values by IDEA StatiCa are 29.4e-3 and -1.2e-3, respectively. The differences in results are likely attributed to the use of the embedded region constraint in ABAQUS compared to the bond-slip method in IDEA StatiCa, as well as variations in load application methodologies between the two software. Bond-slip model in IDEA StatiCa is possibly more accurate because bar slip can be accounted for at large lateral displacements of the specimens. On the other hand, no bar slippage is allowed because full bonding between bars and concrete is assumed in the ABAQUS model.

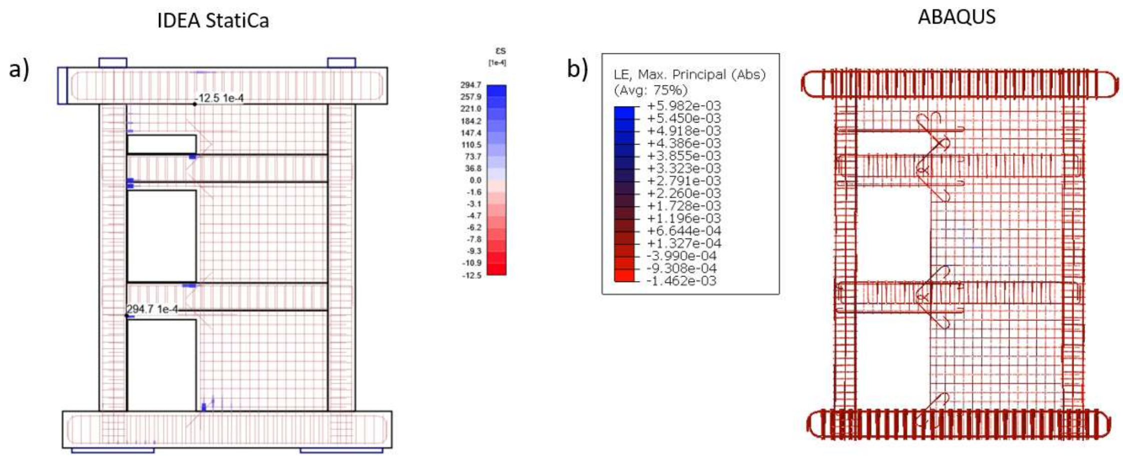

Figure 3.352: Comparison of the strains in the reinforcing bars between a) IDEA StatiCa, and b) ABAQUS.

3.9 Summary and Comparison of Results

3.9.1 Comparison of Capacities for Load Acting in the Positive x Direction

The study examined the behavior of four reinforced concrete (RC) shear walls with openings using IDEA StatiCa. The STM were developed following ACI 318-19 to evaluate their capacities. A baseline model, specimen L1, was used for comparative analysis against an equivalent model in ABAQUS. IDEA StatiCa was used to create detailed models of the four specimens to determine their response when loaded in two directions and then compare the calculated and experimental behavior, including the maximum lateral load-carrying capacity.

Table 3.12 provides a comparative analysis of the measured capacities, STM capacities, and Compatible Stress Field Method (CSFM) capacities obtained from IDEA StatiCa for four RC shear wall specimens subjected to a lateral load in the positive x direction. The capacities of the specimens N1, S1, M1, and L1 are reduced as the number and size of openings in the walls increased (Figure 3.4).

Table 3.12: Capacity comparison for lateral load acting in the positive x direction

Shear wall specimens	Measured capacity, kN (kips)	STM capacity, kN (kips)	CSFM line load, kN/mm (kip/in.)	CSFM capacity, kN (kips)
N1	1179 (265.05)	252 (56.66)	2.38 (13.60)	952 (214.02)
S1	967 (217.40)	174 (39.12)	2.20 (12.57)	880 (197.84)
M1	889 (199.86)	129 (29.01)	1.98 (11.31)	792 (178.05)
L1	686 (154.22)	101 (22.71)	1.82 (10.40)	728 (163.67)

The N1 shear wall, which has no openings, exhibited a measured capacity of 1179 kN (265.05 kips). In contrast, the STM capacity was significantly lower at 252 kN (56.66 kips), representing a 78.6% reduction compared to the measured value. The CSFM capacity was 952 kN (214.02 kips), 19.3% lower than the measured capacity. It should be noted that STM in Figure 3.29 is developed for design purposes. Although the calculated capacity of 252 kN (56.66 kips) does not include load factors for design purposes, the effective strengths of materials in the struts, ties and nodal zones (which are reduced by β_c, β_s, β_n, factors in Tables 2.1 through 2.3 in Chapter 2) are possibly lower than the actual material strengths used in CSFM analysis. For example, $f_c^{'}$ is 25.9 MPa (3.76 ksi) in the walls of specimen N1. However, f_{ce} of 16.5 MPa (2.39 ksi) and 17.6 MPa (2.55 ksi) are used in struts and nodal zones in the most critical locations in the STM in Figure 3.29. The failure occurred in the diagonal strut in the second-story wall, which failed under an axial force of 362.32 kN (81.47 kips). Consequently, the effective concrete strength f_{ce} was 36.6% lower than the specified compressive strength $f_c^{'}$ at that location. It is also important to note that the wall specimens include beams and columns with thicknesses larger than the wall sections, which is difficult to capture in STM because some struts cross beams as shown in Figure 3.29. Similarly, other STM assumptions such as the width of struts or size of nodal zones affect the calculated capacity and corresponding failure mode.

For specimen S1, which has the smallest opening among the three walls with openings (S1, M1, and L1), the measured capacity was 967 kN (217.4 kips). The STM capacity for this specimen was 174 kN (39.12 kips), showing an 82.0% reduction from the measured capacity. The CSFM capacity was 880 kN (197.84 kips), 9.0% lower than the measured capacity. Again, the maximum capacity can be calculated relatively accurately from CSFM analysis while the STM results are significantly low likely due to lower design-based material strengths used and other major assumptions involved in determination of size and location of struts, ties and nodal zones.

The M1 shear wall, which has a moderate-sized opening, had a measured capacity of 889 kN (199.86 kips). The STM capacity was 129 kN (29.01 kips), an 85.5% decrease from the measured capacity. The CSFM capacity was 792 kN (178.05 kips), 11.0% lower than the measured capacity. Lastly, the L1 shear wall, which has the largest opening, demonstrated a measured capacity of 686 kN (154.22 kips). The STM capacity was 101 kN (22.71 kips), reflecting an 85.3% reduction from the measured capacity. The CSFM capacity was 728 kN (163.67 kips), which was 6.1% higher than the measured capacity.

Figure 3.44 compares the measured and CSFM-calculated drift angles (%) for shear wall specimens N1, S1, M1, and L1, while Figure 3.43 illustrates the capacities based on measured data, STM, and CSFM, providing a visual comparison of the three methods and further insight into the structural behavior under applied lateral loads. It should be noted that the maximum drift results presented in Figure 3.44 may be misleading because the complete lateral load-displacement relationships are not provided in the original reference, Taleb et al. (2012). Depending on the ductility and when the cyclic loading stopped during the experiment, the definition of drift may change. The measured and calculated drift values compare reasonably well in Figure 3.44. Specimens S1 and L1 show closer alignment between measured and CSFM-calculated drift angles (%), while specimens N1 and M1 exhibit larger discrepancies, indicating potential modeling challenges for these specimens using CSFM.

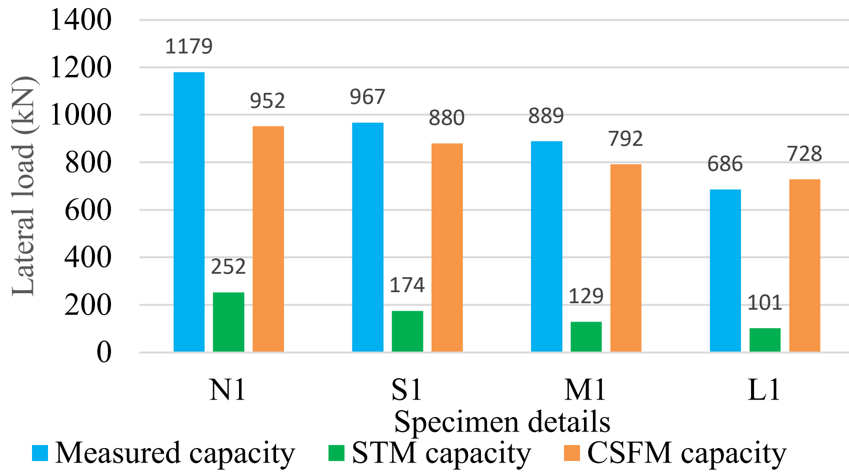

Figure 3.363: Comparison of Measured, STM, and CSFM capacities for load acting in the positive direction.

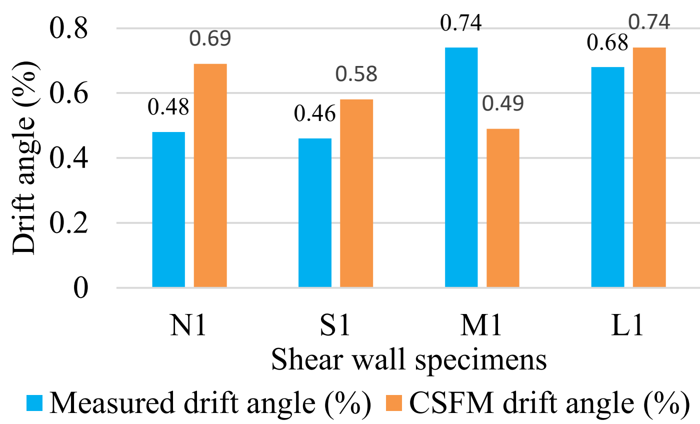

Figure 3.374: Comparison of drift angle (%) for positive loading direction.

Figure 3.45 compares lateral load capacities for specimen L1, which serves as the baseline model for this study. The capacities are determined following different methods: measured capacity, STM, CSFM, and ABAQUS capacities. The ABAQUS analysis for the baseline model yields a capacity of 550 kN (123.65 kips), which is 80.2% of the measured capacity.

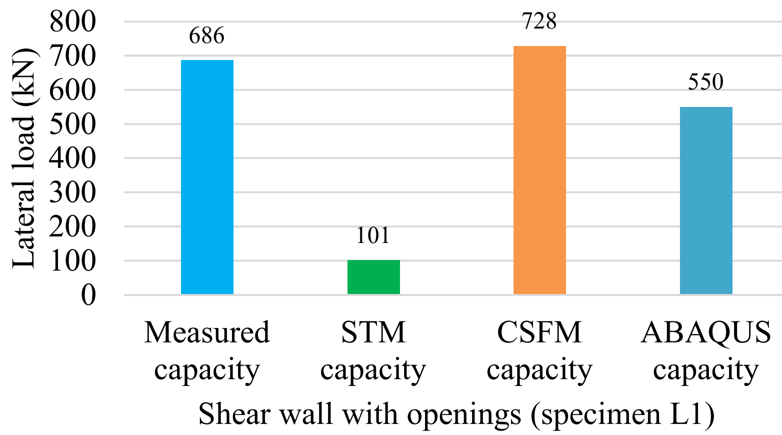

Figure 3.385: Comparison of measured, calculated STM, CSFM, and ABAQUS capacities for baseline model L1.

The observed differences in capacities highlight the varying degrees of accuracy and reliability among the methods. The STM capacity's substantial underestimation can be attributed to the method's composition, which relies on different design formulas to calculate the capacity of nodes and struts more conservatively for design purposes. Depending on the conditions, the strength of concrete in STM can be reduced by 40% for a node and 30% for a strut through β_c, β_n, and β_s factors in Tables 2.1 through 2.3 in Chapter 2. These reductions in concrete strength likely contribute to the significantly lower STM capacities. Such conservative design-based estimations are intended to ensure safety and account for uncertainties in the behavior of the structural materials and elements, but they can result in considerable underestimations compared to actual measured capacities.

Conversely, the CSFM capacity closely matches the measured capacity, indicating high predictive accuracy. The ABAQUS capacity, while lower than the measured value, still shows reasonable proximity, suggesting that it provides a relatively reliable estimate for the baseline model. These variations emphasize the importance of selecting appropriate methods for capacity prediction and design calculations, considering the specific characteristics of the structural elements and the context of the analysis.

3.9.2 Comparison of Capacities for Load Acting in the Negative Direction

Table 3.13 and Figure 3.46 compare the measured and CSFM capacities of four reinforced concrete shear wall specimens subjected to lateral load in the negative horizontal direction (Figure 3.2). The N1 wall, which has no openings, had a measured capacity of 1039 kN (233.58 kips), while the CSFM capacity was 956 kN (214.92 kips), which is 8.0% lower than the measured value. The S1 wall, with the smallest opening, exhibited a measured capacity of 838 kN (188.39 kips), while the CSFM capacity was 928 kN (208.63 kips), 10.7% higher than the measured value. For the M1 wall, with a moderate opening, the measured capacity was 723 kN (162.54 kips), and the CSFM capacity was 784 kN (176.26 kips), 8.4% higher than the measured capacity. The L1 wall, which has the largest opening, had a measured capacity of 649 kN (145.91 kips), while the CSFM capacity was 816 kN (183.45 kips), which is 25.7% higher than the measured value. In general, walls with larger openings tend to show greater differences between the measured and CSFM capacities.

Table 3.13: Capacity comparison for lateral load acting in the negative x direction

Shear wall specimens	Measured capacity, kN (kip)	CSFM line load, kN/mm (kip/in.)	CSFM capacity, kN (kip)
N1	1039 (233.58)	2.39 (13.65)	956 (214.92)
S1	838 (188.39)	2.32 (13.25)	928 (208.63)
M1	723 (162.54)	1.96 (11.20)	784 (176.26)
L1	649 (145.91)	2.04 (11.65)	816 (183.45)

The data indicates that the CSFM capacities generally align closely with the measured capacities, with some variations. Specimens N1 and M1 showed CSFM capacities slightly lower than the measured values, whereas specimens S1 and L1 exhibited CSFM capacities that exceeded the measured values. These differences highlight the variability in the accuracy of the CSFM method, depending on the specific characteristics of each shear wall specimen.

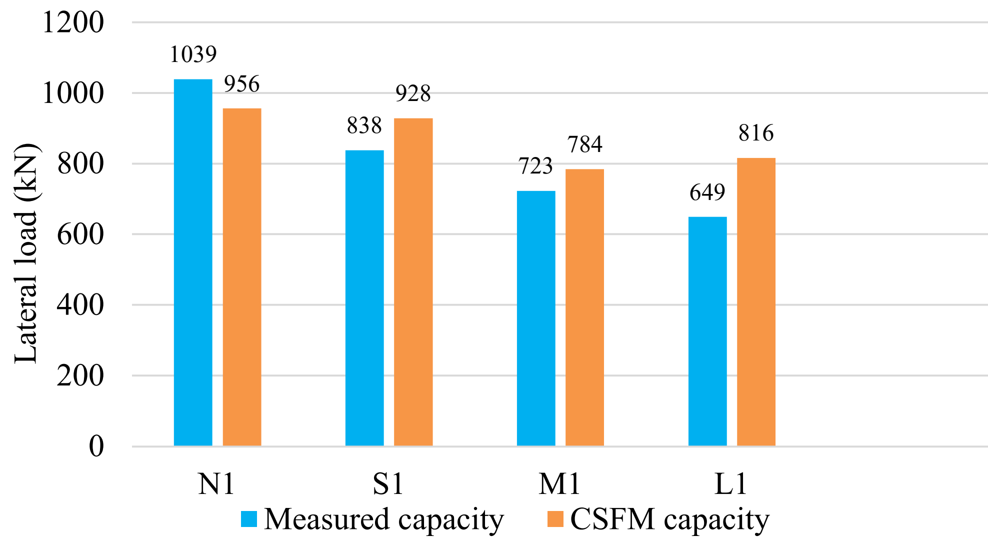

Figure 3.396: Comparison of measured and CSFM capacities for lateral load acting in the negative x direction.

The measured maximum drift angles for the shear wall specimens varied, with N1 at 0.42%, S1 at 0.44%, M1 at 0.48%, and L1 at 0.74%. Conversely, the CSFM drift angles corresponding to the maximum lateral load were 0.70%, 0.74%, 0.46%, and 0.46% for specimens N1, S1, M1, and L1, respectively (Figure 3.47). The comparison reveals that specimens S1 and L1 demonstrate significant discrepancies between the measured and CSFM-calculated drift angles. Specifically, the CSFM drift angles for S1 and L1 were higher by 68.2% and lower by 37.8%, respectively, compared to the measured values. On the other hand, specimens N1 and M1 show a closer alignment, with the CSFM drift angle for N1 being higher by 66.7% and for M1 being lower by 4.2% than the measured drift angle. These differences suggest that the CSFM method provides a more accurate prediction for the drift angles of specimens N1 and M1, while it overestimates and underestimates the drift angles for specimens S1 and L1, respectively. The variability in the accuracy of the CSFM method indicates potential challenges in modeling ductile response (beyond longitudinal steel yielding) and structural behavior in the nonlinear range, emphasizing the need for further refinement and calibration of the method to better capture the nonlinear behavior.

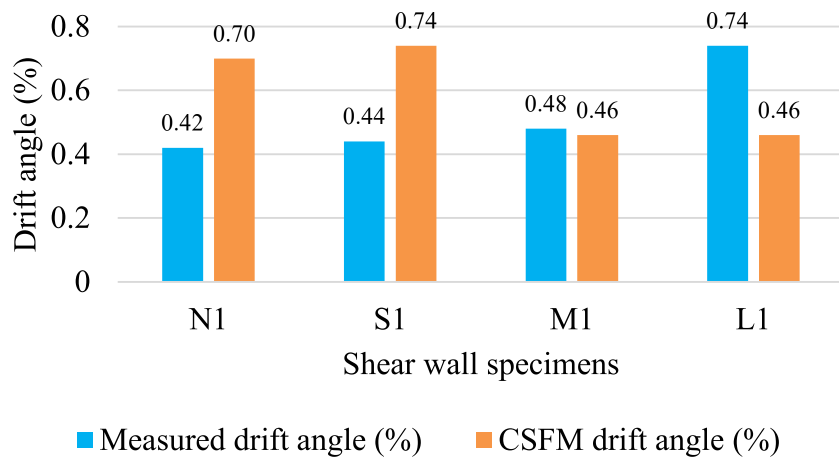

Figure 3.407: Comparison of drift angle (%) for negative loading direction.

3.9.3 Effect of Confined Concrete on the CSFM Results for Lateral Load Acting in the Positive x Direction

The effect of concrete confinement on the lateral load capacity of shear walls with openings was determined using IDEA StatiCa. The Mander et al. (1988) confined concrete model was employed to include the effects of concrete confinement (and corresponding capacity increase) for beams and columns as described in Section 3.6.3. The results are presented in Figure 3.48 and Table 3.14, which provides a comparative analysis of the measured and CSFM capacities for confined concrete, and CSFM capacities for unconfined concrete for four reinforced concrete shear wall specimens subjected to a lateral load in the positive x direction.

Table 3.14: Comparison of lateral load capacity for confined and unconfined concrete in the positive loading direction

Shear wall specimens	Measured capacity, kN (kip)	CSFM line load for confined concrete, kN/mm (kip/in.)	CSFM total capacity for confined concrete, kN (kips)	CSFM line load for unconfined concrete, kN/mm (kip/in.)	CSFM total capacity for unconfined concrete, kN (kips)
N1	1179 (265.05)	2.41 (13.77)	964 (216.72)	2.38 (13.60)	952 (214.02)
S1	967 (217.40)	2.27 (12.97)	908 (204.13)	2.20 (12.57)	880 (197.84)
M1	889 (199.86)	2.05 (11.71)	820 (184.35)	1.98 (11.31)	792 (178.05)
L1	686 (154.22)	1.89 (10.80)	756 (169.96)	1.82 (10.40)	728 (163.67)

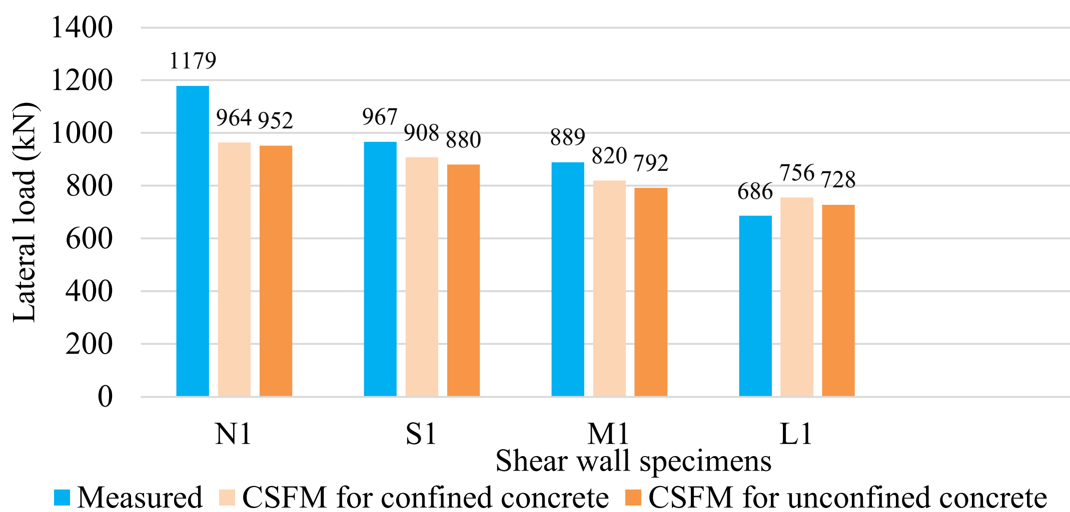

Figure 3.418: Comparison of measured' and CSFM capacities for confined and unconfined concrete for lateral load acting in the positive x direction.

These results suggest that the confinement effect, as modeled using Mander et al. (1988) model for confined concrete, generally enhances the capacity of shear walls with openings. The degree of improvement varies among the specimens, with increases ranging from 1.3% to 3.8%. Figure 3.49 provides a detailed comparison of the measured drift angles (%) with the CSFM-calculated drift angles for confined and unconfined concrete for four RC shear wall specimens, designated as N1, S1, M1, and L1.

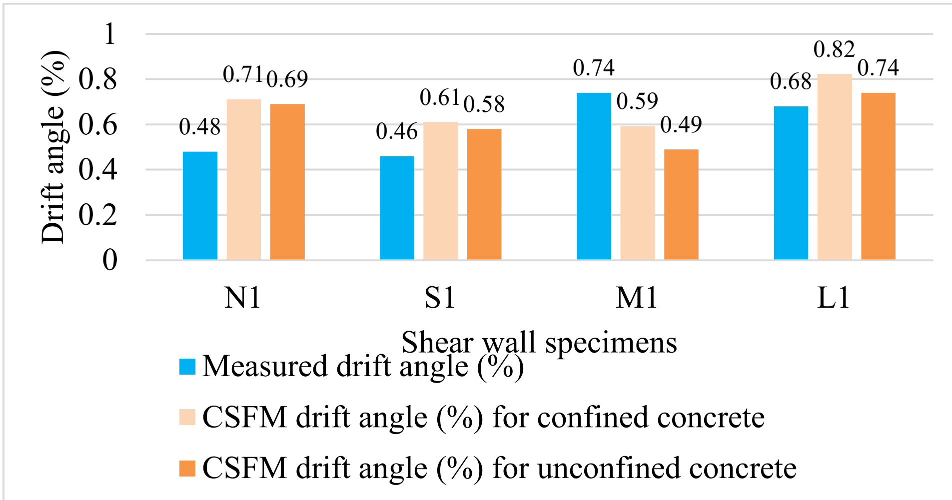

Figure 3.429: Comparison of drift angle (%) for positive loading.

3.9.4 Effect of Confined Concrete on the CSFM Results for Lateral Load Acting in the Negative x Direction

The concrete confinement effects on the capacity of shear walls with openings under negative loading were determined using IDEA StatiCa following the same procedure discussed in Section 3.9.3 for positive loading. The Mander et al. (1988) model was used to calculate the confinement effects as described in Section 3.6.5. Figure 3.50 and Table 3.15 compare the measured and CSFM capacities for confined and unconfined concrete in four RC shear wall specimens subjected to a lateral load in the negative direction. These results suggest that the confinement effect, as modeled using Mander et al.'s model for confined concrete, generally enhances the capacity of shear walls with openings under negative loading. The degree of improvement varies among the specimens, with increases ranging from 1.3% to 18.9%.

Table 3.15: Comparison of CSFM results for confined and unconfined concrete for negative loading.

Shear wall specimens	Measured capacity, kN (kips)	Line load for confined concrete, kN/mm (kip/in.)	Total capacity for confined concrete, kN (kips)	Line load for unconfined concrete, kN/mm (kip/in.)	Total capacity for unconfined concrete, kN (kips)
N1	1039 (233.58)	2.42 (13.82)	968 (217.62)	2.39 (13.65)	956 (214.92)
S1	838 (188.39)	2.38 (13.60)	952 (214.02)	2.32 (13.25)	928 (208.63)
M1	723 (162.54)	2.33 (13.31)	932 (209.53)	1.96 (11.20)	784 (176.26)
L1	649 (145.91)	2.08 (11.88)	832 (187.05)	2.04 (11.65)	816 (183.45)

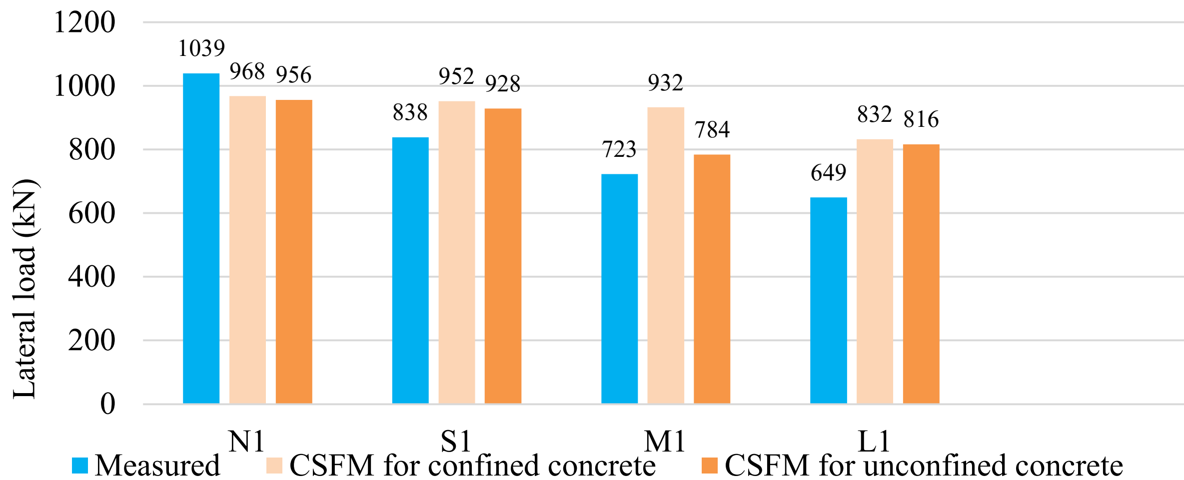

Figure 3.50: Comparison of measured and CSFM capacities for confined and unconfined concrete for load acting toward negative direction.

Figure 3.51 compares the measured drift angles (%) with the CSFM-calculated drift angles (%) for confined and unconfined concrete for four RC shear wall specimens under negative loading conditions. Overall, the effect of confinement on drift angle of N1 and S1 is minimal. For M1, the confinement significantly increases the drift angle, suggesting a substantial effect on the structural behavior including lateral strength (Figure 3.50). For L1, the measured drift angle compares well with that of the confined concrete model, while the unconfined concrete provides a lower estimate.

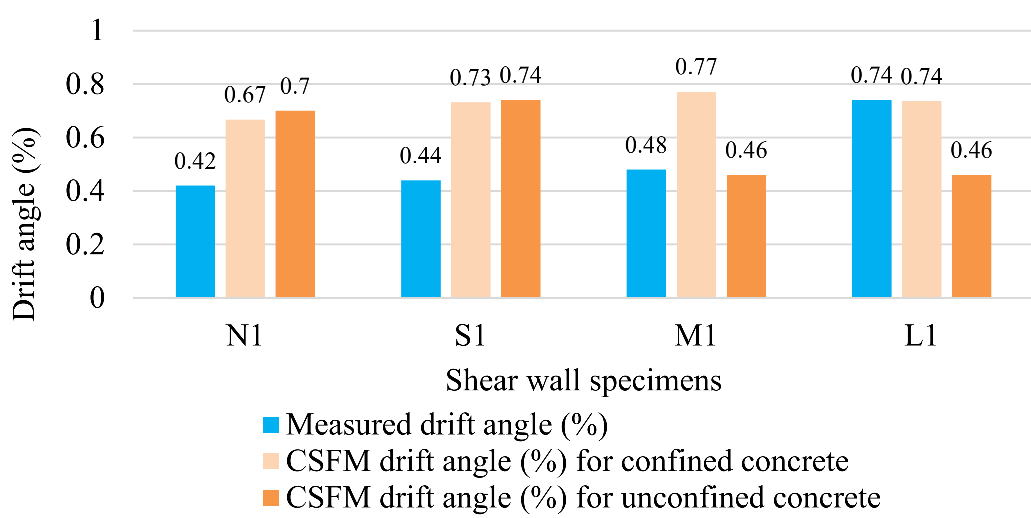

Figure 3.51: Comparison of drift angle (%) for negative loading.

In conclusion, the capacities of reinforced concrete shear walls with openings were evaluated using IDEA StatiCa, comparing the strut and tie model from ACI 318-19, ABAQUS, the Compatible Stress Field Method (CSFM), and experimental data. The study revealed that the STM significantly underestimated the load-carrying capacity due to its conservative design assumptions. In contrast, both the CSFM and ABAQUS provided results that aligned closely with the measured capacities, especially under positive loading conditions. Additionally, the analysis considered the effects of confined versus unconfined concrete material on strength and drift behavior. The results showed that confinement generally improves shear wall capacity, although the impact on drift angles varied among specimens. Overall, the findings highlight the importance of selecting appropriate prediction methods, with CSFM and ABAQUS demonstrating superior accuracy compared to STM and underscore the need for careful consideration of confinement effects in design and analysis.

References

Taleb, R., Bechtoula, H., Sakashita, M., Bourahla, N., & Kono, S. (2012). Investigation of the shear behaviour of multi-story reinforced concrete walls with eccentric openings. *Computers and Concrete, 10*(4), 343-359. https://doi.org/10.12989/cac.2012.10.4.361

ACI Committee 318. (2019). *Building Code Requirements for Structural Concrete (ACI 318R-19).* Farmington Hills, Michigan: American Concrete Institute.

Konstantinidis, D., Kappos, A., & Izzuddin, B. (2007). Analytical stress–strain model for high-strength concrete members under cyclic loading. *Journal of Structural Engineering*, 133(4), 484-494. https://doi.org/10.1061/(ASCE)0733-9445(2007)133:4(484)

Mander, J. B., Priestley, M. J. N., & Park, R. (1988). Theoretical stress-strain model for confined concrete. *Journal of Structural Engineering, 114*(8), 1804-1826. https://doi.org/10.1061/(ASCE)0733-9445(1988)114:8(1804)

Dassault Systèmes. (2023). ABAQUS – 2023: Standard User's Guide. Simulia Corp.

Computers and Structures, Inc. (2023). *SAP2000: Integrated software for structural analysis and design* (Version 23.3.0) [Computer software]. https://www.csiamerica.com/products/sap2000

McNeel, R. (2020). Rhinoceros 3D® (Version 7.0.) [Computer Software]. Robert McNeel & Associates.

Federal Highway Administration. (2006). Optimized sections for high-strength concrete bridge girders: Effect of deck concrete strength. In *Coordinating, developing, and delivering highway transportation innovations* (Publication No. FHWA-HRT-05-058, Chapter 3, Task 2: Analyses of flexural strength and ductility). Retrieved from https://www.fhwa.dot.gov/publications/research/infrastructure/structures/05058/03.cfm

Watanabe, K., Niwa, J., Yokota, H., & Iwanami, M. (2004). Experimental study on stress-strain curve of concrete considering localized failure in compression. *Journal of Advanced Concrete Technology*, 2(3), 395-407.

Appendix A: Calculation of Maximum Drift Angle

A-1 Maximum Drift Calculations Considering Unconfined Concrete

To calculate the maximum drift angle (%) for each shear wall specimen, the displacement of each floor in the x direction was first calculated using IDEA StatiCa. The difference between the upper and lower floor displacements, which is defined as drift, is calculated. Then, the drift was divided by the center-to-center height of the respective story to determine the inter-story drift. The inter-story drift or drift angle is expressed as percentage in this report. Among the drift angles (%) calculated for the three floors, the largest value was taken as the maximum drift angle (%) for that shear wall specimen. Tables A-1 through A-4 show the maximum calculated drift angle (%) when the lateral load is applied in the positive x direction. Tables A-5 through A-8 present the maximum drift angles (%) when the load acted in the negative x direction.

Table A-1: Maximum drift angle (%) for specimen N1 in the positive loading direction

Floor	Displacement, mm (in.)	Story height, mm (in.)	Drift angle (%)	Maximum drift angle (%)
Ground	1.4 (0.06)	0 (0)	0	0.69
First	9.9 (0.39)	1450 (57.09)	0.59	
Second	18.2 (0.72)	1400 (55.12)	0.59	
Third	24.4 (0.97)	900 (35.44)	0.69	

Table A-2: Maximum drift angle (%) for specimen S1 in the positive loading direction

Floor	Displacement, mm (in.)	Story height, mm (in.)	Drift angle (%)	Maximum drift angle (%)
Ground	1.2 (0.05)	0 (0)	0	0.58
First	8.2 (0.33)	1450 (57.09)	0.48	
Second	15.8 (0.63)	1400 (55.12)	0.54	
Third	21.0 (0.83)	900 (35.44)	0.58	

Table A-3: Maximum drift angle (%) for specimen M1 in the positive loading direction

Floor	Displacement, mm (in.)	Story height, mm (in.)	Drift angle (%)	Maximum drift angle (%)
Ground	1.0 (0.04)	0 (0)	0	0.49
First	7.1 (0.28)	1450 (57.09)	0.42	
Second	13.7 (0.54)	1400 (55.12)	0.47	
Third	18.1 (0.72)	900 (35.44)	0.49	

Table A- 4: Maximum drift angle (%) for specimen L1 in the positive loading direction

Floor	Displacement, mm (in.)	Story height, mm (in.)	Drift angle (%)	Maximum drift angle (%)
Ground	1.7 (0.07)	0 (0)	0	0.74
First	12.5 (0.50)	1450 (57.09)	0.74	
Second	21.9 (0.87)	1400 (55.12)	0.67	
Third	28.6 (1.13)	900 (35.44)	0.74	

Table A-5: Maximum drift angle (%) for specimen N1 in the negative loading direction

Floor	Displacement, mm (in.)	Story height, mm (in.)	Drift angle (%)	Maximum drift angle (%)
Ground	1.5 (0.06)	0 (0)	0	0.70
First	10.0 (0.40)	1450 (57.09)	0.59	
Second	18.4 (0.73)	1400 (55.12)	0.60	
Third	24.7 (0.98)	900 (35.44)	0.70	

Table A-6: Maximum drift angle (%) for specimen S1 in the negative loading direction

Floor	Displacement, mm (in.)	Story height, mm (in.)	Drift angle (%)	Maximum drift angle (%)
Ground	1.3 (0.06)	0 (0)	0	0.74
First	11.3 (0.45)	1450 (57.09)	0.69	
Second	21.6 (0.86)	1400 (55.12)	0.74	
Third	27.4 (1.08)	900 (35.44)	0.64	

Table A-7: Maximum drift angle (%) for specimen M1 in the negative loading direction

Floor	Displacement, mm (in.)	Story height, mm (in.)	Drift angle (%)	Maximum drift angle (%)
Ground	0.4 (0.02)	0 (0)	0	0.46
First	6.3 (0.25)	1450 (57.09)	0.41	
Second	12.8 (0.51)	1400 (55.12)	0.46	
Third	15.6 (0.62)	900 (35.44)	0.31	

Table A-8: Maximum drift angle (%) for specimen L1 in the negative loading direction

Floor	Displacement, mm (in.)	Story height, mm (in.)	Drift angle (%)	Maximum drift angle (%)
Ground	0.4 (0.02)	0 (0)	0	0.46
First	6.0 (0.24)	1450 (57.09)	0.39	
Second	12.5 (0.5)	1400 (55.12)	0.46	
Third	15.6 (0.62)	900 (35.44)	0.34	

A-2 Maximum Drift Angle (%) Calculation Considering Confinement Effect of Concrete

The procedure for calculating the maximum drift angle (%) for each shear wall specimen, considering the confinement effect of concrete, followed the same steps as for models with unconfined concrete as described in Section 3.5.4. First, the displacement of each floor in the x direction was calculated from CSFM or IDEA StatiCa analysis. The difference between the displacement of the upper and lower floors or story drift was calculated at failure or when the maximum capacity was reached. This difference (story drift) was then divided by the center-to-center height of the respective story to determine the inter-story drift as percentage. The largest drift angle (%) was considered the maximum drift angle (%) for that shear wall specimen. Tables A-9 through A-12 display the maximum calculated drift angles (%) for the lateral load acting in the positive x direction, and Tables A-13 through A-16 show the maximum drift angles (%) when the lateral load acted in the negative x direction.

Table A-9: Maximum drift angle (%) for specimen N1 in the positive loading direction

Floor	Displacement, mm (in.)	Story height, mm (in.)	Drift angle (%)	Maximum drift angle (%)
Ground	1.4 (0.06)	0 (0)	0	0.71
First	9.4 (0.38)	1450 (57.09)	0.55	
Second	17.3 (0.69)	1400 (55.12)	0.56	
Third	23.7 (0.94)	900 (35.44)	0.71	

Table A-10: Maximum drift angle (%) for specimen S1 in the positive loading direction

Floor	Displacement, mm (in.)	Story height, mm (in.)	Drift angle (%)	Maximum drift angle (%)
Ground	0.5 (0.02)	0 (0)	0	0.61
First	8.6 (0.34)	1450 (57.09)	0.56	
Second	17.0 (0.67)	1400 (55.12)	0.60	
Third	22.5 (0.89)	900 (35.44)	0.61	

Table A-11: Maximum drift angle (%) for specimen M1 in the positive loading direction

Floor	Displacement, mm (in.)	Story height, mm (in.)	Drift angle (%)	Maximum drift angle (%)
Ground	0.9 (0.04)	0 (0)	0	0.59
First	8.1 (0.32)	1450 (57.09)	0.50	
Second	16.4 (0.65)	1400 (55.12)	0.59	
Third	21.6 (0.86)	900 (35.44)	0.58	

Table A-12: Maximum drift angle (%) for specimen L1 in the positive loading direction

Floor	Displacement, mm (in.)	Story height, mm (in.)	Drift angle (%)	Maximum drift angle (%)
Ground	1.9 (0.08)	0 (0)	0	0.82
First	13.7 (0.54)	1450 (57.09)	0.81	
Second	24.5 (0.97)	1400 (55.12)	0.77	
Third	31.9 (1.26)	900 (35.44)	0.82	

Table A-13: Maximum drift angle (%) for specimen N1 in the negative loading direction

Floor	Displacement, mm (in.)	Story height, mm (in.)	Drift angle (%)	Maximum drift angle (%)
Ground	1.4 (0.06)	0 (0)	0	0.67
First	9.6 (0.38)	1450 (57.09)	0.57	
Second	18.1 (0.72)	1400 (55.12)	0.61	
Third	24.1 (0.95)	900 (35.44)	0.67	

Table A-14: Maximum drift angle (%) for specimen S1 in the negative loading direction

Floor	Displacement, mm (in.)	Story height, mm (in.)	Drift angle (%)	Maximum drift angle (%)
Ground	1.4 (0.06)	0 (0)	0	0.73
First	12 (0.48)	1450 (57.09)	0.73	
Second	21.8 (0.86)	1400 (55.12)	0.70	
Third	27.9 (1.1)	900 (35.44)	0.68	

Table A-15: Maximum drift angle (%) for specimen M1 in the negative loading direction

Floor	Displacement, mm (in.)	Story height, mm (in.)	Drift angle (%)	Maximum drift angle (%)
Ground	1.3 (0.06)	0 (0)	0	0.77
First	12.3 (0.49)	1450 (57.09)	0.76	
Second	23.1 (0.91)	1400 (55.12)	0.77	
Third	29.3 (1.16)	900 (35.44)	0.69	

Table A-16: Maximum drift angle (%) for specimen L1 in the negative loading direction

Floor	Displacement, mm (in.)	Story height, mm (in.)	Drift angle (%)	Maximum drift angle (%)
Ground	0.6 (0.03)	0 (0)	0	0.74
First	10.6 (0.42)	1450 (57.09)	0.69	
Second	20.9 (0.83)	1400 (55.12)	0.74	
Third	24.4 (0.97)	900 (35.44)	0.39	

Chapter 4. Modeling and Analysis of Walking Column

4.1 Introduction

A "walking column" is a type of structural column that shifts horizontally between floors, meaning it is not vertically aligned with the columns below it (see Figure 4.1). This lateral shift typically occurs due to architectural or design requirements, allowing flexibility in floor layouts while still transferring loads through the structure. Despite this lateral offset, walking columns are engineered to ensure they effectively carry vertical loads across different levels.

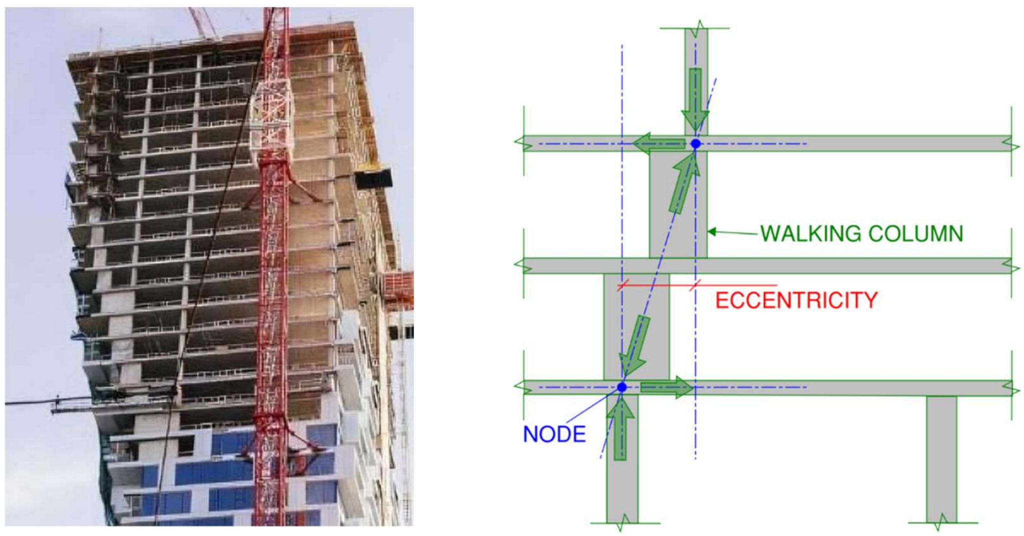

(a) (b)

Figure 4.1: Walking column: a) Walking column in real building, and b) load transfer mechanism of walking column (SheerForce Engineering, 2021).

In this chapter, the structural behavior of four reinforced concrete (RC) walking columns is investigated. The vertical load capacities of these columns were assessed through IDEA StatiCa software and subsequently compared with design capacities derived from the Strut-and-Tie Model (STM) as outlined in ACI 318-19 (2019). One of the four walking column examples was chosen as a baseline for further analysis using ABAQUS software (2023), where its load-bearing capacity, principal stress distribution, and crack patterns were determined and compared to the results obtained from both the Compatible Stress Field Method (CSFM) and ACI 318-19 design procedure.

4.2 Walking Columns in Modern Buildings

4.2.1 The 56 Leonard Building

The 56 Leonard, located in Manhattan, New York, was constructed in 2016. It is a striking example of the application of walking columns in modern architecture (Figure 4.2). Floors of the 821-ft tall and 60-story building appear irregularly stacked, reminiscent of a "Jenga" game (Lubell, 2015). The walking columns in this structure are crucial for transferring vertical loads from the upper floors to the foundation, considering the shifting geometry of the building. These columns are not aligned in the vertical direction, requiring them to redistribute and transfer the loads from misaligned floors while accommodating the architectural design, which includes large cantilevered sections. The incorporation of walking columns into this building design has allowed for flexible floor layouts, catering to high-end residential spaces and achieving and unconventional high-rise structure (Herzog and de Meuron, 2016).

(a) (b)

Figure 4.2: Walking column example: a) 56 Leonard building, and b) walking columns.

4.2.2 Chicago Mercantile Exchange Center

The Chicago Mercantile Exchange Center (CME), completed in 1987, is a prime example of how walking columns can be integrated into a structural design to handle complex load distributions in large commercial buildings (Figure 4.3). The building features two 40-story towers connected by a 10-story base structure, designed to accommodate the functional requirements of a trading exchange, such as large open trading floors on the lower levels. To achieve this, a robust transfer load system was employed, utilizing walking columns to transfer the loads from the upper levels to the foundation.

The walking columns in the CME Center serve as intermediary structural supports, allowing the upper floors to be arranged differently from the lower ones. This system enhances the flexibility of the interior space, especially in the lower levels, where uninterrupted spans are required for open trading areas. The absence of vertical supports in the trading floors would have otherwise obstructed the open space needed for the building's core operations. By incorporating walking columns within the load transfer mechanism, the structural design ensured both stability and the functional adaptability of the large commercial space. The CME Center demonstrates how innovative engineering solutions, such as walking columns, can address the unique spatial and structural demands of commercial skyscrapers (Thornton Tomasetti, 1987).

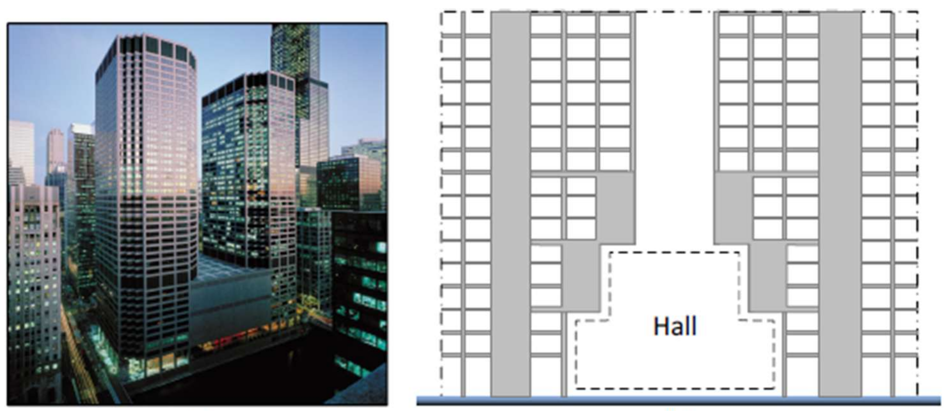

(a) (b)

Figure 4.3: a) Chicago Mercantile Exchange Center, and b) its elevation view and load transfer mechanism.

4.2.3 Beetham Tower

Beetham Tower in Manchester, UK, completed in 2004, is a notable example of a structure utilizing walking columns to achieve both structural and aesthetic objectives (Figure 4.4). At 168 meters (551 ft) tall, it was one of the highest residential buildings in Europe at the time of its completion. The tower’s standout feature is its upper-level cantilever, where walking columns are integral to transferring vertical loads from the upper floors to the lower floors of the building.

(a) (b) (c)

Figure 4.4: a) Beetham Tower, b) walking column, and c) walking column scheme.

The walking columns in Beetham Tower are designed to transfer and redistribute the loads diagonally, ensuring that the structure remains stable despite the unconventional design. This approach allows the building to maintain its unique visual impact while ensuring structural safety (SimpsonHaugh, 2004).

4.2.4 Miami Tower

The 47-story Miami Tower in Miami Florida was completed in 1987 and includes unique setbacks and stepped profile (Figure 4.5). These features required an innovative structural design solution to manage the different load paths throughout the building. Walking columns were used to transfer loads from the smaller upper floors to the larger base below. The Miami Tower illustrates how walking columns can be effectively used in high-rise construction to achieve both functional and visual goals , 1987).

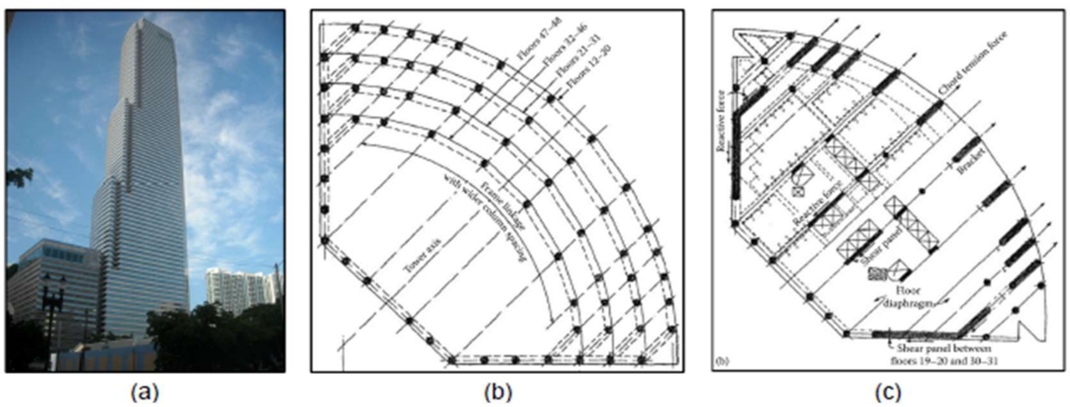

Figure 4.5: a) Miami Tower, b) structural floor layout, and c) walking column layout (Taranath, 2010).

4.3 Description of Walking Column Examples

To assess the structural performance of walking columns, four RC walking columns, identified as Examples 1 through 4, were evaluated. These columns were designed and presented by Schwinger (2021) at a seminar organized by the Delaware Valley Association of Structural Engineers, Eastern Chapter of the Structural Engineers Association of Pennsylvania. The primary objective of these design examples was to provide design guidelines for engineers, due to the lack of experimental studies or design data specifically focusing on walking columns. In Schwinger (2021) critical design considerations for walking columns are highlighted, including nodal zone checks, design and detailing of tension ties and compression struts, and establishment of a proper load path. The concrete and reinforcement strengths were kept consistent across all specimens, while variations were introduced in column sizes at different story levels and in the quantity of reinforcing bars. Example 1 was chosen as the baseline model for further analysis using ABAQUS software in this study.

Schwinger (2021) provided material properties for the four walking column examples that are used in this research. The compressive strength of concrete, f_c' was specified as 10 ksi (69 MPa) for the columns and 8 ksi (55 MPa) for the slabs. For the reinforcement, a yield strength, f_y of 60 ksi (414 MPa) and an ultimate strength, f_u of 80 ksi (552 MPa) were specified. Although Schwinger mentioned that these properties only for walking column Example 1, the same material properties were applied to Examples 2 through 4, as no specific material data were provided for these cases. This approach ensured consistency in the capacity calculations across all examples. The geometric details, including cross-sectional areas and slab thicknesses, are provided in Table 4.1. The reinforcement details for all walking columns are shown in Table 4.2, including the number, size, and spacing of reinforcing bars and lateral ties for the top columns, middle walls or columns, bottom columns, and slabs.

Table 4.1: Geometric details of walking columns

Properties name	Location	Walking column			
		Example 1	Example 2	Example 3	Example 4
Cross section	Top column, in. x in. (mm x mm)	24 x 34 (609.6 x 863.6)	36 x 24 (914.4 x 609.6)	24 x 36 (609.6 x 914.4)	40 x 24 (1016.0 x 609.6)
	Middle wall/column, in. x in. (mm x mm)	72 x 34 (1828.8 x 863.6)	60 x 30 (1524.0 x 762.0)	48 x 36 (1219.2 x 914.4)	91 x 24 (2311.4 x 609.6)
	Bottom column, in. x in. (mm x mm)	24 x 34 (609.6 x 863.6)	42 x 42 (1066.8x 1066.8)	30 x 30 (762.0 x 762.0)	40 x 24 (1016.0 x 609.6)
	Slab thickness, in. (mm)	10 (254.0)	11 (279.4)	15 (381.0)	10 (254.0)

Table 4.2: Reinforcing bars details for walking column

Properties name	Location	Walking column			
		Example 1	Example 2	Example 3	Example 4
Reinforcing bars	Top column	10 #11	16 #11	14 #11	12 #11
	Middle wall or column	24 #11	24 #11	25 #11	28 #11
	Bottom column	10 #11	16 #11	12 #11	12 #11
	Slab (dia @in. center to center)	#3@10	#3@10	#3@10	#3@10
Lateral ties	Top column	#5@6	#5@6	#5@5	#5@4
	Mid wall	#5@6	#5@4	#5@4	#5@4
	Bottom column	#5@6	#5@6	#5@5	#5@4
Shrinkage and temperature bars	Slab (diameter @ center to center distance in inch units)	#3@10	#3@10	#3@10	#3@10

The geometric layouts and reinforcement details for Examples 1 through 4 are shown in Figures 4.6 through 4.9, respectively. For Example 1 (Figure 4.6), the top and bottom columns are reinforced with ten #11 longitudinal bars, while the middle wall (or column) is reinforced with 24 #11 bars. Note that the #11 bars have a 1.41 in. (35.81 mm) diameter. Lateral ties for the top and bottom columns consist of #5 bars spaced at 6 inches. The middle walls have the same transverse reinforcement spacing. All slabs are reinforced with uniformly spaced #3 bars at 10 in. (254 mm) center to center. Shrinkage and temperature bars in the slab are also #3 bars spaced at 10 in. (254 mm) center to center.

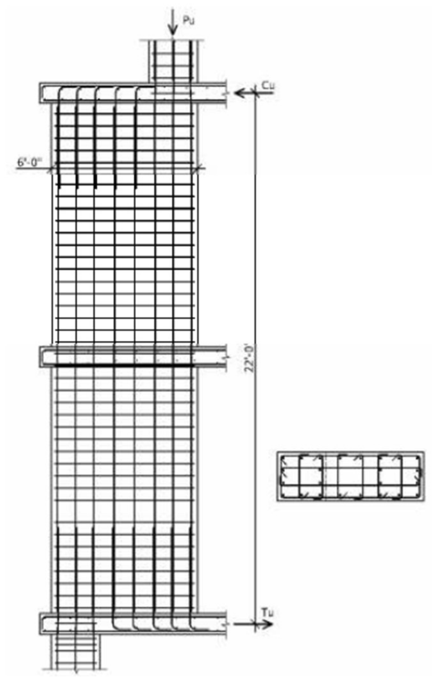

Figure 4.6: Cross section and reinforcing bar details of walking column Example 1.

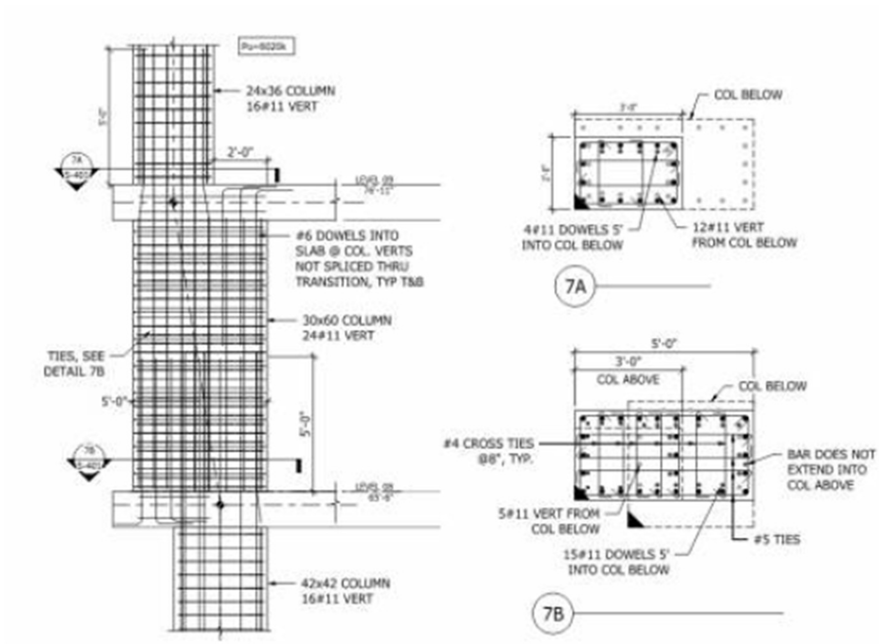

Figure 4.7: Cross section and reinforcing bar details of walking column Example 2.

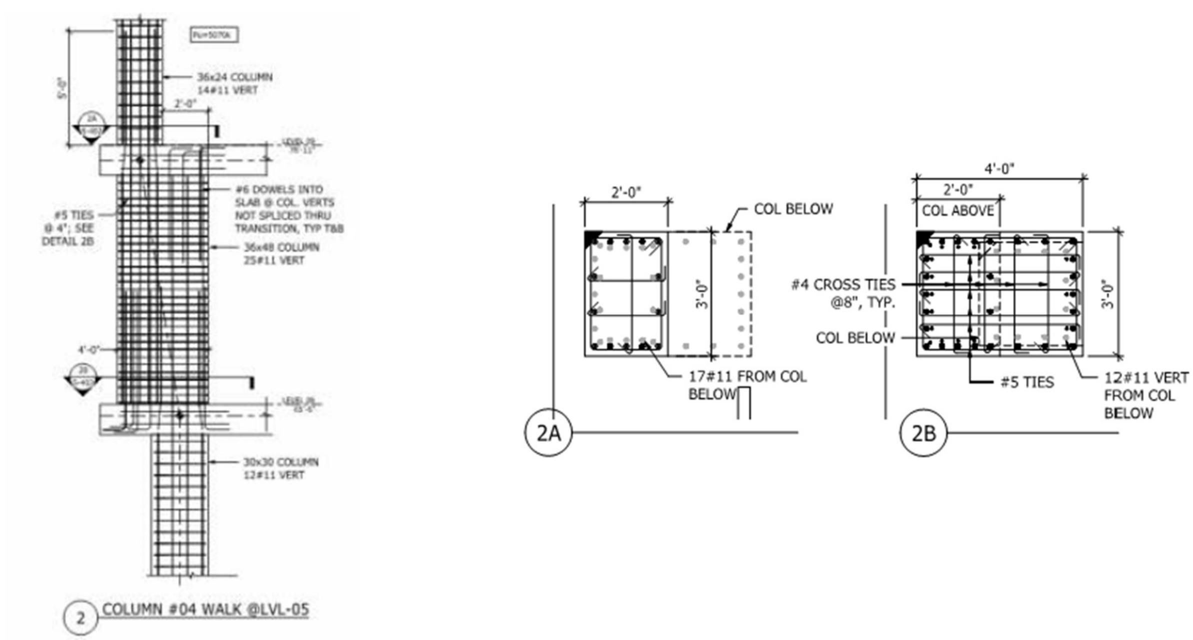

Figure 4.8: Cross section and reinforcing bar details of walking column Example 3.

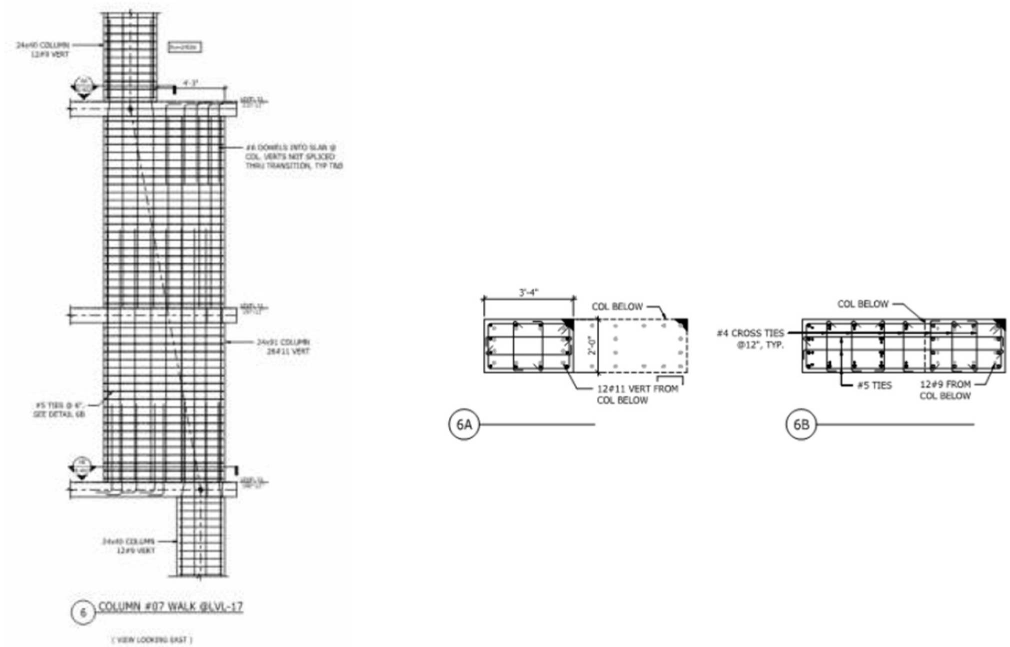

Figure 4.9: Cross section and reinforcing bars details of walking column Example 4.

4.4 ABAQUS Model Development and Analysis

In this section, walking column Example 1 was modeled using the ABAQUS software (2023) for finite element (FE) analysis. Example 1 is also modeled using IDEA StatiCa and analyzed in Section 4.5.1. The results from ABAQUS analysis are compared with those obtained from IDEA StatiCa in Section 4.7. In addition to the self-weight (i.e., Load 1), a vertical force (i.e., Load 2 representing the load in the upper column) of 4300 kips (19127.35 kN) was incrementally applied to a load-bearing plates with a thickness of 4 in, as shown in Figure 4.10a. The reinforcing bars, all made from Grade 60 steel (with f_y of 60 ksi or 413.7 MPa), were assembled in ABAQUS, as shown in Figure 4.10b. To simulate a more realistic scenario using ABAQUS, 12 reference points were defined 200 in. (5080 mm) away from the slab edges in both x and z directions. These reference points were then connected to the sides of the slabs using the connector builder module in ABAQUS. This technique allowed for the slabs to be artificially extended in the x and z directions (see Figure 4.10c).

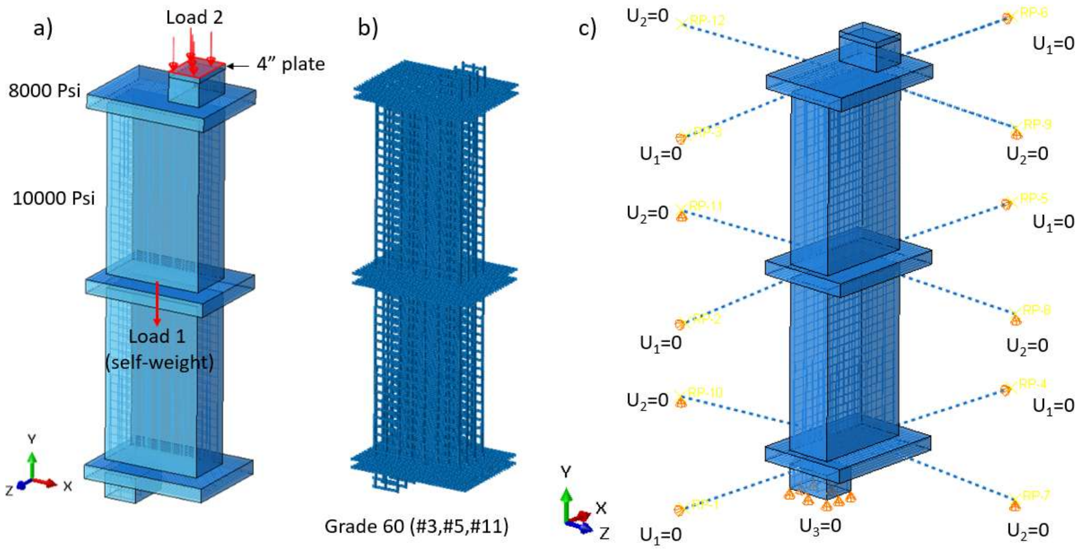

Figure 4.10: Model setup in ABAQUS showing: a) the locations and details of the applied load, b) reinforcement bars details, and c) boundary conditions.

For the boundary conditions, the bottom of the model was fixed to prevent vertical displacement, while the reference points were constrained to restrict lateral movement (see Figure 4.10c again). To accurately capture the crack initiation and evolution, the element size was chosen to be 1 in. (25.4 mm), resulting in a total of 724,504 elements in the model (see Figure 4.11). The concrete was modeled using 3D stress, 8-node linear brick reduced integration elements (C3D8R), while the reinforcing bars were modeled using 1D or axial truss elements (T3D2).

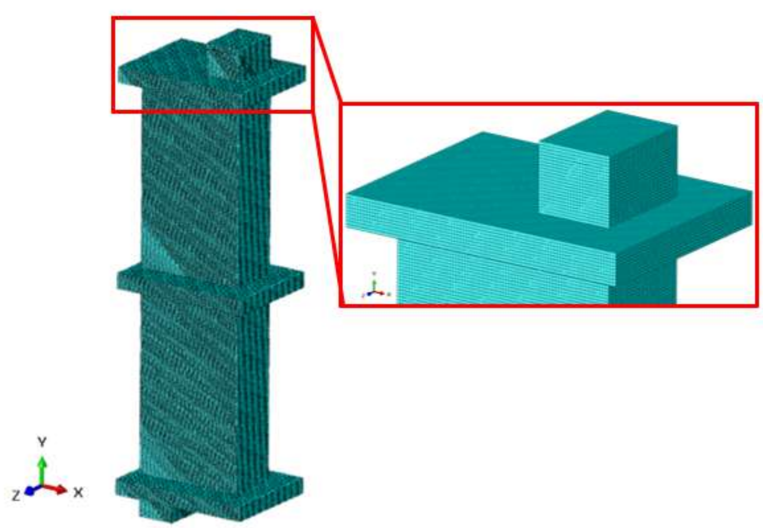

Figure 4.11: Mesh density with element size of 1 in. (25.4 mm).

The embedded region constraint was imposed to incorporate the steel bars within the Example 1 model (see Figure 4.12). Additionally, a general surface-to-surface contact was defined between the load bearing plate and the concrete part. In ABAQUS, the Concrete Damage Plasticity (CDP) constitutive model was employed to represent the concrete's response under loading conditions. The required parameters to describe this model were obtained after calibration from a model given in FHWA (2006), as they were not explicitly indicated in the original document by Schwinger (2021). For the steel bars, the material behavior was modeled using bi-linear plasticity. Other parameters, including density, elastic modulus, and Poisson's ratio, were taken exactly from the IDEA StatiCa materials library. The numerical simulation was carried out on a virtual machine with 16 processors (Intel Xeon® Gold Processor 6430 @2.10GHz) and took approximately 65 minutes to finish, while the IDEA StatiCa analysis (see Section 4.5.1) was completed in less than 100 seconds.

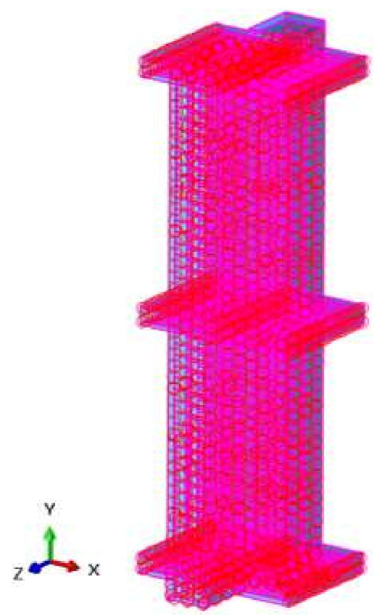

Figure 4.12: Embedded region constraint between the steel bars (depicted in red) and concrete (shown in pink).

The predicted crack initiation and evolution using the ABAQUS model is shown in Figures 4.13 a-c. The initial crack appeared near the bottom, close to the location where the model was fixed, and subsequently propagated vertically through the lower portion of the structure. This was followed by a separate crack on top slab. To visualize the failure of the structure, the applied load was increased in the model, and the result is shown in Figure 4.13d. The numerical result indicates that the structure initially experienced flexural cracking, which later transitioned to shear cracking.

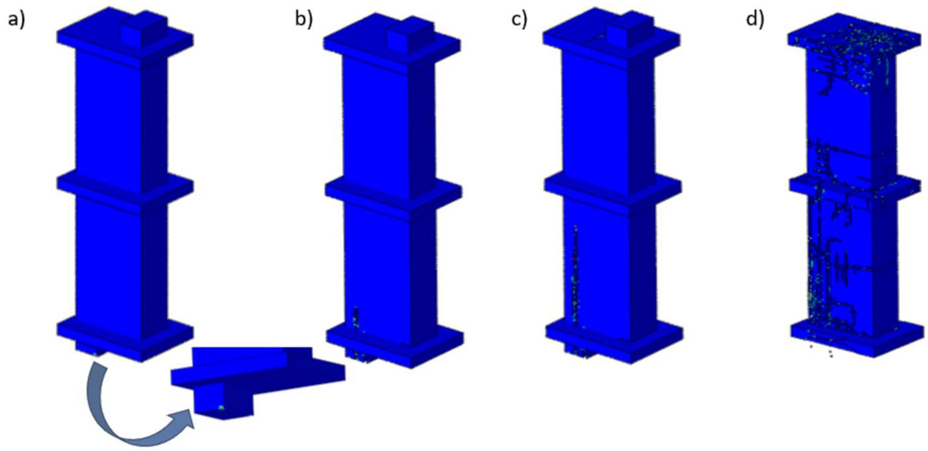

Figure 4.13: a) Crack initiation, b-c) crack evolution, and d) predicted failure pattern by ABAQUS.

Figure 4.14 illustrates a comparison of the vertical displacements of Specimen 1 predicted by IDEA StatiCa (see Section 4.5.1) and ABAQUS. The observed difference between the two results is 49%, which may be attributed to the imposed boundary conditions in the 2D (i.e., IDEA StatiCa) and 3D (i.e., ABAQUS) models. In addition, full bonding between bars and concrete were assumed in ABAQUS, which may reduce the overall displacement of the entire structure.

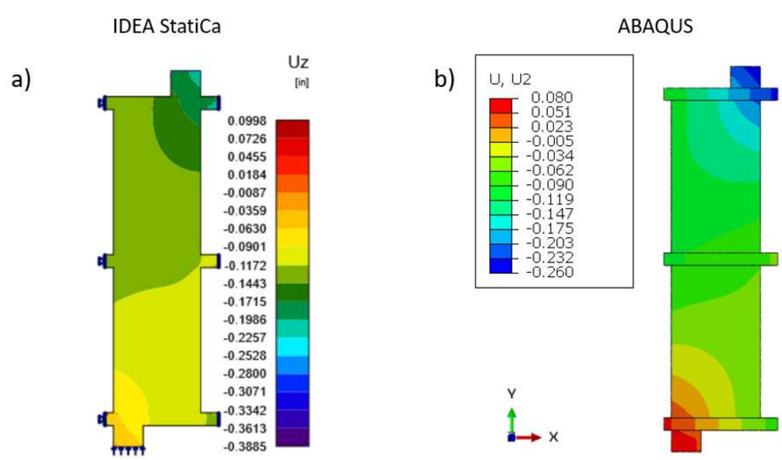

Figure 4.14: Comparison of the vertical displacement between a) IDEA StatiCa model, and b) ABAQUS model.

The calculated and predicted directions of principal stresses from IDEA StatiCa (see Section 4.5.1) and ABAQUS, respectively, are presented in Figure 4.15. Both models offer comparable results, resembling bottle-shaped struts. This suggests that the overall response of the specimen is consistent between the two models, supporting the use of the calculated response to develop a more realistic strut-and-tie model (as done in Section 4.6).

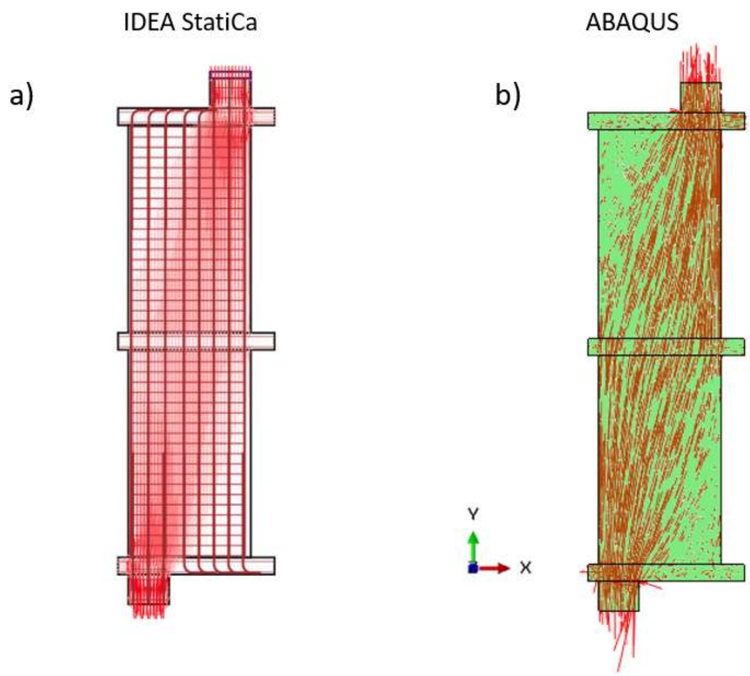

Figure 4.15: Comparison of the direction of principal stresses calculated using the IDEA StatiCa and ABAQUS models.

Figure 4.16 compares the calculated principal stresses in concrete using IDEA StatiCa (see Section 4.5.1) and those predicted by the ABAQUS model. In IDEA StatiCa, the minimum predicted stress was -7.5 ksi (-51.72 MPa), whereas the ABAQUS model predicted a minimum stress of -9.83 ksi (-67.78 MPa) at the same location, above the bottom column. The slight discrepancy in stress distribution can be attributed to several factors, including variations in boundary conditions, the finer mesh employed in the 3D model of ABAQUS, and differences in the constitutive models for concrete between IDEA StatiCa and ABAQUS models (such as the neglect of strain-based failure criteria for concrete in compression in IDEA StatiCa). Furthermore, discrepancies in element types (solid 3D elements in ABAQUS versus 2D shell elements in IDEA StatiCa) and the use of embedded region constraints in ABAQUS versus the bond-slip method in IDEA StatiCa likely contributed to these differences. Additionally, as a 2D solver, IDEA StatiCa cannot capture through-the-thickness properties while computationally it is extremely efficient.

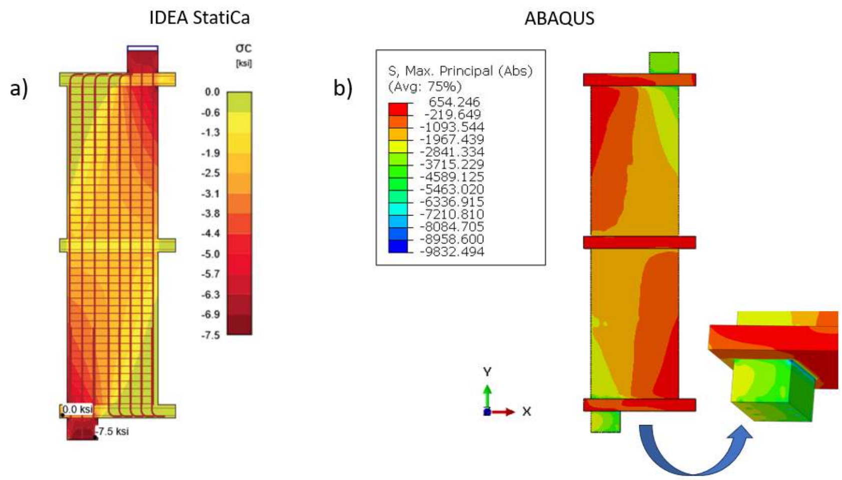

Figure 4.16: Comparison of the calculated principal stresses in concrete a) IDEA StatiCa, and b) ABAQUS.

Figure 4.17 depicts a comparison between the calculated principal strains in concrete using IDEA StatiCa and those predicted by the ABAQUS model. In IDEA StatiCa, the minimum calculated strain was -25.7e-3, whereas the ABAQUS model predicted a minimum strain of -1.81e-3 ksi at the same location near the bottom as shown in Figure 4.17b.

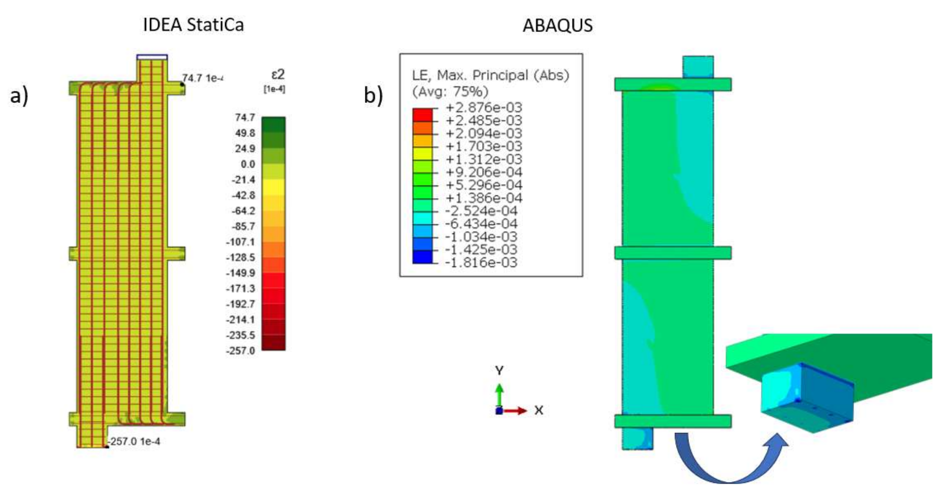

Figure 4.17: Comparison of the calculated principal strains in concrete a) IDEA StatiCa, and b) ABAQUS.

The calculated and predicted stresses in the steel bars from IDEA StatiCa and ABAQUS models are shown in Figure 4.18. In IDEA StatiCa, the calculated maximum and minimum stress values are 47.5 ksi (327.51 MPa) and -37.6 ksi (-259.25 MPa) , respectively, while ABAQUS predicted these values as 29.4 ksi (202.71 MPa) and -34.2 ksi (-235.81 MPa), respectively. The results show good agreement between the two software.

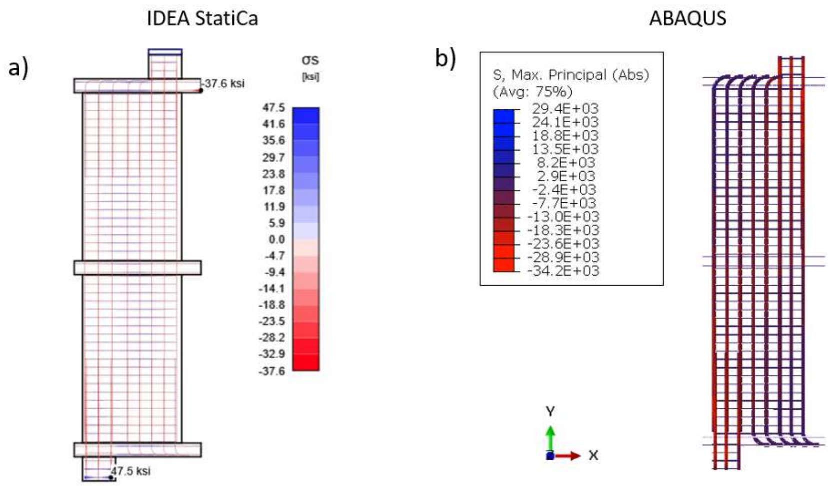

Figure 4.18: Comparison of the stresses in the steel bars between a) IDEA StatiCa, and b) ABAQUS.

Figure 4.19 shows the calculated strains in the steel reinforcement using IDEA StatiCa and ABAQUS. The maximum (tensile) and minimum (compressive) strain values calculated by IDEA StatiCa are 1.16e-3 and -1.3e-3, respectively, while the corresponding predicted values by ABAQUS are 1.01e-3 and -1.18e-3. The differences in results can be attributed to the use of the embedded region constraint in ABAQUS compared to the bond-slip method in IDEA StatiCa, as well as variations in load application methodologies between the two software. Bond-slip model and related cracking in IDEA StatiCa are possibly more accurate because tension stiffening and bar slip can be accounted for at large lateral displacements. On the other hand, no bar slippage is allowed because full bonding between the bars and concrete is assumed in the ABAQUS model.

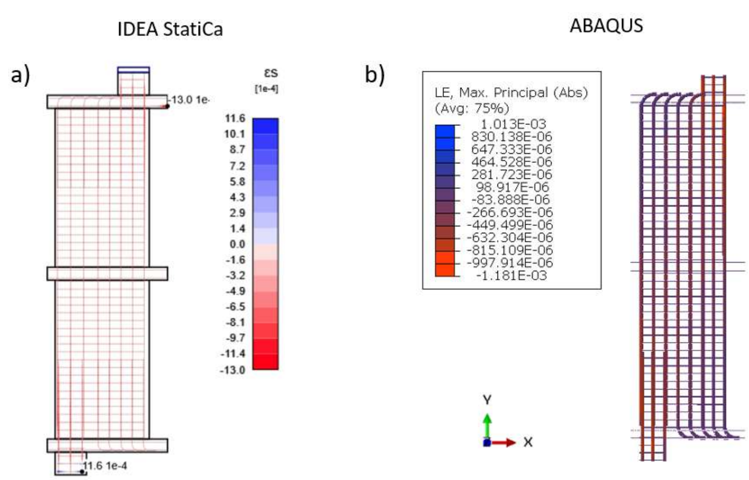

Figure 4.19: Comparison of the strains in the reinforcing bars between a) IDEA StatiCa, and b) ABAQUS.

4.5 IDEA StatiCa Analysis

The behavior of reinforced concrete walking columns (Examples 1 through 4, as described in Section 4.5) was analyzed using IDEA StatiCa software. These designs were selected to examine the effect of vertical load transfer mechanism on their structural performance. The modeling approach employed in IDEA StatiCa incorporated the specified compressive strength of concrete and the yield and ultimate strengths of the reinforcing steel bars, adhering to the parameters established by Schwinger (2021).

In the IDEA StatiCa analysis, load factors of 1.0 were applied to both load patterns—the self-weight and the applied vertical load—reflecting actual behavior without factoring for design safety. To determine the design and actual capacities of the walking column, different material factors were applied: for concrete (ϕ_c), values of 0.65 for design capacity and 1.0 for actual capacity were used; similarly, for reinforcing steel (ϕ_s), factors of 0.9 for design and 1.0 for actual behavior were employed. It is important to clarify that ACI 318-19 prescribes different strength reduction factors depending on the failure mode, such as ϕ = 0.9 for bending, ϕ = 0.75 for shear, and ϕ = 0.65 for axial bearing, rather than uniform factors for all cases. However, in this study, uniform material's strength reduction factors were employed within IDEA StatiCa to estimate the design capacity due to the lack of experimental data for the walking column. Currently, IDEA StatiCa software (version 24.0.6.1216) also does not provide the option to assign different strength reduction factors, ϕ for different failure conditions. Since CSFM is finite-element based continuous stress field analysis it will never be possible to apply different reduction factors in particular structural part.

4.5.1 Analysis of Baseline Model (Example 1)

The IDEA StatiCa model for the baseline model (Example 1) in this study was developed based on the material properties and reinforcing bars detailed in Tables 4.1 and 4.2. The analysis primarily focused on the vertical loads applied to the walking column, with the self-weight of the column considered a secondary load due to its relatively small magnitude. A downward vertical line load was applied across the entire column width (24 in. or 609.6 mm) at the top story. This load was gradually increased in 100 increments from zero to its peak using IDEA StatiCa. A 4 in. (101.6 mm) thick bearing plate was used at the top column in the specimen to support the applied vertical load. The bearing plate's dimensions, 24 in. by 34 in. (609.6 mm by 863.6 mm), matched the full cross-sectional area of the top column.

A line support at the base of the column, fixed in the vertical (z) direction, was included in the analysis. To provide lateral stiffness to the model, roller supports fixed in the horizontal (x) direction were applied at all floor levels on either side of the slab. This arrangement represents the fixity conditions a column would experience in a real building with slabs. The width of the slab in the transverse or y direction was considered to be double (2*b*) the thickness of the middle wall or column (*b*) in that direction. The anchorage of the reinforcing bars within the slabs was assumed to be continuous in the directions where the slabs extend into the building.

The capacity calculation process for IDEA StatiCa involved incrementally increasing the applied vertical load at the top of the walking column until reaching any of the following conditions:

1. The concrete at any point in the model reached 100% of its strength capacity under the applied load.
2. The reinforcing steel reached 100% of its strength capacity under the applied load.
3. The anchorage steel reached 100% of its strength capacity under the applied load.

At an applied line load of 145 kip/in. (25.4 kN/mm), equivalent to a total vertical load of 145 kip/in. x 24 in. = 3,480 kips (15,481 kN) across the full column width (24 in. or 609.6 mm), the concrete reached 99.8% of its capacity near the bottom right corner of the lower column (Figure 4.20a). The reinforcing bars reached 84.5% of their capacity, while the anchoring steel was at 100% capacity, as illustrated in Figure 4.20a. Any further increase in load would exceed the concrete's strength, marking this as the maximum load capacity according to the IDEA StatiCa analysis using the CSFM Under this vertical load, the displacement in the x-direction for walking column Example 1 was calculated to be 0.27 in. (6.86 mm) at the bottom right corner of the lower column (Figure 4.20e), while the displacement in the z-direction was recorded as -0.39 in. (-9.91 mm) at the bottom right corner of the top slab (Figure 4.20f). The maximum principal stress in the concrete was -4.9 ksi (-33.79 MPa) at the bottom right corner of the first-story column (Figure 4.20c), and the maximum stress in the reinforcement reached 45.6 ksi (314.41 MPa) at the tie bars in the lower column (Figure 4.20d). The detailed results for walking column Example 1 under the applied vertical load of 3480 kips (15479.81 kN) are presented in Figure 4.20 from the IDEA StatiCa analysis.

Based on the CSFM analysis, it can be concluded that the regions immediately below the top column and above the bottom column are susceptible to failure likely initiating through the crushing of concrete at those locations. In contrast, the reinforcing bars, having reached 84.5% of their capacity, indicate that they have the potential to withstand additional vertical load before reaching their maximum limit.

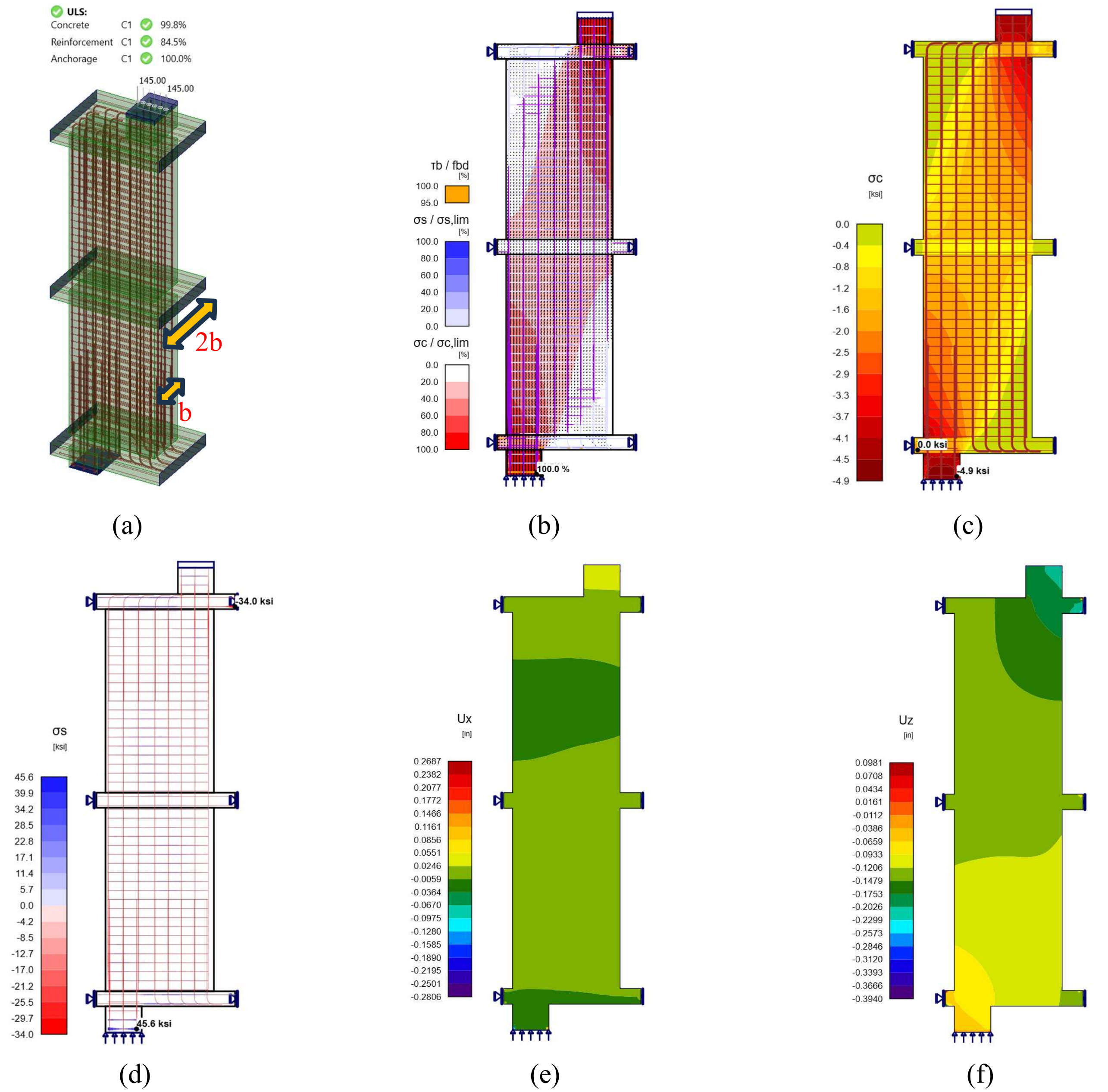

Figure 4.20: CSFM results for walking column Example 1: a) 3D view, b) stress flow, c) concrete principal stresses (σ_c), d) stresses in the reinforcement (σ_s), (e) displacement in x direction (U_x), and (f) displacement in z direction (U_z).

4.5.2 CSFM Analysis for Other Walking Column Examples

For walking column Example 2, the results are presented in Figure 4.21. As illustrated in Figure 4.21a, an applied vertical line load of 119 kip/in (20.83 kN/mm), corresponding to a total load of

4,284 kips (19,061 kN), results in the concrete reaching 99.6% of its capacity, while the reinforcing steel bars achieve 72.3% of their capacity at that point, and the anchorage reaches 100% of its limit. The maximum principal stress in the concrete is recorded at -4.9 ksi (-33.79 MPa), as shown in Figure 4.21c. The significant concentration of stress in the concrete inside the top-story column indicates that failure in walking column Example 2 is likely to initiate from concrete crushing at the top of the column. Additionally, Figure 4.21d reveals that the maximum stress in the reinforcing bars is 39.1 ksi (269.59 MPa), which remains well below the yield strength of the steel bars, measured at 60 ksi (414 MPa). This observation suggests that the steel rebars possess the capacity to withstand additional vertical loads and are less prone to failure compared to the concrete. Furthermore, the maximum displacement in the x-direction is noted as 0.12 in. (3.05 mm) at the lower right corner of the bottom column (Figure 4.22e), while the z-direction displacement reaches -0.24 in. (-6.10 mm) at the lower left corner of the top-story slab (Figure 4.22f).

Overall, walking column Example 2 is expected to fail due to the crushing of the concrete, as the concrete reaches its capacity, while the reinforcing steel still has the capacity to carry additional load.

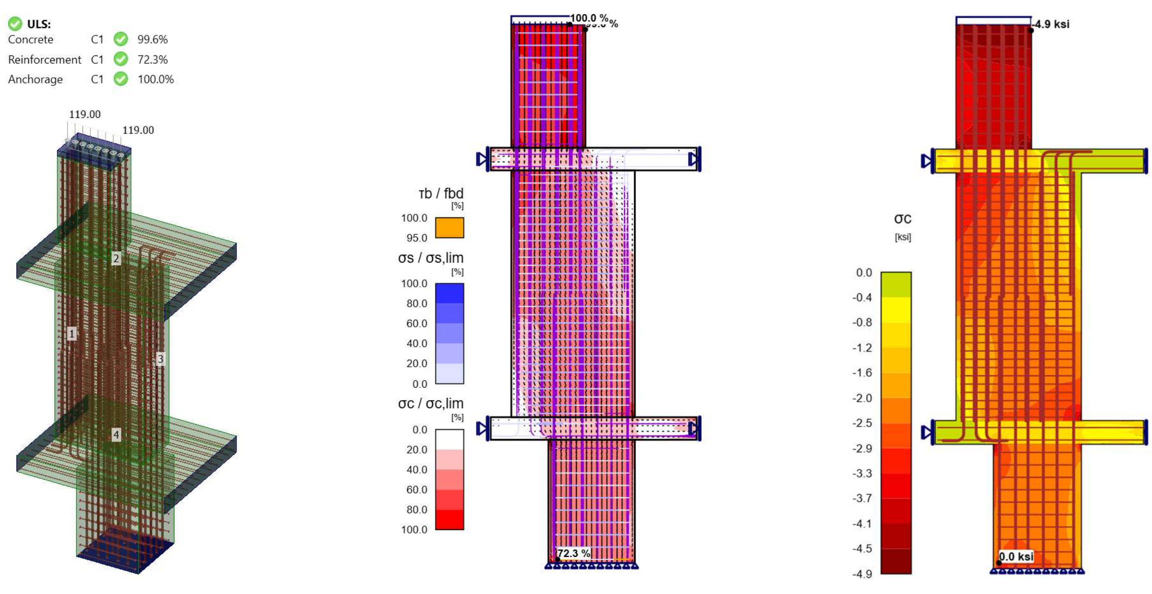

(a) (b) (c)

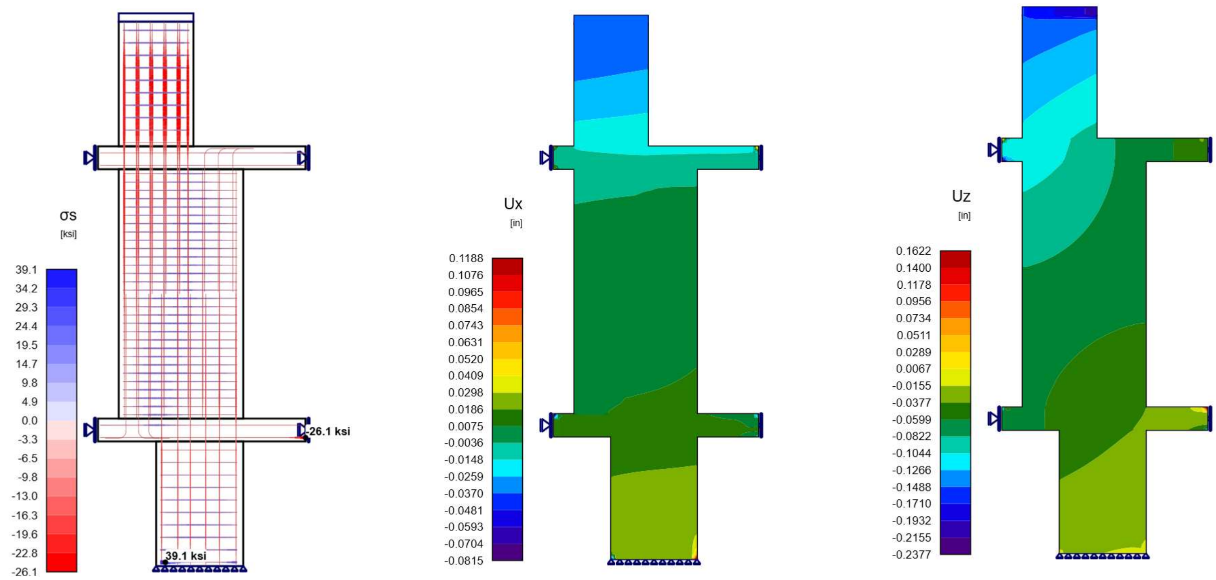

(d) (e) (f)

Figure 4.21: CSFM results for walking column Example 2: a) 3D view, b) stress flow, c) concrete principal stresses (σ_c), d) stresses in the reinforcement (σ_s), (e) displacement in x direction (U_x), and (f) displacement in z direction (U_z).

The CSFM results for walking column Example 3 are presented in Figure 4.22. As illustrated in Figure 4.22a, an applied line load of 165 kip/in (28.87 kN/mm), equivalent to a total load of 3,960 kips (17,615 kN), results in the concrete reaching 99.9% of its capacity, while the reinforcing bars in the column attain 99.0% of their capacity, and the anchorage reaches 100% of its capacity. The maximum principal stress, observed at -4.9 ksi (-33.79 MPa), is concentrated at the bottom of the first-story column, as indicated by the CSFM analysis in Figure 4.22c. This significant concentration of stress suggests that the first-story column is particularly vulnerable to failure under the applied load, primarily due to concrete crushing. The displacement results reveal a maximum displacement in the x-direction of 0.42 in. (10.67 mm) at the lower right corner of the bottom column (Figure 4.22e), while a displacement of -0.32 in. (-8.13 mm) is noted in the z-direction at the bottom left corner of the top-story slab (Figure 4.22f).

Overall, the analysis indicates that walking column Example 3 is nearing failure, with the concrete at the bottom of the first-story column identified as the most critical area. Additionally, the steel reinforcement, having reached 99% of its capacity, suggests that both the concrete and reinforcement are operating at their structural limits under the applied load, indicating that failure is likely to occur due to concrete crushing.

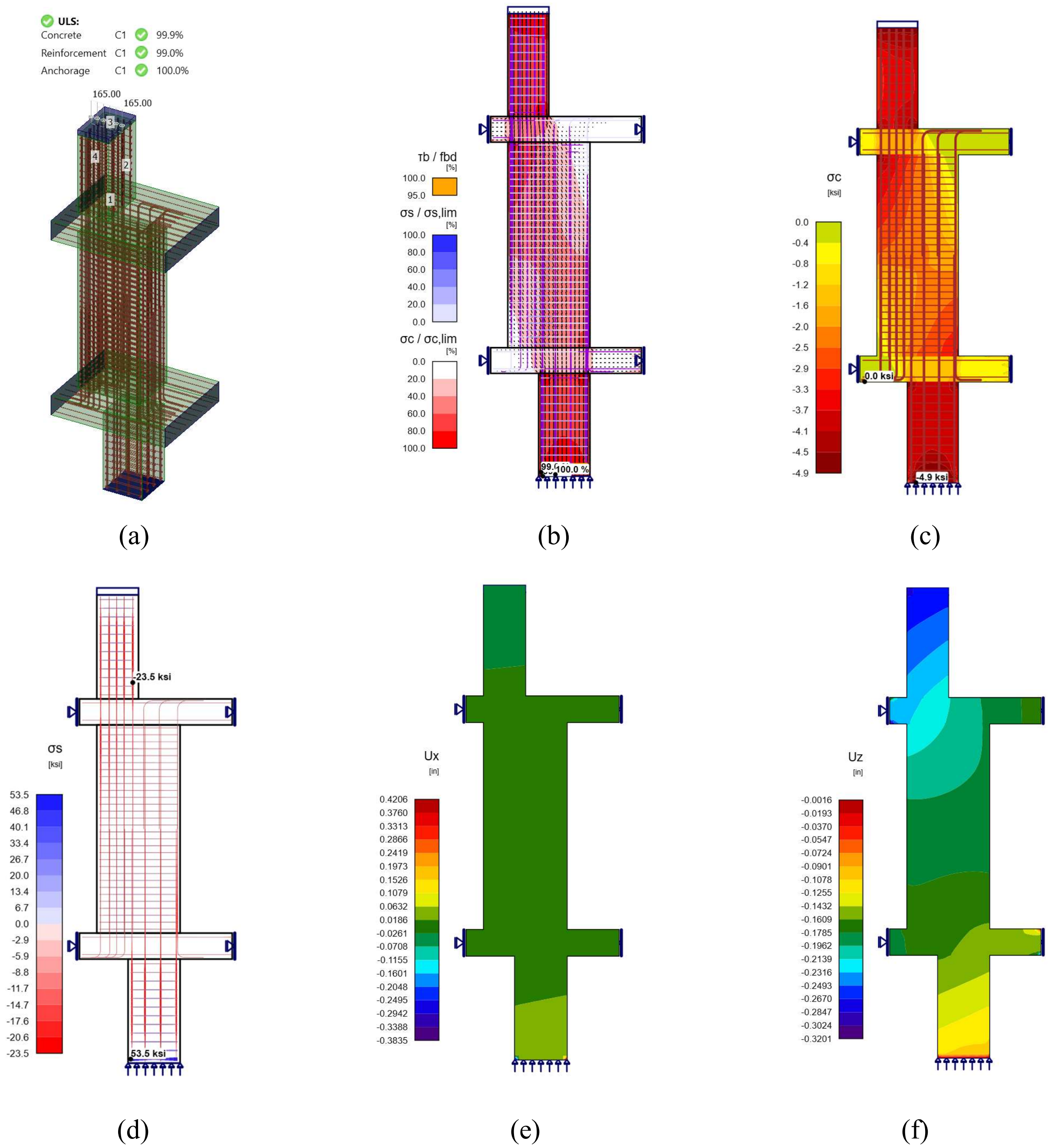

Figure 4.22: CSFM results for walking column Example 3: a) 3D view, b) stress flow, c) concrete principal stresses (σ_c), d) stresses in the reinforcement (σ_s), (e) displacement in x direction (U_x), and (f) displacement in z direction (U_z).

For walking column Example 4, an applied line load of 107 kip/in (18.73 kN/mm), which corresponds to a total load of 4,280 kips (19,038 kN), caused failure (Figure 4.23). Under this load, the concrete reaches 99.9% of its capacity, the reinforcement attains 100% of its capacity, and the anchorage exceeds its limit at 100.1% of capacity. The CSFM analysis indicates that the principal stress in the concrete is -4.9 ksi (-33.79 MPa) at the bottom-story column, suggesting that this region is highly stressed and particularly vulnerable to failure (Figure 4.23c). Moreover, the maximum stress in the reinforcing bars is recorded at -54 ksi (372.32 MPa) in the top-story slab (Figure 4.23d). Displacement analysis reveals a maximum displacement in the x-direction of 0.45 in. (11.43 mm) at the bottom right corner of the first-story column (Figure 4.23e), while a maximum displacement of -0.79 in. (-20.07 mm) occurs in the z-direction at the top right corner of the first-story slab (Figure 4.23f).

These results indicate that under the applied load, both the concrete and reinforcement in walking column Example 4 are approaching their structural limits, with failure likely to initiate due to the excessive stress experienced by both materials. In particular, the concrete at the bottom of the column is more vulnerable to potential crushing failure.

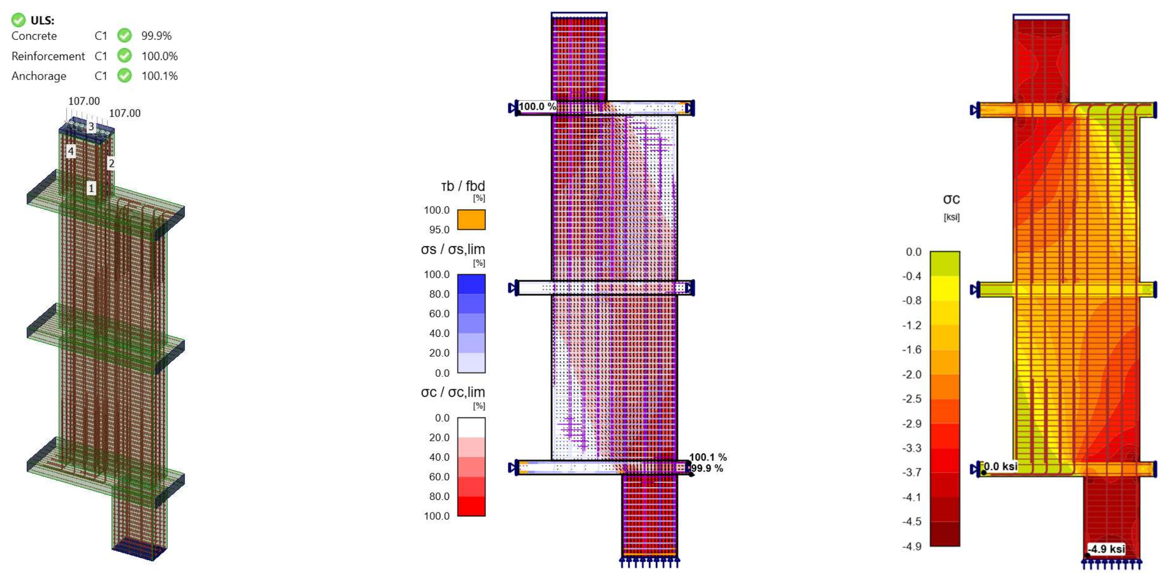

(a) (b) (c)

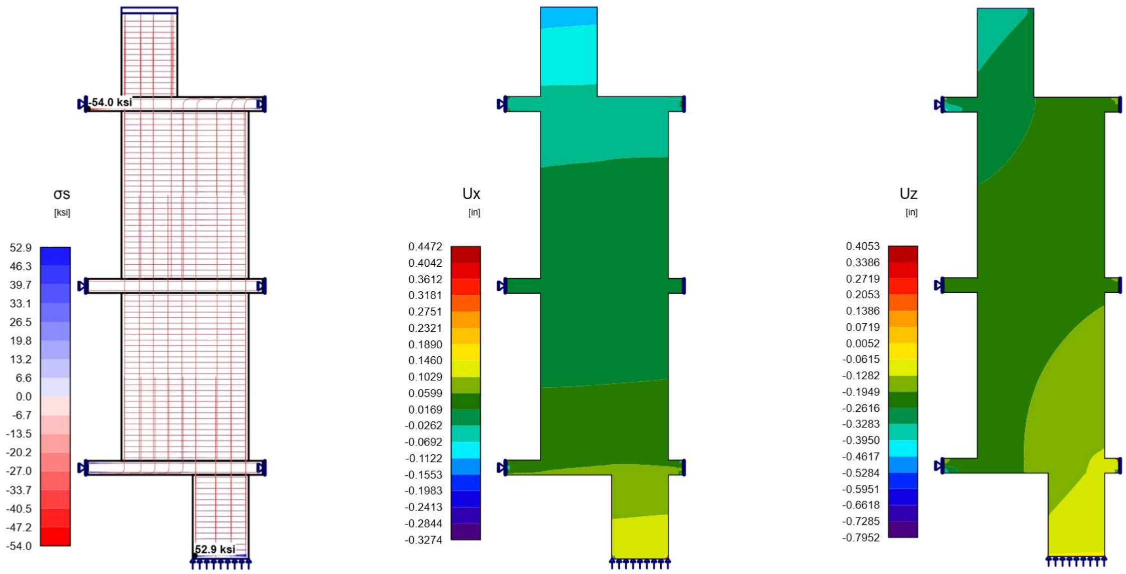

(d) (e) (f)

Figure 4.23: CSFM results for walking column Example 4: a) 3D view, b) stress flow, c) concrete principal stresses (σ_c), d) stresses in the reinforcement (σ_s), (e) displacement in x direction (U_x), and (f) displacement in z direction (U_z).

4.6 Capacity Calculation Using Strut and Tie Model

The capacity of the walking column examples was determined using the Strut and Tie Model (STM) methodology, as outlined in the ACI 318-19 code. The STM approach was applied to assess the performance of discontinuous regions, ensuring full compliance with the design principles established in Chapter 23 of ACI 318-19. By modeling force transfer through compressive struts and tensile ties, the STM method effectively represents the load distribution within the structure, particularly in areas with geometric discontinuities. For each walking column example, the design capacity was calculated using the STM framework, incorporating the appropriate strength reduction factors, ϕ as specified in ACI 318-19. The capacities of key structural elements within the walking columns were assessed, including:

- Capacity of the top column: The load-carrying capacity of the top column was calculated in accordance with the requirements for tied columns in ACI 318-19, taking into account both the concrete strength and the provided reinforcement.
- Capacity of the bottom column: Similarly, the capacity of the bottom column was calculated following the tied column provisions in ACI 318-19.
- Bearing capacity of the slabs: The bearing capacity of the slabs, located at the top and bottom of the columns, was evaluated to ensure sufficient concrete resistance against applied vertical forces.

- Vertical shear in the middle column/wall: The vertical shear capacity of the middle column or wall between the slabs was assessed to ensure that shear failure would not occur before the structure reaches its ultimate capacity.

The minimum capacity of these structural components was selected as the final design capacity for each walking column example, thereby identifying the most critical failure mode in accordance with ACI 318-19 code. In the analysis, the effective compressive strength of concrete, f_{ce} in the struts and nodal zones was calculated using the relevant equations from ACI 318-19, as detailed in Section 2.3 of Chapter 2 of this study. The strut and node confinement modification factor β_c, strut coefficient β_s, and nodal zone coefficient β_n were determined using the values from Tables 2.1 to 2.3 in Chapter 2, respectively. The effective compressive strengths of concrete in strut and nodal zones were computed using Equations 2.4 and 2.9, respectively.

During the analysis, topology optimization techniques were employed to identify the most efficient stress flow paths within the structure. This process was carried out by IDEA StatiCa using effective volumes of 20% and 60%, which contributed to refining the STM design by optimizing load distribution through the struts and steel ties. This approach allowed for the creation of a more effective strut and tie model, with properly sized struts to ensure accuracy in force transmission.

Lastly, the STM models for each walking column example were developed utilizing stress flow diagrams and topology optimization plots generated through IDEA StatiCa software. These models provided a simplified yet precise representation of the load transfer mechanisms within the walking columns under the applied loads, effectively capturing the behavior of both compressive struts and tensile ties.

For walking column Example 1, a simplified STM was developed (Figure 4.24c). This model was informed by the topology optimization plots presented in Figures 4.24a and 4.24b. The model consists of two nodes: Node A, characterized by compression-compression-tension (CCT), and Node B, characterized by compression-compression-compression (CCC). A bottle-shaped strut (AB) was incorporated between the nodes. The analysis was conducted using a confinement modification factor β_c of 1.00, a strut coefficient β_s of 0.75, and nodal zone coefficients β_n of 0.80 for Node A and 1.00 for Node B.

The STM analysis revealed that an applied design load of 4158 kips (18495.7 kN) resulted in both nodes reaching their maximum capacity, with concrete crushing expected at these nodes under further loading. The capacities of different elements were subsequently evaluated according to ACI 318-19, revealing that the capacities of both the top and bottom columns were determined to be 4024 kips (17899.64 kN), calculated using Equations 22.4.2.1(a) and 22.4.2.2 from ACI 318-19, representing a 3.2% reduction from the STM capacity. The vertical shear capacity was assessed at 4500 kips (20016.99 kN) using Equation 9.9.2.1 from ACI 318-19, indicating an 8.2% increase over the STM capacity. Meanwhile, the capacity derived from the CSFM was calculated to be 3480 kips (15479.81 kN), 16.3% lower than the STM capacity. All the results for Example 1 are illustrated in Figure 4.25.

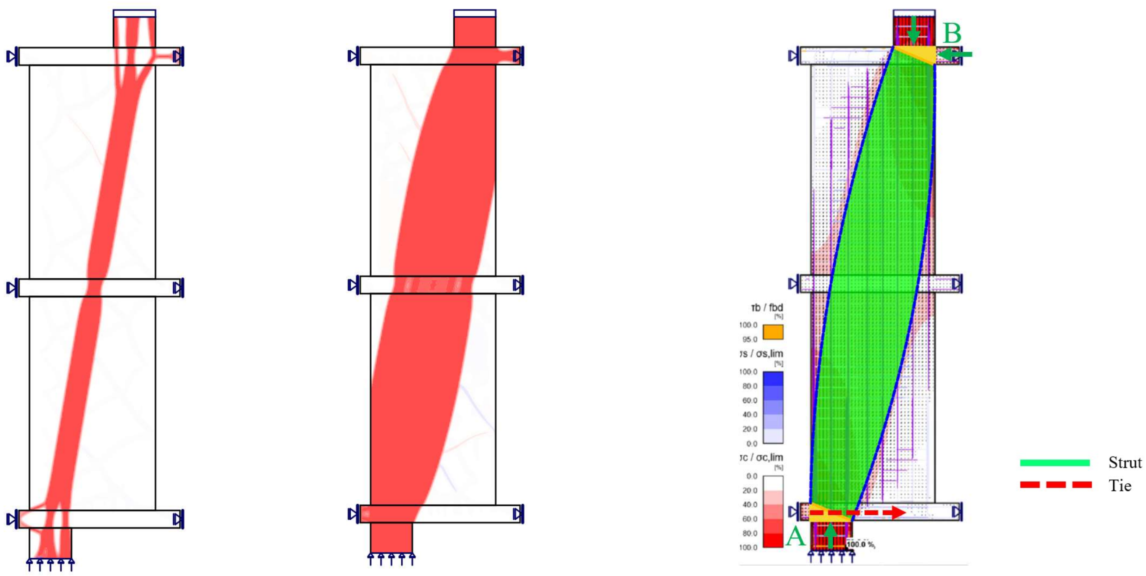

(a) (b) (c)

Figure 4.24: Strut and tie model for Example 1: a) topology optimization with 20% effective volume from IDEA StatiCa, b) topology optimization with 60% effective volume from IDEA StatiCa, and c) strut and tie model with stress flow.

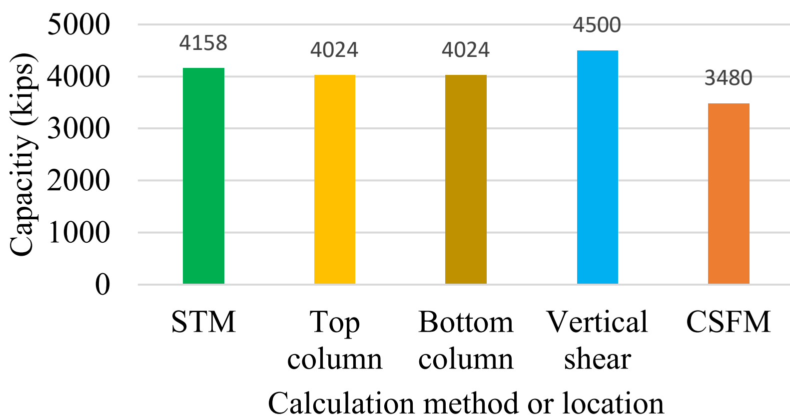

Figure 4.25: Capacity comparison among different elements of Example 1.

In walking column Example 2, a strut-and-tie model was formulated (Figure 4.26c) considering the topology optimization results displayed in Figures 4.26a and 4.26b. The model incorporates two nodes: Node A, characterized by compression-compression-compression (CCC), and Node B, characterized by compression-compression-tension (CCT), with a bottle-shaped strut connecting the nodes. The analysis utilized a confinement modification factor, β_c of 1.00, a strut coefficient, β_s of 0.75, and nodal zone coefficients, β_n of 1.00 for Node A and 0.80 for Node B.

The STM analysis determined that an applied load of 2350 kips (10453.32 kN) led Node B to reach its ultimate capacity, with concrete crushing anticipated under additional loading. The capacities of various elements were further examined in accordance with ACI 318-19. The top and bottom column capacities were found to be 4487 kips (19959.17 kN) and 8465 kips (37654.19 kN), respectively, determined using Equations 22.4.2.1(a) and 22.4.2.2 from ACI 318-19, indicating a 91% increase in the top column and a 260% increase in the bottom column capacities compared to the STM capacity. The vertical shear capacity was calculated using Equation 9.9.2.1 from ACI 318-19 and found to be 2,700 kips (12,010 kN), representing a 15% increase over the STM capacity. In contrast, the capacity derived from the CSFM was 4284 kips (19056.18 kN), reflecting an 82% increase relative to the STM capacity. These findings are summarized in Figure 4.27.

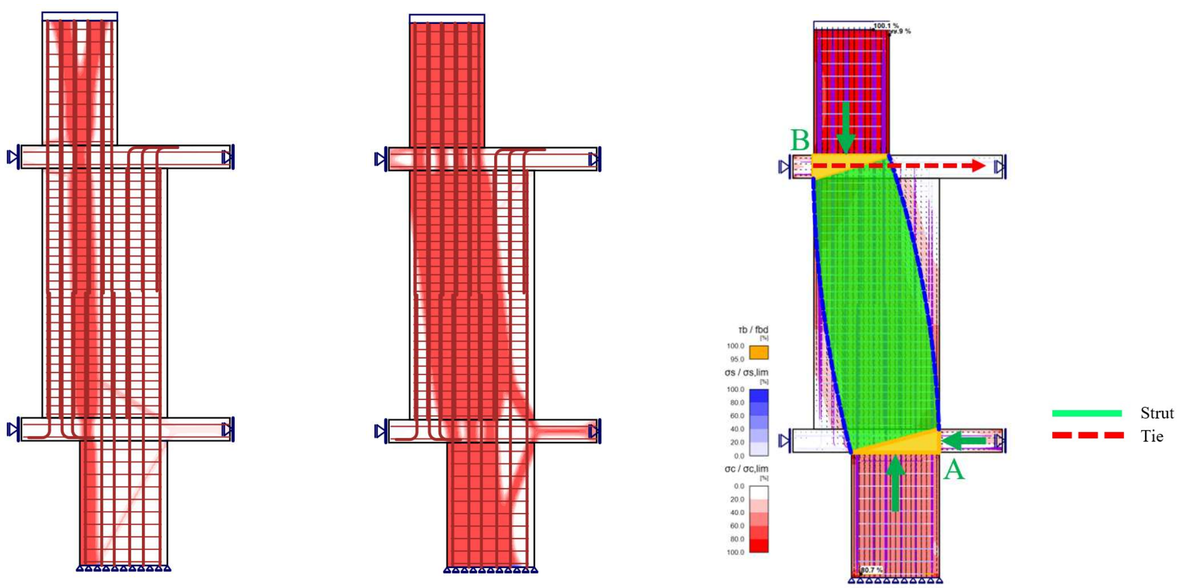

(a) (b) (c)

Figure 4.26: Strut and tie model for walking column Example 2: a) topology optimization with 20% effective volume from IDEA StatiCa, b) topology optimization with 60% effective volume from IDEA StatiCa, and c) strut and tie model with stress flow.

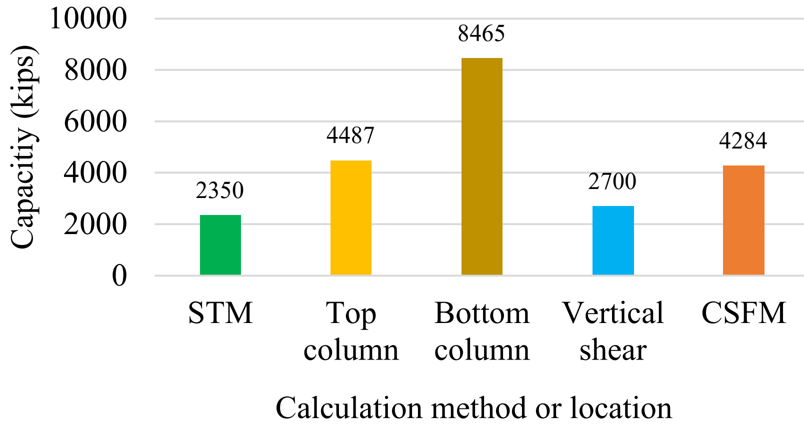

Figure 4.27: Capacity comparison among different elements of walking column Example 2.

For walking column Example 3, an STM was established (Figure 4.28c) based on the topology optimization diagrams illustrated in Figures 4.28a and 4.28b. This model incorporates two principal nodes: Node A, designated as CCC node, and Node B, designated as CCT node, which are interconnected by a bottle-shaped strut. The analysis utilized a confinement modification factor, β_c of 1.00, a strut coefficient, β_s of 0.75, and nodal zone coefficients, β_n of 1.00 for Node A and 0.80 for Node B.

The STM analysis indicated that the application of a load of 3525 kips (15679.98 kN) led to Node B achieving its maximum capacity when concrete reached its crushing strength. The capacities of the elements were assessed in accordance with ACI 318-19. The top and bottom column capacities were calculated using Equations 22.4.2.1(a) and 22.4.2.2 from ACI 318-19. The capacity of the top column was determined to be 4404 kips (19589.97 kN), while the capacity of the bottom column was found to be 4479 kips (19923.58 kN). This indicates an increase of 25% in the capacity of the top column and 27% in the capacity of the bottom column when compared to the STM capacity.

The vertical shear capacity was calculated using Equation 9.9.2.1 from ACI 318-19 as 3240 kips (14412.24 kN), reflecting an 8% decrease from the STM capacity. In contrast, the capacity derived from the CSFM was calculated to be 3960 kips (17614.96 kN), representing a 12% increase in comparison to the STM capacity. These results are compared in Figure 4.29. This analysis illustrates that the STM methodology yields a more conservative capacity prediction when compared to the CSFM approach.

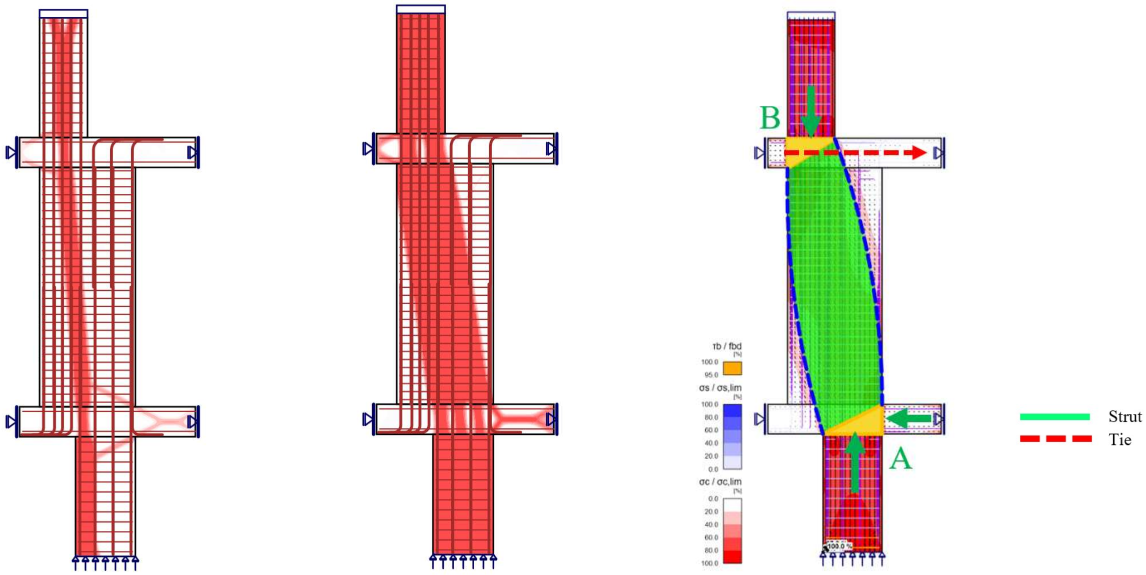

(a) (b) (c)

Figure 4.28: Strut and tie model for Example 3: a) topology optimization with 20% effective volume from IDEA StatiCa, b) topology optimization with 60% effective volume from IDEA StatiCa, and c) strut and tie model with stress flow.

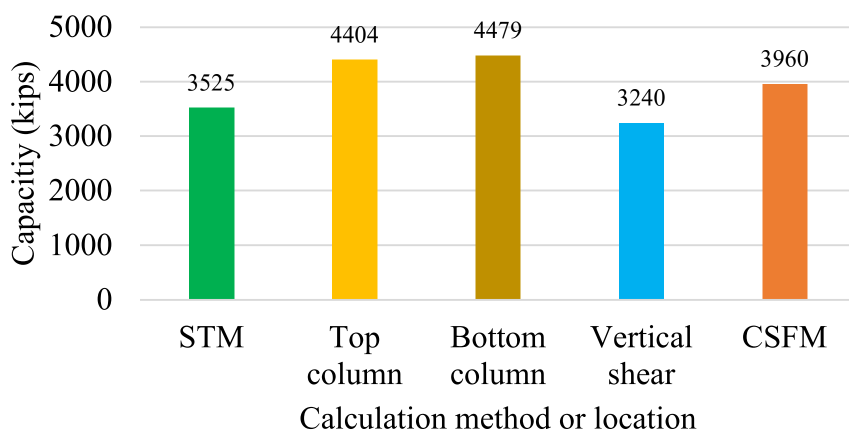

Figure 4.29: Capacity comparison among different elements of walking column Example 3.

In walking column Example 4, a STM was created (Figure 4.30c) based on the topology optimization diagrams presented in Figures 4.30a and 4.30b. The model comprises two main nodes: Node A, characterized by CCT, and Node B, characterized by CCC. These nodes are linked by a bottle-shaped strut. The analysis employed a confinement modification factor, β_c of 1.00, a strut coefficient, β_s of 0.75, and nodal zone coefficients, β_n of 0.80 for Node A and 1.00 for Node B.

The STM analysis revealed that the application of a load of 3917 kips (17423.68 kN) caused Node A to reach its ultimate capacity, with concrete crushing expected under further loading. Capacities of the structural elements were evaluated based on the provisions of ACI 318-19. The capacities of the top and bottom columns were calculated using Equations 22.4.2.1(a) and 22.4.2.2 from ACI 318-19, both demonstrating a capacity of 4745 kips (21106.81 kN), indicating a 21% increase in comparison to the STM capacity for both columns. The vertical shear capacity was calculated using Equation 9.9.2.1 from ACI 318-19 and found to be 4,500 kips (20,017 kN), reflecting a 15% increase over the STM capacity. Conversely, the capacity determined using the CSFM was 4280 kips (19038.39 kN), representing a 9% increase relative to the STM capacity.

It is important to note that the minimum capacity obtained from the STM analysis, 3917 kips (17423.68 kN), was selected as the ACI 318-19 capacity for design purposes, ensuring a more conservative and safe structural performance. These findings are illustrated in Figure 4.31 for the capacity comparison.

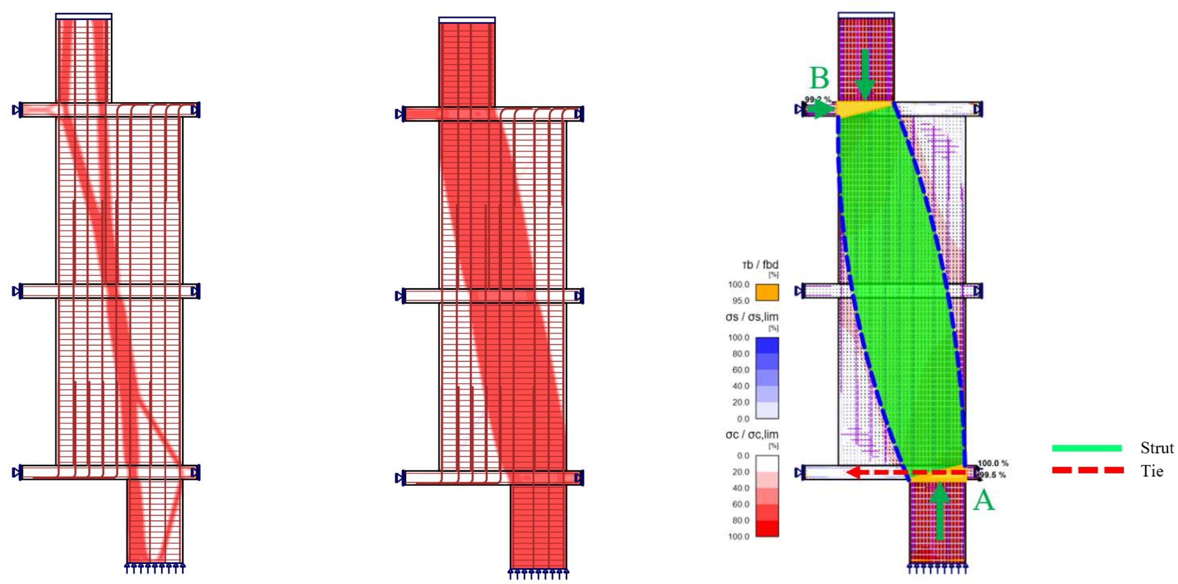

(a) (b) (c)

Figure 4.30:Strut and tie model for Example 4: a) topology optimization with 20% effective volume from IDEA StatiCa, b) topology optimization with 60% effective volume from IDEA StatiCa, and c) strut and tie model with stress flow.

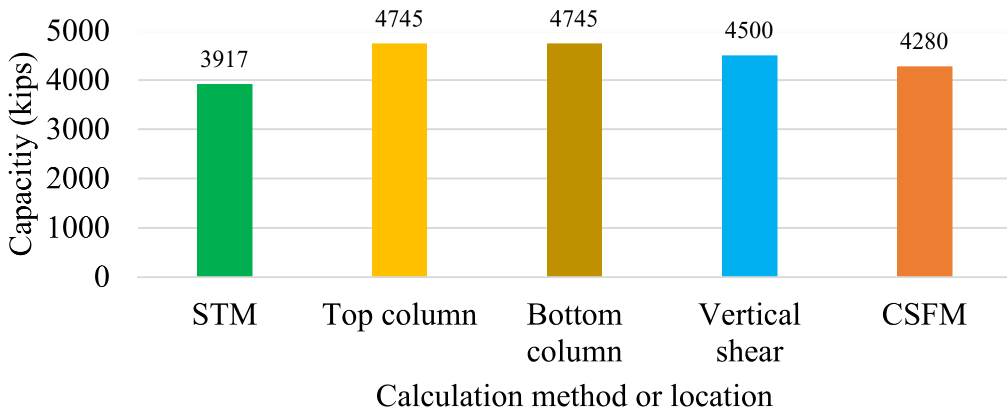

Figure 4.31:Capacity comparison among different elements of Example 4.

The comparison of capacities between the STM and CSFM across four walking column examples demonstrates the extent to which these methods align. In Example 1, the capacity predicted by CSFM (3480 kips or, 15479.81 kN) was approximately 16% lower than the capacity determined by STM (4158 kips or, 18495.7 kN). In Example 2, CSFM predicted a capacity of 4284 kips (19056.18 kN), which was significantly higher than the STM capacity of 2350 kips (10453.32 kN), reflecting an 82% increase. This variation may suggest that STM provides more conservative results, particularly in cases with specific geometries or load conditions.

In Example 3, the capacity predicted by CSFM (3960 kips or, 17614.96 kN) exceeded the STM capacity (3525 kips or, 15679.98 kN) by 12%, indicating a closer agreement between the two methods compared to the earlier examples. Similarly, in Example 4, CSFM yielded a capacity of 4280 kips (19038.39 kN), which was 9% higher than the STM capacity of 3917 kips (17423.68 kN).

Overall, it is observed that CSFM generally predicts higher capacities than STM, though the difference ranges from relatively minor (around 9%) to substantial (over 80%). In cases where the results are more comparable, such as Example 3 and Example 4, it may be concluded that CSFM captures design capacities with reasonable accuracy, while the STM method provides more conservative estimates. The notable difference in Example 2, however, suggests that additional considerations or validation may be needed for certain structural configurations.

In conclusion, while CSFM often predicts higher capacities, it is generally close to STM for practical design purposes, especially when differences are small. However, it's important to use CSFM carefully, as STM provides more conservative predictions that can help ensure safety margins.

4.7 Summary and Comparison of Results

The behavior of four walking column examples (Examples 1 through 4) was evaluated using the STM in accordance with ACI 318-19, along with IDEA StatiCa and ABAQUS. The baseline model, Walking Column Example 1, served as the reference for comparative analysis. A vertical load was applied to the top of each column to represent the design load, with strength reduction factors incorporated into the STM analysis based on ACI 318-19. Additionally, the maximum capacities of the walking columns were determined using the CSFM without the application of the ϕ values.

Table 4.3 compares the capacities of walking columns, evaluated using ACI 318-19, STM, and CSFM both with and without strength reduction factors, ϕ. The data reveal several patterns and distinctions in the behavior of the columns under varying analytical approaches. A detailed comparison of the results demonstrates that the capacities predicted by CSFM without ϕ are consistently higher than those obtained using STM and CSFM with ϕ, with variations depending on the specific example analyzed.

Table 4.3: Comparison of walking column capacities for different methods

Walking Column	ACI 318-19, kips (kN)	STM, kips (kN)	CSFM with ϕ, kips (kN)	CSFM without ϕ, kips (kN)
Example 1	4024 (17899.64)	4158 (18495.7)	3480 (15479.81)	5256 (23379.85)
Example 2	2350 (10453.32)	2350 (10453.32)	4284 (19056.18)	6588 (29304.88)
Example 3	3240 (14412.24)	3525 (15679.98)	3960 (17614.96)	5952 (26475.81)
Example 4	3917 (17423.68)	3917 (17423.68)	4280 (19038.39)	5320 (23664.54)

Additionally, Table 4.4 provides a summary of the failure modes for each walking column example across the three methods. For instance, in Example 1, STM and ACI 318-19 predict failure due to the crushing of node A or B, while CSFM identifies failure at the bottom of the column. Similarly, in Example 2, STM and ACI 318-19 predict crushing of node B, while CSFM forecasts failure of concrete at the top of the column. These differences in predicted failure modes highlight the variation in stress distribution and structural behavior captured by each method. The detailed results of failure modes for all walking column examples are summarized in Table 4.4, providing crucial insights into the failure mechanisms under different analytical approaches.

Table 4.4: Failure modes for all walking column examples

Failure modes			
Walking Column	STM	ACI 318-19	CSFM
Example 1	Crushing of node, A or B	Failure of top or bottom column	Failure of concrete at bottom column
Example 2	Crushing of node, B	Crushing of node, B	Failure of concrete at top column
Example 3	Crushing of node, B	Shear failure of mid wall or column	Failure of concrete at the middle of bottom column
Example 4	Crushing of node, A	Crushing of node, A	Concrete crushing at the middle of bottom column

In Figure 4.32, which provides a graphical comparison of the capacities across all methods and examples, the relationship between the different analytical approaches is clearly illustrated. The figure emphasizes the notable increases in capacity when strength reduction factors are not applied in the CSFM analysis. The visual representation distinctly shows how the capacities predicted by CSFM without ϕ values are consistently higher across all examples compared to both STM and ACI 318-19.

The graphical comparison in Figure 4.32 complements the data presented in Table 4.8, offering an intuitive understanding of the relative differences between the methods. It becomes evident that the inclusion of ϕ values significantly reduces the predicted capacity in both the CSFM and STM analyses, reinforcing the conservative nature of these strength reduction factors. This makes it easier to discern the impact of ϕ values on the structural performance predictions of walking columns.

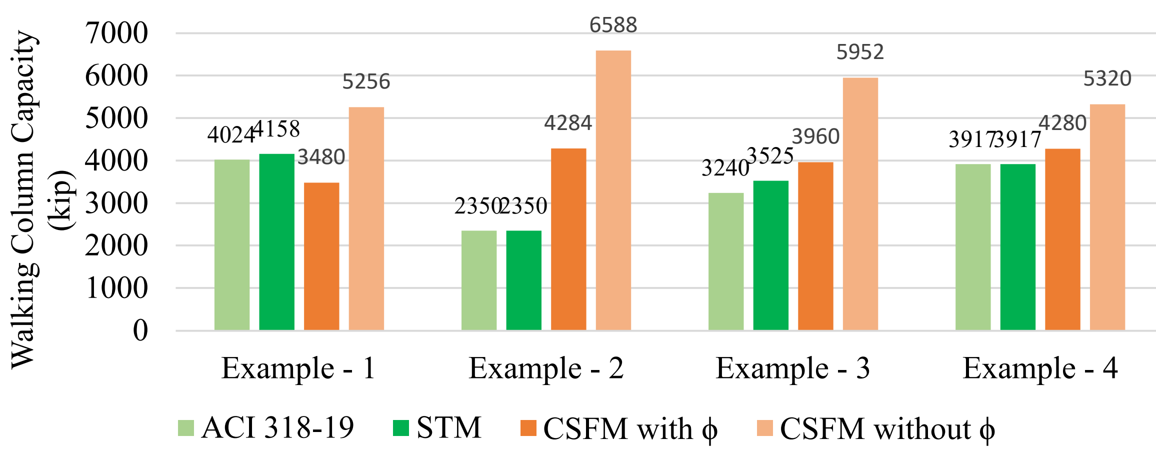

Figure 4.32: Capacity comparison for walking column examples.

The results presented in Figure 4.33 illustrates the capacities of Example 1, evaluated through various analytical methods: ABAQUS, ACI 318-19, STM, and CSFM with ϕ. The capacities predicted by ABAQUS at 4300 kips (19127.35 kN), STM at 4158 kips (18495.7 kN), and ACI 318-19 at 4024 kips (17899.64 kN) demonstrate a close alignment among these methods, suggesting a consistent approach to modeling the structural behavior of walking columns. Specifically, the differences between ABAQUS and STM are minimal, with STM yielding a capacity only 3.3% lower than ABAQUS, indicating that both methods effectively capture the performance of the column.

In comparison, the CSFM with ϕ analysis produced a capacity of 3480 kips (15479.81 kN), which, while lower than those from ABAQUS and STM, still reflects a reasonable prediction within the context of the expected behavior of walking columns. The difference of approximately 19.1% from the ABAQUS result may indicate a more conservative approach inherent in the CSFM methodology, which can be advantageous in design scenarios where safety and reliability are paramount.

Overall, the close results between ABAQUS, STM, and CSFM suggest that these methodologies are complementary, each contributing valuable insights into the capacity predictions of walking columns. The findings underscore the robustness of CSFM as a reliable method for structural analysis, while also validating the capacities predicted by ABAQUS and STM.

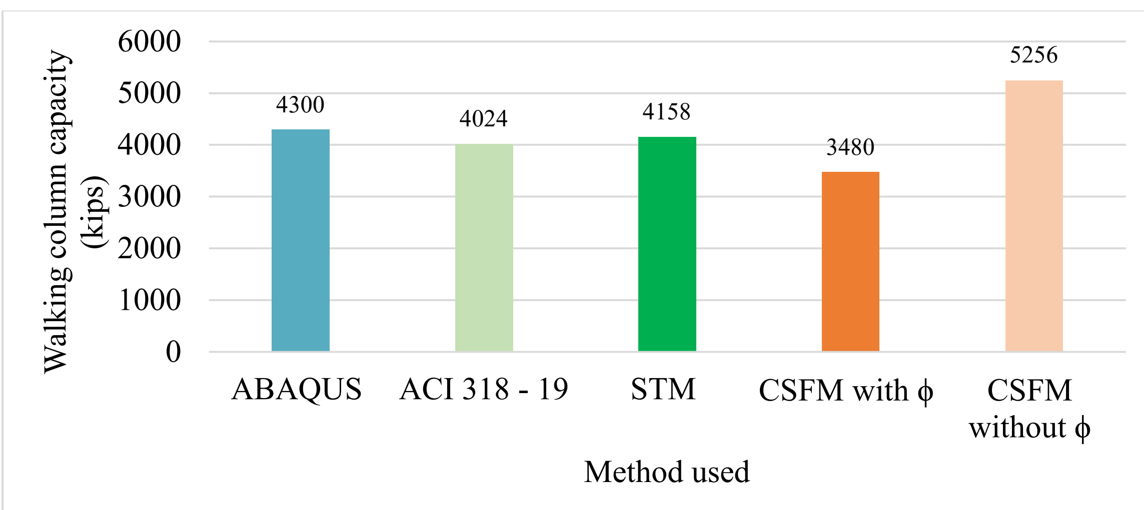

Figure 4.33: Capacity comparison with ABAQUs for Example 1.

The results presented in Tables 4.8 and 4.9 and Figures 4.32 and 33 offer a comprehensive understanding of the behavior of walking columns under different analytical approaches, while also identifying critical failure modes for each example.

For Example 1, the STM capacity of 4158 kips (18495.7 kN) exceeds the ACI 318-19 value of 4024 kips (17899.64 kN) by 3.3%, suggesting that the STM provides a slightly larger estimate of the walking column's capacity. Additionally, the ABAQUS analysis predicts a capacity of 4300 kips (19127.35 kN), which is higher than both the ACI 318-19 and STM results. The difference of 3.4% between ABAQUS and STM indicates that ABAQUS may account for more nuanced material behavior or geometric effects, further supporting the reliability of its predictions. However, the CSFM analysis with ϕ results in a much lower capacity of 3480 kips (15479.81 kN), which is 13.3% less than the STM value, indicating the conservative nature of the strength reduction factors. When ϕ is not applied in the CSFM analysis, the capacity reaches 5256 kips (23379.85 kN), which is 26.4% higher than the STM value, demonstrating the significant impact of removing strength reduction factors. Comparatively, while ABAQUS provides a higher value than CSFM with ϕ, the latter still plays a crucial role in ensuring safety by incorporating conservative assumptions.

The failure mode data in Table 4.9 show that the primary failure mechanism in STM involves crushing at nodes A or B, which aligns with the overall behavior calculated using ACI 318-19, where failure occurs at either the top or bottom of the column. In contrast, the CSFM analysis identifies failure at the bottom of the column, suggesting that the behavior captured by CSFM highlights critical stress concentrations at the base. Overall, these results underscore the utility of each method in predicting the capacity of walking columns. While ABAQUS offers a valuable benchmark with its higher capacities, the conservative approach of CSFM ensures that potential failure modes are adequately considered, contributing to a more comprehensive understanding of structural performance.

In Example 2, the discrepancy between the STM [2350 kips (10453.32 kN)] and CSFM with ϕ [4284 kips (19056.18 kN)] capacities is striking, with the CSFM value being 82.3% higher. Without ϕ, the CSFM capacity surges to 6588 kips (29304.88 kN), representing a 180.3% increase over the STM result. This considerable difference suggests that the design assumptions inherent in STM are much more conservative for this particular column configuration. The failure modes from Table 4.9 reinforce this observation. Crushing of node B is identified as the critical failure point in both STM and ACI 318-19 analyses, while CSFM predicts failure at the top of the column, indicating a shift in the failure pattern under different loading assumptions.

For Example 3, the STM capacity [3525 kips (15679.98 kN)] is 8.8% lower than the CSFM with ϕ result [3960 kips (17614.96 kN)], indicating that the CSFM with ϕ captures slightly higher strength. When ϕ is not applied, the capacity rises to 5952 kips (26475.81 kN), reflecting a significant 68.8% increase compared to the STM value. This difference underscores the conservatism embedded in the STM approach. The failure mode for STM, which involves crushing of node B, contrasts with the ACI 318-19 mode, where shear failure occurs at the mid-wall or column. Meanwhile, the CSFM failure mode highlights failure at the middle of the bottom column due to concrete crushing. This suggests that CSFM more accurately captures stress concentrations in the bottom section, which could explain the higher capacities predicted by the method.

In Example 4, the STM and ACI 318-19 capacities are identical at 3917 kips (17423.68 kN), while the CSFM with ϕ value is slightly higher at 4280 kips (19038.39 kN), representing a 9.3% increase over the STM prediction. When ϕ is omitted, the CSFM capacity rises significantly to 5320 kips (23664.54 kN), which is 35.8% greater than the STM result. This indicates that, in Example 4, the STM and ACI 318-19 analyses align more closely with the CSFM results. The failure mode for STM is identified as crushing of node A, whereas the CSFM analysis predicts concrete crushing at the middle of the bottom column. This suggests that CSFM captures stress distributions differently, focusing on potential failure at the bottom rather than at node A. Although the capacity differences are not as pronounced in this example, the shift in failure modes among the different methods indicates that CSFM may provide a more nuanced understanding of the stress distributions leading to failure, particularly at the base of the column.

In summary, the comparative analysis of the capacities of walking columns using ABAQUS, STM, and CSFM reveals notable patterns and relationships among these methods. The results indicate that ABAQUS consistently provides higher capacity estimates than both STM and CSFM, demonstrating its ability to capture complex material behaviors and loading conditions. The differences in capacities emphasize the conservative nature of the STM and CSFM with ϕ, which often leads to lower predictions compared to ABAQUS.

Overall, the CSFM analysis has proven to be a reliable tool for evaluating the capacities of walking columns. Its ability to offer insights into potential failure mechanisms and structural performance enhances its value in design applications. The flexibility of CSFM in adjusting for various loading scenarios and its sensitivity to strength reduction factors make it a beneficial method for structural engineers. Therefore, incorporating CSFM alongside other analytical approaches can lead to a more comprehensive understanding of the performance of walking columns, ultimately contributing to more robust and effective structural engineering practices.

References

ACI Committee 318. (2019). *Building Code Requirements for Structural Concrete (ACI 318R-19)*. Farmington Hills, Michigan: American Concrete Institute.

Schwinger, C. (2021, October 20). *Walking columns – A proposed design methodology* [Presentation]. Seminar organized by the Delaware Valley Association of Structural Engineers, Eastern Chapter of the Structural Engineers Association of Pennsylvania. https://www.dvase.org/docs/Breakfast%20Seminar/2021oct.pdf

Dassault Systèmes. (2023). ABAQUS – 2023: Standard User's Guide. Simulia Corp.

Herzog & de Meuron. (2016). *56 Leonard Street*.

Lubell, S. (2015, April 23). *NYC's Jenga tower: Herzog & de Meuron's new 56 Leonard*. *The Architect's Newspaper*.

Thornton Tomasetti. (1987). *Chicago Mercantile Exchange Center*.

Simpson Haugh. (2004). *Beetham Tower, Manchester, UK*. Retrieved from

B. S. Taranath, "Cent Trust Tower, Miami, Florida," in *Reinforced Concrete Design of Tall. Buildings*, 2010, pp. 749-751.

SheerForce Engineering. (2021, December 15). *What is a walking column*. https://sheerforceeng.com/2021/12/15/what-is-a-walking-column/

5.0 Chapter 5 Summary, Conclusion, and Recommendations

In Chapter 1, the performance of seven reinforced concrete corbels was investigated using the Compatible Stress Field Method (CSFM) method, following the provisions of the Strut-and-Tie Model (STM) per ACI 318-19 for corbels C0 through C3, which were tested by Wilson (2017), and for corbels S1, S2, and S3, designed according to the STM provisions from AASHTO LRFD (2016) and tested by Khosravikia et al. (2018). Additionally, the baseline model (Corbel C0) was analyzed using both CSFM and ABAQUS to compare their accuracies. The results were compared with experimental data, focusing on maximum load-carrying capacity and load versus displacement behavior.

The results highlight that the CSFM method consistently produced reliable predictions of the maximum load capacities for all specimens, closely aligning with the experimental data. The CSFM analysis outperformed traditional STM methods in estimating corbel performance, particularly for specimens C0 to C3, where the calculated capacities were in close agreement with experimental results (see Figure 5.1). The study also revealed the influence of the a_v/d ratio on corbel capacity, showing that the load-carrying capacity decreased as the a_v/d ratio increased.

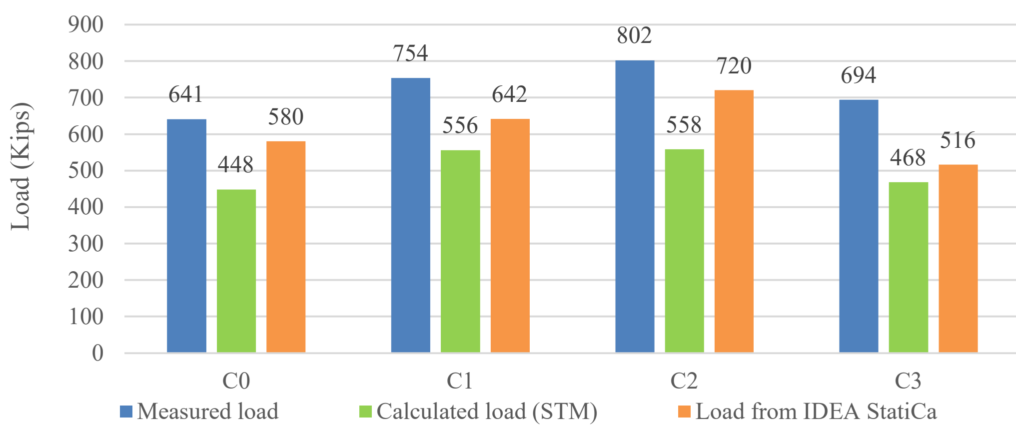

Figure 5.1: Comparison of measured, calculated (STM) and maximum load from CSFM for C specimens.

In comparison, the results for specimens S1, S2, and S3 showed slight discrepancies, with CSFM predicting slightly higher strengths for S1 and S3, and a lower strength for S2 (see Figure 5.2). These differences may be attributed to variations in material properties or boundary conditions during experimental testing which could not be fully implemented in IDEA StatiCa as a 2D software package.

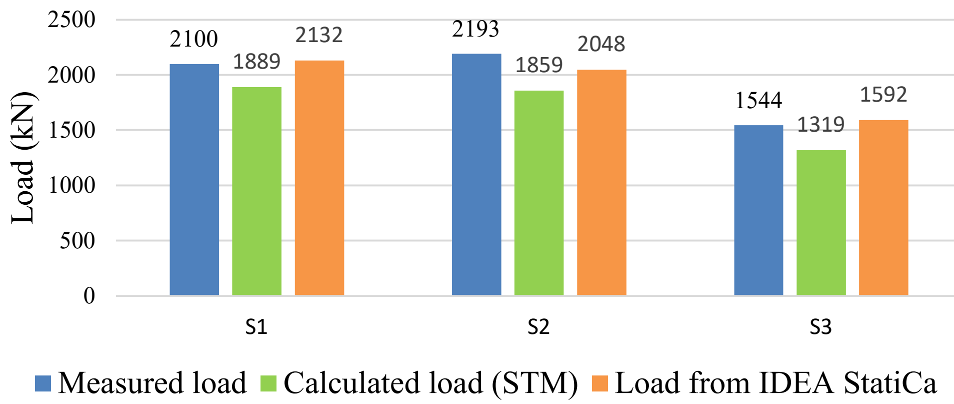

Figure 5.2: Comparison of measured, calculated (STM), and maximum load from IDEA StatiCa for S specimens.

Furthermore, a comparison between CSFM and ABAQUS for the baseline specimen C0 demonstrated that both software tools produced closely matching predictions (see Figure 5.3), with only minor differences in stress and load estimations. The load versus displacement curves, however, indicated that IDEA StatiCa tended to predict lower displacements compared to experimental results, particularly for C-specimens, likely due to modeling simplifications.

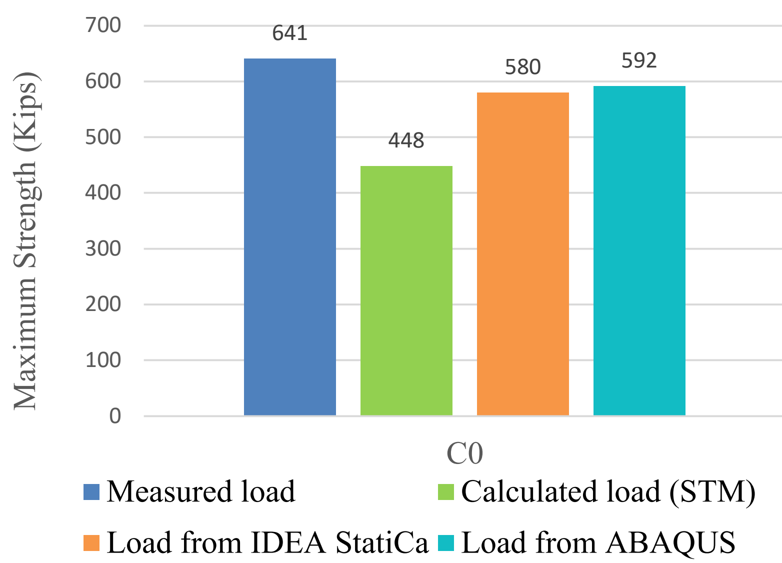

Figure 5.3: Comparison of measured, calculated (STM), and maximum strengths from IDEA StatiCa and maximum strength from ABAQUS for baseline model (C0).

Overall, Chapter 1 demonstrates the effectiveness and reliability of CSFM in analyzing reinforced concrete corbels. The CSFM analysis provides results that are comparable to ABAQUS and closely aligned with experimental data, making it a reliable tool for structural analysis and design.

However, the study also emphasizes the importance of validating analytical models with experimental data to ensure the accuracy and robustness of the predictions.

In Chapter 2, the structural performance of five reinforced concrete (RC) deep beams was examined using CSFM analysis through IDEA StatiCa, with their capacities also evaluated through the STM as per ACI 318-19. A comparative study was carried out between the results from CSFM for deep beam 1A and those from an equivalent ABAQUS model. The deep beams were modeled in IDEA StatiCa to accurately replicate their experimental behavior, and the resulting maximum load-carrying capacities and load versus displacement relationships were compared to experimental data.

Figure 5.4 highlights the comparison of measured loads from experimental tests with those predicted by STM and CSFM for the five deep beams. The results demonstrate that CSFM consistently aligned closely with the experimental outcomes, surpassing STM in terms of accuracy. For instance, CSFM predicted the load capacities of deep beams 1A, 1B, 2A, 3A, and 3B more accurately, with discrepancies between measured and predicted loads ranging from 5% to 26%. STM, being designed for conservative estimates, showed larger deviations from experimental results.

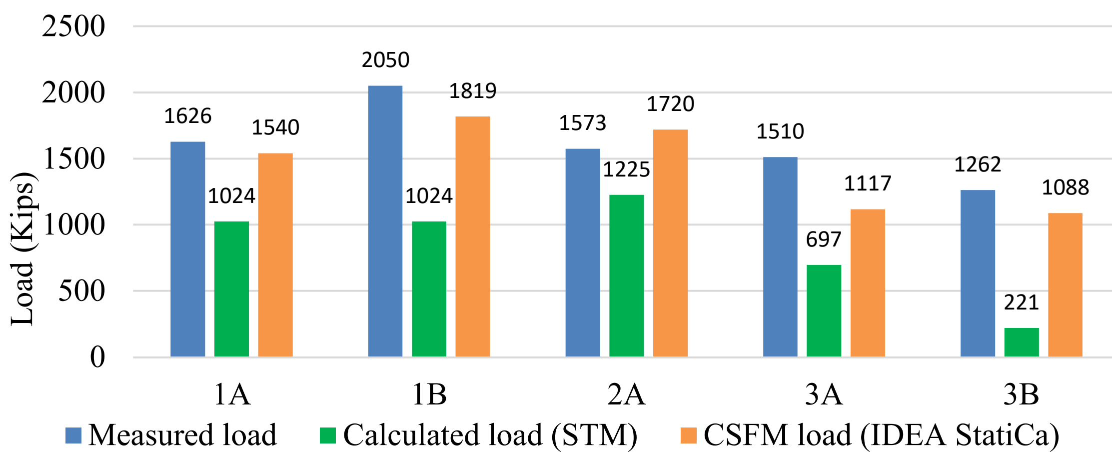

Figure 5.4: Comparison of measured, calculated (STM) and maximum load from CSFM for deep beam specimens.

Figure 5.5 compares the maximum load predictions of CSFM and ABAQUS for deep beam 1A. Both software tools produced results that were close to the experimental data, with IDEA StatiCa predicting 1540 kips (6,850.2 kN) and ABAQUS 1573 kips (6,997 kN), resulting in discrepancies of 5.3% and 3.3%, respectively. This highlights the reliability and accuracy of both methods in predicting the behavior of deep beams, with ABAQUS showing slightly better alignment with experimental data.

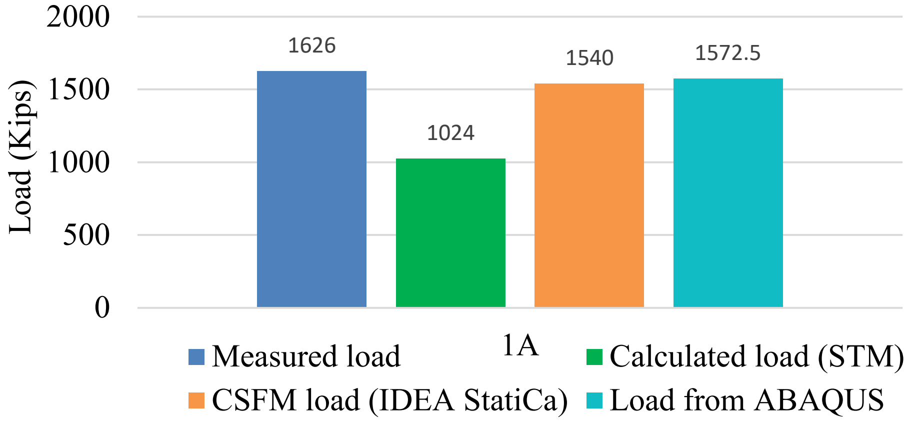

Figure 5.5: Comparison of measured, calculated (STM), maximum strength from IDEA StatiCa, and maximum strength from ABAQUS for baseline model (1A).

Load versus displacement curves for deep beam 1A (Figure 5.6) revealed that IDEA StatiCa tended to underestimate displacements compared to experimental data, likely due to simplifications in the analytical model. These differences may also be influenced by boundary conditions and material properties in the experiments.

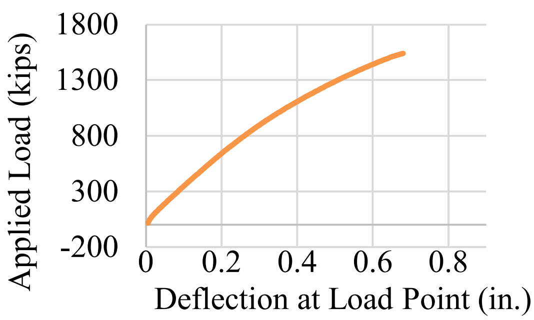

(b)

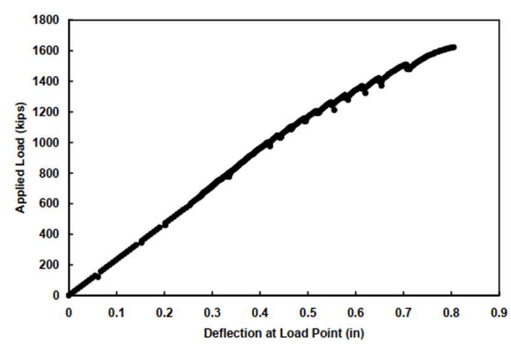

(b)

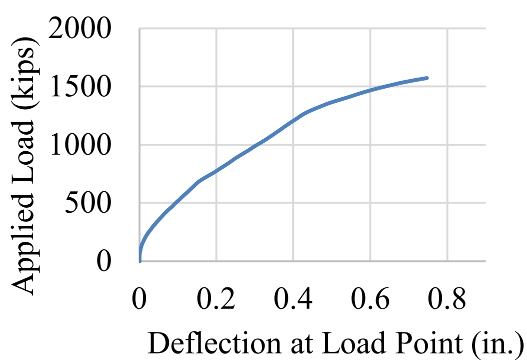

(c)

Figure 5.6: a) Calculated load versus displacement curve for Specimen 1A at $P_{IDEA\ StatiCa}$, b) measured load versus displacement curve for Specimen 1A (Huizinga, 2007), and c) estimated load versus deflection curve for specimen 1A using ABAQUS at 1573 kips (6,997 kN).

In summary, Chapter 2 demonstrates the reliability of IDEA StatiCa in predicting the load-carrying capacities and structural behavior of RC deep beams. While some discrepancies in displacement predictions were observed, the CSFM proved to be an accurate method for predicting stress distribution, load paths, and strain in reinforcement in a fraction of the time compared to ABAQUS as a traditional FEA method.

In Chapter 3, the performance of four reinforced concrete (RC) shear walls with varying sizes of openings was evaluated using the CSFM and the STM in accordance with ACI 318-19. The shear wall specimens, labeled N1, S1, M1, and L1, represent walls with progressively larger openings. The results were compared with the experimental data, focusing on the capacity of the shear walls to resist lateral loads.

Figure 5.7 illustrate the lateral load-carrying capacities as obtained from the three methods: measured capacity, STM analysis, and CSFM analysis using IDEA StatiCa. The experimental results showed a consistent trend where the load capacity decreased as the size of the openings increased. For example, shear wall specimen N1, which had no opening, achieved the highest measured capacity of 1179 kN (265.05 kips), while specimen L1, with the largest opening, demonstrated a significantly lower capacity of 686 kN (154.22 kips). This pattern was mirrored in both STM and CSFM predictions, although with some discrepancies in the magnitude of the predicted capacities. The STM method generally produced conservative estimates of load capacity, consistently predicting lower strengths compared to the experimental results and CSFM calculations. In contrast, CSFM predictions were closer to the measured capacities, particularly for specimens N1 and S1.

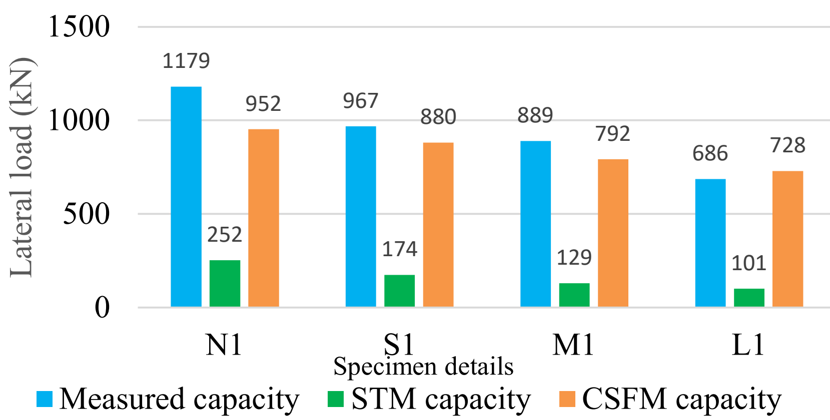

Figure 5.7: Comparison of Measured, STM, and CSFM capacities for load acting in the positive direction.

Among the specimens, Specimen L1 was selected as the baseline model, with its capacity analyzed using ABAQUS and compared against the measured capacity, STM, and CSFM. Figure 5.8 presents a comparison of lateral load capacities for this specimen. The ABAQUS simulation yielded a capacity of 550 kN (123.65 kips), which is 80.2% of the measured capacity (686 kN). The CSFM, however, predicted a capacity of 728 kN, exceeding the measured capacity by 6.1%. This suggests that the CSFM overestimated the strength of the specimen. In contrast, the STM provided a much lower estimate of 101 kN, representing only 14.7% of the actual measured capacity, indicating a significant underestimation. The CSFM's higher estimate suggests that it missed capturing certain failure mechanisms or boundary conditions that were present in the experimental test.

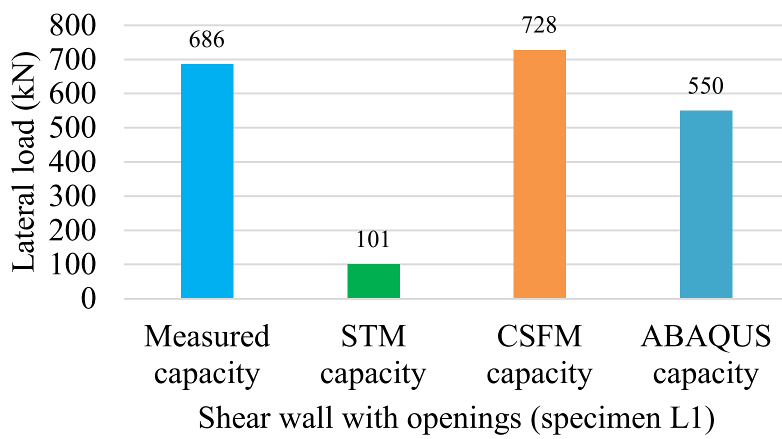

Figure 5. 8: Comparison of measured, calculated STM, CSFM, and ABAQUS capacities for baseline model L1.

When lateral loads acted toward negative x direction, however, CSFM tended to slightly overestimate the capacities compared to the experimental data for walls with openings, such as S1, M1 and L1, as illustrated in Figures 5.9.

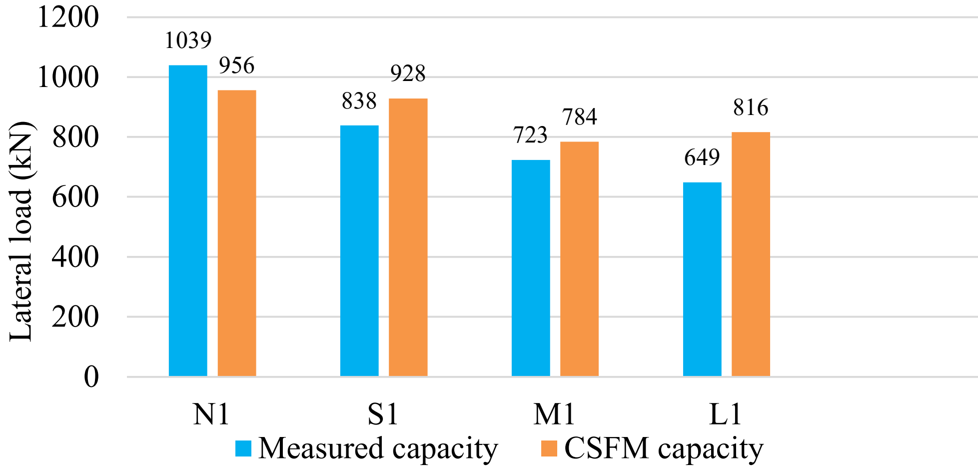

Figure 5.9: Comparison of measured and CSFM capacities for lateral load acting in the negative x direction.

Overall, Chapter 3 confirms that CSFM, as implemented in IDEA StatiCa, provides reliable predictions for the capacity of RC shear walls with openings under lateral load, closely aligning with experimental data. STM, while useful for conservative design, tended to underestimate capacities, especially for walls with larger openings. These findings further validate CSFM as an effective tool for analyzing RC structures with complex geometries and discontinuities caused by openings.

In Chapter 4, the structural behavior of four walking column examples (Examples 1 through 4) was evaluated using STM based on ACI 318-19, CSFM, and the traditional FEA method using ABAQUS. Walking Column Example 1 was chosen as the baseline model for comparative analysis. Each column was subjected to vertical loading, with strength reduction factors (ϕ) applied in the STM analysis in line with ACI 318-19. For CSFM, uniform strength reduction factors were applied to both concrete and steel, though ACI 318-19 does not prescribe a uniform ϕ factor. Additionally, CSFM analyses were conducted without ϕ values to explore the maximum capacities of the columns. The capacity comparisons are presented in Figures 5.10 and 5.11, contrasting the outcomes of ACI 318-19, STM, and CSFM, with and without ϕ values. These figures clearly illustrate the variations in capacity estimates across the different methods.

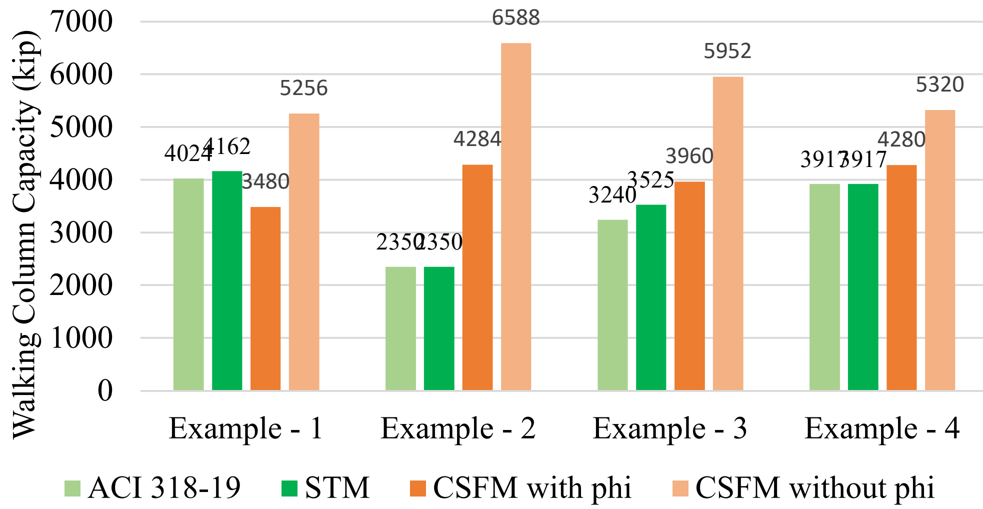

Figure 5.10: Capacity comparison for walking column examples.

The capacity results for Walking Column Example 1 are particularly noteworthy. As shown in Figure 5.11, ABAQUS predicted the highest capacity at 4300 kips (19,079 kN), with STM closely following at 4158 kips (18,503 kN). By contrast, CSFM with ϕ predicted a more conservative value of 3480 kips (15,481 kN), approximately 19.1% lower than ABAQUS. Notably, when strength reduction factors were excluded, CSFM predicted a significantly higher capacity of 5256 kips (23,379 kN), exceeding the STM prediction by 26.4%.

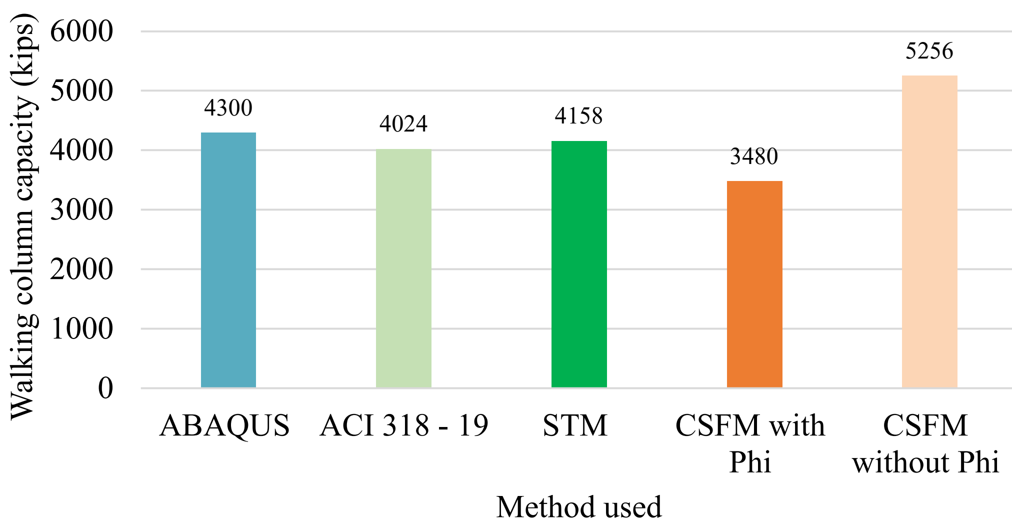

Figure 5.11: Capacity comparison with ABAQUs for walking column example 1.

These comparisons confirm that ABAQUS consistently offers the highest capacity estimates, reflecting its ability to model complex material behaviors. STM, while slightly more conservative, aligns closely with ABAQUS, validating its reliability for structural analysis. In contrast, CSFM with ϕ values presents a more conservative approach, producing lower capacity estimates compared to both ABAQUS and STM. This conservative prediction from CSFM with ϕ values highlights its focus on ensuring structural safety by incorporating strength reduction factors. It proves particularly valuable in design scenarios where conservative estimates are essential to account for uncertainties in material properties and loading conditions.

In conclusion, the analysis in Chapter 4 emphasizes the importance of using multiple methods to fully assess the behavior of walking columns. CSFM, especially without strength reduction factors, demonstrates its utility in predicting higher capacities and identifying failure modes, while ABAQUS provides the most comprehensive estimates of structural behavior. Together, these methods provide a thorough understanding of the performance and safety of walking columns, contributing to better design decisions.

Overall, the IDEA StatiCa's CSFM method showed strong alignment with experimental results and ABAQUS simulations for predicting the capacities of reinforced concrete structures. However, there are areas where improvements could enhance its usability and precision. In summary:

- CSFM provided highly reliable predictions of load-carrying capacities across a range of reinforced concrete structural members with discontinuities (corbels, deep beams, shear walls, and walking columns), often matching or surpassing the precision of traditional STM methods.

- CSFM's ability to integrate stress distribution and load path analysis proved highly effective, particularly for structures with discontinuities (e.g., openings in shear walls).

- The use of CSFM in design ensures both safety and performance optimization by offering more conservative predictions with strength reduction factors, allowing for robust structural design.

- CSFM tended to produce conservative capacity estimates when strength reduction factors (ϕ) were applied, particularly for walking columns, where it underestimated capacities relative to ABAQUS and even STM in some cases.

- Displacement predictions were generally lower than experimental results, particularly in corbel and deep beams, indicating potential oversimplifications in the modeling assumptions. This could be correlated to 2D nature of the CSFM method.

- The method's handling of material properties and boundary conditions could be refined to further align with experimental behavior, as slight overestimation or underestimation of capacities occurred for certain specimens (e.g., shear walls with large openings).
- The meshing algorithm can be revised. The sensitivity of the results to mesh size was observed in a few cases.
- The IDEA StatiCa software package (i.e., version 24) lacks full incorporation of the ACI code. The complete integration would enhance its reliability for US engineers.

Finally, the IDEA StatiCa website with numerous examples and theoretical backgrounds is an invaluable source for beginners and learners. However, the materials could be better categorized to make them easier to navigate and find. Perhaps restructuring the content into more defined sections or adding a more intuitive search/filter system could help users access the right materials more quickly.